Developments of High-speed Near-infrared Fourier-domain Mode-locking Optical Coherence Tomography for Clinical Applications

Rui Yuan

A thesis submitted in partial fulfilment of the requirements for the degree of Doctor of Philosophy

The University of Sheffield
Faculty of Engineering
Department/School of Electrical and Electronic Engineering

Jan 2025

List of Contents

Please ensure that the following is included in your declaration:

I, the author, confirm that the Thesis is my own work. I am aware of the University's Guidance on the Use of Unfair Means (www.sheffield.ac.uk/ssid/unfair-means). This work has not been previously presented for an award at this, or any other, university.

Please ensure that any publications arising from the thesis are acknowledged in this section.

[1] R. Yuan, D. Revin, R. Byers, and S. Matcher, "Towards cutaneous blood flow velocity estimation using VISTA processing on a 1.6 MHz FDML OCT system," in Biomedical Spectroscopy, Microscopy, and Imaging III, 2024, vol. 13006: SPIE, pp. 77-83.

[2] R. Yuan, R. Byers, D. Revin, and S. Matcher, "Rapid measurement of epidermal thickness with a 1.6 MHz FDML OCT system," in Biomedical Spectroscopy, Microscopy, and Imaging III, 2024, vol. 13006: SPIE, pp. 252-257.

[3] F. S. Hooper, R. Yuan, D. G. Revin, D. O. Anumba, and S. J. Matcher, "Optical design and simulation of a cervical scanning probe for polarization-sensitive optical coherence tomography using Ansys Zemax OpticStudio," in European Conference on Biomedical Optics, 2023: Optica Publishing Group, p. 126321U.

Acknowledgements

I have saved this section for last, marking the near completion of my PhD thesis. The four months of writing have left me utterly exhausted, but I still feel genuinely happy and proud of myself. Unknowingly, my PhD journey has reached its end. Looking back over these four years, I feel my greatest achievement lies not only in academic progress but also in the process of self-discovery, self-reflection, character building, and learning to embrace solitude. Of course, this journey would not have been possible without the support and help of many people.

First and foremost, I would like to express my heartfelt gratitude to my supervisor, Prof. Stephen Matcher. As my guide in the field of OCT, he has provided me with invaluable advice and direction in research. Under his leadership, our lab offers a relaxed yet academically stimulating environment where I was able to explore my potential and continuously learn.

I am also deeply grateful to Dr. Dmitry Revin, whose rich engineering experience has been a tremendous help to me. Our many conversations, spanning a variety of topics, not only improved my spoken English but also made my lab life engaging and enjoyable.

I extend my sincere thanks to Dr. Robert Byers for his selfless sharing and willingness to help, which significantly improved my programming skills. This was crucial for the achievements in my PhD research.

I wish to thank Dr. Wei Li, who, despite being in the lab only during my first year, helped me adapt quickly to the research environment and guided me in getting started.

I am also thankful to the members of the Sheffield dermatology team—Simon, Abi, Kirsty, and others—who greatly contributed to the success of my clinical research.

My heartfelt thanks go to my colleagues, Sophie and Tayclyn, whose companionship made the PhD journey less monotonous.

I am equally grateful to all the friends I met during my PhD—Yaoxun, Aek, Tian, Sha, Zhipeng, Jackey, Rock, Guanbo, Weiqian, Huanyu, Han, and many more.

Above all, I want to express my deepest gratitude to my parents and other family members for their unwavering support. They have always been my safe harbor.

Lastly, I sincerely thank the Faculty of Engineering at the University of Sheffield for providing me with a full scholarship, which allowed me to focus on my studies without financial worries and successfully complete my PhD. I am also grateful to the funding bodies — the Engineering and Physical Sciences Research Council (EPSRC) (EP/S025944/1), the National Institute for Health and Care Research (NIHR) Sheffield Biomedical Research Centre (NIHR203321), and the Kuwait Ministry of Health (187150) — for supporting this research.

Abstract

Optical coherence tomography (OCT) has gained significant attention in both medical and non-medical fields due to its non-invasive, real-time, three-dimensional, in-vivo, and multi-functional imaging capabilities. In dermatology, OCT enables the visualisation of tissue microstructure, vasculature, and collagen distribution, making it highly effective for diagnosing and monitoring conditions such as skin cancers and inflammatory diseases. However, the slow scan rates of commercial systems limit the acquisition speed of functional information.

This thesis addresses that challenge through the development of a high-speed near-infrared Fourier-domain mode-locked (FDML) OCT system tailored for clinical dermatological applications. Chapter 2 presents the system, which achieves an ultrahigh A-scan rate of 1.67 MHz, with axial and lateral resolutions of ~13 μm and ~25 μm respectively, sensitivity of ~100 dB, and imaging depth of ~4.8 mm in air. Real-time imaging and data acquisition are enabled through custom software, and the system's capability is demonstrated through in-vivo imaging of various skin sites.

Chapter 3 demonstrates rapid measurement of skin biomarkers, including epidermal thickness and vascular morphology, using custom automated segmentation and OCT angiography algorithms. Chapter 4 presents the first application of variable interscan time analysis (VISTA) for quantifying cutaneous blood flow using an FDML OCT system. A novel auto-fitting method is also introduced into the VISTA framework, improving the accuracy of decorrelation coefficient estimation.

Chapter 5 proposes a novel algorithm for skin topographical matching to enable precise re-scanning of treated sites. This is the first OCT-based approach that automatically estimates matching scores to support longitudinal skin monitoring.

Additionally, this FDML OCT system is combined with an in-house designed colposcopic scanning probe to aid in its alignment and characterisation.

Finally, Chapter 6 summarises the system's development and discusses its potential applications and future extensions. This high-speed FDML OCT system demonstrates readiness for translation into dermatological clinics.

Table of Contents

List of Tables

List of Figures

Glossary of Terms

The following terms are arranged in the order in which they first appear in the main text.

OCT: optical coherence tomography

SiC: silicon carbide

HFUS: high-frequency ultrasound

RCM: reflectance confocal microscopy

MPT: multiphoton tomography

CARS: coherent anti-Stokes Raman scattering

FOV: field of view

SS-OCT: swept-source optical coherence tomography

LC-OCT: line-field confocal optical coherence tomography

SD-OCT: spectral-domain optical coherence tomography

SC: stratum corneum

SL: stratum lucidum

UV: ultraviolet

DEJ: dermal-epidermal Junction

NMSC: non-melanoma skin cancers

$I_D(k)$: the photocurrent of a photodetector in an optical coherence tomography system

ρ: the responsivity of a photodetector (unit: amperes/watt)

k: wavenumber, the spatial frequency of a wave

$S(k)$: the power spectral dependence of light source

R_R: the power reflectivity of reference reflector in an optical coherence tomography system

R_{Sn} (n=1,2,3...): the power reflectivity of sample reflectors in an optical coherence tomography system, the subscript 'n' denotes the various depth of sample

z_R: the path length from the beam splitter to reference reflector in an optical coherence tomography system

z_{S_n}: the path length from the beam splitter to sample reflectors in an optical coherence tomography system

TD-OCT: time-domain optical coherence tomography

cw: continuous wave

FD-OCT: Fourier-domain optical coherence tomography

CCD: charge-coupled device

CMOS: complementary metal-oxide-semiconductor

$\sqrt{R_S(z_S)}$: the internal sample electric field reflectivity profile

$i_D(z)$: the inverse Fourier transform of $I_D(k)$

$\otimes$: a mathematical operation of convolution

$S(k)$: the normalized Gaussian function

$\gamma(z)$: the coherence function, namely the inverse Fourier transform of a normalized Gaussian function $S(k)$

k_0: the central wavenumber of the light source spectrum

Δk: the half-width of the light source spectrum at $1/e$ of maximum

z: the path length

OCTA: optical coherence tomography angiography

RBC: red blood cell

N: the total number of acquisitions at the same location

x: lateral index

z: depth index

T: the time interval

$Flow_{PV}$: the phase variance of the flow signal measured by a Doppler optical coherence tomography

$\Delta\emptyset$: the phase difference

$\overline{\Delta\emptyset}$: the mean phase difference

$Flow_{SV}$: the amplitude or intensity speckle variance of the flow signal measured by a Fourier-domain optical coherence tomography

I: the intensity of light

$\bar{I}$: the mean intensity of light

OMAG: optical microangiography

$Flow_{OMAG}$: the complex-signal-based variance of the flow signal measured by an optical coherence tomography based microangiography

C: the complex signal

$\bar{C}$: the mean complex signal

AD: atopic dermatitis

TCS: topical corticosteroid creams

FDML: Fourier-domain Mode-locking

MEMS: micro-electromechanical systems

VISTA: variable interscan time analysis

$T_{roundtrip}$: the round-trip time of the light within the cavity of a tunable laser

$T_{filter\ drive}$: the period of one cycle that the tunable optical bandpass filter is periodically driven to transmit the light at selected spectral position in a tunable laser

dB: decibel, a logarithmic unit used to measure signal level

SM: single-mode

SOA: semiconductor optical amplifier

DAC: digital-to-analogue converter

Pk-Pk: peak-to-peak

DC: direct current

TTL: transistor-transistor logic

VDD: voltage drain drain, the drain or positive supply voltage

VDC: volts direct current, the voltage required to create a direct current (DC) circuit

GND: ground

EN: enable

FCLK: filter clock

BDQ: bias-differential quad-channel

PC: polarization controller

ND: neutral density filter

ROI: region of interest

AR: anti-reflection

UVFS: ultra-violet fused silica

OD: optical density

OPD: optical path difference

InGaAs: indium gallium arsenide

GS/s: gigasamples per second, a unit of the digitizing rate measurement

RIN: relative intensity noise (unit: dB/Hz)

SNR: signal-to-noise ratio

AEL: accessible emission limit

FFT: fast Fourier transform

λ: wavelength

PSF: point spread function

FWHM: the full width at half maximum

λ_0: the centre wavelength of a laser spectrum

$\Delta\lambda$: the measured full width at half maximum of a laser spectrum

NA: numerical aperture

D: the entrance pupil diameter of an objective

f: the effective focal length of an objective

USAF: United States Air Force

DOF: depth of field

d_{shot}: the shot noise density in an optical coherence tomography system (unit: A/$\sqrt{\text{Hz}}$)

e: the electronic charge

$d_{detector}$: the detector noise density in an optical coherence tomography system (unit: A/$\sqrt{\text{Hz}}$)

NEP: the noise-equivalent power

ADC: analogue-to-digital converter

$d_{digitizer}$: the digitizer noise density in an optical coherence tomography system (unit: A/$\sqrt{\text{Hz}}$)

V_{max}: the maximum single-side voltage range of the analogue-to-digital converter

X: the analogue-to-digital sampling rate

n: the number of bits of the analogue-to-digital converter

G: the transimpedance gain of the photodetector

σ_{RIN}^2: the relative intensity noise variance of the laser output power

B: the detection bandwidth of an optical coherence tomography system

i: the mean detector photocurrent

σ_{total}^2: the total noise variance

$\sigma_{digitizer}{}^2$: the digitizer noise variance

$\sigma_{detector}{}^2$: the detector noise variance

$\sigma_{shot}{}^2$: the shot noise variance

$\langle I_D \rangle^2$: the mean-square peak signal power detected by the photodetector

I_S: the power reflected from the sample arm

I_R: the power reflected from the reference arm

m: the number of spectral sampling channels

σ^2: the detected noise variance of an optical coherence tomography system

d_{RIN}: the relative intensity noise density in an optical coherence tomography system (unit: A/$\sqrt{\text{Hz}}$)

SNR_{shot}: shot-noise-limited signal-to-noise ratio

F: the A-scan rate of the FDML laser

δ_λ: the average spectral sampling interval

USB: universal serial bus

PCIe: peripheral component interconnect express, a type of connection used for high-speed data transfer between electronic components

ΔT: a parameter used to adjust the time interval for angiographic imaging using the FDML optical coherence tomography system

RT: resampling table

NaN: not a number

SV: speckle variance

$OCTA_{normalized}$: the normalised mean amplitude difference of optical coherence tomography signal

M: the number of consecutive B-scan repetitions in a time series of B-scan repetitions with a total number of N

Δt: the fundamental interscan time

A_i: the amplitude matrix of the i^{th} repeated B-scan.

Var: the variance of the signal amplitude

$OCTA_{SV}$: the mean variance of the signal amplitude

LDF: laser Doppler flowmetry

SVOCT: speckle variance optical coherence tomography

CMOCT: correlation mapping optical coherence tomography

SSADA: split-spectrum amplitude-decorrelation angiography

SLS: sodium lauryl sulphate

$D_{normalized}$: the normalized decorrelation

α: the temporal autocorrelation decay or decorrelation constant/coefficient

R^2: coefficient of determination

UREC: University Research Ethics Committee

OOF: Optimally Oriented Flux

3D: three-dimensional

GPU: graphics processing unit

θ: the angle between the direction of a blood vessel and the B-scan plane

CPU: central processing unit

SSD: solid-state drive

PBS: polarisation beam splitter

QWP: quarter-wave plate

PMC: polarisation-maintaining coupler

Δz: optical path length difference

PS: polarisation-sensitive

PS-OCT: polarisation-sensitive optical coherence tomography

1. Introduction and Literature Review

1.1. Introduction

Optical Coherence Tomography (OCT) is a versatile imaging modality initially developed for medical diagnostics but is now widely adopted across various fields [1]. By detecting the echoes of backscattered light, OCT can generate high-resolution, depth-resolved cross-sectional and three-dimensional volumetric images of materials and structures. These capabilities make it a valuable tool for both biological and non-biological applications [2-5].

Beyond medicine, OCT has broad applications in industrial inspection and material science [6, 7]. Its ability to image subsurface structures in situ and in real-time makes it ideal for quality control in manufacturing [8, 9], such as detecting defects in multilayered materials [10], inspecting microelectronics [11], monitoring pharmaceutical film coatings [12], assessing ceramics [13], and tracking the process in laser beam welding [14]. In the semiconductor industry, OCT can be employed to measure structural parameters, identify defects, and investigate the formation mechanisms of devices such as fabricated semiconductor optical waveguides [15] and silicon carbide (SiC) wafers [16].

In cultural heritage and art conservation, OCT can help analyse, preserve, and clean historical artefacts by imaging subsurface layers of paintings, manuscripts, and other delicate objects without causing damage [17-20]. It provides insights into the techniques and materials used by artists, aiding both restoration and examination [21].

In aerospace and automotive industries, OCT can be used to inspect composite materials and detect delamination or voids in structural components. Its non-contact, high-speed imaging capability is particularly valuable for ensuring the integrity of

lightweight materials used in these sectors [22-25].

In biomaterials and tissue engineering, OCT can be utilized to evaluate the structure and integration of scaffolds and other engineered tissues. Its ability to monitor cell growth profiles and dynamic biological processes in real-time makes it a powerful tool in regenerative medicine research, supporting the development of new therapeutic strategies for repairing or regenerating damaged tissues and organs [26-30].

In agriculture, OCT can enable non-invasive imaging of plant structures, monitoring water transport, disease detection, and post-harvest quality control. It aids in seed analysis, soil-root interaction studies, and precision agriculture, improving crop health, sustainability, and yield through early stress detection and optimized resource management [31-35].

The versatility of OCT is further extended by functional enhancements such as Doppler OCT for flow measurements [36] and optical coherence elastography for assessing mechanical properties [37]. These advancements solidify its role as an indispensable tool across an expanding range of scientific and industrial domains.

In medicine, OCT has become a key tool in ophthalmology, widely used for diagnosing and managing retinal diseases, glaucoma, and corneal disorders [38-41]. It has also been applied to clinical fields including cardiology [42-44], dermatology [45-47], oncology [48-50], gastroenterology [51, 52], neurology [53, 54], dentistry [55, 56], and gynaecology [57, 58], providing real-time non-invasive imaging. This thesis focuses on the development of an OCT system for clinical diagnosis in dermatology.

1.2. Optical Coherence Tomography in Dermatology

Histopathology remains the gold standard for the morphological investigation of the skin, offering highly detailed structural and cellular information. However, it requires an invasive skin biopsy, causes tissue damage, and cannot be repeated at the same site [45, 59, 60]. To address these limitations, numerous non-invasive imaging modalities have emerged over the past decades, such as OCT, high-frequency ultrasound (HFUS), reflectance confocal microscopy (RCM), multiphoton tomography (MPT), coherent anti-Stokes Raman scattering (CARS) imaging, optoacoustic imaging, hyperspectral imaging, and terahertz imaging [47].

HFUS, typically employing ultrasound frequencies higher than 20 MHz, can enable submillimetre-resolution imaging of superficial anatomical structures, from the stratum corneum to the deep fascia. While HFUS offers good penetration depth in tissues, it lacks the spatial resolution necessary for detailed visualization of fine structures. Generally, higher ultrasound frequencies provide better resolution but at the cost of reduced penetration depth [61-65].

RCM can provide cellular resolution enface images of different skin layers through optical sectioning, but its imaging range is limited from the stratum corneum to the superficial dermis. The scan length of a single RCM image ranges from 0.2 to 1 mm, depending on magnification. However, commercial systems such as VivaScope 1500 and VivaScope 3000 can extend the field of view (FOV) to 8 × 8 mm^2 or unlimited coverage through mosaic scanning [66-68].

MPT and CARS allow molecular-level imaging but require expensive equipment and are time-intensive [69, 70]. Optoacoustic imaging and hyperspectral imaging are promising for functional imaging but are not yet widely adopted for clinical

dermatology due to limited resolution or complex instrumentation [71, 72]. Terahertz imaging, though useful for detecting skin hydration and other properties, suffers from low spatial resolution [73].

Among these techniques, OCT strikes a balance between resolution, penetration depth, and practicality. It provides non-invasive, high-resolution, cross-sectional images of the epidermis and dermis in real-time, with a penetration depth of 1–2 mm. The axial resolution of 1-15 μm also makes it able to detect sweat glands, sebaceous glands, hair follicles, blisters, and blood vessels [74]. While not as high-resolution as RCM or molecularly specific as CARS, OCT is faster, simpler to operate, and better suited for imaging both superficial and deeper skin structures. Extensions like Doppler OCT for blood flow imaging [75] and polarization-sensitive OCT for structural details [76] further enhance its utility.

Table 1.1 provides a comparison of various OCT setups with HFUS, RCM, and MPT, including their penetration depth, axial resolution, lateral resolution, and FOV. All the systems included are either commercially available or constructed using commercial components.

Table 1.1: Comparison of OCT setups with HFUS, RCM, and MPT in dermatology.

	Penetration depth (mm)	Axial resolution (μm)	Lateral resolution (μm)	FOV (mm)
HFUS [47, 61-65] (20-100 MHz)	25-0.15	80-17	250-33	16-8
RCM [66-68] (VivaScope 1500 / 3000, 830 nm diode laser)	< 0.35	1-5	0.5-1	Single: < 1 x 1 Mosaic: 8x8 / unlimited

MPT [69] (MPTflex, 710–920 nm laser)	0.2	< 2	< 0.5	0.35 x 0.35
SS-OCT [77, 78] (Vivosight DX, 1300 nm swept laser)	1	5.5	7.5	6 x 6
LC-OCT [77] (Damae Medical, 600-900 nm supercontinuum laser)	0.5	1.1	1.3	1.2 x 0.5
SD-OCT [78] (custom-made, 490-700 nm supercontinuum laser)	< 0.6	1	< 7	8 x 8

HFUS, high-frequency ultrasound; **RCM**, reflectance confocal microscopy; **MPT**, multiphoton tomography; **SS-OCT**, swept-source OCT; **LC-OCT**, line-field confocal OCT; **SD-OCT**, spectral-domain OCT.

1.2.1. OCT Imaging of Skin

OCT was first employed for skin imaging in 1997 [79]. The skin, as an easily accessible organ, presents unique imaging challenges due to its highly scattering properties [74]. Unlike transparent tissues such as the eye, skin's strong scattering attenuates light intensity and limits imaging depth. The choice of central wavelength significantly affects penetration depth and resolution. Longer wavelengths penetrate deeper, but water absorption reduces signal intensity. The minimum absorption window (700–1300 nm) and a secondary low-absorption window (around 1700 nm) are most suitable for skin imaging [80].

As shown in **Table 1.1**, OCT systems operating at wavelengths below 1 μm can achieve axial resolutions as fine as 1 μm but are limited to penetration depths of less than 0.6 mm [77, 78]. In contrast, near-infrared OCT systems (typically operating at

1300 nm) can penetrate up to 2 mm into tissue, albeit with a reduced axial resolution of approximately 10 μm [81]. This trade-off between resolution and penetration depth must be balanced to address specific diagnostic requirements in dermatology.

1.2.2. Key Skin Biomarkers of OCT in Dermatology

The skin comprises three primary layers: the epidermis, dermis, and hypodermis (**Figure 1.1**). The epidermis itself is composed of multiple sublayers, including the stratum corneum (SC) and stratum lucidum (SL) [60, 82]. Since the hypodermis is typically located deeper than 2 mm, it falls beyond the detection range of OCT. However, in regions where the dermis is thin, the low-reflectivity hypodermis may appear in the lower portions of OCT images [74].

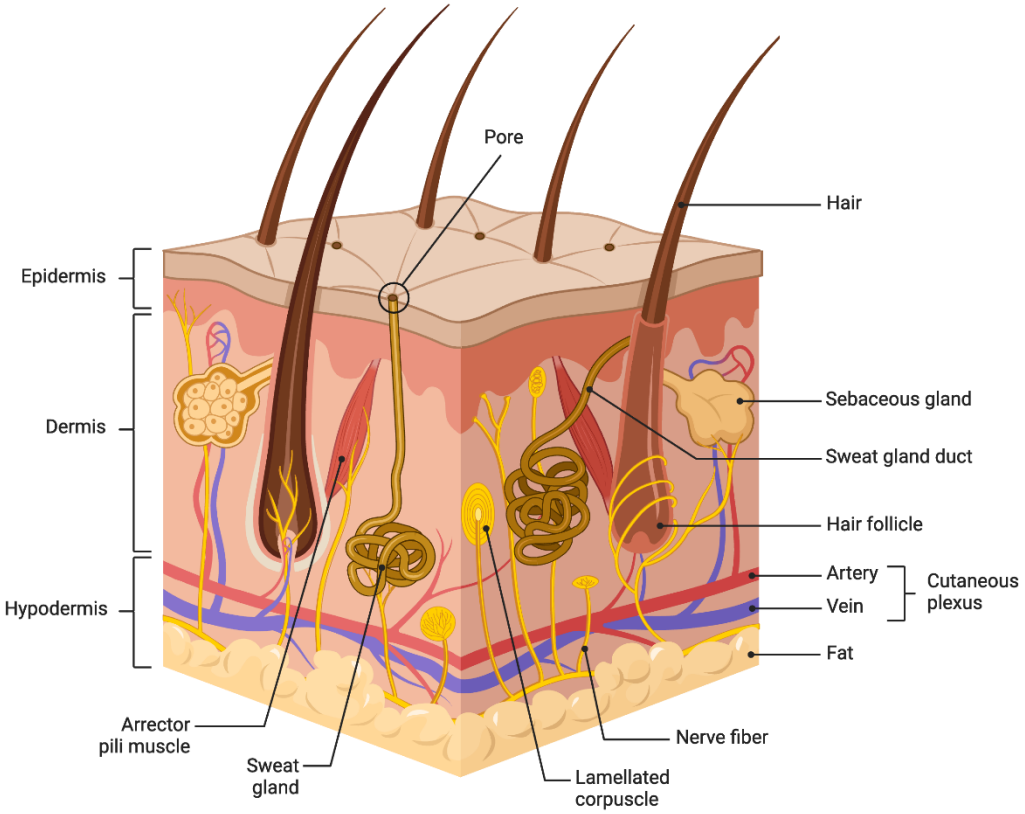

Figure 1.1: Structure of skin showing three primary layers: epidermis, dermis, and hypodermis.

This section focuses primarily on the epidermis and dermis and their corresponding biomarkers relevant to dermatological diagnosis using OCT:

1) Stratum Corneum (SC) Thickness: The SC is the outermost layer, serving as a barrier against UV radiation, dehydration, and penetration of external substances [83]. Its thickness ranges from 10–30 μm on dorsal skin [83] to several hundred microns on palmar surfaces [59]. The SC appears less bright than the epidermis and surface in OCT images due to its low scattering properties, allowing precise measurement of its thickness. SC thickness serves as a biomarker for skin barrier function, hyperkeratosis, and wound healing [46].
2) Epidermal Thickness: The epidermis typically ranges from 50 to 100 μm in thickness, with the dermis extending up to 2000 μm or more [46]. The epidermis exhibits less intense OCT signals compared to the dermis [45]. Measuring epidermal thickness is essential, as abnormal thickening can indicate conditions such as psoriasis, eczema, or dysplasia [84].
3) Dermo-epidermal Junction (DEJ): At the interface of the epidermis and dermis lies the dermo-epidermal junction, a critical site for diagnosing conditions such as epidermolysis bullosa [84]. The DEJ also serves as a reference for accurate epidermal thickness measurements.
4) Dermis and Vascular Features: The dermis shows strong OCT signals interspersed with low-reflecting areas corresponding to hair follicles and sebaceous glands [74]. Superficial blood vessels within the dermis can be visualized using angiographic OCT, which enables the detection of vascular depth, diameter, morphology, and blood flow—important biomarkers for diagnosing inflammatory and vascular skin diseases [85].
5) Collagen in Dermis: Collagen, a key structural component of the dermis, is

highly birefringent. Its optical properties can be studied using polarization-sensitive OCT, which is particularly valuable for assessing burn injuries, as collagen denaturation by heat results in a loss of birefringence [46].

1.2.3. Applications of OCT in Dermatology

The integration of structural and functional imaging capabilities establishes OCT as an essential tool in dermatological research and clinical practice. This section reviews the primary applications of OCT in dermatology [45, 47, 59, 60, 74, 86]:

1) Skin cancer diagnosis: OCT is particularly effective for assessing non-melanoma skin cancers (NMSC), such as basal cell carcinoma and squamous cell carcinoma. It enables visualization of tumor margins, depth of invasion, and structural alterations, aiding in diagnosis and treatment planning. This reduces reliance on biopsies for monitoring and follow-up.
2) Inflammatory skin conditions: In diseases like psoriasis, atopic dermatitis, and eczema, OCT can provide quantitative data on skin thickness, vascularity, and structural changes. Doppler OCT further aids in visualizing blood flow, offering insights into the degree of inflammation and therapeutic response.
3) Cosmetic dermatology: OCT can be used to assess skin aging, collagen structure, and treatment effects. It helps monitor changes in skin structure following procedures like chemical peels, laser therapies, and fillers, ensuring precise and effective cosmetic interventions.
4) Tattoo imaging: OCT can be utilized for detailed imaging of pigment distribution in the dermis, making it a valuable tool for evaluating tattoo removal processes and monitoring pigment clearance after laser treatment.
5) Treatment monitoring and drug delivery: OCT can play a vital role in monitoring the effectiveness of topical treatments and transdermal drug delivery

systems. It tracks the structural changes in the skin and evaluates the penetration depth of delivered agents.

6) Wound healing and scar assessment: OCT has been used to monitor healing dynamics in wounds and assess scar formation over time. Its non-invasive nature makes it ideal for repeated evaluations without disrupting the healing process.

1.3. Theory of Optical Coherence Tomography

1.3.1. Optical Coherence Tomography

Optical coherence tomography (OCT) has become a powerful imaging technique in the biomedical field since it was first proposed in 1991 by Huang et al based on the principle of low-coherence interferometry [1]. **Figure 1.2** illustrates the schematic of a generic fibre-optic OCT system adopting a simple Michelson interferometer. A low-coherence light source emits light that is split by a fibre coupler into two beams. These beams are directed into the reference arm and sample arm, respectively, via optical fibres. After interacting with the reference mirror and the sample, the two beams are reflected back and recombined by the fibre coupler before propagating to a detector or photoreceiver [87].

The detector converts the optical signals into electronic signals, producing coherence fringes or a spectral interference pattern. Through signal processing, this spectral interference pattern is transformed into an A-scan, which represents the depth-resolved reflectivity profile of the sample at the focal spot of the sample beam for a fixed lateral position. When the scanning mirror in the sample arm moves or steps the focused beam across the sample along the X-axis, multiple A-scans are acquired and

compiled into a two-dimensional cross-sectional image of the sample, referred to as a B-scan. By extending the scanning process to both the X-axis and Y-axis, multiple B-scans are acquired along the Y-axis, forming a three-dimensional OCT volume dataset, commonly referred to as a C-scan. The scanning protocol for data acquisition is user-defined and can be customized to enable multidimensional scanning based on the specific imaging requirements.

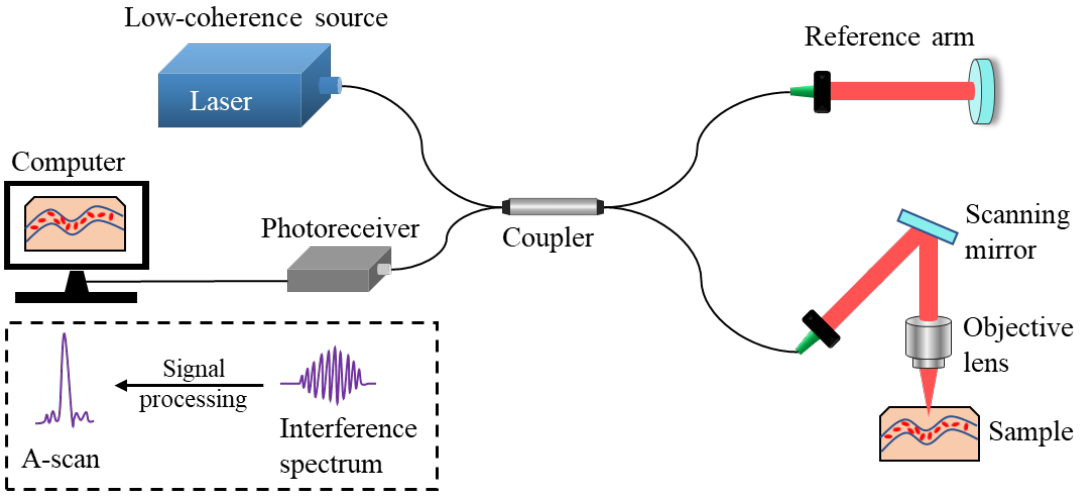

Figure 1.2: Schematic of a generic fibre-optic OCT system.

Assume that the detector in **Figure 1.2** is a square-law detector, it produces a photocurrent proportional to the square of the sum of the electric fields of two returning beams. This photocurrent ($I_D(k)$) of the detector can be explained and simplified as:

$$I_D(k) = \frac{\rho}{4}\left[S(k)[R_R + R_{S1} + R_{S2} + \cdots]\right] + \frac{\rho}{2}\left[S(k)\sum_{n=1}^{N}\sqrt{R_R R_{Sn}}(\cos\left[2k(z_R - z_{S_n})\right])\right] + \frac{\rho}{4}\left[S(k)\sum_{n\neq m=1}^{N}\sqrt{R_{Sn}R_{Sm}}(\cos\left[2k(z_{Sn} - z_{Sm})\right])\right] \quad (1.1)$$

where ρ is the responsivity of the detector (units amperes/watt), k is wave number, $S(k)$ is the power spectral dependence of light source, R_R and R_{Sn} (n=1,2,3...) are power reflectivities of reference and sample reflectors respectively, the subscript 'n' denotes the various depth of sample, and z_R and z_{S_n} are the path length from the beam splitter to reference and sample reflectors respectively [87].

Equation 1.1 describes the spectral interferogram, which forms the basis for further analysis in OCT.

1.3.2. Fourier-domain Optical Coherence Tomography

The traditional OCT setup, known as time-domain OCT (TD-OCT), employs a broadband continuous wave (cw) light source and a single-channel (spectrally integrating) detector. In TD-OCT, the reference arm length is scanned periodically, and the signal processing involves detecting the envelope of the fringe burst pattern generated by constructive interference between the reference arm light and successive scattering sites within the sample. However, the periodic scanning of the reference arm significantly limits the acquisition speed of TD-OCT. To overcome this limitation, Fourier-domain techniques have been introduced to OCT [88].

Based on the type of low-coherence light source and detector used (as illustrated in **Figure 1.2**), Fourier-domain OCT (FD-OCT) can be categorized into spectral-domain OCT (SD-OCT) and swept-source OCT (SS-OCT). In SD-OCT, a broadband light source is employed, and all spectral components of $I_D(k)$ are collected simultaneously using an array detector at the output of a spectrometer, such as a charge-coupled device (CCD) or complementary metal-oxide-semiconductor (CMOS) camera. In contrast, SS-OCT utilizes a narrowband swept-laser source, and the spectral components of $I_D(k)$ are captured sequentially by recording the signal with a single

detector over time, synchronized with the wavenumber sweeping of the laser. In both SD-OCT and SS-OCT, the reference arm length remains fixed and corresponds to the length of the sample arm. Despite differences in capturing the photocurrent of the interference spectrum, the signal processing used in SD-OCT and SS-OCT are identical [87].

In FD-OCT, the wavenumber-dependent photocurrent $I_D(k)$ from Equation 1.1 is processed using the inverse Fourier transform to estimate the sample field reflectivity profile $\sqrt{R_S(z_S)}$. The inverse Fourier transform of $I_D(k)$ is given by:

$$i_D(z) = \frac{\rho}{8}[\gamma(z)[R_R + R_{S1} + R_{S2} + \cdots]] + \frac{\rho}{4}\left[\gamma(z) \otimes \sum_{n=1}^{N} \sqrt{R_R R_{Sn}}\left(\delta\left[\left(z \pm 2\left(z_R - z_{S_n}\right)\right)\right]\right)\right] + \frac{\rho}{8}\left[\gamma(z) \otimes \sum_{n \neq m=1}^{N} \sqrt{R_{Sn} R_{Sm}}\left(\delta\left[\left(z \pm 2(z_{Sn} - z_{Sm})\right)\right]\right)\right] \quad (1.2)$$

where $\otimes$ represents convolution, and $\gamma(z)$ is the coherence function, namely the inverse Fourier transform of a normalized Gaussian function $S(k)$ [87].

The coherence function $\gamma(z)$ governs the axial point spread function (PSF) in OCT imaging systems. The PSF is typically characterized by its full width at half the maximum (FWHM), which defines the round-trip "coherence length" of the light source. The coherence function $\gamma(z)$ can be expressed as:

$$\gamma(z) = e^{-(z)^2 \Delta k^2} \overset{F}{\leftrightarrow} S(k) = \frac{1}{\Delta k \sqrt{\pi}} e^{-\left[\frac{(k-k_0)}{\Delta k}\right]^2} \quad (1.3)$$

where k_0 is the central wavenumber of the light source spectrum, Δk is the half-

width of the spectrum at $1/e$ of maximum and z is the path length [87].

By performing the convolutions in Equation 1.2 and utilizing the sifting property of the delta function, the result of the interferometric measurement, known as the "A-scan", is obtained:

$$i_D(z) = \frac{\rho}{8}[\gamma(z)[R_R + R_{S1} + R_{S2} + \cdots]] + \frac{\rho}{4}\sum_{n=1}^{N}\sqrt{R_R R_{Sn}}\left[\gamma\left[2\left(z_R - z_{S_n}\right)\right] + \gamma\left[-2\left(z_R - z_{S_n}\right)\right]\right] + \frac{\rho}{8}\sum_{n\neq m=1}^{N}\sqrt{R_{Sn}R_{Sm}}\left[\gamma\left[2\left(z_{S_n} - z_{S_m}\right)\right] + \gamma\left[-2\left(z_{S_n} - z_{S_m}\right)\right]\right] \quad (1.4)$$

The first, second, and third terms in Equation 1.2 and 1.4 are referred to as the DC terms, cross-correlation terms, and auto-correlation terms, respectively. The results of these equations, considering discrete sample reflectors and a Gaussian-shaped source spectrum, are illustrated in **Figure 1.3**(a). The DC terms produce a large artefactual signal centred at zero path length difference ($z = 0$) with a FWHM of one coherence length. Since this DC-term artefact mainly originates from the reference mirror, it can be effectively removed by subtracting the recorded reference mirror signal from the detected spectral interferometric signal with the sample arm blocked [87].

The auto-correlation terms generate a series of weak artefacts at or near the zero-path length difference position. These artefacts arise from adjacent sample reflectors located within a coherence length. As the distance between reflectors in a sample is typically much smaller than the distance between the sample reflectors and the reference arm path length, the best way to eliminate auto-correlation artefacts is to ensure that the reference arm reflectivity is sufficiently high. This reduces the amplitude of the auto-correlation terms relative to the cross-correlation terms.

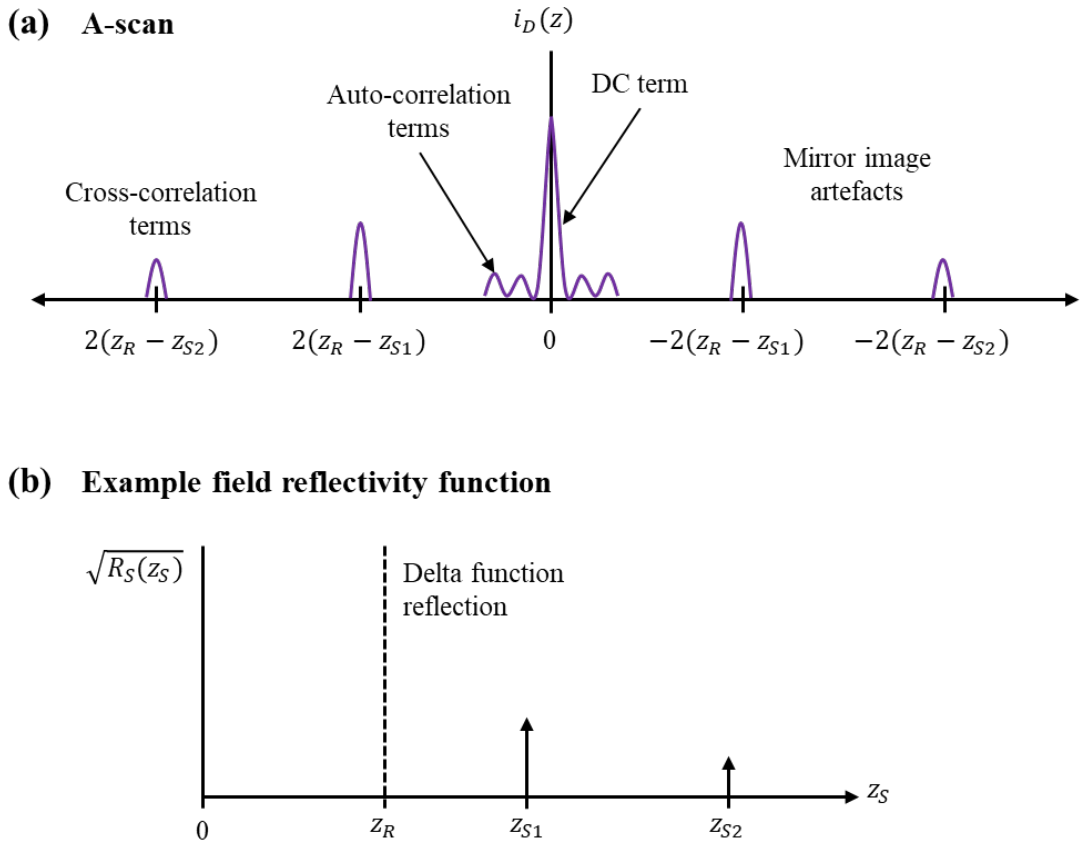

Figure 1.3: Illustration of Fourier process of Fourier-domain OCT [87]. (a) A-scan. (b) Example field reflectivity function.

The cross-correlation terms in **Figure 1.3**(a) include the internal sample reflectivity profile and its symmetric mirror image on the opposite side of zero path length, known as the complex conjugate artefact. To address this mirror artefact, the sample is positioned entirely on one side of the zero-path length, and only the positive sample reflectivity profile is used to generate the A-scan [38]. With the position of the reference reflector (z_R) fixed, the desired internal sample reflectivity profile can be expressed as $\sqrt{R_S(z_S)} = \sum_{n=1}^{N} \sqrt{R_{Sn}} \delta[(z_S - z_{S_n})]$), as shown in **Figure 1.3**(b) [87].

This project aims to develop an SS-OCT system using a swept light source. By eliminating the above artefacts, the approximate depth-resolved A-scan or internal

sample reflectivity profile can be obtained through Fourier analysis of the interference spectral photocurrent $I_D(k)$.

1.4. Theory of Optical Coherence Tomography Angiography

Optical coherence tomography angiography (OCTA) is a variant of optical coherence tomography (OCT) that utilizes specialized scanning protocols and algorithms. By detecting the backscattering signals from moving red blood cells (RBCs), OCTA can visualize the cell-perfused vasculature and provide vascular information without requiring exogenous contrast agents [89, 90].

OCTA operates on the principle of OCT by capturing a time series of reconstructed A-scan repetitions at the same spatial position with specific time intervals. In static tissue, these repeated A-scans remain unchanged, whereas in dynamic tissue, they exhibit time-dependent variations in amplitude and phase. Algorithms based on the difference or variance in these time-series A-scans allow for the segmentation of blood vessels from surrounding static tissue. This capability enables OCTA to provide information on vascular depth, diameter, density, and morphology. Furthermore, by analysing the temporal changes in these A-scans, OCTA can also offer insights into blood flow dynamics.

During A-scan reconstruction via Fourier transform, the OCT signal comprises amplitude (intensity) and phase components. Current OCTA algorithms leverage different aspects of these Fourier components and can be broadly categorized into three types: phase-based OCTA, amplitude-/intensity- based OCTA, and complex signal-based OCTA [90, 91].

1.4.1. Phase-based OCTA Algorithm

Phase-based OCTA algorithms rely on the Doppler phase shift of the OCT signal to distinguish dynamic and static tissue. In 2007, Finger et al. developed phase-variance OCT that measures the phase variance between adjacent B-scans [92]. The flow signal in phase-variance OCT is calculated by the following equation:

$$Flow_{PV}(x,z) = \frac{1}{N-1} \sum_{t=0}^{(N-2)T} \left[\Delta\emptyset(x,z,t) - \overline{\Delta\emptyset(x,z)}\right]^2 \quad (1.5)$$

$$\Delta\emptyset(x,z,t) = \emptyset(x,z,t+T) - \emptyset(x,z,t) \quad (1.6)$$

where N is the total number of acquisitions at the same location, x and z are lateral and depth indices respectively, T is the time interval, and $\Delta\emptyset(x,z,t)$ and $\overline{\Delta\emptyset(x,z)}$ represents the phase difference and its average over time respectively [90].

1.4.2. Amplitude-/Intensity- based OCTA Algorithm

Phase-based OCT initiated the functional extension of the OCT technique. However, this technique suffered from an angular dependence of the measured blood flow, and it was insensitive to the flow perpendicular to the scanning beam. To resolve this issue, an intensity-based method was proposed by measuring the speckle variance in the OCT signal. In 2008, Mariampillai et al. used interframe speckle variance based on FD-OCT to image the microcirculation [93]. The speckle variance signal can be defined as:

$$Flow_{SV}(x,z) = \frac{1}{N} \sum_{t=0}^{(N-1)T} \left[I(x,z,t) - \overline{I(x,z)}\right]^2 \quad (1.7)$$

where $I(x,z,t)$ and $\overline{I(x,z)}$ represents the intensity and its average over time respectively [90].

1.4.3. Complex-signal-based OCTA Algorithm

The third category utilizes both the intensity and phase information of the OCT signal to calculate the flow signal. The representative of complex-signal-based OCTA technique is optical microangiography, proposed first by Wang et al. in 2007 [88]. After phase compensation, the flow signal based on the OMAG algorithm is calculated by subtracting consecutive complex signals, as shown in the following equation:

$$Flow_{OMAG}(x,z) = \frac{1}{N}\sum_{t=0}^{(N-1)T}\left[C(x,z,t) - \overline{C(x,z)}\right]^2 \quad (1.8)$$

where $C(x,z,t)$ and $\overline{C(x,z)}$ represents the complex signal and its average over time respectively [90].

1.5. Thesis Overview

Atopic dermatitis (AD), also known as eczema, is a chronic inflammatory dermatological condition affecting up to 30% of children and 10% of adults in the UK. The estimated direct cost to the NHS for treating AD and its associated conditions exceeds £1 billion annually [94]. The current gold-standard treatment for AD involves topical corticosteroid creams (TCS), with over 6 million prescriptions issued annually in the UK. Additionally, AD patients often require repeated courses of oral antibiotics to manage infected skin lesions, a growing concern in the context of antimicrobial resistance [95].

The Sheffield dermatology research team focuses on developing and translating new treatments for atopic dermatitis into clinical practice. The team has pioneered the application of various OCT setups for imaging skin conditions, identifying useful

biomarkers for clinical diagnosis, and aiding the development of therapeutic interventions. For instance, Lu et al. quantitatively monitored epidermal thickness changes to evaluate the effects of two commercially available eczema treatments using a multi-channel OCT system (Michelson Diagnostics Ltd EX1301) operating at up to 20 kHz scan rates [95]. Furthermore, Byers et al. assessed the severity of clinical and subclinical AD by quantifying vascular depth and morphology of the superficial plexus with angiographic OCT, employing a multi-beam OCT system (Vivosight, Michelson Diagnostics Ltd, Orpington, Kent, UK) running at a 20 kHz scan rate [85]. Using the same Vivosight OCT system, Maiti et al. reported in vivo variations in skin morphological parameters such as thickness, roughness, and undulation concerning posture, gender, and site [82].

These studies indicate that the structural and angiographic information obtained using OCT can serve as valuable biomarkers for diagnosing skin conditions and monitoring topical treatments. However, the OCT systems employed in previous research operate at relatively slow scan speeds, resulting in prolonged acquisition times and discomfort for patients.

This thesis aims to address these limitations by developing an ultrahigh-speed OCT system for structural and angiographic detection, facilitating improved dermatological diagnosis.

The main research objectives of this thesis are:

- To design and construct a high-speed near-infrared FDML OCT system with improved temporal and spatial resolution for dermatological imaging.
- To achieve structural imaging of the skin by developing and implementing an automatic algorithm for skin layer segmentation.

- To enable angiographic imaging by developing and implementing an automatic algorithm for visualising cutaneous vasculature.
- To establish a method for quantifying blood flow velocity using angiographic OCT techniques.
- To explore additional applications of the system, including long-term skin pattern tracking and potential system extension or upgrade.

The thesis is structured as follows:

1) Chapter 2 introduces the development of a near-infrared high-speed Fourier-domain Mode-locking (FDML) OCT system, incorporating a 1.6 MHz FDML laser, an ultrafast MEMS scanner, a gigahertz bandwidth photodetector, and a high-sample-rate digitizer card. The system operates at a scanning frequency of 3 kHz, with its characteristics and imaging performance evaluated. MATLAB-based controlling software for the OCT system is also developed and presented.
2) Chapter 3 applies the in-house high-speed FDML OCT system to detect the epidermal thickness and superficial plexus vasculature on dorsal hand skin, achieving a volume scan of 2.8 x 2.8 x 5 mm^3 (XYZ) within less than one second acquisition time. Automatic segmentation algorithms are developed to detect the skin surface and epidermal-dermal junction, alongside angiographic algorithms based on speckle variance to visualize vasculature.
3) Chapter 4 utilizes the in-house FDML OCT system for quantifying cutaneous blood flow velocity using angiographic OCT and variable interscan time analysis (VISTA). Scan protocols enabling flow velocity quantification are discussed. Validation is performed using an in-house glass capillary flow phantom perfused with milk, followed by in vivo mapping of cutaneous blood flow velocity.

4) Chapter 5 demonstrates two additional applications of the in-house FDML OCT system. A preliminary study on skin topographical matching involves repeated imaging of dorsal hand skin patterns over 128 days, showing its potential for clinically localizing skin lesions and monitoring site-specific changes. The FDML OCT system is also employed to align and test an in-house colposcopic scanning probe designed for imaging hard-to-reach areas.
5) Chapter 6 concludes the thesis and discusses future developments and potential applications of the current FDML OCT system.

References

[1] D. Huang *et al.*, "Optical coherence tomography," *science,* vol. 254, no. 5035, pp. 1178-1181, 1991.

[2] A. F. Fercher, W. Drexler, C. K. Hitzenberger, and T. Lasser, "Optical coherence tomography-principles and applications," *Reports on progress in physics,* vol. 66, no. 2, p. 239, 2003.

[3] W. Drexler and J. G. Fujimoto, *Optical coherence tomography: technology and applications*. Springer Science & Business Media, 2008.

[4] B. E. Bouma *et al.*, "Optical coherence tomography," *Nature Reviews Methods Primers,* vol. 2, no. 1, p. 79, 2022.

[5] G. Song and K. Harding, "OCT for industrial applications," in *Optical metrology and inspection for industrial applications II*, 2012, vol. 8563: SPIE, pp. 142-151.

[6] D. Stifter, "Beyond biomedicine: a review of alternative applications and developments for optical coherence tomography," *Applied Physics B,* vol. 88, pp. 337-357, 2007.

[7] M.-Y. Fu *et al.*, "The Progress of Optical Coherence Tomography in Industry Applications," *Advanced Devices & Instrumentation,* vol. 5, 2024.

[8] A. Nemeth, G. Hannesschläger, E. Leiss-Holzinger, K. Wiesauer, and M. Leitner, "Optical coherence tomography–applications in non-destructive testing and evaluation," *Optical coherence tomography,* vol. 6, pp. 163-186, 2013.

[9] Z. Zhang *et al.*, "Rapid imaging and product screening with low-cost line-field Fourier domain optical coherence tomography," *Scientific reports,* vol. 13, no. 1, p. 10809, 2023.

[10] G. Hannesschläger *et al.*, "Optical coherence tomography as a tool for non destructive quality control of multi-layered foils," *Proceedings of the 6th NDT in Progress,* pp. 10.09-12.09, 2011.

[11] K. A. Serrels, M. Renner, and D. T. Reid, "Optical coherence tomography for non-destructive investigation of silicon integrated-circuits," *Microelectronic Engineering,* vol. 87, no. 9, pp. 1785-1791, 2010.

[12] D. Markl, G. Hannesschläger, S. Sacher, M. Leitner, and J. G. Khinast, "Optical coherence tomography as a novel tool for in-line monitoring of a pharmaceutical film-coating process," *European Journal of Pharmaceutical Sciences,* vol. 55, pp. 58-67, 2014.

[13] R. Su, M. Kirillin, E. W. Chang, E. Sergeeva, S. H. Yun, and L. Mattsson, "Perspectives of mid-infrared optical coherence tomography for inspection and micrometrology of industrial ceramics," *Optics express,* vol. 22, no. 13, pp. 15804-15819, 2014.

[14] C. Stadter, M. Schmoeller, L. von Rhein, and M. F. Zaeh, "Real-time prediction of quality characteristics in laser beam welding using optical coherence tomography and machine learning," *Journal of Laser Applications,* vol. 32, no. 2, 2020.

[15] K. Ishida, N. Ozaki, H. Ohsato, E. Watanabe, N. Ikeda, and Y. Sugimoto, "Non-destructive and non-contact measurement of semiconductor optical waveguide using optical coherence tomography with a visible broadband light source," *Japanese Journal of Applied Physics,* vol. 57, no. 8S2, p. 08PE03, 2018.

[16] P. Ma, J. Ni, J. Sun, X. Zhang, J. Li, and H. Chen, "Three-dimensional detection and quantification of defects in SiC by optical coherence tomography," *Applied Optics,* vol. 59, no. 6, pp. 1746-1755, 2020.

[17] H. Liang, B. Peric, M. Hughes, A. G. Podoleanu, M. Spring, and S. Roehrs, "Optical coherence tomography in archaeological and conservation science-a new emerging field," in *1st Canterbury Workshop on Optical Coherence Tomography and Adaptive Optics*, 2008, vol. 7139: SPIE, pp. 314-322.

[18] P. Targowski and M. Iwanicka, "Optical coherence tomography: its role in the non-invasive structural examination and conservation of cultural heritage objects—a review," *Applied Physics A,* vol. 106, pp. 265-277, 2012.

[19] X. Zhou *et al.*, "A Note on Macroscopic Optical Coherence Tomography Imaging Enabled 3D Scanning for Museum and Cultural Heritage Applications," *Journal of the American Institute for Conservation,* vol. 62, no. 3, pp. 178-187, 2023.

[20] C. B. Prinsi, P. Buscaglia, M. Olivero, S. Grassini, A. Vallan, and G. Perrone, "Optical Coherence Tomography Based Measurements to Support Cleaning Treatments of Painted Ancient Artifacts," in *2024 IEEE International Instrumentation and Measurement Technology Conference (I2MTC)*, 2024: IEEE, pp. 1-6.

[21] F. Zaki, I. Hou, D. Cooper, D. Patel, Y. Yang, and X. Liu, "High-definition optical coherence tomography imaging for noninvasive examination of heritage works," *Applied optics,* vol. 55, no. 36, pp. 10313-10317, 2016.

[22] P. Liu, R. M. Groves, and R. Benedictus, "Signal processing in optical coherence tomography for aerospace material characterization," *Optical Engineering,* vol. 52, no. 3, pp. 033201-033201, 2013.

[23] P. Liu, R. M. Groves, and R. Benedictus, "3D monitoring of delamination growth in a wind turbine blade composite using optical coherence tomography," *Ndt & E International,* vol. 64, pp. 52-58, 2014.

[24] S. Lawman, B. M. Williams, J. Zhang, Y.-C. Shen, and Y. Zheng, "Scan-less line field optical coherence tomography, with automatic image segmentation, as a measurement tool for automotive coatings," *Applied Sciences,* vol. 7, no. 4, p. 351, 2017.

[25] M. Sokolov *et al.*, "Applying optical coherence tomography for weld depth monitoring in remote laser welding of automotive battery tab connectors," *Journal of Laser Applications,* vol. 33, no. 1, 2021.

[26] A. A. Appel, M. A. Anastasio, J. C. Larson, and E. M. Brey, "Imaging challenges in biomaterials and tissue engineering," *Biomaterials,* vol. 34, no. 28, pp. 6615-6630, 2013.

[27] Y. Yang, A. Dubois, X.-p. Qin, J. Li, A. El Haj, and R. K. Wang, "Investigation of optical coherence tomography as an imaging modality in tissue engineering," *Physics in Medicine & Biology,* vol. 51, no. 7, p. 1649, 2006.

[28] Y. Onuma *et al.*, "Intracoronary optical coherence tomography and histology at 1 month and 2, 3, and 4 years after implantation of everolimus-eluting bioresorbable vascular scaffolds in a porcine coronary artery model: an attempt to decipher the human optical coherence tomography images in the ABSORB trial," *Circulation,* vol. 122, no. 22, pp. 2288-2300, 2010.

[29] F. Cuculi *et al.*, "Optical coherence tomography findings in bioresorbable vascular scaffolds thrombosis," *Circulation: Cardiovascular Interventions,* vol. 8, no. 10, p. e002518, 2015.

[30] Z. Chen, Q. Cheng, L. Wang, Y. Mo, K. Li, and J. Mo, "Optical coherence tomography for in vivo longitudinal monitoring of artificial dermal scaffold," *Lasers in Surgery and Medicine,* vol. 55, no. 3, pp. 316-326, 2023.
[31] S. A. Saleah *et al.*, "Optical coherence tomography as a non-invasive tool for plant material characterization in agriculture: A review," *Sensors,* vol. 24, no. 1, p. 219, 2023.
[32] I. Meglinski, C. Buranachai, and L. Terry, "Plant photonics: application of optical coherence tomography to monitor defects and rots in onion," *Laser Physics Letters,* vol. 7, no. 4, p. 307, 2010.
[33] M. Li, S. Landahl, A. R. East, P. Verboven, and L. A. Terry, "Optical coherence tomography—A review of the opportunities and challenges for postharvest quality evaluation," *Postharvest biology and technology,* vol. 150, pp. 9-18, 2019.
[34] C. J. Larimer, E. H. Denis, J. D. Suter, and J. J. Moran, "Optical coherence tomography imaging of plant root growth in soil," *Applied Optics,* vol. 59, no. 8, pp. 2474-2481, 2020.
[35] J. de Wit, S. Tonn, M.-R. Shao, G. Van den Ackerveken, and J. Kalkman, "Revealing real-time 3D in vivo pathogen dynamics in plants by label-free optical coherence tomography," *Nature Communications,* vol. 15, no. 1, p. 8353, 2024.
[36] A. I. Koponen and S. Haavisto, "Analysis of industry-related flows by optical coherence tomography—A review," *KONA Powder and Particle Journal,* vol. 37, pp. 42-63, 2020.
[37] H.-J. Ko, W. Tan, R. Stack, and S. A. Boppart, "Optical coherence elastography of engineered and developing tissue," *Tissue engineering,* vol. 12, no. 1, pp. 63-73, 2006.
[38] W. Drexler, U. Morgner, R. K. Ghanta, F. X. Kärtner, J. S. Schuman, and J. G. Fujimoto, "Ultrahigh-resolution ophthalmic optical coherence tomography," *Nature medicine,* vol. 7, no. 4, pp. 502-507, 2001.
[39] J. G. Fujimoto, W. Drexler, J. S. Schuman, and C. K. Hitzenberger, "Optical Coherence Tomography (OCT) in ophthalmology: introduction," *Optics express,* vol. 17, no. 5, pp. 3978-3979, 2009.
[40] A. M. Hagag, S. S. Gao, Y. Jia, and D. Huang, "Optical coherence tomography angiography: technical principles and clinical applications in ophthalmology," *Taiwan journal of ophthalmology,* vol. 7, no. 3, pp. 115-129, 2017.
[41] J. S. Schuman, J. G. Fujimoto, J. Duker, and H. Ishikawa, *Optical coherence tomography of ocular diseases*. CRC Press, 2024.
[42] H. G. Bezerra, M. A. Costa, G. Guagliumi, A. M. Rollins, and D. I. Simon, "Intracoronary optical coherence tomography: a comprehensive review: clinical and research applications," *JACC: Cardiovascular Interventions,* vol. 2, no. 11, pp. 1035-1046, 2009.
[43] T. Yonetsu, B. E. Bouma, K. Kato, J. G. Fujimoto, and I.-K. Jang, "Optical coherence tomography–15 years in cardiology–," *Circulation Journal,* vol. 77, no. 8, pp. 1933-1940, 2013.
[44] M. Araki *et al.*, "Optical coherence tomography in coronary atherosclerosis assessment and intervention," *Nature Reviews Cardiology,* vol. 19, no. 10, pp. 684-703, 2022.
[45] E. Sattler, R. Kästle, and J. Welzel, "Optical coherence tomography in dermatology," *Journal of biomedical optics,* vol. 18, no. 6, pp. 061224-061224, 2013.

[46] J. Olsen, J. Holmes, and G. B. Jemec, "Advances in optical coherence tomography in dermatology—a review," *Journal of biomedical optics,* vol. 23, no. 4, pp. 040901-040901, 2018.
[47] B. Wan *et al.*, "Applications and future directions for optical coherence tomography in dermatology," *British Journal of Dermatology,* vol. 184, no. 6, pp. 1014-1022, 2021.
[48] B. J. Vakoc, D. Fukumura, R. K. Jain, and B. E. Bouma, "Cancer imaging by optical coherence tomography: preclinical progress and clinical potential," *Nature Reviews Cancer,* vol. 12, no. 5, pp. 363-368, 2012.
[49] J. Wang, Y. Xu, and S. A. Boppart, "Review of optical coherence tomography in oncology," *Journal of biomedical optics,* vol. 22, no. 12, pp. 121711-121711, 2017.
[50] L. Yang *et al.*, "Research progress on the application of optical coherence tomography in the field of oncology," *Frontiers in oncology,* vol. 12, p. 953934, 2022.
[51] T.-H. Tsai *et al.*, "Endoscopic optical coherence angiography enables 3-dimensional visualization of subsurface microvasculature," *Gastroenterology,* vol. 147, no. 6, pp. 1219-1221, 2014.
[52] T.-H. Tsai *et al.*, "Optical coherence tomography in gastroenterology: a review and future outlook," *Journal of biomedical optics,* vol. 22, no. 12, pp. 121716-121716, 2017.
[53] L. Wang, O. Murphy, N. G. Caldito, P. A. Calabresi, and S. Saidha, "Emerging applications of optical coherence tomography angiography (OCTA) in neurological research," *Eye and Vision,* vol. 5, pp. 1-11, 2018.
[54] J. S. Xie, L. Donaldson, and E. Margolin, "The use of optical coherence tomography in neurology: a review," *Brain,* vol. 145, no. 12, pp. 4160-4177, 2022.
[55] Y.-S. Hsieh *et al.*, "Dental optical coherence tomography," *Sensors,* vol. 13, no. 7, pp. 8928-8949, 2013.
[56] H. Schneider *et al.*, "Dental applications of optical coherence tomography (OCT) in cariology," *Applied Sciences,* vol. 7, no. 5, p. 472, 2017.
[57] L. P. Hariri *et al.*, "Laparoscopic optical coherence tomography imaging of human ovarian cancer," *Gynecologic oncology,* vol. 114, no. 2, pp. 188-194, 2009.
[58] M. Kirillin, T. Motovilova, and N. Shakhova, "Optical coherence tomography in gynecology: a narrative review," *Journal of Biomedical Optics,* vol. 22, no. 12, pp. 121709-121709, 2017.
[59] T. Gambichler, G. Moussa, M. Sand, D. Sand, P. Altmeyer, and K. Hoffmann, "Applications of optical coherence tomography in dermatology," *Journal of dermatological science,* vol. 40, no. 2, pp. 85-94, 2005.
[60] M. Mogensen, L. Thrane, T. M. Jørgensen, P. E. Andersen, and G. B. Jemec, "OCT imaging of skin cancer and other dermatological diseases," *Journal of biophotonics,* vol. 2, no. 6-7, pp. 442-451, 2009.
[61] A. K. Bhatta, U. Keyal, and Y. Liu, "Application of high frequency ultrasound in dermatology," *Discovery medicine,* vol. 26, no. 145, pp. 237-242, 2018.
[62] R. Izzetti, T. Oranges, A. Janowska, M. Gabriele, F. Graziani, and M. Romanelli, "The application of ultra-high-frequency ultrasound in dermatology and wound management," *The International Journal of Lower Extremity Wounds,* vol. 19, no. 4, pp. 334-340, 2020.

[63] J. Levy, D. L. Barrett, N. Harris, J. J. Jeong, X. Yang, and S. C. Chen, "High-frequency ultrasound in clinical dermatology: A review," *The Ultrasound Journal,* vol. 13, pp. 1-12, 2021.
[64] M. M. Vergilio, S. A. Monteiro e Silva, R. M. Jales, and G. R. Leonardi, "High-frequency ultrasound as a scientific tool for skin imaging analysis," *Experimental dermatology,* vol. 30, no. 7, pp. 897-910, 2021.
[65] G. Granieri *et al.*, "Ultra-high frequency ultrasound detection of the dermo-epidermal junction: Its potential role in dermatology," *Experimental Dermatology,* vol. 31, no. 12, pp. 1863-1871, 2022.
[66] K. S. Nehal, D. Gareau, and M. Rajadhyaksha, "Skin imaging with reflectance confocal microscopy," in *Seminars in cutaneous medicine and surgery*, 2008, vol. 27, no. 1: WB Saunders, pp. 37-43.
[67] N. Shahriari, J. M. Grant-Kels, H. Rabinovitz, M. Oliviero, and A. Scope, "Reflectance confocal microscopy: Principles, basic terminology, clinical indications, limitations, and practical considerations," *Journal of the American Academy of Dermatology,* vol. 84, no. 1, pp. 1-14, 2021.
[68] Q. Lu and G. Jiang, "Progress in the application of reflectance confocal microscopy in dermatology," *Advances in Dermatology and Allergology/Postępy Dermatologii i Alergologii,* vol. 38, no. 5, pp. 709-715, 2021.
[69] E. A. Csuka, S. C. Ward, C. Ekelem, D. A. Csuka, M. Ardigò, and N. A. Mesinkovska, "Reflectance confocal microscopy, optical coherence tomography, and multiphoton microscopy in inflammatory skin disease diagnosis," *Lasers in Surgery and Medicine,* vol. 53, no. 6, pp. 776-797, 2021.
[70] Y. Jung, J. Tam, H. R. Jalian, R. R. Anderson, and C. L. Evans, "Longitudinal, 3D in vivo imaging of sebaceous glands by coherent anti-stokes Raman scattering microscopy: normal function and response to cryotherapy," *Journal of Investigative Dermatology,* vol. 135, no. 1, pp. 39-44, 2015.
[71] X. L. Deán-Ben and D. Razansky, "Optoacoustic imaging of the skin," *Experimental dermatology,* vol. 30, no. 11, pp. 1598-1609, 2021.
[72] s. L. P. Aggarwal and F. A. Papay, "Applications of multispectral and hyperspectral imaging in dermatology," *Experimental Dermatology,* vol. 31, no. 8, pp. 1128-1135, 2022.
[73] A. I. Nikitkina *et al.*, "Terahertz radiation and the skin: a review," *Journal of Biomedical Optics,* vol. 26, no. 4, pp. 043005-043005, 2021.
[74] J. Welzel, "Optical coherence tomography in dermatology: a review," *Skin Research and Technology: Review article,* vol. 7, no. 1, pp. 1-9, 2001.
[75] U. Baran, W. J. Choi, and R. K. Wang, "Potential use of OCT-based microangiography in clinical dermatology," *Skin research and technology,* vol. 22, no. 2, pp. 238-246, 2016.
[76] M. C. Pierce, J. Strasswimmer, B. Hyle Park, B. Cense, and J. F. De Boer, "Birefringence measurements in human skin using polarization-sensitive optical coherence tomography," *Journal of biomedical optics,* vol. 9, no. 2, pp. 287-291, 2004.
[77] C. Ruini, S. Schuh, E. Sattler, and J. Welzel, "Line-field confocal optical coherence tomography—practical applications in dermatology and comparison with established imaging methods," *Skin Research and Technology,* vol. 27, no. 3, pp. 340-352, 2021.

[78] D. G. Revin, R. A. Byers, M. Q. Duan, W. Li, and S. J. Matcher, "Visible-light optical coherence tomography platform for the characterization of the skin barrier," *Biomedical optics express,* vol. 14, no. 8, pp. 3914-3923, 2023.
[79] J. Welzel, E. Lankenau, R. Birngruber, and R. Engelhardt, "Optical coherence tomography of the human skin," *Journal of the American Academy of Dermatology,* vol. 37, no. 6, pp. 958-963, 1997.
[80] U. Sharma, E. W. Chang, and S. H. Yun, "Long-wavelength optical coherence tomography at 1.7 μm for enhanced imaging depth," *Optics express,* vol. 16, no. 24, pp. 19712-19723, 2008.
[81] J. Holmes, S. Hattersley, N. Stone, F. Bazant-Hegemark, and H. Barr, "Multi-channel Fourier domain OCT system with superior lateral resolution for biomedical applications," in *Coherence domain optical methods and optical coherence tomography in biomedicine XII*, 2008, vol. 6847: SPIE, pp. 86-94.
[82] R. Maiti, M. Duan, S. G. Danby, R. Lewis, S. J. Matcher, and M. J. Carré, "Morphological parametric mapping of 21 skin sites throughout the body using optical coherence tomography," *journal of the mechanical behavior of biomedical materials,* vol. 102, p. 103501, 2020.
[83] C. Czekalla, K. H. Schönborn, J. Lademann, and M. C. Meinke, "Noninvasive determination of epidermal and stratum corneum thickness in vivo using two-photon microscopy and optical coherence tomography: impact of body area, age, and gender," *Skin pharmacology and physiology,* vol. 32, no. 3, pp. 142-150, 2019.
[84] N. M. Israelsen *et al.*, "The value of ultrahigh resolution OCT in dermatology-delineating the dermo-epidermal junction, capillaries in the dermal papillae and vellus hairs," *Biomedical optics express,* vol. 9, no. 5, pp. 2240-2265, 2018.
[85] R. A. Byers *et al.*, "Sub-clinical assessment of atopic dermatitis severity using angiographic optical coherence tomography," *Biomedical optics express,* vol. 9, no. 4, pp. 2001-2017, 2018.
[86] M. Ulrich *et al.*, "Dynamic optical coherence tomography in dermatology," *Dermatology,* vol. 232, no. 3, pp. 298-311, 2016.
[87] J. A. Izatt and M. A. Choma, "Theory of optical coherence tomography," in *Optical Coherence Tomography: Technology and Applications*: Springer, 2008, pp. 47-72.
[88] A. G. Podoleanu, "Optical coherence tomography," *Journal of microscopy,* vol. 247, no. 3, pp. 209-219, 2012.
[89] R. K. Wang, S. L. Jacques, Z. Ma, S. Hurst, S. R. Hanson, and A. Gruber, "Three dimensional optical angiography," *Optics express,* vol. 15, no. 7, pp. 4083-4097, 2007.
[90] J. Zhu, C. W. Merkle, M. T. Bernucci, S. P. Chong, and V. J. Srinivasan, "Can OCT angiography be made a quantitative blood measurement tool?," *Applied sciences,* vol. 7, no. 7, p. 687, 2017.
[91] A. H. Kashani *et al.*, "Optical coherence tomography angiography: a comprehensive review of current methods and clinical applications," *Progress in retinal and eye research,* vol. 60, pp. 66-100, 2017.
[92] J. Fingler, D. Schwartz, C. Yang, and S. E. Fraser, "Mobility and transverse flow visualization using phase variance contrast with spectral domain optical coherence tomography," *Optics express,* vol. 15, no. 20, pp. 12636-12653, 2007.
[93] A. Mariampillai *et al.*, "Speckle variance detection of microvasculature using swept-source optical coherence tomography," *Optics letters,* vol. 33, no. 13, pp. 1530-1532, 2008.

[94] R. Gupta, A. Sheikh, D. Strachan, and H. Anderson, "Burden of allergic disease in the UK: secondary analyses of national databases," *Clinical & Experimental Allergy,* vol. 34, no. 4, pp. 520-526, 2004.

[95] Z. Lu, J. Boadi, S. Danby, M. Cork, and S. J. Matcher, "Optical coherence tomography demonstrates differential epidermal thinning of human forearm volar skin after 2 weeks application of a topical corticosteroid vs a non-steroidal anti-inflammatory alternative," in *Photonic Therapeutics and Diagnostics IX*, 2013, vol. 8565: SPIE, pp. 43-49.

2. Development of Swept-source Fourier-domain Mode-locking (FDML) OCT

2.1. Summary

Following the objective of achieving high-speed imaging, this chapter introduces an FDML OCT system based on a Michelson interferometer. The system utilizes a 1.6 MHz FDML laser, a MEMS scanner, and a high-speed data acquisition unit to enable rapid imaging. Key performance metrics, including axial and lateral resolution, sensitivity, and imaging depth, are characterized after system calibration. Various OCT scan protocols are outlined, followed by example B-scan and enface images, demonstrating the system's capabilities at a 3 kHz frame rate. Custom software developed for real-time imaging control and data collection is also introduced.

2.2. Construction of FDML OCT System

The FDML OCT system is composed of three main components: the light source, the interferometer, and the data acquisition unit. To achieve high-speed scanning, the system employs an FDML laser as the light source, offering a 1.67 MHz sweep rate, and a micro-electromechanical systems (MEMS) scanner to deliver a 3 kHz frame rate. The Michelson interferometer setup is used to capture coherence fringes from the sample. These fringe signals are then collected by a high-speed data acquisition unit, which consists of a gigahertz bandwidth photodetector and a high-sample-rate digitizer card.

2.2.1. FDML Laser

This section introduces the working principle of the FDML laser and explains why it was chosen for OCT imaging. The optical and electrical characteristics of the FDML laser are then tested and validated before being integrated into the OCT system as the light source.

2.2.1.1.Introduction

The FDML (Fourier Domain Mode-Locking) laser operates based on the principle of laser mode-locking, a technique widely used for generating short optical pulses. In traditional mode-locking, the longitudinal modes of the laser cavity are phase-locked, creating a series of short, intense optical pulses. Mode-locking can be achieved actively or passively through amplitude or phase modulation in sync with the cavity round-trip time. While this technique is effective for producing short pulses, for high-speed imaging applications such as optical coherence tomography (OCT), narrowband, frequency-swept lasers are more appropriate.

Conventional tunable lasers use a narrowband optical filter that sweeps through a range of wavelengths. However, the maximum sweep speed is limited because laser emission must be rebuilt from spontaneous emission at each new wavelength. This process introduces increased noise, reduced coherence, and a limited tuning range, especially at higher sweep speeds [1].

The FDML laser overcomes these limitations by incorporating a long delay line within the laser cavity and synchronising the filter’s tuning with the round-trip time of the light within the cavity. Unlike conventional tunable lasers, where lasing must be reinitiated at each new wavelength, the FDML laser "recycles" light from previous sweeps, maintaining coherence over time. This synchronisation between the filter and

the cavity results in high-speed operation with minimal power loss and excellent coherence.

As illustrated in **Figure 2.1**, the key distinction between a conventional tunable laser and an FDML laser is the use of a dispersion-managed delay line in the FDML laser. This feature ensures that the frequency-swept light returns to the filter precisely when it is tuned to the same wavelength, enabling a continuous, high-speed frequency sweep, which is highly beneficial for fast imaging applications [2].

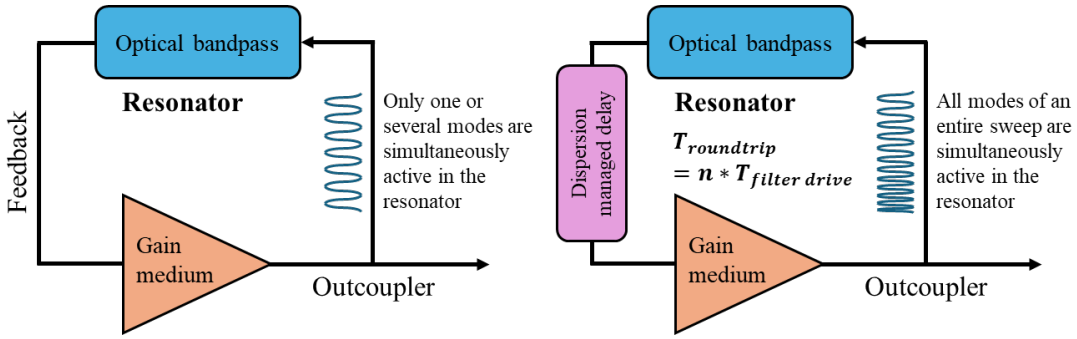

Figure 2.1: Left: Standard tunable laser, where light from a broadband gain medium is filtered by a tunable narrowband optical bandpass filter. Right: FDML laser, where the entire frequency sweep is stored within the cavity, with the tunable filter synchronised to the round-trip time of the cavity [2].

By employing the FDML laser for OCT imaging, the system can achieve sweep rates far higher than those of conventional swept lasers, with sweep frequencies in the megahertz range [1-3]. The FDML laser in our OCT system (NG-FDML, Optores GmbH) operates at an A-scan rate of 1.67 MHz, with a 6 dB coherence length exceeding 10 mm and a sweep range of more than 100 nm, centred around a wavelength of 1309

nm. These features make the FDML laser ideal for high-speed, high-resolution, and deep-penetration OCT imaging.

2.2.1.2. Optical Testing

Before connecting the FDML laser to the interferometer, its optical performance was assessed. First, the output power from the main aperture was measured using a thermal power meter (Melles Griot). The thermal sensor head was placed directly in front of the laser main aperture, and then in front of the aperture end of a single-mode (SM) fibre, with the other end connected to the laser aperture. The measured power values were 51.5 mW and 45.6 mW, respectively. To verify these results, a second thermal power meter (Fieldmate) was used under identical conditions, yielding values of 52.9 mW and 46.5 mW. The measured power from the aperture is close to the official test report value of 53 mW, recorded when the booster semiconductor optical amplifier (SOA) current was set to 306 mA. Additionally, coupling the light into the SM fibre resulted in a loss of approximately 6 mW.

The output power of the FDML laser can also be adjusted by varying the booster SOA current. This adjustment is controlled by modifying the digital-to-analogue converter (DAC) value. To investigate the relationship between SOA current amplitude and output power, different DAC values were set, and the corresponding power values were measured using a thermal power meter. **Figure 2.2** validates the linear relationship between the measured laser output power and the DAC value. An amplitude of 14,000 DAC corresponded to approximately 50 mW of laser power.

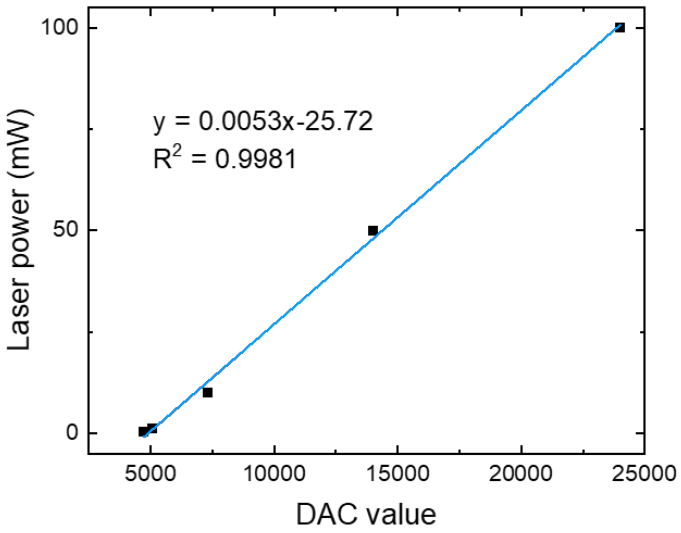

Figure 2.2: Measured output power of the FDML laser as a function of the DAC value.

2.2.1.3. Electrical Testing

The FDML laser can also generate an analogue signal to control the movement of a scanner. For X-axis (fast axis) scanning, the X analogue waveform uses the FDML cycle as the step source. Each FDML cycle contains four buffered A-scans. A cycle of the X waveform consists of a preset number of rising and falling steps. Thus, the frequency of the X waveform can be calculated by dividing the FDML A-scan rate by four times the total number of rises and falls in the X waveform. As shown in **Figure 2.3**(a), the frequency of the X waveform can be adjusted from 102 Hz to 209 kHz by varying the total number (integer) of rises and falls from 4096 to 2. **Figure 2.3**(b) shows a linear relationship between the peak-to-peak (Pk-Pk) amplitude of the X waveform and the preset DAC value. The frequency and Pk-Pk amplitude (in volts) of the X waveform were measured using an oscilloscope.

For Y-axis (slow axis) scanning, each step of the Y analogue waveform is triggered by one complete cycle of the X waveform, as depicted in **Figure 2.4**. **Figure 2.4**

compares the X waveform (magenta) with the Y waveform (green). **Figure 2.4**(a) displays one cycle of the Y waveform, while **Figure 2.4**(b) shows that one step of the Y waveform corresponds to one cycle of the X waveform.

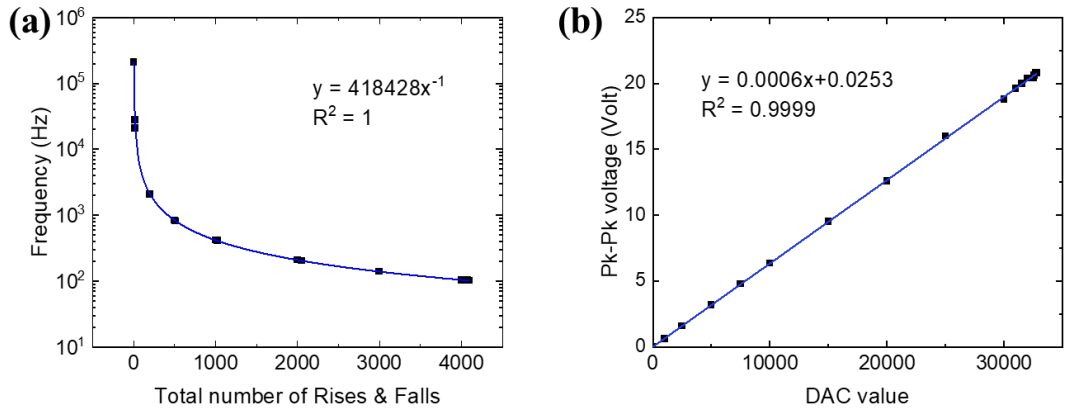

Figure 2.3: (a) Output frequency of the X-axis analogue waveform as a function of the total number of rises and falls in one cycle of the X waveform. (b) Output voltage of the X-axis analogue waveform as a function of the DAC value.

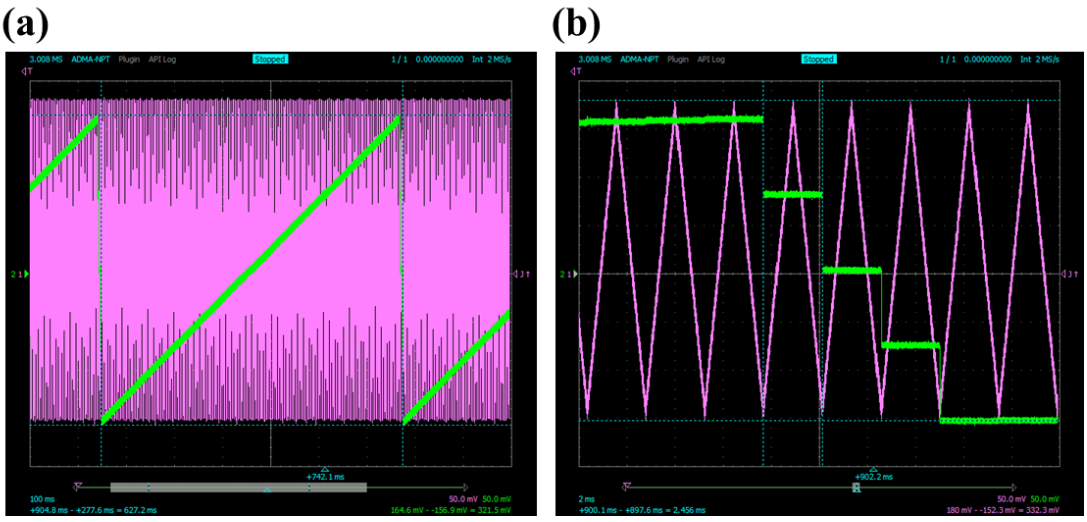

Figure 2.4: Example of analogue waveforms for X-axis and Y-axis scanning generated from the FDML laser. (a) Comparison between one cycle of the Y waveform (green) and the X waveform (magenta). (b) Comparison between one step of the Y waveform and one cycle of the X waveform.

2.2.2. MEMS Scanner

After investigating the FDML analogue signal for driving the scanner, the FDML laser was used as a function generator to provide the waveform needed to test a MEMS scanner. This MEMS scanner (A5L2.2, Mirrorcle Technologies Inc.) was integrated into the sample arm of the interferometer to enable a fast B-scan rate or frame rate. Compared with galvo-resonant scanners, the MEMS scanner offers portability and a lightweight design, making it suitable for miniaturising our interferometer while maintaining rapid scanning capabilities.

2.2.2.1.Driving the MEMS Scanner

To drive the MEMS scanner, a MEMS driver board (T180) with integrated electronics was employed, connecting the MEMS scanner to the FDML laser and other devices. **Table 2.1** presents the pinout configuration and functions of the 10-pin connector on the MEMS T180 driver board. Pins 1 and 2 were connected to the FDML laser to provide the X-axis and Y-axis analogue scanning signals. A dual power supply (TTi EX354D) supplied a +5 V direct current (DC) output to Pin 3, powering the embedded DC/DC converter, and to Pin 5, enabling the MEMS driver. A function generator (Thandar TG501) delivered a 3.3 V TTL signal with a 50% duty cycle to Pins 9 and 10, setting the filter clock for the X and Y axes. The filter clock frequency determined the cut-off frequency for four embedded Bessel low-pass filters, with separate controls for the X and Y axes. Pin 4 was used as the ground, with all negative connections routed there, while Pins 6 to 8 were left unused.

Table 2.1: Pinout, functions, and connections of the 10-pin connector on the MEMS T180 driver board.

Input: 10 - Pin Header			
J1-Pin	**Name**	**Description**	**Connection**
1	XIN	Analogue Input X	FDML laser
2	YIN	Analogue Input Y	
3	+5V	VDD (+5VDC)	Dual power supply (TTi EX354D)
4	GND	Ground	All devices
5	EN	MEMS Driver Output Enable	Dual power supply (TTi EX354D)
6&7&8	N/C	No Connection	
9	FCLK_X	Filter Clock for X-Axis	~3.3V TTL signal with 50% duty cycle from a function generator (Thandar TG501)
10	FCLK_Y	Filter Clock for Y-Axis	

The MEMS scanner is driven using Bias-Differential Quad-channel (BDQ) control [4-6]. Each axis of the MEMS mirror is governed by two channels—positive and negative. All four channels are biased at 90 volts, representing the mirror's neutral position. After configuring the driver board, the FDML laser provided voltages to the X and Y axes through Pins 1 and 2. Each channel pair then applied differential voltages to each axis, rotating the mirror. The positive channel's voltage was the biased voltage plus the FDML voltage multiplied by 9, while the negative channel's voltage was the biased voltage minus the FDML voltage multiplied by 9. The differential voltage for each axis was the difference between the positive and negative channel voltages. Since

the FDML laser output ranged from -10 V to 10 V, the differential voltage spanned from -180 V to 180 V. The MEMS mirror's rotation was approximately proportional to the differential voltage applied to each axis, making the bias and differential voltages crucial parameters for driving the MEMS scanner.

2.2.2.2. Verification of MEMS Frequency Response

Once the MEMS scanner was driven using the FDML analogue waveform, its frequency response was measured to verify proper operation and ensure safe parameter settings. As mentioned earlier, the driver board contains four 6th-order Bessel low-pass filters that shape the waveforms applied to the four channels. The Bessel filter frequency response was tested first. **Figure 2.5** shows the measured (green dots) and simulated (red line) signal magnitudes across various frequencies. The cut-off frequency of the Bessel filters was set to 1800 Hz, corresponding to a 108 kHz filter clock frequency (60 times the cut-off frequency). The FDML laser generated waveform signals with a fixed voltage at different frequencies. The differential voltage on the driver board was then measured with an oscilloscope, and the magnitude was normalised. As shown in **Figure 2.5**, the Bessel filter attenuated the differential voltage as the frequency increased. Additionally, a 6th-order Bessel filter was simulated using MATLAB, with the simulated response curve (red line) closely matching the measured results.

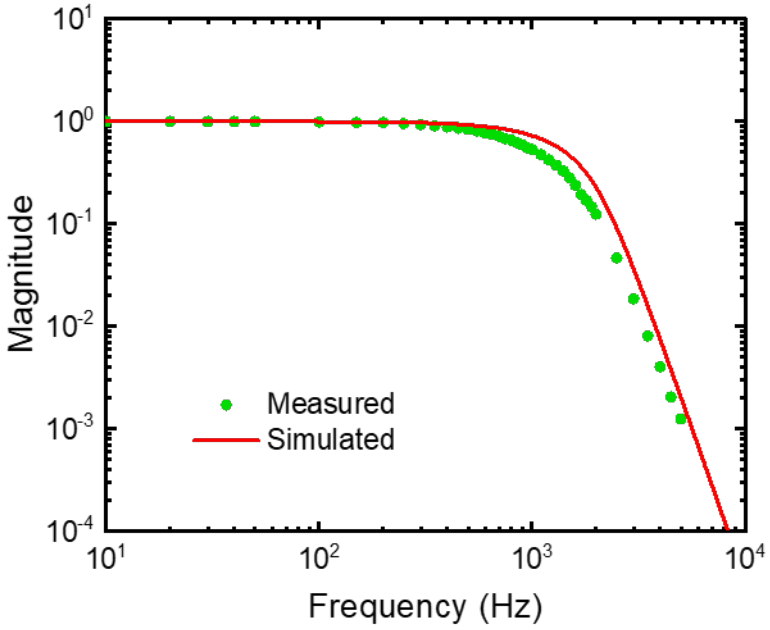

Figure 2.5: Frequency response of the embedded 6th-order Bessel low-pass filters in the MEMS driver board with a cut-off frequency of 1.8 kHz. Green dots represent measured normalised magnitudes. Red curve indicates the simulated response from MATLAB. The agreement between the measured and simulated results is acceptable.

To achieve the full differential voltage range without attenuation from the Bessel filter, a 102 Hz waveform with varying voltage amplitudes from the FDML laser was applied to verify the relationship between the mechanical angle and the differential voltage for each MEMS mirror axis. **Figure 2.6** illustrates the relationship between the mechanical tilt angle of the X-axis MEMS mirror and the differential voltage, compared with the curves provided in the manufacturer's test report. The results show a close match. The mechanical angle was estimated by positioning the MEMS scanner at a fixed distance from a wall, where the MEMS mirror reflected the laser beam perpendicular to the wall. The mechanical angle was then calculated based on the scan

length on the wall and the distance between the scanner and the wall. Further details regarding the setup for measuring mechanical angles can be found in Appendix 7.1.

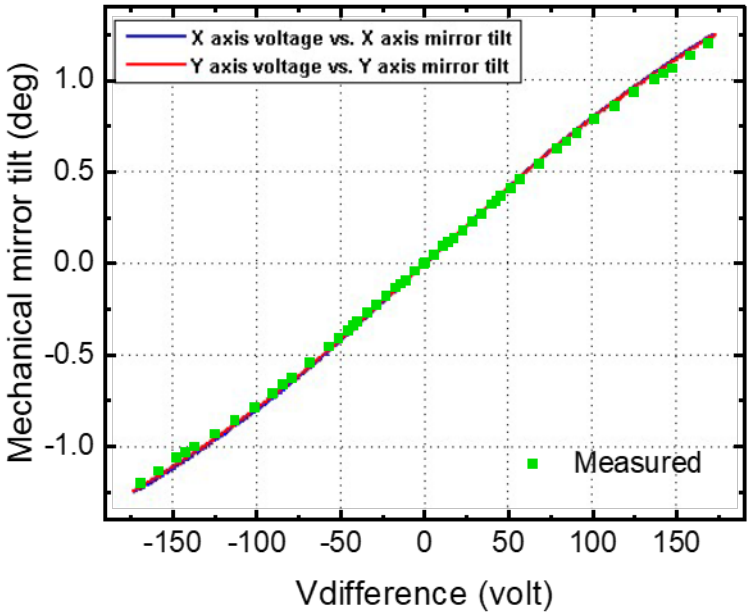

Figure 2.6: Relationship between the mechanical tilt angle of the MEMS mirror and the differential voltage applied to the X axis. Green dots indicate the measured results. The blue and red curves are from the manufacturer's test report.

To validate the small signal frequency response of the MEMS mirror's mechanical tilt angle under specific analogue input voltages, the magnitude was measured by estimating and normalising the mechanical angles across different scanning frequencies. The input voltage waveform from the FDML laser remained fixed while the scanning frequency varied. The setup for measuring the mechanical angle was retained. The varying Bessel filter magnitudes for different frequencies resulted in different differential voltages for each axis. After estimating the mechanical angle based on the wall measurements, the magnitude for each frequency was calculated by dividing the mechanical angle by the Bessel filter magnitude and normalising the result. **Figure 2.7**

presents the small signal frequency response, which aligns well with the manufacturer's response curves.

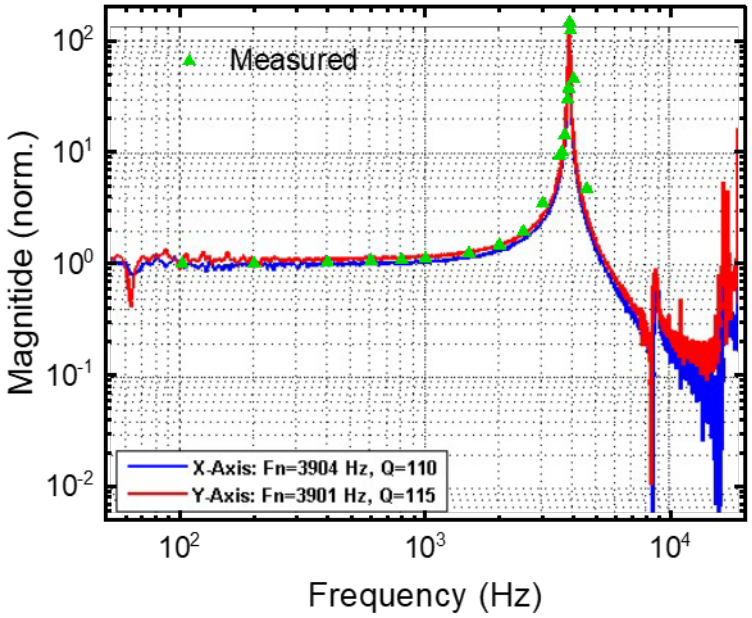

Figure 2.7: Relationship between the magnitude of the mechanical tilt angle of the MEMS mirror and the scanning frequency applied to the X axis. Green dots indicate the measured results. The blue and red curves are from the manufacturer's test report.

2.2.2.3. Resonance of MEMS

During the measurement of the MEMS frequency response, resonant and sub-harmonic scanning patterns were observed. **Figure 2.8**(a) illustrates the scanning pattern on a wall when the MEMS X axis was driven at its resonant frequency, showing unexpected Y-axis movement. **Figure 2.8**(b) depicts the scanning pattern when the X axis was driven at the third sub-harmonic of its resonant frequency, with the pattern confirmed through comparison with MATLAB simulations. In contrast, **Figure 2.8**(c) shows the linear scanning pattern observed at non-resonant frequencies. These results underscore the

importance of avoiding operation at resonant, sub-harmonic, and harmonic frequencies to prevent unexpected scanning behaviour.

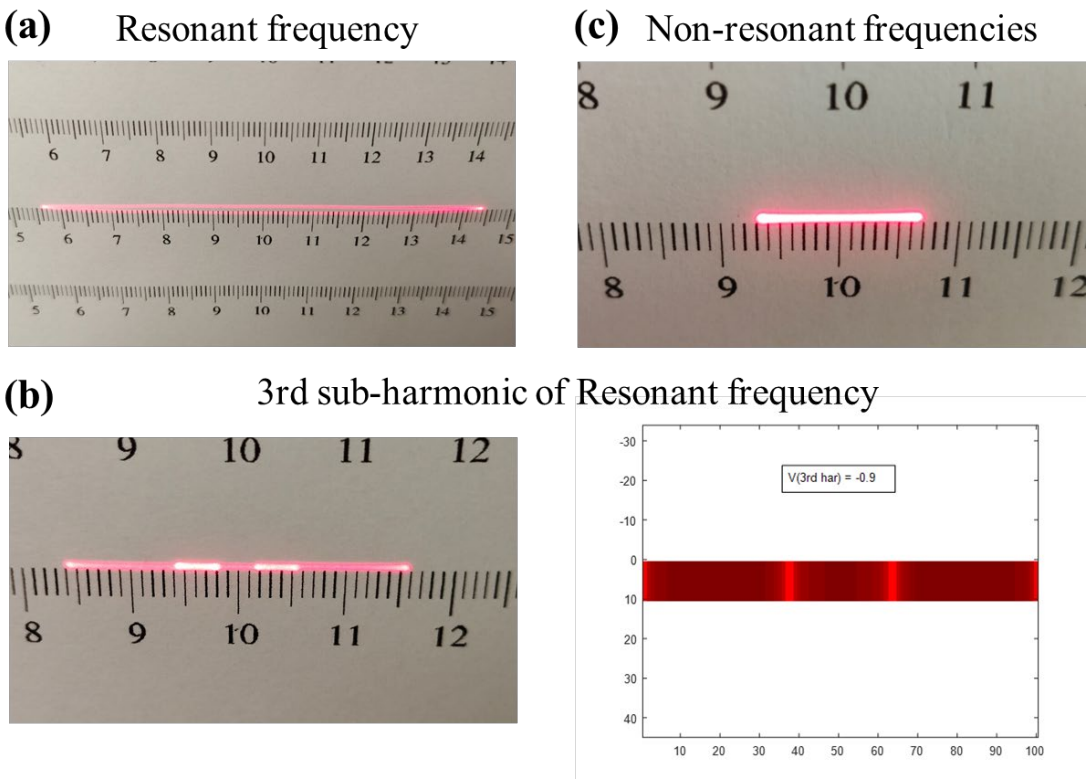

Figure 2.8: MEMS scanning patterns on a wall. (a) MEMS X-axis scanning at its resonant frequency. (b) Left: MEMS X-axis scanning at the third sub-harmonic of its resonant frequency. Right: MATLAB simulation of the third sub-harmonic scanning. (c) MEMS X-axis scanning at non-resonant frequencies.

2.2.3. Interferometer

This section introduces the structure and the components of the interferometer in the FDML OCT system.

As shown in **Figure 2.9**, the FDML laser emits a swept light with a power of approximately 50 mW to the interferometer via a single-mode fibre. The interferometer

employs a balanced, single-mode fibre-based Michelson setup. Initially, the laser light is coupled into a 3-port fibre optic circulator (FCIR-31-2, NOVAWAVE), followed by a 50/50 coupler (TW1300R5A2, Thorlabs Inc.) that splits the light equally between the reference and sample arms. Two polarisation controllers (PLC-002, PolaRITE™) are integrated to maximise signal power in both arms.

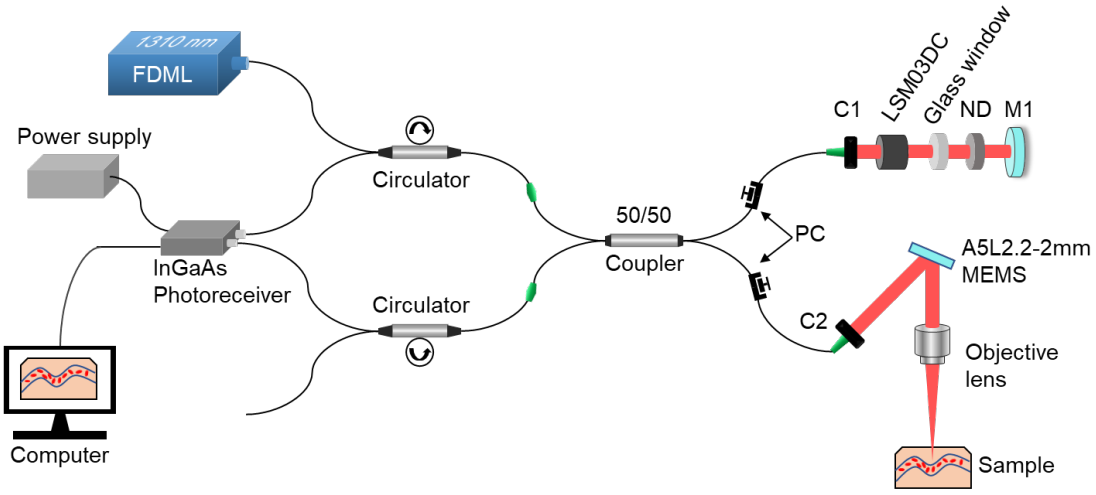

Figure 2.9: Schematic of the high-speed near-infrared FDML OCT system. C1, C2: fibre collimator. PC: polarization controller. LSM03DC: dispersion compensator for the objective. ND: wedged neutral density filter. M1: reflective mirror.

In the sample arm, a collimator (PAF-X-7-C, Thorlabs) expands the laser beam to a 1.4 mm diameter before directing it to the MEMS scanner (A5L2.2, Mirrorcle Technologies Inc.), which includes a 2.0 mm diameter reflective mirror. The beam is reflected towards an objective lens (LSM03, Thorlabs Inc.) with a focal length of 36 mm, focusing on the sample surface. The backscattered optical signal from the sample is collected by the objective and coupled back into the sample arm. The region of interest (ROI) of the sample should be positioned at the focal plane, 25 mm beyond the objective's aperture. The maximum field of view (FOV) is 2.9 mm x 2.9 mm, limited

by the MEMS mirror's mechanical tilt angle. The X axis of the MEMS scanner is driven by an analogue signal from the FDML laser at approximately 3 kHz, achieving an inter-frame time of 0.33 milliseconds and an A-scan spacing of 10 microns.

In the reference arm, an identical collimator directs the laser beam through a dispersion compensator (LSM03DC, Thorlabs Inc.), an anti-reflection (AR) coated UVFS broadband precision window (WG41010-C, Thorlabs Inc.), and a wedged UVFS reflective neutral density filter (NDUVW05B, Thorlabs Inc.). The beam is then reflected back into the reference arm by a mirror. The dispersion compensator corrects the dispersion caused by the objective in the sample arm. The neutral density filter, with an optical density (OD) of 0.5, optimises dynamic range sensitivity, providing roughly 25% transmission for near-infrared light at 1310 nm. Due to the optical path difference (OPD) between the reference and sample arms, a 1 mm thick AR coated window is used to further balance dispersion between the two arms.

The back-reflected optical signals from both arms of the interferometer are recombined and re-split by the coupler into two circulators, which send the optical signals to the data acquisition unit for further processing and OCT imaging.

2.2.4. Data Acquisition Unit

The data acquisition unit consists of a 1 GHz dual-balanced InGaAs photodetector (WL-BPD1GA, Wieserlabs) and a computer integrated with a 12-bit digitiser (ATS9373, AlazarTech Inc.) capable of sampling at rates up to 4 GS/s. The optical signals from the interferometer are transmitted to the two ports of the balanced photodetector, where they are converted into electrical signals. These signals share the same DC background from the laser spectrum but contain coherence fringes with a

phase difference of π radians. The photodetector suppresses the d.c. signal and relative intensity noise (RIN) noise and improves the signal-to-noise ratio (SNR) by subtracting the two signals, thereby compensating for the DC background while doubling the amplitude of the coherence fringes.

The amplified OCT fringes are collected and processed by the ultrafast digitiser. This digitiser features 8 gigabytes of on-board dual-port memory, enabling simultaneous data capture and transfer. While capturing sample data to the on-board memory, the digitiser also transfers data to application buffers in the host computer memory. This parallel process enables real-time OCT imaging. The accompanying software that manages data acquisition and imaging is described in Section 2.6.

Additionally, the photodetector has a high transimpedance gain of 3300 V/W for optical signals at approximately 1310 nm. To examine the relationship between the converted signal voltage and the input laser power, various laser power levels were applied, and the corresponding signal voltages were measured with an oscilloscope after the photodetector converted the optical signals to electrical signals. **Figure 2.10**(a) shows that the converted signal voltage increases with increasing laser power. However, as shown in **Figure 2.10**(b), this relationship remains linear only when the laser power is below 0.45 mW, and it saturates at power levels above 4 mW. The measured transimpedance gain of 3308.7 V/W closely matches the specification.

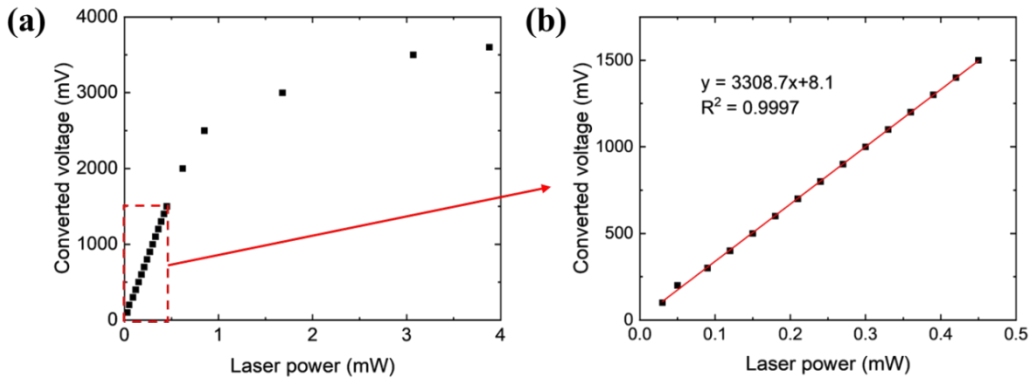

Figure 2.10: (a) Relationship between the converted signal voltage and input laser power. (b) Enlargement of the red dashed box in (a) showing the linear relationship.

2.3. Optimisation for FDML OCT

Before using the FDML OCT system for imaging, the system must be optimised after assembly.

2.3.1. Connection of the Fibre Coupler

The first step in optimisation is verifying the connection of the fibre coupler. The suggested configuration from Thorlabs is shown in **Figure 2.11**(a) [7]. In the interferometer, the fibre coupler is designed to split the laser signal's power equally. However, the coupling ratio of this coupler is wavelength-dependent, meaning the splitting ratio is not exactly 50/50 for all wavelengths, as illustrated in **Figure 2.11**(b). As a result, the optical signals from the two interferometer arms reaching the detector's two ports may not be identical. To achieve optimal balancing of the OCT signal, two connection methods were tested. The laser output was connected to the input white port of the coupler. **Figure 2.11**(c) shows the balanced OCT signal after subtraction by the detector, when the white signal output port was connected to the sample arm, and the

red tap output port to the reference arm. In contrast, **Figure 2.11**(d) shows the result of the inverse connection, where the red port was connected to the sample arm. The connection shown in **Figure 2.11**(c) demonstrated a flatter signal and better balance between the two interferometer arms.

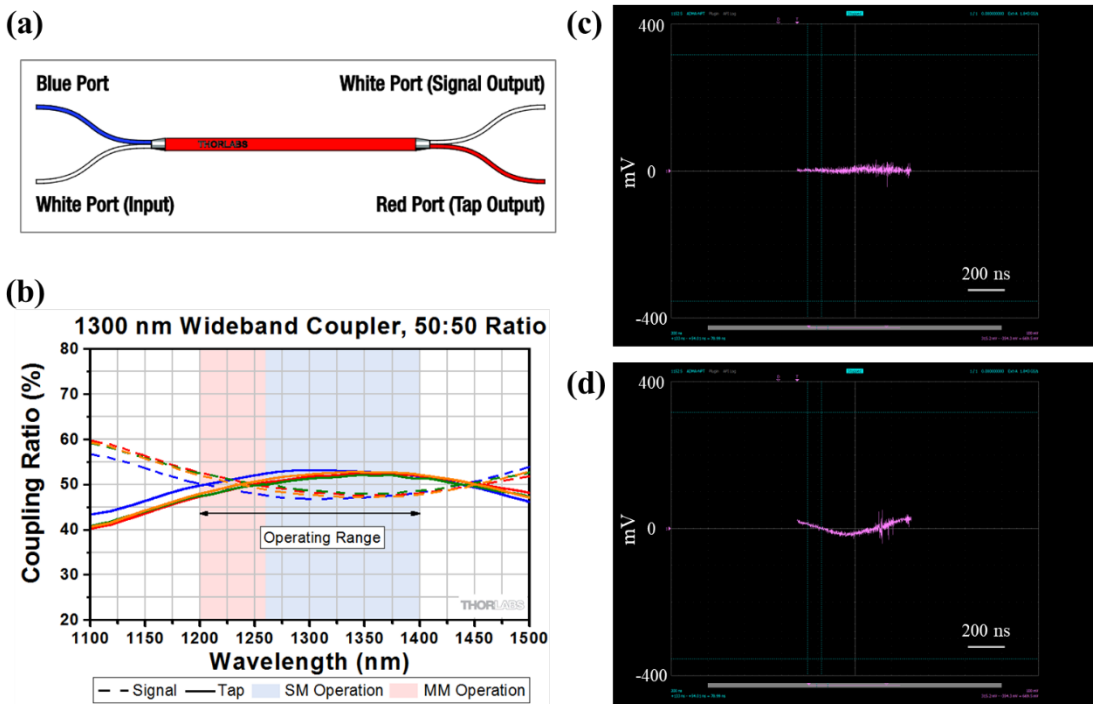

Figure 2.11: (a) Connection of the fibre coupler from Thorlabs. (b) The wavelength-dependent coupling ratio of the fibre coupler from Thorlabs [7]. (c) Balanced OCT signal when the signal output of the coupler is connected to the sample arm. (d) Balanced OCT signal when the tap output of the coupler is connected to the sample arm. The OCT signals were acquired using the FDML OCT system.

2.3.2. Coupling Efficiency of the Sample Arm

After determining the optimal coupler connection and aligning the optics in the sample arm, the coupling efficiency of the laser power in the sample arm was measured to

ensure sufficient signal power was collected from the sample. The laser power at the input white port of the coupler was 44.9 mW, with 20.7 mW directed to the sample arm. With the reference arm blocked and a reflective mirror placed after the objective as the sample, the back-coupled signal power at the blue port of the coupler (**Figure 2.11**(a)) to the detector was measured at 5 mW, 3.9 mW, and 3.4 mW when the MEMS scanner was disabled, X scanning enabled, and both X and Y scanning enabled, respectively. The corresponding coupling efficiencies were 52%, 41%, and 35%. These values indicate good alignment of the sample arm, with sufficient power being collected from the sample's backscattered signal.

2.3.3. Laser Safety Classification

Considering human skin as a potential imaging sample, the laser power emitted from the sample arm must be classified as safe. Therefore, the accessible emission limit (AEL) was calculated to classify the laser power in the sample arm, following the BS EN 60825-1:2014 standard [8]. The FDML laser output spans a spectral region from 1260 nm to 1360 nm, and the emission duration is assumed to be between 10 and 30,000 seconds. For this spectral range, the AEL for Class 1 and 1M laser output is given by:

$$AEL = 3.9 \times 10^{-4} \cdot C_4 \cdot C_7 \text{ (Watts)} \tag{2.1}$$

For Class 3R laser output, the AEL is:

$$AEL = 2.0 \times 10^{-3} \cdot C_4 \cdot C_7 \text{ (Watts)} \tag{2.2}$$

The AEL for Class 3B laser output is 0.5 W. In our case, the correction factor C_4 is 5 and C_7 is given by:

$$C_7 = 8 + 10^{0.04*(\lambda - 1250)} \tag{2.3}$$

For the minimum wavelength of 1260 nm, C_7 equals 10.5. Thus, the AEL for Class 1 and 1M lasers is 20.48 mW, and for Class 3R, it is 105 mW. As noted in the previous section, the signal output to the sample arm is 20.7 mW. Due to insertion loss, the power reaching the sample after the objective is less than the AEL for Class 1 and 1M lasers. Therefore, the laser output to the sample is classified as Class 1, making it safe for human skin, even though the main laser output is classified as Class 3R.

2.3.4. Obtaining Coherence Fringes

With the optical alignment complete and the safety evaluation verified, the FDML OCT system is ready to generate coherence fringes, also referred to as the interference spectrum. A reflective mirror was placed in the sample arm for this purpose. To achieve interference, the zero optical path difference (OPD) position between the two interferometer arms must be identified. **Figure 2.12** shows an example of interference, as displayed on an oscilloscope using a swept laser (HSL-2000, Santec) with a 10 kHz scan rate. **Figure 2.12**(a) and (b) depict the spectral signals from the reference and sample arms, respectively, while **Figure 2.12**(c) shows the coherence fringes superimposed on the laser spectrum. At this stage, the OCT signal is not balanced, resulting in the laser spectrum still being visible as the background. This slow-speed laser was used for practical experience and system understanding prior to using the FDML laser.

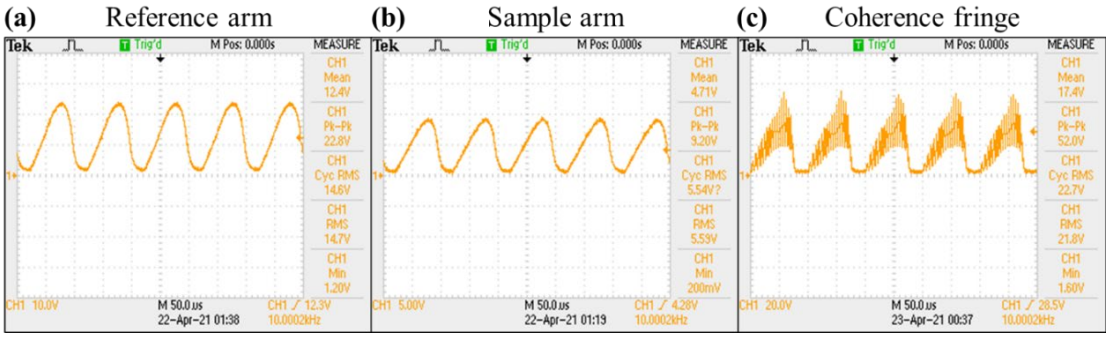

Figure 2.12: Example of the coherence fringes displayed on an oscilloscope using the FDML OCT system with a swept laser (HSL-2000, Santec) with a 10 kHz scan rate. (a) Spectral signal from the reference arm. (b) Spectral signal from the sample arm. (c) Coherence fringes on top of the laser spectrum.

2.4. Characteristics of FDML OCT

This section describes the performance of the optimised FDML OCT system, detailing the process of optimising the basic imaging unit, the A-scan, using zero-crossing resampling. Based on this, the system's imaging resolution, field of view, sensitivity, imaging depth, and intensity roll-off are evaluated.

2.4.1. Resampling and Fourier Transform

By combining the FDML laser and the balanced detector, the laser spectral background is removed, leaving only the coherence fringes signal, which is also doubled. **Figure 2.13**(a) shows a well-balanced, symmetrical coherence fringes signal from one complete sweep of the FDML OCT system, recorded with a reflective mirror in the sample arm.

Since the FDML laser performs frequency sweeping, its intracavity filter is tuned to select each wavelength over time, and the laser emits an internal sampling clock of

1.93 GHz. This results in 1152 samples per sweep, covering the wavelength range from 1259 nm to 1362 nm, all recorded sequentially by a single detector. As described in Section 1.3, the interference spectrum $I(k) \propto \cos(k \cdot z)$, where k (wavenumber) and z (axial depth) form a Fourier transform pair. Therefore, the reflectivity profile along the depth (Z axis) of the sample, or the A-scan, can be reconstructed via a fast Fourier transform (FFT) of the recorded sweep [3]. However, the wavelength λ (or wavenumber $k = 2\pi/\lambda$) is a nonlinear function of time during the FDML laser sweep [2]. Direct application of FFT to the interference spectrum can broaden the FFT peaks in the A-scan and attenuate their amplitudes as imaging depth z increases. This distortion negatively impacts axial resolution and imaging depth [9-12].

To correct this, uniform resampling of the interference spectrum in k-space is necessary. A flat reflective mirror was placed in the sample arm, without MEMS scanning, to provide a stable interference spectrum (blue line in **Figure 2.13**(a)), allowing extraction of the uniform resampling signal by zero-crossing detection. Since the mirror is positioned at a fixed depth z_0, the interference spectrum $I(k) \propto \cos(k \cdot z_0)$ should exhibit a specific single frequency when the wavenumber k is linearly sampled.

The first step is to locate the zero crossings of the fringes. However, the fringes are not always symmetrical with respect to the horizontal axis at y=0. To address this, the upper (orange) and lower (yellow) envelopes were detected to find the true horizontal line where the fringes are symmetric. This line is then shifted to y=0 (purple line) to accurately detect the zero crossings. Since the zero crossings are unevenly spaced, the second step involves applying linear interpolation to create a spline-fitting curve for these zero crossings, generating a resampling table. **Figure 2.13**(b) shows the corrected spectral sample positions corresponding to the resampling table. By interpolating the

interference spectrum of the mirror using the resampling table, the zero crossings are made equidistant in wavenumber k.

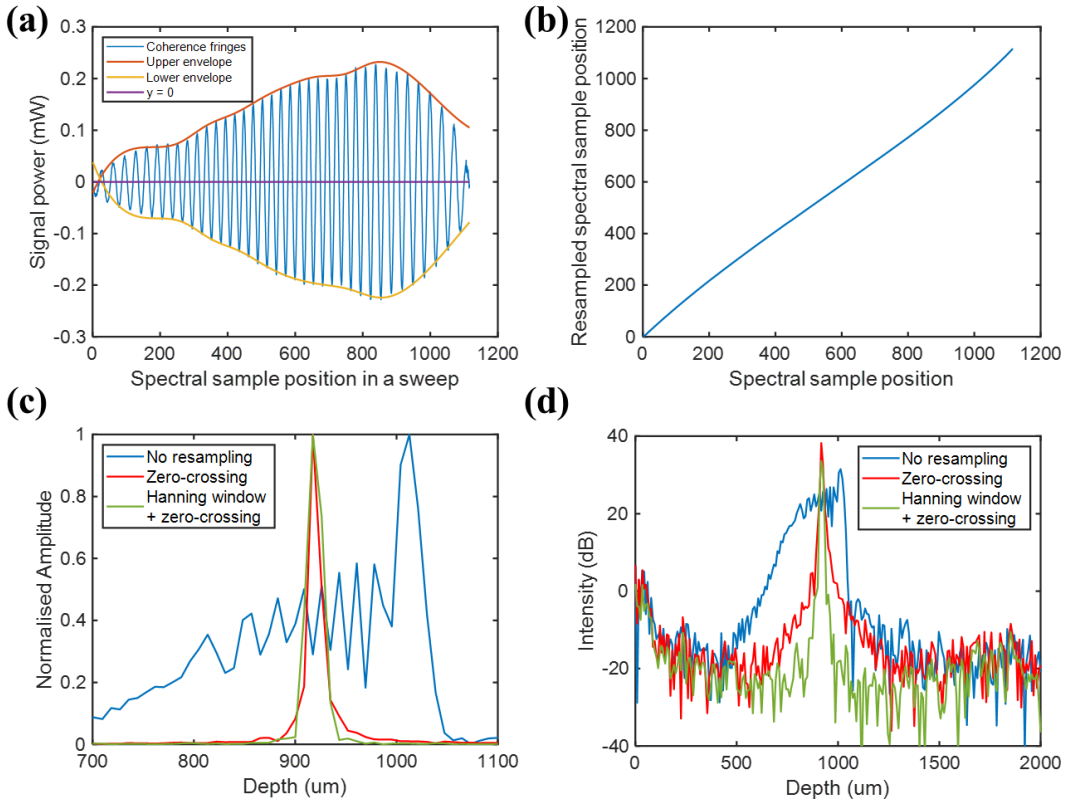

Figure 2.13: (a) Balanced interference spectrum from one typical sweep of the FDML OCT system with a reflective mirror in the sample arm. (b) Resample table generated using the zero-crossing method. (c-d) Comparison of A-scan peaks after FFT of the interference spectra, with no resampling, zero-crossing resampling, and Hann-window smoothed zero-crossing resampling.

As shown in **Figure 2.13**(c), the blue line represents a broad peak in the A-scan after applying direct FFT to the mirror's interference spectrum without resampling. In contrast, the red line represents the A-scan peak after resampling using the zero-crossing method. This peak is significantly narrower, indicating a more accurate depth position of the mirror at approximately 918 μm and an improved axial resolution, or

point spread function (PSF), of ~13.5 μm. The axial resolution is estimated based on the full width at half maximum (FWHM) of the peak. Unlike the normalised amplitude in **Figure 2.13**(c), **Figure 2.13**(d) compares A-scan peaks processed in terms of intensity (dB). After resampling, the peak intensity is significantly higher, enhancing the signal-to-noise ratio. Additionally, applying a 1152-point symmetric Hann window to the resampled interference spectrum (green line in **Figure 2.13**(d)) provides a smoother A-scan peak with fewer and lower sidelobes (roughly 15 to 25 dB intensity decrease), though this slightly reduces the axial resolution to ~19.8 μm.

In the FDML OCT system, the resampling table, generated from a flat mirror, is acquired before imaging and used for resampling the interference spectra of other samples in k-space. This resampling process is incorporated into the OCT data processing to produce the basic imaging unit, the A-scan. The resampling procedure is also efficient enough to enable real-time cross-sectional OCT imaging with high axial resolution.

2.4.2. Axial Resolution

Continuing from the previous section, a flat reflective mirror was placed in the sample arm at a depth of 1 mm from the zero optical path difference (OPD) to generate a resampling table. To evaluate how the axial resolution or PSF of the FDML OCT system changes with increasing imaging depth, the mirror was moved to various positions. The pre-acquired resampling table was then used to resample the interference spectra of the mirror at these different depths. After performing a FFT on the wavenumber-resampled fringe spectra, the axial resolution at each depth was measured, as shown in **Figure 2.14**(a). The measured axial resolutions over a 2 mm range in air, starting from the zero

OPD, varied between 13.2 μm and 13.9 μm. This consistent change in resolution indicates that the dispersion between the two interferometer arms is well-compensated.

The theoretical axial resolution of the FDML OCT system in air is 10 μm, calculated using the formula $0.44 \cdot \lambda_0^2/\Delta\lambda$ [3]. Here, the spectral centre wavelength λ_0 is 1309 nm, and the measured FWHM of the FDML laser spectrum $\Delta\lambda$ is 75 nm, as shown in **Figure 2.14**(b). This FWHM closely matches the value of 74 nm reported by Huber et al [2]. The discrepancy between the measured and theoretical axial resolutions is primarily due to imperfect k-space resampling and hardware limitations, such as dispersion. Additionally, the formula $0.44 \cdot \lambda_0^2/\Delta\lambda$ is only valid for a Gaussian spectrum. The shape of the FDML laser spectrum can also lead to the discrepancy, even when resampling and dispersion are optimally controlled.

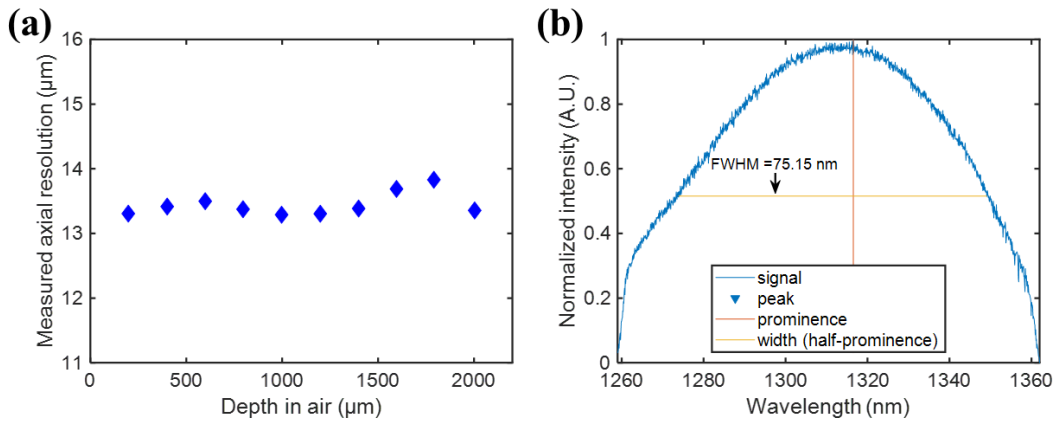

Figure 2.14: (a) Axial resolution (PSF) of the FDML OCT in different imaging depths in air. (b) Measured FWHM of the FDML laser spectrum.

Axial resolution can be further improved by using alternative computational approaches, such as non-uniform sampling direct reconstruction [12], multi-shaping/multi-window techniques [13, 14], or O-PRESS [15]. However, these methods

are more complex and time-consuming compared to zero-crossing resampling. While they can be applied as post-processing techniques to enhance the axial resolution of OCT images, they are not suitable for real-time imaging.

2.4.3. Lateral Resolution

Lateral resolution is another critical factor for evaluating the imaging quality of an OCT system. It depends on laser's spectral centre wavelength λ_0 and the numerical aperture (NA) of the objective, and it can be calculated using the equation $0.37\,\lambda_0/NA$. The NA is defined as $D/2f$, where f is the effective focal length and D is the entrance pupil diameter of the objective [3].

In our FDML OCT setup, the LSM03 objective has an effective focal length of 36 mm and an entrance pupil of 4 mm, resulting in an ideal lateral resolution of 8.7 μm in air. However, the laser beam diameter is constrained by the 2 mm diameter of the MEMS mirror, which limits the best achievable theoretical lateral resolution to 17.4 μm in air.

To estimate the actual lateral resolution of the FDML OCT system in air, a US Air Force (USAF) 1951 resolution test target (Thorlabs Inc.) was positioned at the focal plane of the objective in the sample arm. The FDML OCT image of the USAF target is compared with a reference image from Thorlabs in the same region of 1.3 mm x 1.3 mm, as shown in **Figure 2.15**. The smallest resolvable line pairs in the USAF OCT image are in element 3 of group 5, indicating a measured lateral resolution of 24.8 μm in air. This discrepancy is due to the actual beam diameter being less than 2 mm during MEMS mirror scanning.

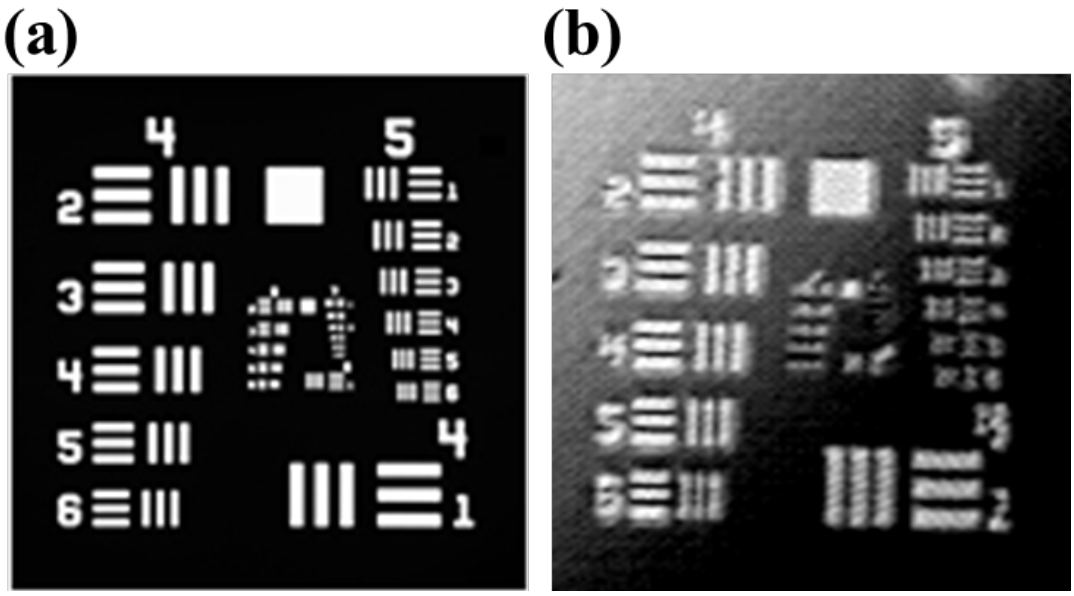

Figure 2.15: Images of a US Air Force (USAF) 1951 resolution test target. (a) Reference image from Thorlabs. (b) A 1.3 mm x 1.3 mm image under the FDML OCT system.

2.4.4. Field of View

The axial field of view (FOV), also referred to as the depth of field (DOF), is another parameter dependent on the numerical aperture that is typically discussed when characterizing the focusing optics of an OCT system. It represents the axial range over which the OCT system can maintain good lateral resolution (image sharpness). The DOF is inversely proportional to the square of the effective NA of the system, meaning that there is a trade-off between DOF and lateral resolution in the confocal sample arm. Lateral resolution can be enhanced by using an objective with a higher NA, but this simultaneously reduces the DOF due to diffraction effects [3, 16].

The DOF can be calculated by the equation $0.221\lambda/(\sin[\sin^{-1}(NA)/2])^2$ [3]. Given the 2 mm entrance pupil diameter, the objective used in our FDML OCT has a

relatively low NA. Therefore, the equation can be simplified to $0.221\lambda/(NA/2)^2$, resulting in a theoretical axial FOV (or DOF) of 1.5 mm at of wavelength of 1309 nm.

The lateral FOV in an OCT system is largely determined by the maximum scan angle of the laser beam through the objective. Although the LSM03 objective has a maximum lateral FOV of 9.4 x 9.4 mm^2, the actual lateral FOV is constrained by the 2.3° maximum scan angle of the MEMS mirror, reducing the effective lateral FOV to less than 2.9 x 2.9 mm^2.

2.4.5. Sensitivity

Sensitivity, also referred to as the signal-to-noise ratio (SNR) or dynamic range, defines the ability of an OCT system to detect weak signals reflected from within a sample [3]. In a swept-source OCT (SS-OCT) system, sensitivity refers to the minimum detectable reflectivity from a sample relative to the noise floor, which includes shot noise, detector noise, and laser relative intensity noise (RIN). Higher sensitivity allows for the detection of weaker backscattering signals from deeper within the sample, improving image quality and depth penetration. To accurately analyse the SNR in an OCT system, it is important to consider various noise sources.

2.4.5.1.Noise Sources in an FDML OCT System

The primary noise sources in an FDML OCT system include photon shot noise, detector noise, digitizer noise, and relative intensity noise (RIN) [17-19].

1) Shot noise

Shot noise is quantum noise resulting from the random arrival of photons at the detector. It is intrinsic and cannot be eliminated but can be mitigated by reducing illumination

intensity or using longer exposure times to average out fluctuations. Shot noise is proportional to the square root of the signal intensity and places a fundamental limit on the system's sensitivity. The shot noise density in our FDML OCT system can be described by [3]:

$$d_{shot} = \sqrt{2e\rho I} \tag{2.4}$$

where e is the electronic charge, ρ is the detector's responsivity, and I is the average optical power. Since the signal from the sample is generally much weaker than that from the reference arm, the mean photocurrent is dominated by the reference arm power I_R, i.e., $I \approx I_R$.

2) Detector noise

Detector noise arises from fluctuations in the electrical signal generated when light is converted into electrons. This noise is characterized by the noise-equivalent power (NEP) of the photodetector. The detector noise density can be expressed as [17, 19]:

$$d_{detector} = NEP \cdot \rho \tag{2.5}$$

3) Digitizer noise

Digitizer noise is introduced during the conversion of the analogue signal to digital format by the analogue-to-digital converter (ADC). Quantization noise, a key component of digitizer noise, arises from the finite resolution of the ADC. It is referred to the error introduced by the difference between the actual signal value and the quantised value [18]. The quantisation noise density is defined as:

$$d_{digitizer} = \frac{V_{max} \cdot \rho}{\sqrt{3X} \cdot 2^n \cdot G} \tag{2.6}$$

where V_{max} is the maximum single-side range of the ADC, X is the analogue-to-digital sampling rate, n is the number of bits of the ADC, and G is the transimpedance gain of the photodetector.

4) Relative intensity noise (RIN)

RIN refers to random fluctuations in the intensity of the laser output relative to its average power. These fluctuations result from instabilities or imperfections in the laser source and can dominate the noise profile, especially at higher power levels [20-22]. RIN is typically quantified in dB/Hz and can be expressed as:

$$RIN = 10\log_{10}\frac{\sigma_{RIN}^2}{I^2 \cdot B} \tag{2.7}$$

where σ_{RIN}^2 is the variance of the laser output power, I is the average optical power, and B is the detection bandwidth of the system. Since the signal from the sample is generally weaker, $I \approx I_R$.

2.4.5.2. Measuring the RIN of the FDML Laser

To measure the RIN of the FDML laser, the laser light was emitted through a 50:50 coupler, with one output connected to a power meter and the other to the detector. Laser spectra were recorded by the digitizer, and 11 different output levels were tested. The power measured by the power meter ranged from 0.0005 mW to 0.141 mW, with each spectrum obtained by averaging 20 laser sweeps (**Figure 2.16**(a)).

To measure intensity fluctuations relative to the average power, each laser spectrum was smoothed using a large-kernel window (red line in **Figure 2.16**(b)), and the noise variance was obtained by subtracting the original spectrum from the smoothed one. The noise variance of the photocurrent is shown in **Figure 2.16**(c).

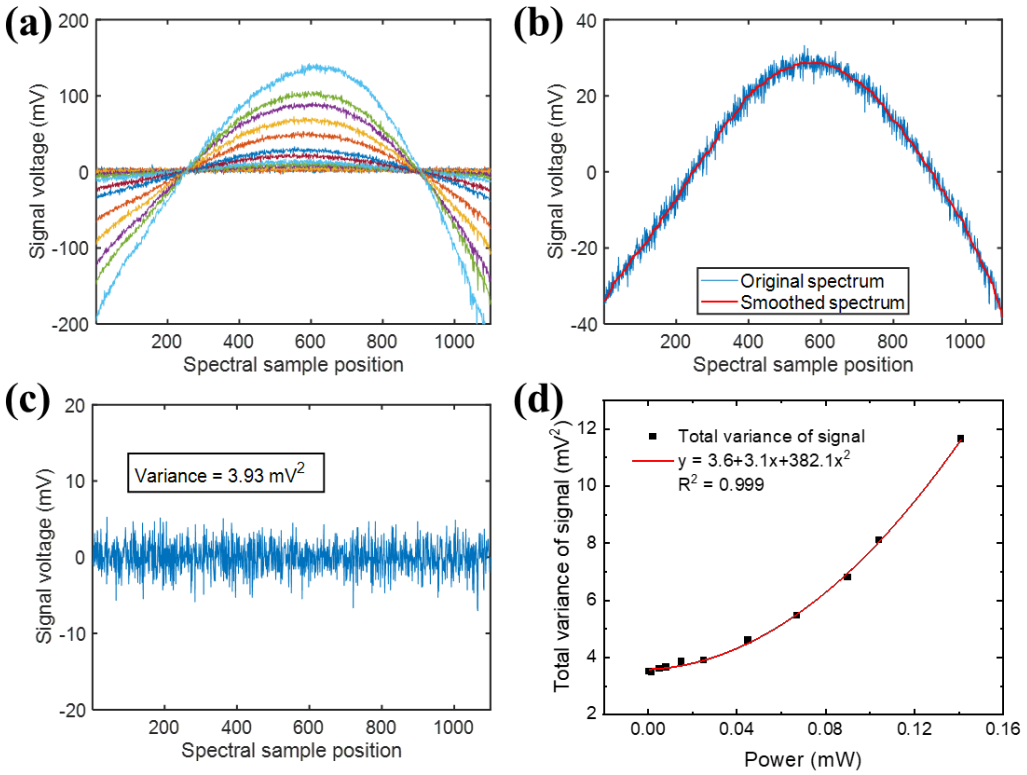

Figure 2.16: (a) Eleven FDML laser spectra recorded by the digitizer. (b) Comparison between one laser spectrum and its smoothed version using a large-kernel window. (c) Noise variance obtained by subtracting the original spectrum from the smoothed spectrum. (d) Quadratic fit of noise variance measurements against corresponding input power for all eleven data points.

The total noise variance of the laser spectrum, including RIN, shot noise, detector noise, and digitizer noise, can be expressed as [17-19]:

$$\begin{aligned}\sigma_{total}^2 &= {\sigma_{digitizer}}^2 + {\sigma_{detector}}^2 + {\sigma_{shot}}^2 + {\sigma_{RIN}}^2 \\ &= B\left({d_{digitizer}}^2 + {d_{detector}}^2 + {d_{shot}}^2 + {d_{RIN}}^2\right) \\ &= B\left({d_{digitizer}}^2 + {d_{detector}}^2\right) + 2eB \cdot i + 10^{RIN/10} B \cdot i^2 \end{aligned} \tag{2.8}$$

where i is the mean detector photocurrent, and the other parameters are constant. Since the total noise variance σ_{total}^2 was measured in voltage, the photocurrent i can be

calculated by multiplying the measured power I by the transimpedance gain G of the detector, i.e., $i = G \cdot I$. Hence, the 11 measurements of noise variance and corresponding input power were fitted with a quadratic function. As shown in **Figure 2.16**(d), the red curve represents the fitted quadratic equation, where the constant coefficient of 382.1 corresponds $10^{RIN/10}BG^2$. The detection bandwidth B for an SS-OCT system is limited by the sampling frequency X. Assuming $B = X$, based on this analysis, the RIN of the FDML laser was measured to be -137.4 dB/Hz.

2.4.5.3. Evaluating the Sensitivity of the FDML OCT System

After identifying the main noise sources in the FDML OCT system, the theoretical SNR can be calculated. Assuming a single reflector in the sample arm, the mean-square peak signal power $\langle I_D \rangle^2$ detected by the photodetector is given by [3]:

$$\langle I_D \rangle^2 = \rho^2 \cdot I_S \cdot I_R \cdot m^2 \tag{2.9}$$

where I_S and I_R are the powers reflected from the reference and sample arms, respectively, and m is the number of spectral sampling channels.

The detected noise variance σ^2 of the FDML OCT system can be calculated by multiplying the square of noise density by the detection bandwidth B and the number of sampling channels m. The SNR can then be expressed as [3]

$$SNR = 10 \log \frac{\langle I_D \rangle^2}{\sigma^2} \tag{2.10}$$

in decibels (dB). **Table 2.2** provides the equations for calculating both the shot-noise-limited SNR and the total noise-limited SNR for the FDML OCT system, along with the noise density calculation formulas [3, 17-19]. The key parameters of the FDML OCT system used for these calculations are summarized in **Table 2.3**.

Table 2.2: Equations for calculating the shot-noise-limited SNR and the total noise-limited SNR for the FDML OCT system, including formulas for noise density calculations.

	Equations
Shot noise density (A/$\sqrt{\text{Hz}}$)	$d_{shot} = \sqrt{2e \cdot \rho \cdot I_R}$
Detector noise density (A/$\sqrt{\text{Hz}}$)	$d_{detector} = NEP \cdot \rho$
Digitizer quantisation noise density (A/$\sqrt{\text{Hz}}$)	$d_{digitizer} = \frac{V_{max} \cdot \rho}{\sqrt{3X} \cdot 2^n \cdot G}$
RIN density (A/$\sqrt{\text{Hz}}$)	$d_{RIN} = 10^{RIN/20} \cdot \rho \cdot I_R$
Mean-square peak signal power	$\langle I_D \rangle^2 = \rho^2 \cdot I_S \cdot I_R \cdot m^2$
Shot-noise-limited SNR (dB)	$SNR_{shot} = 10 \log \frac{\langle I_D \rangle^2}{{d_{shot}}^2 \cdot B \cdot m}$
Total noise-limited SNR of the FDML OCT system (dB)	$SNR = 10 \log \frac{\langle I_D \rangle^2}{{d_{total}}^2 \cdot B \cdot m}$ $= 10 \log \frac{\langle I_D \rangle^2}{\left({d_{digitizer}}^2 + {d_{detector}}^2 + {d_{shot}}^2 + {d_{RIN}}^2\right) \cdot B \cdot m}$

Table 2.3: Key parameters of the FDML OCT system used for SNR and noise density calculations.

Technical parameters	Abbreviation	Value	Unit
Responsivity	ρ	0.9	A/W
Elementary charge	e	1.60E-19	C
Transimpedance gain of Wieserlabs detector	G	3300	V/W
Noise-equivalent power (NEP) of Wieserlabs detector	NEP	2.00E-11	W/$\sqrt{\text{Hz}}$
Voltage range of ATS9373 digitizer	V_{max}	0.4	volt
Resolution of ATS9373 digitizer	n	12	bit
Number of spectral sampling channel	m	1152	
A-scan rate of FDML laser	F	1.67	MHz
Sampling rate of ATS9373 digitizer	$X = M \cdot F$	1.93	GHz
Detection bandwidth of FDML OCT	$B = X$	1.93	GHz
Measured RIN level of FDML laser	RIN	-137.4	dB/Hz
Sample arm power of FDML OCT	I_S	0.02	W

According to the SNR equations in **Table 2.2**, the shot-noise-limited SNR is independent of the reference arm power I_R. However, in practice, the SNR of FDML OCT varies with different reference arm power levels. Assuming a reasonable sample arm power of 0.02 W, the relationship between the theoretical SNR of the FDML OCT system and the reference arm power is shown in **Figure 2.17**. The blue dashed line shows the calculated shot-noise-limited SNR, which is approximately 105 dB.

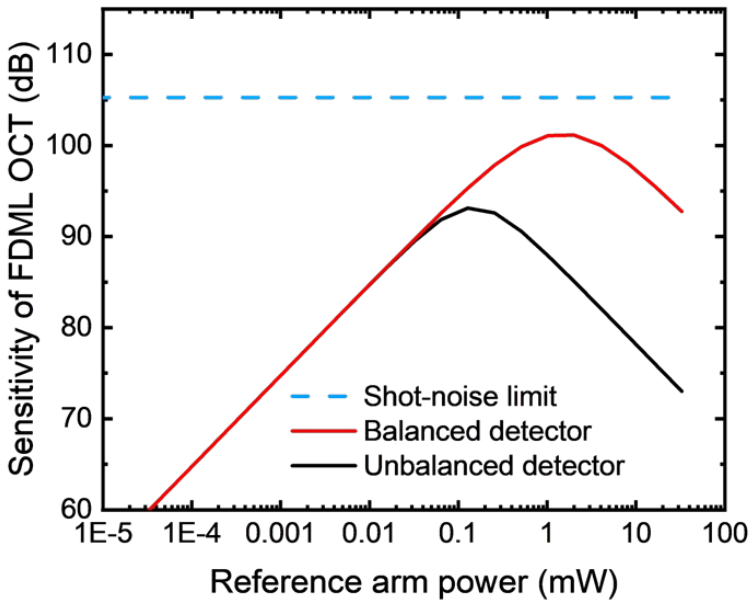

Figure 2.17: Comparison of the calculated shot-noise-limited SNR, dynamic range of the FDML OCT system with an unbalanced detector, and dynamic range of the FDML OCT system with a balanced detector. A 10 times RIN reduction was assumed for calculating the balanced dynamic range (red curve).

The black curve shows the calculated dynamic range (SNR) of the FDML OCT system when using an unbalanced detector. However, the balanced detector employed in our system mitigates the relative intensity noise (RIN) by subtracting the two light signals measured simultaneously from the two ports [17, 23]. To account for this, an

attenuation coefficient of 0.1 is assumed for the RIN density. The red curve illustrates the calculated dynamic range of the balanced FDML OCT system, with the optimal sensitivity of approximately 101 dB.

To measure the sensitivity of the FDML OCT system, a flat reflective mirror was placed in the sample arm, and a round continuously variable neutral density (ND) filter (NDC-50C-4, Thorlabs Inc.) was positioned between the collimator and the MEMS scanner in the sample arm. The ND filter was rotated to a position that provided a power intensity reduction of approximately 38 dB. The interference spectrum was then acquired using the FDML OCT system. After resampling and applying an FFT to the spectrum, an A-scan peak with an intensity of roughly 24 dB was observed at 1 mm OPD. Since the laser beam was attenuated twice by the ND filter, the sensitivity of the FDML OCT system was measured as 38 dB x 2 + 24 dB = 100 dB at 1 mm OPD in air, which is close to the calculated sensitivity of 101 dB.

2.4.6. Imaging Depth and Intensity Roll-off

The imaging depth in air of an OCT system can be calculated using the formula $\lambda_0^2/4\delta_\lambda$. Here, λ_0 is the centre wavelength of the laser spectrum. δ_λ is the average spectral sampling interval, which is obtained by dividing the laser sweep range by the number of samples in a sweep [3]. In our FDML OCT system, this yields an imaging depth of 4.8 mm in air. However, in biological tissues, the actual tissue imaging depth is limited by light scattering, with longer wavelengths (e.g., near-infrared) offering greater penetration due to reduced scattering. In our case, the 1310 nm FDML OCT system can penetrate up to 2 mm in tissue.

To experimentally measure the detection roll-off of the FDML OCT system, a flat reflective mirror was placed in the sample arm and moved to different depth positions from 0 OPD to 4 mm. FFT was performed on each mirror interference spectrum, and the intensity of each A-scan peak is shown in **Figure 2.18**. The results demonstrate that the FDML OCT system has an intensity roll-off of less than -1 dB over a 2 mm range in air, starting from the zero OPD position. Additionally, from 0 to 2 mm in air, the noise floor of each A-scan remains nearly constant at 63 dB. Thus, the sensitivity roll-off of the FDML OCT system, defined as the difference between the A-scan peak and the noise floor, is approximately equal to the intensity roll-off.

Beyond 2 mm, the noise floor intensity clearly increases with depth. This can be attributed to the axial PSF degradation due to reduced performance of the resampling table. Therefore, it is advisable to position the sample closer to the zero OPD to reduce artifacts and noise during FDML OCT imaging.

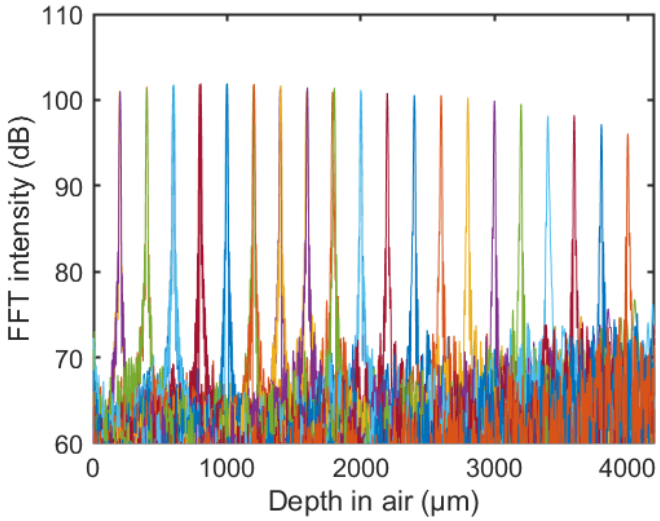

Figure 2.18: Intensity roll-off of the A-scan peak from a mirror at various depth position relative to the zero OPD, measured using the FDML OCT system.

2.5. Imaging using FDML OCT

The previous section demonstrated the excellent resolution and sensitivity of the FDML OCT system, indicating that it is well-suited for imaging. In this section, the preparation for displaying images and the scan protocols are described first, followed by the presentation of some representative imaging results (acquired by a self-developed FDML OCT control software detailed in Section 2.6).

2.5.1. Preparation for Displaying Images

2.5.1.1.Synchronisation for Scanning and Data Collection

Before displaying OCT images correctly on screen, it is crucial to acquire accurate datasets for image processing. This requires the synchronisation of the timing sequence between the FDML laser sweeping, MEMS scanning, and digitizer acquisition, which can be achieved by configuring relevant settings using a FDML OCT control software (Section 2.6) based on the FDML firmware.

First, the start of digitizer acquisition must be synchronised with the sampling clock provided by the FDML laser. This ensures the correct A-scan sampling delay, allowing the digitizer to capture one complete A-scan interference spectrum with 1152 samples within the laser sweep range from 1259 nm to 1362 nm.

Second, the digitizer's B-scan acquisition trigger waveform must be synchronised with the MEMS X-axis analogue waveform, also generated by the FDML laser. One trigger event corresponds to one B-scan, which comprises a series of A-scans. Therefore, the B-scan trigger frequency must match the X-axis scanning frequency of the MEMS. This synchronisation ensures that the digitizer starts acquiring backscattered signals

from the correct position at the beginning of each cross-sectional scan while the MEMS scanner moves according to the X-axis analogue waveform. A phase delay typically exists between the B-scan trigger and the X-axis waveform, which must be accounted for.

Finally, for volume imaging, which consists of multiple B-scans, Y-axis scanning is enabled alongside X-axis scanning. The digitizer's acquisition start trigger must be synchronised with the Y-axis scanning waveform, which controls the Y-axis movement of the MEMS scanner. This synchronisation ensures that signals are captured from the entire 3D volume of the sample, starting at the correct position along the Y-axis.

2.5.1.2. Distortion Calibration

Another important step before displaying images is calibrating any distortions. Starting with the A-scan, the imaging depth must be calibrated to ensure that the sample layer position matches the FFT peak position of that layer. To achieve this, a mirror was placed in the sample arm, and the reference arm's moving stage was adjusted by rotating the knob. This adjustment aligns the FFT peak position with the physical moving distance, with the MEMS scanner disabled during this process.

For the B-scan, the FDML laser provides a sinusoidal waveform to control the X-axis scanning of the MEMS mirror by applying periodic differential voltages to the two X-axis channels of the MEMS, as detailed in Section 2.2.2.1. Due to the slower rotation of the MEMS mirror at the edges, B-scan images typically appear stretched at the edges. To correct this, the B-scan images must be resampled using the same sinusoidal waveform to eliminate the distortion. After X-axis resampling, a distortion test target (R1L3S12N, Thorlabs Inc.) was placed 1 mm away from the zero OPD to verify the accuracy of the X-axis resampling. The target image, shown in **Figure 2.19**, reveals a

scan length of 2.8 mm with 28 evenly distributed gratings, and no distortion was observed. Additionally, the target was moved to different depths, and the scan length, axial resolution, and lateral resolution remained consistent, indicating that the optical alignment between the MEMS scanner and the objective was well-calibrated.

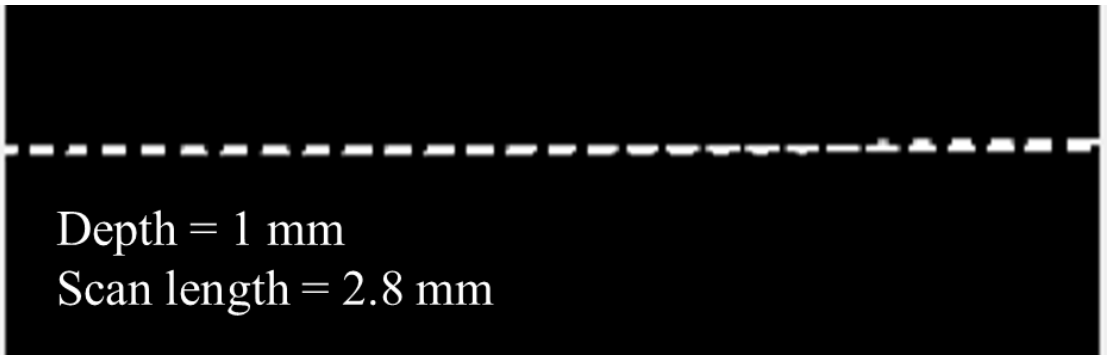

Figure 2.19: B-scan image of a distortion test target acquired using the FDML OCT system.

For volume scans, since the Y-axis scanning is much slower, the FDML laser provides a triangular waveform to the MEMS for uniform scanning along the Y-axis. This uniformity eliminates the need for resampling in the Y-axis. However, it is crucial to ensure that the number of falling steps in one cycle of the Y-axis waveform is not significantly smaller than the number of rising steps. If the number of falling steps in one cycle is too small, the MEMS scanner mirror repositions too quickly. During the transition from backward to forward scanning, the inertia of the MEMS scanner mirror can cause unstable motion, leading to distortion or an unstable scanning pattern at the start of the Y-axis volume scan. Additionally, during the Y-axis scanning, the MEMS mirror performs a forward scan and backward scan along the X-axis at each Y position, returning to its original starting position before moving to the next Y position.

2.5.2. Scan Protocols for OCT Imaging

In an OCT setup, various scan protocols are used depending on the specific application, such as traditional OCT imaging or angiographic imaging. These protocols define how the system acquires data and can influence imaging resolution, contrast, and the ability to detect flow signals. The primary scan modes used in OCT are described below [24]:

1) M-mode scan

   An M-mode scan involves repeated A-scans at the same position without enabling X-axis or Y-axis scanning of the MEMS. This mode is useful for observing changes over time at a fixed point, using a fundamental interval time between two consecutive A-scans.

2) MB-mode scan

   In an MB-mode scan, X-axis scanning is enabled in addition to M-mode. It performs B-scans with repeated A-scans at each X-axis position. This mode can improve image contrast by averaging multiple A-scans per position to reduce the background noise.

3) B-mode scan

   A B-mode scan differs from MB-mode in that it repeats the entire B-scan at the same cross-sectional location rather than repeating A-scans. In this mode, each B-scan consists of a single A-scan at each X-axis position. This mode is beneficial for capturing dynamic changes over time at the same location, with a fundamental interval time between two consecutive B-scans.

4) BM-mode scan

   The BM-mode scan enables both X-axis and Y-axis scanning, making it a volume scan (C-scan). It involves B-scan repetitions at each Y-axis position, providing 3D volumetric data. Unlike MB-mode, there are no A-scan repetitions

at each X-axis position. This mode captures additional information along the Y-axis, with the same fundamental interval time between two consecutive B-scans, building on the B-mode scan.

5) CM-mode scan

   In CM-mode scanning, the system repeats C-scans (volume scans) over the same X-Y region without repeating A-scans or B-scans at any specific location. This mode is useful for capturing dynamic changes in a region, with a fundamental interval time between two consecutive C-scans.

These scan protocols vary in interscan time depending on the mode and number of repetitions. Repetition at the same position not only averages out noise and enhances image contrast but also allows for the detection of flow signal fluctuations, which is crucial for OCT angiographic (OCTA) imaging. The fundamental interscan time of CM-mode scans is typically longer than that of B-mode and BM-mode scans, which in turn is longer than that of M-mode and MB-mode scans. By selecting an appropriate fundamental interscan time, flow signals with different velocities can be detected and quantified.

These scan protocols are applied to image the vasculature of human hand skin in Chapter 3 and estimate the cutaneous blood flow velocities in superficial vessels in Chapter 4. **Table 2.4** compares the scan areas, fundamental interscan times, and acquisition times for the different scan modes using example scan parameters.

Table 2.4: Comparison of scan parameter settings in different scan protocols using the FDML OCT system.

Scan parameters	**M-mode**	**MB-mode**	**B-mode**	**BM-mode**	**CM-mode**
Scan area	-	2.8 mm	2.8 mm	2.8 x 2.8 mm^2	2.8 x 2.8 mm^2
A-scan spacing	-	10 µm	10 µm	10 µm	10 µm
B-scan spacing	-	-	-	10 µm	10 µm
A-scan repeats	10	10	1	1	1
A-scans per B-scan	-	2800	280	280	280
B-scan repeats	-	1	10	10	1
B-scans per C-scan	-	-	-	280	280 + 50 (Forward + Backward B-scans)[b]
C-scan repeats	-	-	-	1	10
Frame rate[a]	1.67 MHz	300 Hz	3 kHz	3 kHz	3 kHz
Fundamental interscan time	0.6 µs	0.6 µs	0.33 ms	0.33 ms	110 ms
Acquisition time	6 µs	1.67 ms	3.34 ms	0.93 s	1.1 s

[a]In M-mode, the frame rate is equal to the A-scan rate of the FDML laser; In other modes, the frame rate refers to the effective X-axis scanning frequency of the MEMS scanner at which the fundamental dataset can be acquired.

[b]In CM-mode, the mirror returns to its starting position after completing 50 backward B-scans along the Y-axis.

2.5.3. Imaging results

This section presents example images of B-scans and enface mean intensity projections taken by the FDML OCT system.

2.5.3.1. B-scan Imaging in Different Frame Rates

First, B-scans of dorsal hand skin acquired at different frame rates are compared in **Figure 2.20**. **Figure 2.20**(a) shows a B-scan in MB-mode with a scan length of 2.8 mm and 30 A-scan repetitions at each of the 280 X-axis positions, resulting in a frame rate of 100 Hz. In contrast, **Figure 2.20**(b) shows a B-scan with the same 2.8 mm scan length, but with 280 A-scans along the X-axis (one per position), resulting in a much faster frame rate of 3 kHz.

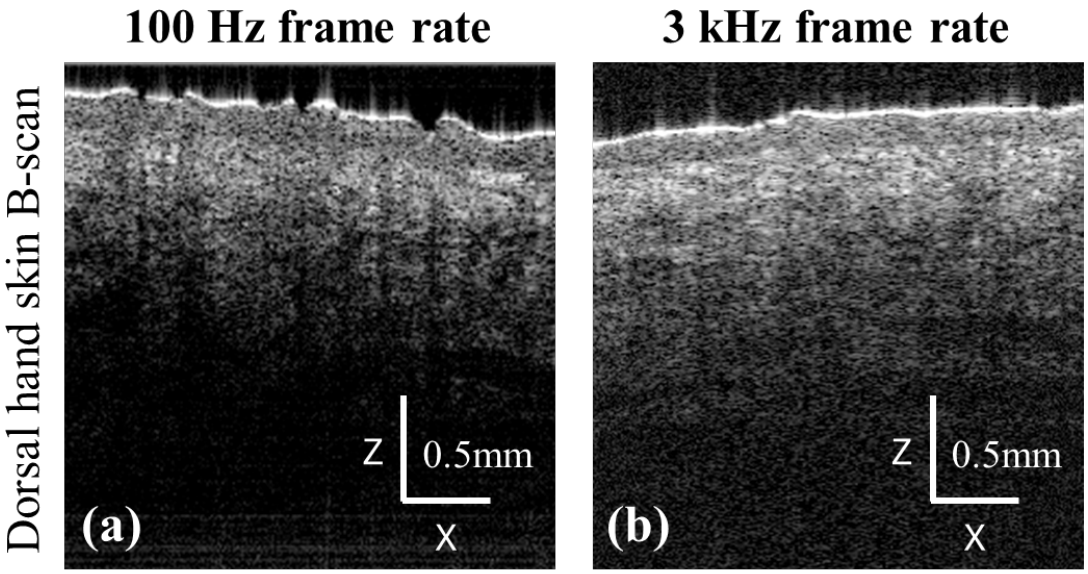

Figure 2.20: Comparison of B-scans of dorsal hand skin (at different sites of the same hand) taken by the FDML OCT system at different frame rates. (a) B-scan in MB-mode with a scan length of 2.8 mm, 280 X-axis positions, and 30 A-scan repetitions per position, resulting in a frame rate of 100 Hz. (b) B-scan with a scan length of 2.8 mm, 280 A-scans along the X-axis (one per position), resulting in a frame rate of 3 kHz.

In **Figure 2.20**(a), with 30 A-scan repetitions per X-axis position, the image displays a cleaner noise background and better contrast compared to **Figure 2.20**(b), which has only one A-scan per position. However, despite the reduced contrast or SNR in **Figure 2.20**(b) due to less averaging, the skin structure is still recognizable at the higher frame rate of 3 kHz.

While the slower frame rate used in **Figure 2.20**(a) offers slightly better contrast, the faster frame rate used in **Figure 2.20**(b) demonstrates the advantage of using a much higher X-axis scanning frequency of the MEMS scanner, with only a small loss in contrast. This highlights the capability of our FDML OCT system to maintain good imaging quality even at high scan speeds, showcasing the benefit of rapid scanning with a 3 kHz frame rate.

2.5.3.2. Imaging Comparison for Different Samples

To maintain the advantage of fast imaging, a 3 kHz frame rate is used for all imaging in this section and the following chapters. **Figure 2.21** compares B-scans and enface mean intensity projections of various samples imaged using the FDML OCT system, including a ribbon cable, thumb nail, index fingertip skin, palmar skin, dorsal hand skin, and forearm skin.

All B-scans have a scan length of 2.8 mm and consist of 280 A-scans along the X-axis. The enface images correspond to volume scans with a 2.8 mm x 2.8 mm scan area (280 pixels x 280 pixels), and each volume scan includes 280 B-scans along the Y-axis. Each volume scan takes approximately 0.1 seconds to complete. The enface images are generated by averaging the intensity values along the A-scan direction (Z-axis) for each pixel in the X-Y region after acquiring the 3D volumetric scan.

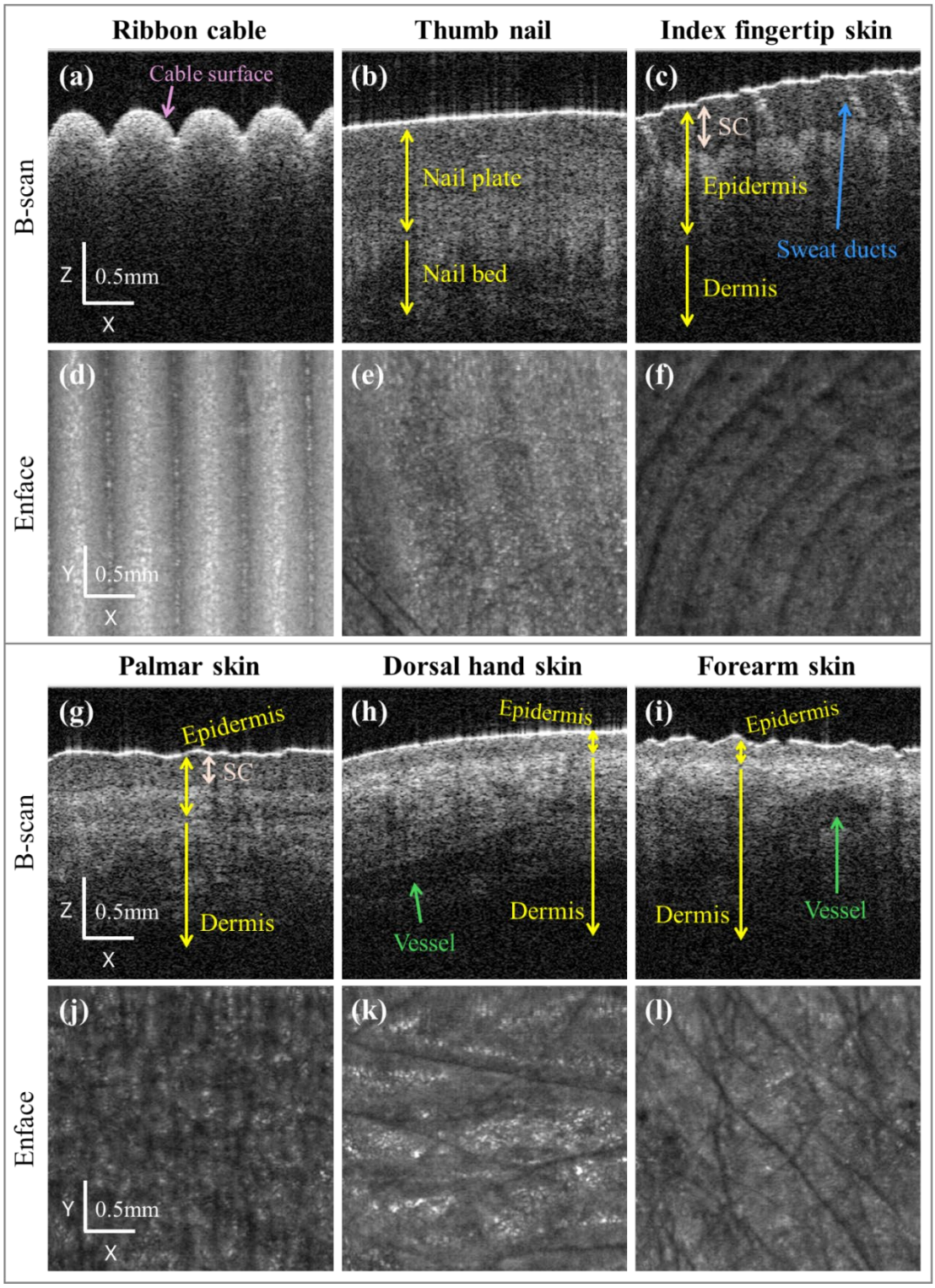

Figure 2.21: B-scans and enface mean intensity projections of various samples imaged using the FDML OCT system, including a ribbon cable, thumb nail, index fingertip skin, palmar skin, dorsal hand skin, and forearm skin. All B-scans have a scan length of 2.8 mm (280 A-scans along the X-axis). Enface images correspond to a 2.8 mm x 2.8 mm

scan area with 280 B-scans along the Y-axis. Each enface image is generated by averaging intensity values across the A-scan (Z-axis) for each pixel in the X-Y plane. The B-scans reveal structural details, including the stratum corneum, epidermis, and dermis, while the enface images display surface features like fingerprints and skin furrows. SC: stratum corneum.

As shown in **Figure 2.21**, the B-scans reveal the detailed structure of the ribbon cable, nail, and different areas of human skin. In particular, for the skin samples, the stratum corneum is visible in the fingertip and palmar skin, while both the epidermis and dermis are evident in all skin B-scans. The thickness of the stratum corneum and epidermis can be measured directly from the images. Additionally, vessels and sweat ducts are discernible in certain areas.

While the B-scans provide detailed cross-sectional views of the structures, the enface images highlight the surfaces of the samples. Notably, the fingerprint features and skin furrow patterns are clearly visible in the skin samples.

2.6. Development of FDML OCT Control Software

This section introduces the FDML OCT control software, developed using MATLAB App Designer. The main purpose of this software is to control the FDML laser and digitizer for real-time B-scan imaging and data collection, supporting different scan protocols for further offline image processing. Real-time A-scan and B-scan imaging also assist in the alignment of the FDML OCT system. The software includes five tabs, each designed for specific functions, which will be briefly described.

The FDML laser connects to the computer via a USB cable, while the digitizer card is integrated into the computer's motherboard through a PCI Express slot. Once the physical connections are established, the computer detects the devices, and the laser and digitizer can communicate through the serial port or PCIe slot by sending commands. The software has been developed based on these connections and is continuously updated to meet evolving imaging requirements. The software interface primarily consists of a panel for scan information, a panel for scan settings, and five functional tabs, as shown in the following figures.

The scan information panel allows users to set filenames, select drive locations for saving OCT datasets, and sync date and time, with the option to compress files. The scan settings panel enables users to configure the scan format for data collection. Users can adjust the scan width and height to set the scan length along the X-axis and Y-axis on the sample. The X and Y resolution settings adjust the spacing between A-scans and B-scans, respectively. Additionally, the panel provides information such as acquisition time, file saving time, X-axis scan frequency, and approximate file size.

Figure 2.22 shows the software interface with the first tab, labelled "Image," which is designed for real-time B-scan imaging. Users can adjust both the depth and greyscale of the image. The quality of the imaging is directly reflected in this tab, making it especially useful for aligning the optics, positioning the sample, and assessing system performance. This tab also supports functions such as resampling the image along the X-axis and saving the B-scan image.

In the top left corner, the "Image" tab displays a standard OCT B-scan when $\Delta T = 0$. When ΔT is set to any positive integer, the tab displays a simple difference-based

OCT angiographic image. The ΔT value determines the time interval for OCTA imaging, calculated as ΔT times the fundamental B-scan acquisition time.

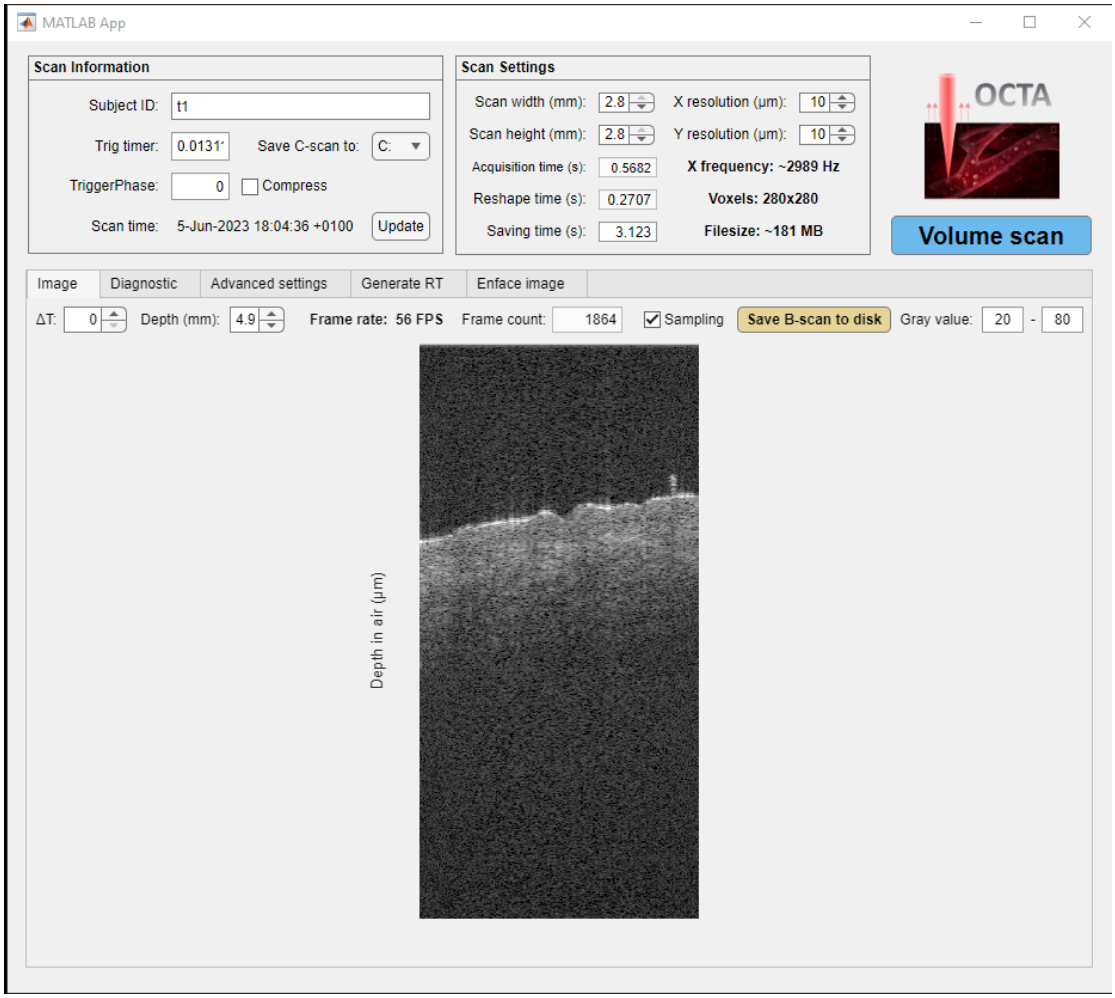

Figure 2.22: FDML OCT control software interface showing the "Image" tab for real-time B-scan imaging. The tab allows adjustments to imaging depth and greyscale, as well as functions for X-axis resampling and saving B-scan images. In the top left corner, a standard OCT B-scan is displayed when ΔT = 0, and a simple difference-based OCT angiographic image is shown when ΔT is set to a positive integer, determining the time interval for OCTA imaging.

Figure 2.23 shows the second tab, labelled "Diagnostic". This tab contains three windows: the first displays the raw interference spectrum within the FDML laser's spectral wavelength range, the second shows the raw interference spectrum resampled in the wavenumber range using a preset resampling table, and the third presents the reconstructed A-scan after performing FFT on the wavenumber-resampled interference spectrum. All windows provide real-time views of the interference spectrum or A-scan, with adjustable Y-axis units and axis ranges. This tab is particularly useful for checking the coherence fringes or A-scans from the sample, monitoring whether the fringe power exceeds the digitizer's maximum voltage limit (±400 mW), assessing the quality of wavenumber resampling, verifying synchronisation between the acquisition trigger and the sampling clock, and other diagnostic tasks.

Figure 2.24 shows the third tab, labelled "Advanced Settings". This tab allows users to finely adjust the X-axis and Y-axis analogue waveforms for controlling the MEMS scanner, configure technical settings for synchronizing the digitizer and FDML laser, acquire and subtract background signals, and load pre-acquired resample tables, among other advanced functions.

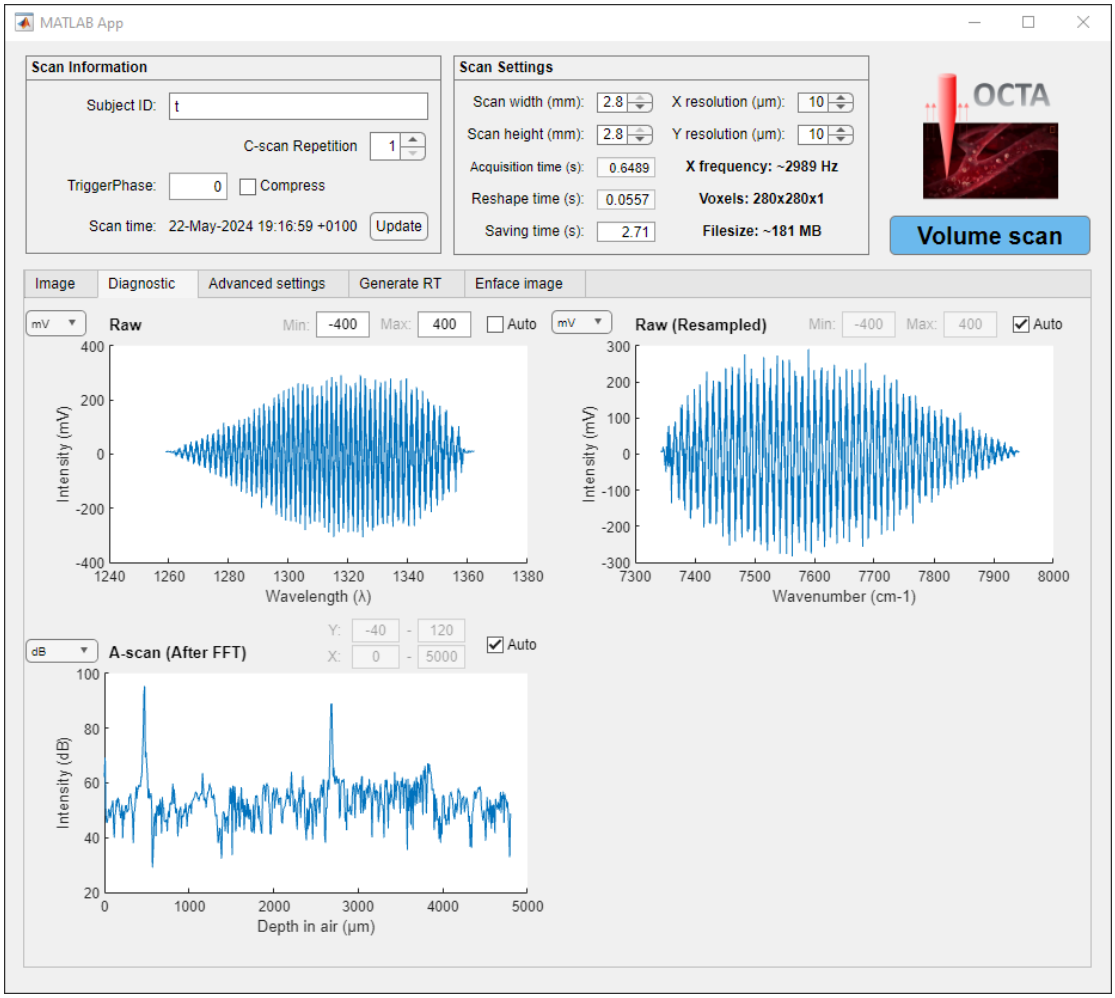

Figure 2.23: The "Diagnostic" tab displaying the raw interference spectrum, resampled spectrum, and reconstructed A-scan, with real-time views and adjustable axis settings for system diagnostics.

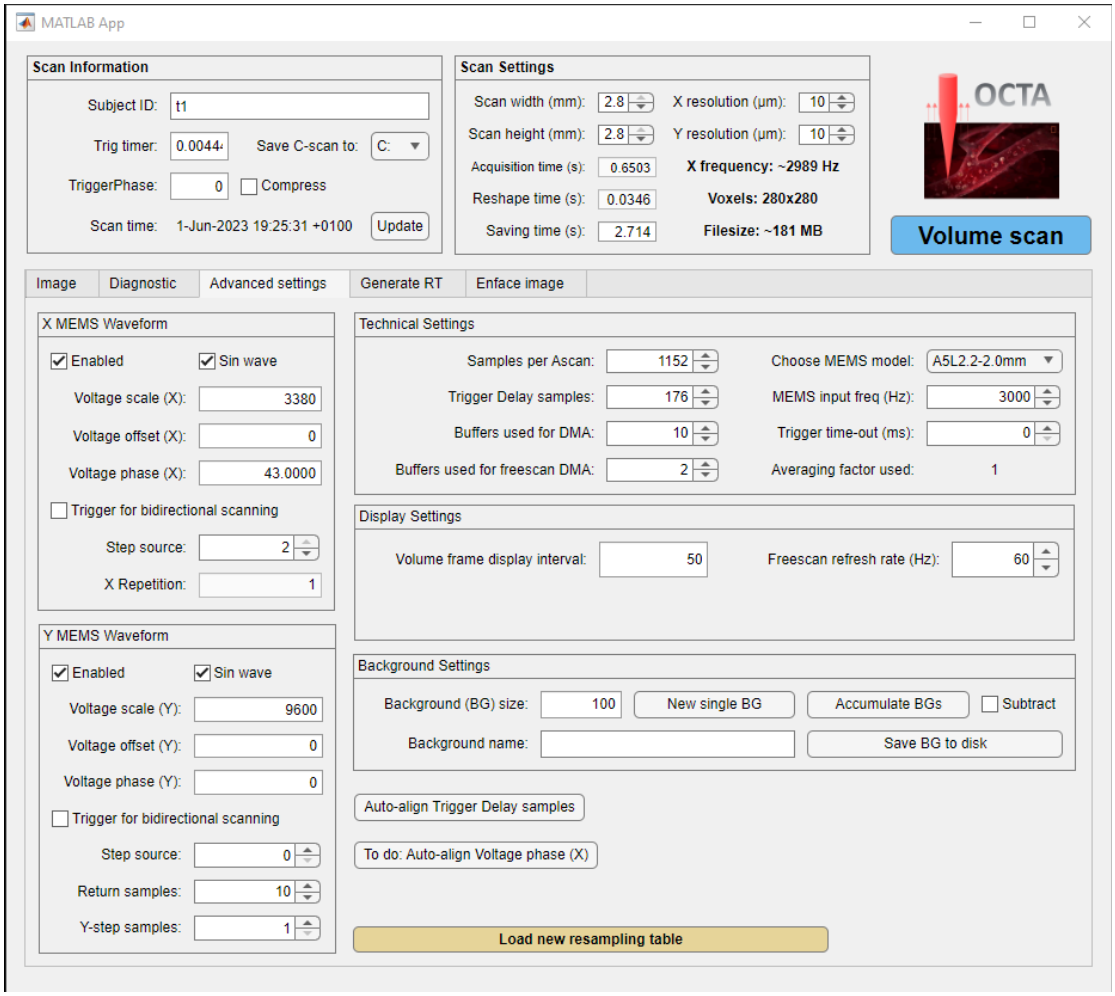

Figure 2.24: The "Advanced Settings" tab for adjusting MEMS control waveforms, configuring digitizer and FDML laser synchronisation, background subtraction, and loading resample tables.

Figure 2.25 shows the fourth tab, labelled "Generate RT". This tab is designed to generate the wavenumber resampling table using a mirror, which is then applied to resample images of other samples in different tabs or for offline image processing. Additionally, this tab can be used to measure axial resolution, its variation with depth, and the intensity roll-off with depth.

Figure 2.26 shows the fifth tab, labelled "Enface Image." This tab is designed to display the enface mean intensity projection of a volume scan from the sample. It includes features for adjusting the depth range for intensity averaging, changing the greyscale of the enface image, enabling X-axis and Y-axis resampling, and making phase delay adjustments for synchronization. It also supports saving images. Although real-time volume scanning is implemented, the time from acquisition to presenting the enface image takes 4-5 seconds, meaning the system responds to sample movement every 4-5 seconds, but not in real time. This tab is useful for finding the focal plane of the objective, evaluating the lateral resolution of the FDML OCT system, and checking synchronisation and sample stability.

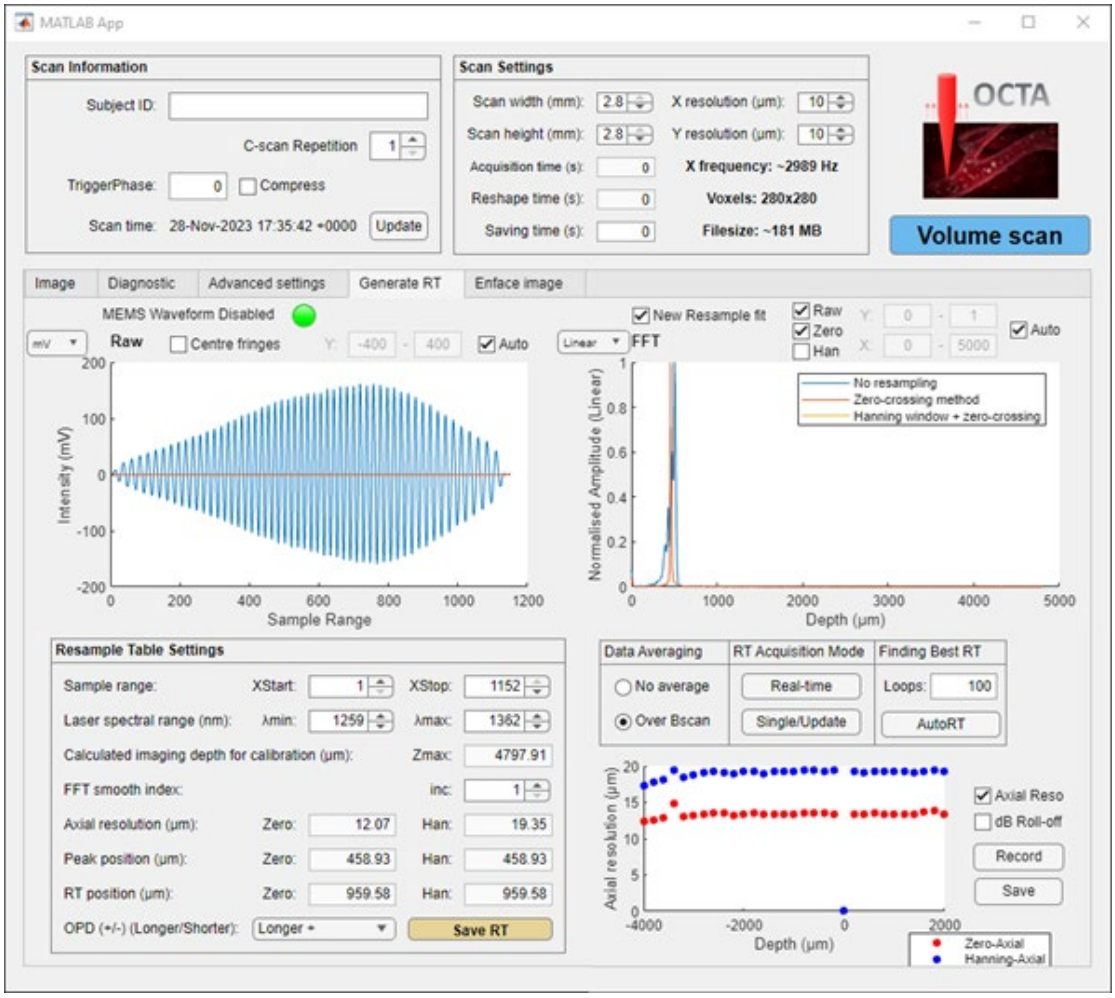

Figure 2.25: The "Generate RT" tab for creating the wavenumber resampling table and measuring axial resolution and intensity roll-off with depth.

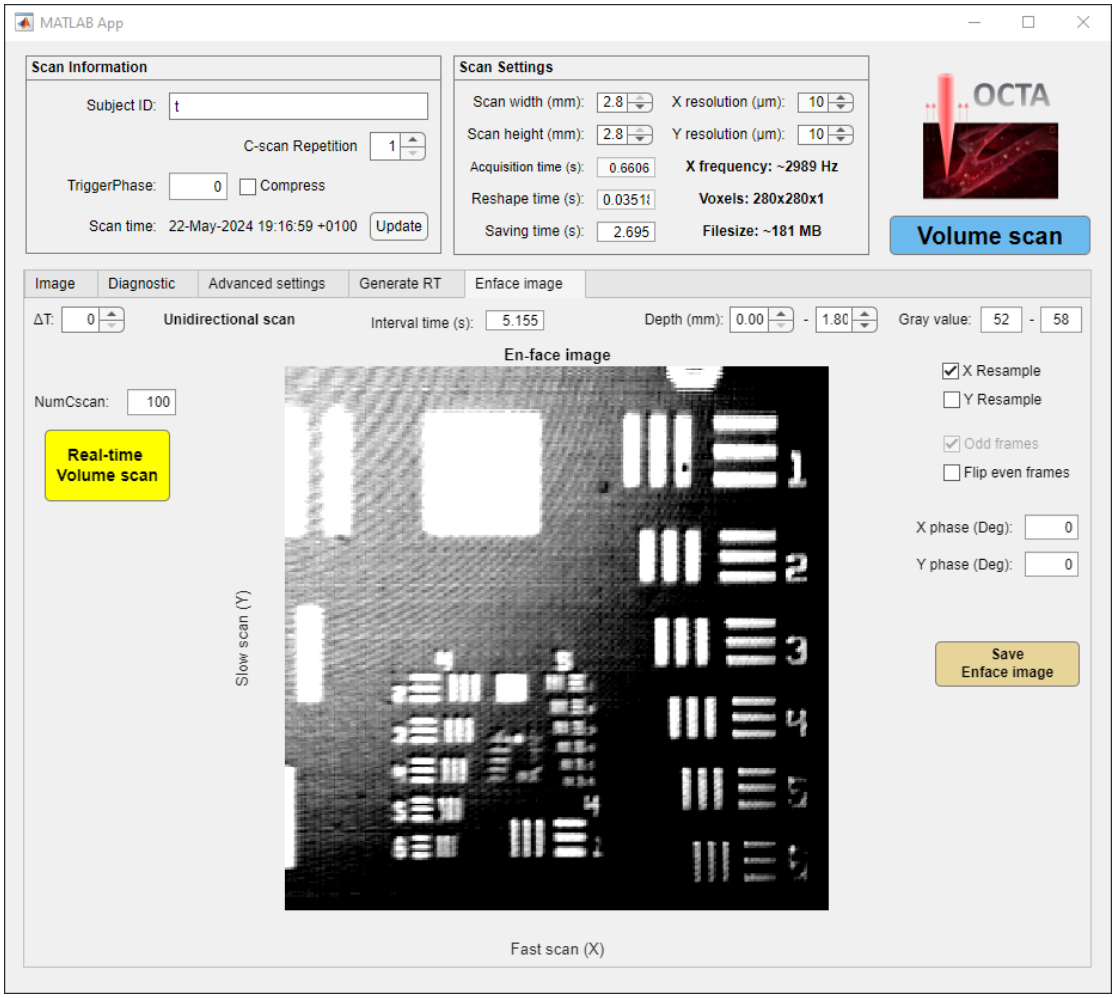

Figure 2.26: The "Enface Image" tab for displaying the enface mean intensity projection of a volume scan, with functions for depth adjustment, resampling, synchronisation, and image saving.

2.7. Conclusion

This chapter first introduced the construction of an FDML OCT system based on a Michelson interferometer, highlighting its advantage of high-speed imaging through the integration of an ultrafast 1.6 MHz FDML swept laser, a rapid MEMS scanner, and a high-speed digitizer for data acquisition. After the system was constructed, the optical components were optimized to ensure efficient imaging performance while maintaining safety standards for clinical applications, such as skin imaging.

The performance of the FDML OCT system was then characterised. The system achieved a measured axial resolution in air of approximately 13 μm, a measured lateral resolution in air of 24.8 μm, a measured sensitivity of 100 dB, an imaging depth in air of 4.8 mm, and an intensity roll-off of less than -1 dB over a 2 mm range. Following the synchronisation and calibration of the system to correct imaging distortions, the various scan protocols for OCT imaging were summarised.

Several example B-scan and enface images were presented, showcasing scans of a ribbon cable, human nail, index fingertip skin, palmar skin, dorsal hand skin, and forearm skin. The system clearly captured structural details, particularly in skin samples, where layers such as the stratum corneum, epidermis, and dermis were easily identifiable. These images were acquired at a 3 kHz B-scan acquisition rate (X-axis scanning frequency of MEMS scanner), enabling volumetric datasets to be collected in approximately 0.1 seconds over a 2.8 mm x 2.8 mm area. The results demonstrated good stability, contrast, and resolution, illustrating that the 3 kHz B-scan acquisition rate fully leverages the high-speed capabilities of the FDML OCT system while maintaining high image quality. This 3 kHz B-scan acquisition rate will be used in subsequent chapters for OCT imaging.

Lastly, custom software was developed to control the FDML OCT system, enabling real-time imaging, data collection, and system alignment. The key functions of the software were outlined. This software will be employed throughout the following chapters for all experiments. Specific scan protocols will be designed to align with the objectives of each experiment.

References

[1] R. Huber, M. Wojtkowski, K. Taira, J. G. Fujimoto, and K. Hsu, "Amplified, frequency swept lasers for frequency domain reflectometry and OCT imaging: design and scaling principles," *Optics express,* vol. 13, no. 9, pp. 3513-3528, 2005.

[2] R. Huber, M. Wojtkowski, and J. Fujimoto, "Fourier Domain Mode Locking (FDML): A new laser operating regime and applications for optical coherence tomography," *Optics express,* vol. 14, no. 8, pp. 3225-3237, 2006.

[3] W. Drexler and J. G. Fujimoto, *Optical coherence tomography: technology and applications*. Springer Science & Business Media, 2008.

[4] V. Milanovic, "Linearized gimbal-less two-axis MEMS mirrors," in *Optical Fiber Communication Conference*, 2009: Optica Publishing Group, p. JThA19.

[5] V. Milanović, A. Kasturi, J. Yang, Y. R. Su, and F. Hu, "Novel packaging approaches for increased robustness and overall performance of gimbal-less MEMS mirrors," in *MOEMS and Miniaturized Systems XVI*, 2017, vol. 10116: SPIE, pp. 44-56.

[6] V. Milanović, A. Kasturi, J. Yang, and F. Hu, "Closed-loop control of gimbal-less MEMS mirrors for increased bandwidth in LiDAR applications," in *Laser Radar Technology and Applications XXII*, 2017, vol. 10191: SPIE, pp. 157-169.

[7] Thorlabs. "TW1300R5A2 - 2x2 Wideband Fiber Optic Coupler, 1300 ± 100 nm, 50:50 Split, FC/APC Connectors." Thorlabs. https://www.thorlabs.com/thorproduct.cfm?partnumber=TW1300R5A2 (accessed Jan 09, 2025).

[8] *Safety of laser products: Part 1. Equipment classification and requirements*, BS EN 60825-1, 2014.

[9] S. Van der Jeught, A. Bradu, and A. G. Podoleanu, "Real-time resampling in Fourier domain optical coherence tomography using a graphics processing unit," *Journal of Biomedical Optics,* vol. 15, no. 3, pp. 030511-030511-3, 2010.

[10] N. Uribe-Patarroyo, S. H. Kassani, M. Villiger, and B. E. Bouma, "Robust wavenumber and dispersion calibration for Fourier-domain optical coherence tomography," *Optics express,* vol. 26, no. 7, pp. 9081-9094, 2018.

[11] K. Nagib, B. Mezgebo, N. Fernando, B. Kordi, and S. S. Sherif, "Generalized image reconstruction in optical coherence tomography using redundant and non-uniformly-spaced samples," *Sensors,* vol. 21, no. 21, p. 7057, 2021.

[12] Y. Yang, Y. Dai, Y. Zhou, and Y. Yang, "Comparison of uniform resampling and nonuniform sampling direct-reconstruction methods in k-space for FD-OCT," *Journal of Innovative Optical Health Sciences,* vol. 16, no. 05, p. 2350002, 2023.

[13] Y. Chen, J. Fingler, and S. E. Fraser, "Multi-shaping technique reduces sidelobe magnitude in optical coherence tomography," *Biomedical Optics Express,* vol. 8, no. 11, pp. 5267-5281, 2017.

[14] C. B. Walker *et al.*, "Multi-window approach enables two-fold improvement in OCT axial resolution with strong side-lobe suppression and improved phase sensitivity," *Biomedical Optics Express,* vol. 14, no. 12, pp. 6301-6316, 2023.

[15] K. Li *et al.*, "O-PRESS: Boosting OCT axial resolution with Prior guidance, Recurrence, and Equivariant Self-Supervision," *Medical Image Analysis,* vol. 99, p. 103319, 2025.

[16] E. Bousi and C. Pitris, "Lateral resolution improvement in Optical Coherence Tomography (OCT) images," in *2012 IEEE 12th International Conference on Bioinformatics & Bioengineering (BIBE)*, 2012: IEEE, pp. 598-601.

[17] D. Liao, A. E. Pivonka, B. R. Haberle, D. C. Petersen, B. M. Hoeling, and R. C. Haskell, "Limits to performance improvement provided by balanced interferometers and balanced detection in OCT/OCM instruments," in *Coherence Domain Optical Methods and Optical Coherence Tomography in Biomedicine VIII*, 2004, vol. 5316: SPIE, pp. 467-472.

[18] B. Liu and M. E. Brezinski, "Noise sources and optoelectronics which affect axial detection performance of time domain, Fourier domain, and swept source optical coherence tomography," in *Coherence Domain Optical Methods and Optical Coherence Tomography in Biomedicine X*, 2006, vol. 6079: SPIE, pp. 213-225.

[19] B. Johnson *et al.*, "Advantage of low NEP balanced receivers in swept source OCT," in *Optical Coherence Tomography and Coherence Domain Optical Methods in Biomedicine XXV*, 2021, vol. 11630: SPIE, pp. 56-62.

[20] B. R. Biedermann, W. Wieser, C. M. Eigenwillig, T. Klein, and R. Huber, "Dispersion, coherence and noise of Fourier domain mode locked lasers," *Optics Express,* vol. 17, no. 12, pp. 9947-9961, 2009.

[21] S. Shin, U. Sharma, H. Tu, W. Jung, and S. A. Boppart, "Characterization and analysis of relative intensity noise in broadband optical sources for optical coherence tomography," *IEEE Photonics Technology Letters,* vol. 22, no. 14, pp. 1057-1059, 2010.

[22] T. Klein, W. Wieser, C. M. Eigenwillig, B. R. Biedermann, and R. Huber, "Megahertz OCT for ultrawide-field retinal imaging with a 1050nm Fourier domain mode-locked laser," *Optics express,* vol. 19, no. 4, pp. 3044-3062, 2011.

[23] A. G. Podoleanu, "Unbalanced versus balanced operation in an optical coherence tomography system," *Applied Optics,* vol. 39, no. 1, pp. 173-182, 2000.

[24] J. Zhu, C. W. Merkle, M. T. Bernucci, S. P. Chong, and V. J. Srinivasan, "Can OCT angiography be made a quantitative blood measurement tool?," *Applied sciences,* vol. 7, no. 7, p. 687, 2017.

3. Fast Detection of Epidermal Thickness and Cutaneous Blood Vessels on Dorsal Hand using FDML OCT

3.1. Summary

This chapter demonstrates the application of the in-house high-speed FDML OCT system (described in the last chapter) to non-invasively image human dorsal hand skin in vivo. It presents two major developments: 1) an automatic algorithm for epidermal thickness measurement based on structural OCT imaging, and 2) a vascular imaging method using difference-based and speckle-variance OCT angiography (OCTA). The imaging protocols, algorithmic frameworks, and representative results are discussed in detail to highlight the clinical potential of FDML OCT in dermatological assessment.

Note that parts of sections 3.2 and 3.3 have been published in a conference paper [1].

3.2. Introduction

Atopic dermatitis (AD), a chronic inflammatory dermatosis, is marked by pruritus. The inflammation and subsequent scratching often lead to lichenification or skin thickening [2]. Traditional treatment of AD involves the use of topical corticosteroid creams (TCS), which may also decrease skin thickness [3]. Therefore, monitoring epidermal thickness could serve as a valuable biomarker for evaluating both the severity and therapeutic response in AD. Additionally, angiographic OCT measurements of vascular depth and morphology offer a promising biomarker for quantifying the severity of both clinical and subclinical AD [4].

In our previous study on sub-clinical detection of AD, we utilized a multi-beam OCT system (Vivosight, Michelson Diagnostics) equipped with a 1305 nm swept-source Axsun laser, operating at an A-scan rate of 20 kHz [4]. The acquisition time at 40 frame/s required at least several seconds, making it challenging for some patients to remain motionless.

To overcome the lengthy acquisition times, we have developed a high-speed OCT system featuring a 1310 nm Fourier-domain Mode-locked (FDML) laser with a 1.67 MHz A-scan rate and a MEMS scanner providing a 3 kHz frame rate. As described in Chapter 2, this system measured axial and lateral resolutions of approximately 13 μm and 25 μm in air, respectively. Volume scans measuring 2.8 x 2.8 x 5 mm^3 (XYZ directions) were acquired from the dorsal hand skin of a healthy volunteer. The acquisition time for a single volume scan, consisting of 280 B-scans, is 0.1 seconds.

In Section 3.3, we describe the development of an automatic segmentation algorithm for detecting the skin surface and the dermal-epidermal junction (DEJ), enabling epidermal thickness estimation. The dorsal hand skin's epidermal thickness was analysed, and an epidermal thickness map was generated for overlay on the enface skin image.

In Section 3.4, we present an automatic algorithm based on difference-based and speckle-variance angiography for visualizing the superficial vasculature. The scan protocols and several image enhancement techniques are discussed. The angiographic B-scan and enface vasculature images of dorsal hand are demonstrated. We also investigated the optimal time interval for generating angiographic cross-sectional and enface images effectively.

3.3. Epidermal Thickness Analysis using FDML OCT

3.3.1. Skin Layer Automatic Segmentation Algorithm

An automatic segmentation algorithm has been developed in MATLAB to assess the epidermal thickness of the dorsal hand skin. This algorithm is an unsupervised algorithm without ground truth data training. **Figure 3.1** shows the algorithm's sequence of how the surface and DEJ of the skin are detected for epidermal thickness estimation. The core idea is to calculate the maximum gradient of the pixel intensity/brightness along the axial direction. For skin surface detection, the laser beam propagates through the air and then hits the surface, so the brightness changes from dark in the air (background noise) to white on the surface. For DEJ detection, the epidermal area below the surface is also darker than the DEJ.

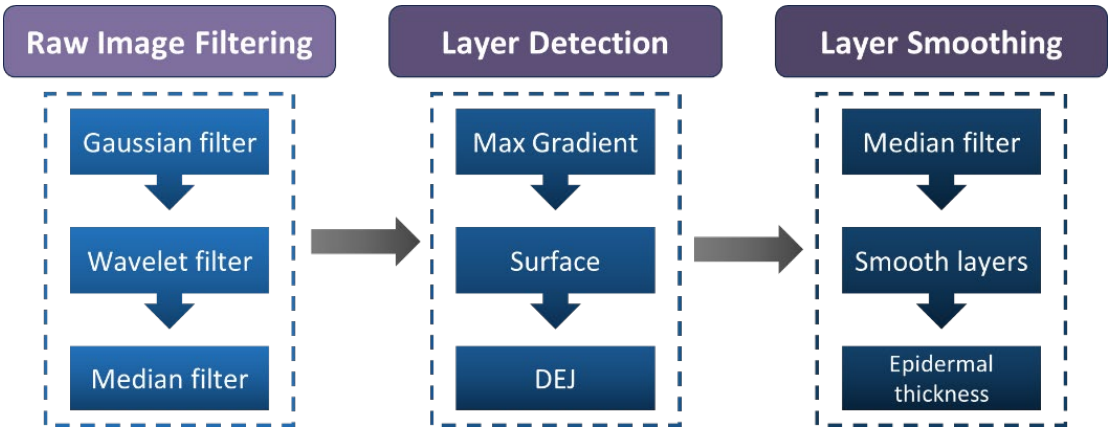

Figure 3.1: The schematic of the skin layer automatic segmentation algorithm.

Figure 3.2(a) shows a typical raw B-scan image acquired on dorsal hand skin using the FDML OCT system without any filtering, resulting in a bad layer detection for both surface (green) and DEJ (red). So, the first step is to apply pre-filters (Gaussian, Wavelet, and Median) to the raw B-scan images. A one-dimensional Gaussian filter with a standard deviation (sigma) of 2 was applied to the raw B-scan image in the axial

direction. An optional wavelet filter followed by a two-dimensional 5x5 pixel median filter was then used. The details of this wavelet filter can be found in our previous work [4, 5].

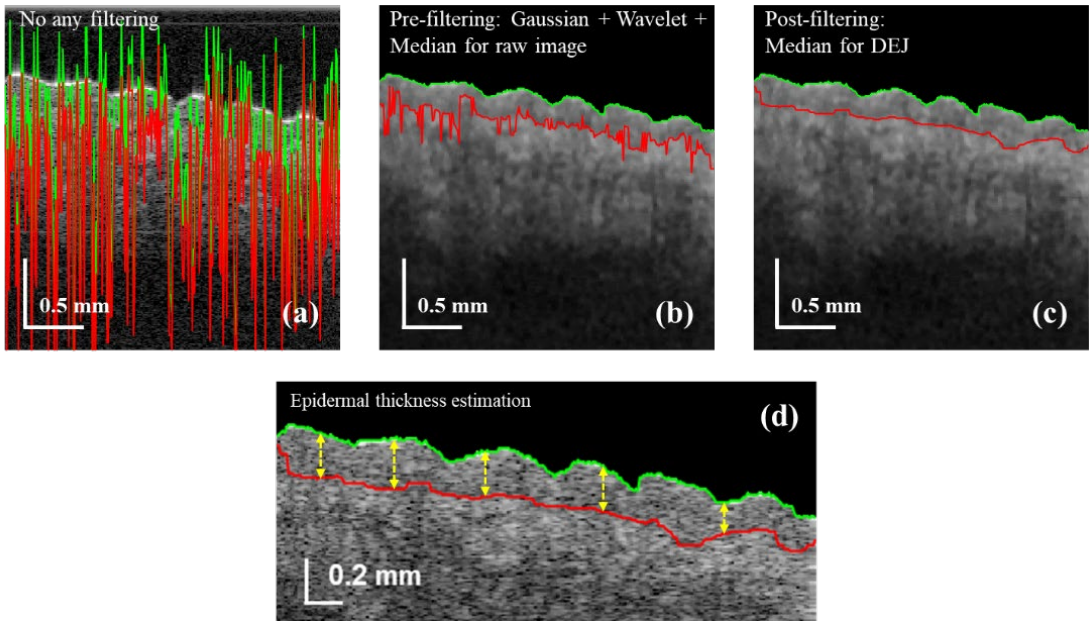

Figure 3.2: (a) Surface and DEJ detection for a typical raw B-scan image acquired on dorsal hand skin using the FDML OCT system without any filtering. (b) Surface and DEJ detection for the image pre-filtered by Gaussian, Wavelet, and Median filters. (c) DEJ after one-dimensional median post-filtering of (b). (d) The distance between the surface and DEJ corresponds to the epidermal thickness. Green: detected surface. Red: detected DEJ.

After pre-filtering the raw image with the Gaussian filter, the detection of both the surface and DEJ is noticeably improved. Application of the wavelet and median filters can further help with the detection accuracy (**Figure 3.2**(b)). To optimize the detected DEJ, a one-dimensional median filter of 25 pixels was applied to the detected DEJ in **Figure 3.2**(b) and a smoother DEJ is shown in **Figure 3.2**(c).

After finding the skin surface and DEJ, the epidermal thickness can be estimated by counting the pixels vertically between the surface and DEJ as marked by the yellow arrows in **Figure 3.2**(d). One pixel in an A-scan corresponds to ~8.65 μm in air and ~6.18 μm in tissue, assuming the refractive index of skin tissue n = 1.4 [6].

During layer segmentation, spike artefacts such as hairs, as shown in **Figure 3.3**, often decrease the accuracy of segmentation and epidermal thickness estimation. To address this issue, we implemented an additional layer refinement process within the skin layer segmentation algorithm.

As illustrated in **Figure 3.3**, the refinement process involves the following steps:

1) Initial smoothing: The detected raw max-gradient surface is first smoothed using a one-dimensional median filter with a small kernel size (e.g., 3 pixels). This generates a rough surface, denoted as *S1*, which still contains spikes.
2) Surface flattening: In the second step, a flattened surface *S2* is created by smoothing *S1* with a larger kernel size (e.g., 50 pixels).
3) Spike detection and removal: The spikes are identified by calculating the absolute difference between *S1* and *S2*. Any position where this difference exceeds a defined threshold (e.g., 3 pixels) is marked as NaN (Not a Number). This removes the spike artefacts from the surface.
4) Refining NaN positions: For each NaN position, the maximum gradient of brightness along the axial direction is recalculated within a refined axial range. This range, shown as yellow lines in **Figure 3.3**, is defined as ±15 pixels relative to *S2* at each NaN position (red lines). The value of 15 pixels is empirical and can be adjusted depending on the image or OCT system setup.

5) Merging refined surface: The refined values at NaN positions (red) are merged with *S3* to create a more accurate surface.

6) Final smoothing: A final smoothing step applies a 5-pixel median filter to *S5*, generating the final refined surface.

This process can be repeated iteratively to achieve further surface refinement. Beyond surface refinement, this method can also enhance the accuracy of DEJ detection and epidermal thickness estimation by mitigating the effects of hair follicles.

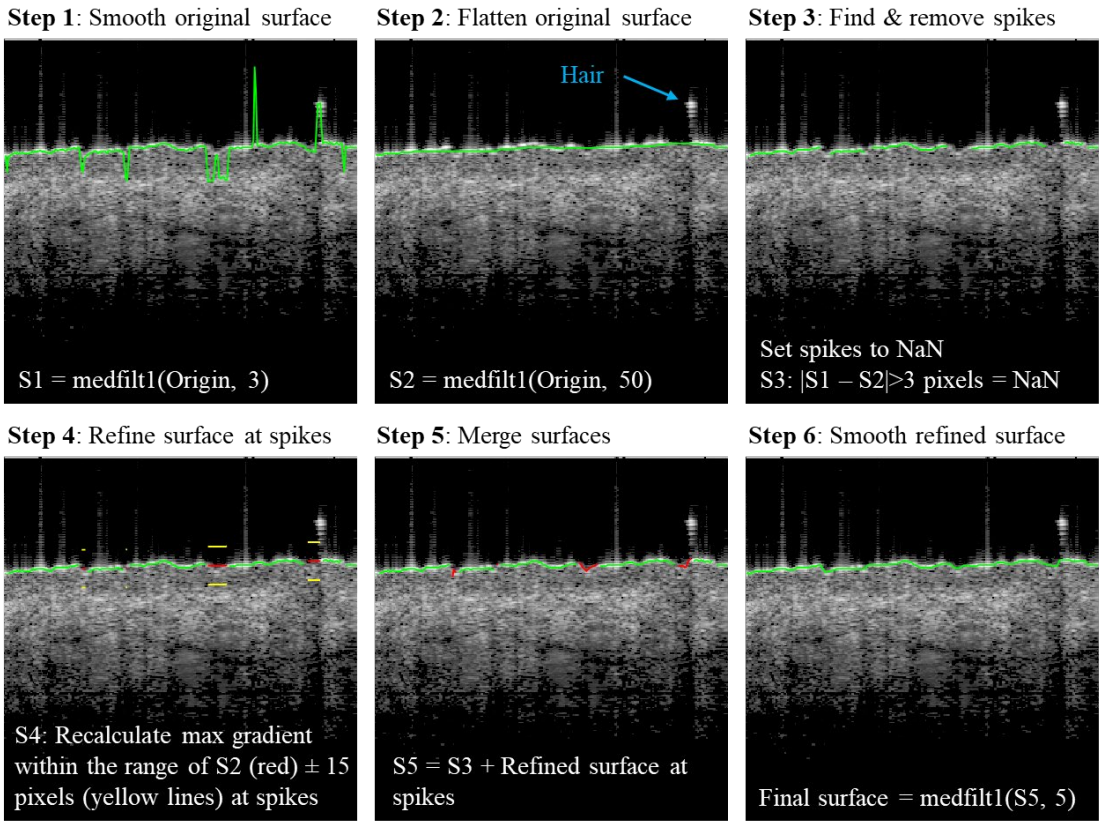

Figure 3.3: Skin surface refinement process with removing spike artefacts (e.g., hairs).

3.3.2. Results

Figure 3.4 illustrates the variation in epidermal thickness along the fast scan (X-axis) direction in the B-scan image in **Figure 3.2**(d) acquired on dorsal hand skin using the FDML OCT system. The epidermal thickness ranges from 70 to 200 µm, with a mean thickness of 134.54 µm. **Figure 3.5**(a) demonstrates a typical enface image of the dorsal hand skin (2.8 mm x 2.8 mm) acquired using the FDML OCT system, obtained by averaging the intensity of the volume scan data along the A-scan direction. Epidermal thickness estimation was performed for all B-scans in this volume scan. A detailed epidermal thickness map (**Figure 3.5**(b)) with a colour bar was generated and overlaid on **Figure 3.5**(a). The epidermal thickness in most areas falls within the range of 110 to 150 µm.

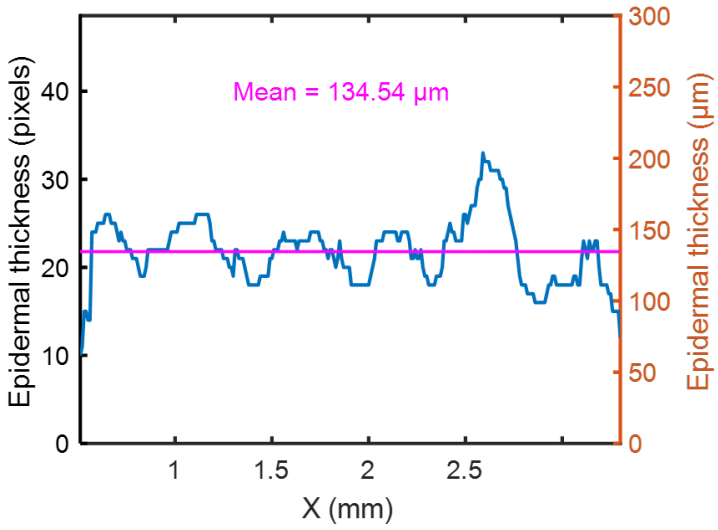

Figure 3.4: Epidermal thickness in the X-axis of a typical B-scan image (in pixels or µm) acquired on dorsal hand skin using the FDML OCT system. The magenta line shows the mean epidermal thickness.

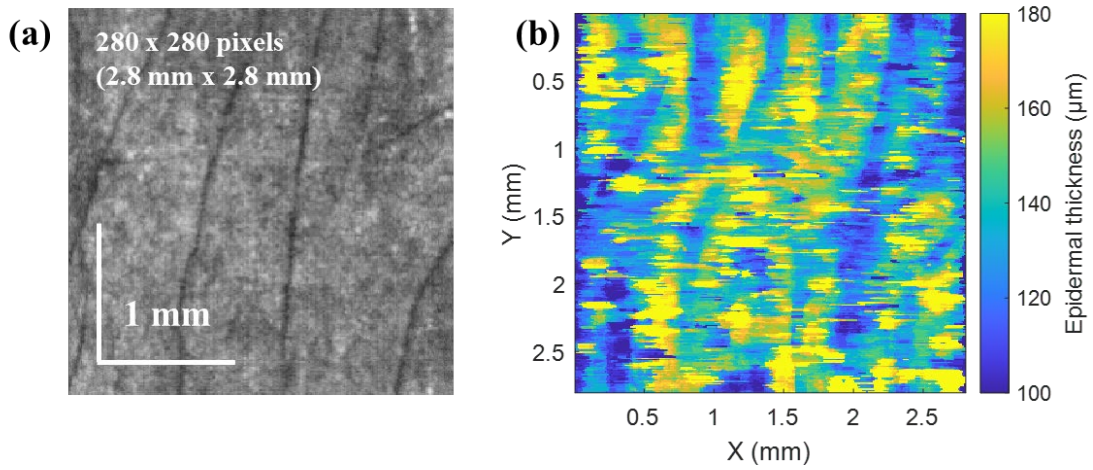

Figure 3.5: (a) A typical enface image of human dorsal hand skin acquired using the FDML OCT system, covering an area of 2.8 mm × 2.8 mm. (b) Epidermal thickness map overlaid on the enface image (a).

3.4. Angiographic Imaging using FDML OCT

This section introduces an algorithm based on difference-based and speckle-variance OCTA for achieving angiographic imaging using an FDML OCT system. The theory is detailed in Section 1.4. The scan protocol and image processing techniques for identifying blood vessels are presented first. This method is validated on a static plastic sample and then applied to the dorsal hand in vivo. The optimal time interval for generating angiographic B-scans or enface vasculature images is investigated. The results obtained by difference-based OCTA and speckle-variance OCTA are also compared.

3.4.1. Methods

3.4.1.1.OCTA Calculations

To visualize the superficial vessels, an automatic MATLAB algorithm has been developed based on difference-based OCTA and speckle-variance (SV) OCTA. The amplitude or intensity of the OCT signals from FDML OCT system is used for both OCTA calculations.

The difference-based OCTA calculates the normalised mean amplitude difference between two B-scans with a time interval of $M\Delta t$, as shown in Equation 3.1. In the flow area, the normalised mean difference $OCTA_{normalized}$ increases with time interval increasing until saturation. While in the static tissue, since the signal amplitude almost remains the same i.e. $A_{i+M} \approx A_i$, the normalised mean difference $OCTA_{normalized}$ is close to zero. The normalized mean amplitude difference can be calculated as [7],

$$OCTA_{normalized}(M\Delta t) = \frac{1}{N-M}\sum_{i=1}^{N-M}\frac{(A_{i+M}-A_i)^2}{(A_{i+M})^2+(A_i)^2} \quad (3.1)$$

where Δt is the fundamental interscan time, N is the total number of B-scan repeats, and A_i is the amplitude of the i^{th} repeated B-scan.

The SV calculation is based on Equation 1.7 (Section 1.4.2). The core idea is to calculate the signal fluctuation or variance in the same position within a specific time interval. The flow area can be differentiated from the static area because the former has much stronger variance. The signal variance in the static area is mainly caused by background noise, which can be mitigated by averaging. By setting a time interval of $M\Delta t$ (when $M < N$), the variance of the signal amplitude can be calculated for each set of sequential $M + 1$ B-scan repeats (Equation 3.2). The mean SV is then obtained by averaging the $N - M$ sets of variance values (Equation 3.3).

$$Var(M\Delta t) = \frac{1}{M}\sum_{i=j}^{M+j}[A_i - \bar{A}]^2 \tag{3.2}$$

$$OCTA_{SV}(M\Delta t) = \frac{1}{N-M}\sum_{j=1}^{N-M} Var(M\Delta t)\,, (M < N) \tag{3.3}$$

where $\bar{A}$ is the mean amplitude of all B-scan repetitions from the j^{th} B-scan to $(M + j)^{th}$ B-scan.

3.4.1.2.OCTA Scan Protocols

To acquire the OCT signal fluctuation, scan repetitions at the same position on the sample need to be recorded. A scan protocol can be M-mode, B-mode, or CM-mode (refer to Section 2.5.2). From our previous study [4], an interscan time of milliseconds was used for angiographic imaging. However, in M-mode, A-scans are repeated with a fundamental interscan time of 0.6 μs (**Table 2.4**). Adopting M-mode scan protocol will lead to excess data acquisition exceeding the on-board memory of the digitiser.

In the present study, only B-mode and CM-mode scan protocols are utilized. In B-mode, a number of B-scans (280 A-scans per B-scan in 2.8 mm) are repeated in the

same Y-axis position with a fundamental interscan time of 0.33 ms. While B-mode scan protocol is used to reveal blood vessels, CM-mode scan protocol is used to visualize the superficial vasculature. In CM-mode, a number of volume scans or C-scans with a fundamental interscan time of 110 ms are repeated in an area of 2.8 mm x 2.8 mm on dorsal hand skin. Each volume scan includes 280 B-scans in the forward scanning direction along Y axis and 50 B-scans in the backward scanning direction to step the scanner back to the start position. The backward 50 B-scans are recorded but excluded for OCTA calculations.

3.4.1.3. OCTA Processing

After collecting the dataset using B-mode or CM-mode scan protocol, the angiographic images can be obtained by our difference-based or speckle-variance OCTA algorithm. In our OCTA algorithm, several techniques are used to enhance the angiographic image contrast.

One step is to multiply the speckle-variance B-scan image by the intensity B-scan image. The tissue area in the intensity B-scan image usually has higher intensity than background noise area, so the intensity B-scan image works as a filter to enhance the OCTA signal in tissue. This step is only used for SV OCTA.

In the following section, we introduce the imaging processing techniques that can be applied to both difference-based and SV OCTA. The first step is to remove the noise background. **Figure 3.6**(a) represents a typical background B-scan in amplitude averaged from 1000 B-scan repetitions acquired when blocking the sample arm in FDML OCT system. **Figure 3.6**(b) shows the typical mean amplitude B-scan of dorsal hand skin from 1000 B-scan repetitions by FDML OCT system. By defining a threshold as two standard deviations above the mean background value from the 1000 B-scan

repeats, **Figure 3.6**(c) can be obtained by filtering the image of **Figure 3.6**(b) with setting any pixel amplitude less than this threshold to zero [7].

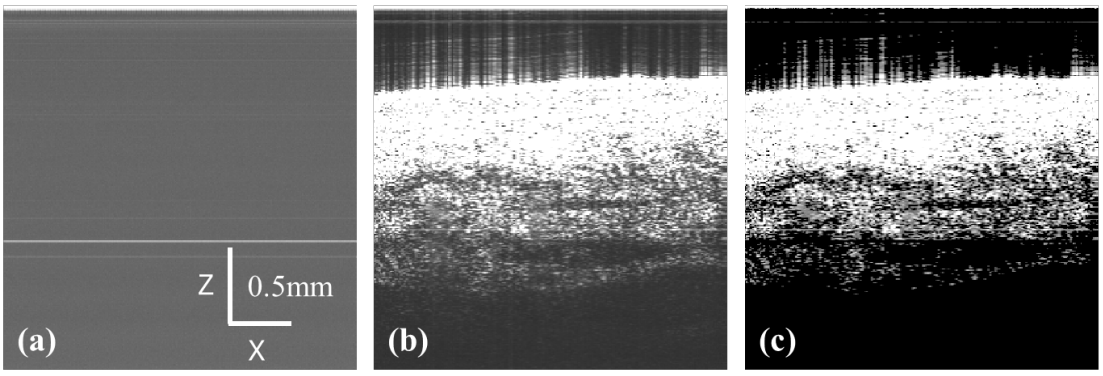

Figure 3.6: Background removal processing. (a) Typical mean amplitude B-scan image of background noise from 1000 B-scan repetitions acquired when blocking the sample arm in the FDML OCT system. (b) Typical mean amplitude B-scan image of dorsal hand from 1000 B-scan repetitions acquired by the FDML OCT system. (c) Thresholded B-scan image of (b) with background removed. The threshold is defined as two standard deviations above the mean background value from the 1000 background B-scan repeats in (a).

Skin flattening is another useful technique employed in this OCTA algorithm. As shown in **Figure 3.7**(a), the skin surface (green) is detected using the layer segmentation algorithm in Section 3.3.1 for a typical intensity B-scan image on dorsal hand by FDML OCT system. By aligning the skin surface to the top horizontal line, the skin tissue can be flattened to the top (**Figure 3.7**(b)). **Figure 3.7**(c) shows the typical SV angiographic image of **Figure 3.7**(b) after the above two image enhancement steps. To further improve the image contrast, a two-dimensional median filter of 7x3 pixels was applied to **Figure 3.7**(c) to further mitigate the speckle noise. **Figure 3.7**(d) shows the median-filtered image with proper greyscale adjustment, indicating a good contrast

for visualizing the blood vessels. The vertical tail artefacts can be seen below blood vessels which is because of the shadowing of vessels.

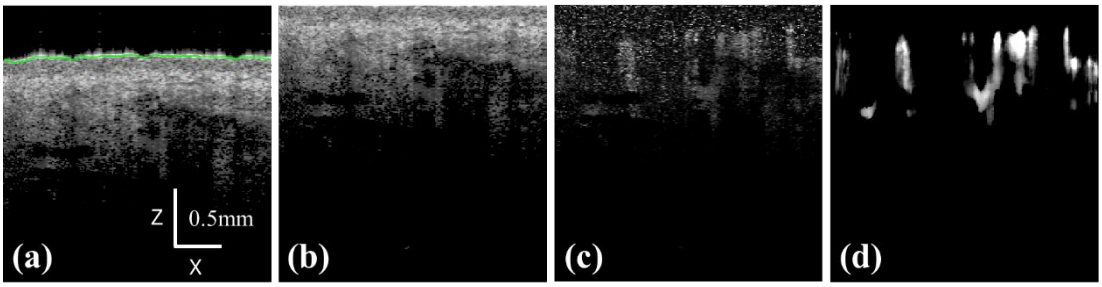

Figure 3.7: (a) Typical intensity B-scan image of dorsal hand taken by the FDML OCT system with background removed and skin surface detected (green). (b) B-scan image of (a) after the skin surface was flattened to the top horizontal line. (c) Angiographic B-scan image of (b) processed by the speckle-variance OCTA. (d) Angiographic B-scan of (c) with contrast enhanced by a 2D median filter of 7x3 pixels and proper greyscale adjustment.

The skin surface may affect the visualization of cutaneous vessels. One direct advantage of flattening skin is that the surface effect can be easily subtracted from the angiographic image. This is implemented by averaging the angiographic values vertically from the top first pixel to the 10^{th} pixel below (within epidermis) for each X-axis position and setting this average horizontal line as the surface background. This step is optional to subtract the angiographic image by the surface background.

Apart from those image processing techniques, frame registration is also optional to registrate the B-scan repetitions to the exact same position. Due to the short fundamental interscan time of 0.33 ms, it only takes 0.33 seconds to acquire 1000 B-scan repetitions, and no movement of hand usually can be observed within this period.

To ensure the hand remaining static, we also adapted an adjustable lens tube after the objective in the sample arm of FDML OCT system to fix the hand by attaching the hand to the tube. Another issue of causing vertical line artefacts in the angiographic image is the sampling of X-axis of the B-scan image. The X-axis sampling (refer to Section 2.5.1.2) must be applied to calibrate the distortion after all the angiographic process and only before showing the angiographic image.

3.4.2. Results

3.4.2.1.B-mode Comparison between Plastic and Dorsal Hand

To validate our OCTA algorithm, the difference-based OCTA process was applied to a plastic sample first. The time interval was set to 330 times the fundamental time (110 ms), i.e. $M = 330$ in Equation 3.1. This plastic sample was placed and remain static in the sample arm of the FDML OCT system. B-mode scan was adopted to acquire 1000 B-scan repetitions from the plastic sample. **Figure 3.8**(a) shows a mean amplitude B-scan image of this plastic sample without X-axis resampling. After applying the basic OCTA calculation without background removal and median filtering to **Figure 3.8**(a), the raw angiographic image of **Figure 3.8**(b) is obtained. No moving angiographic signal is observed in the cross-sectional area of the plastic. The artefacts above surface may be caused by the movement of the MEMS scanner and can be eliminated by the background removal or surface flattening in Section 3.4.1.2.

Compared with the OCTA results of plastic, 1000 B-scan repetitions were acquired from the dorsal hand skin and same OCTA processing was applied. **Figure 3.8**(c) and (d) shows a mean amplitude B-scan image of the dorsal hand without X-axis resampling and its corresponding difference-based raw angiographic image with a time interval of

110 ms. We can clearly see the blood vessels and their tail artefacts. Hence, this comparison in **Figure 3.8** illustrates that our OCTA algorithm can effectively differentiate the moving area from static area and visualize blood vessels.

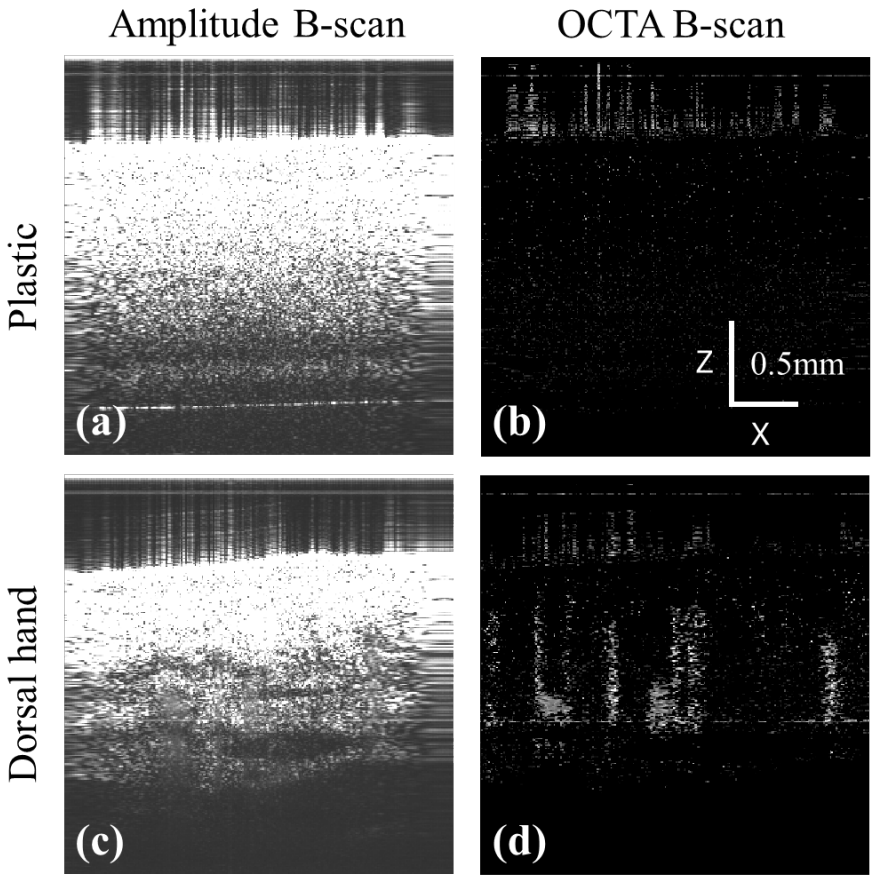

Figure 3.8: (a) Typical mean amplitude B-scan image without X-axis resampling of a static plastic sample from 1000 B-scan repetitions acquired by FDML OCT system. (b) Angiographic image of (a) without background removal and median filtering, indicating no moving signal. (c) Typical mean amplitude B-scan image without X-axis resampling of dorsal hand from 1000 B-scan repetitions acquired by FDML OCT system. The hand was maintained motionless. (d) Angiographic image of (c) without background removal and median filtering, indicating blood flow signals (vessels) and tail artefacts (vessel shadowing). (b) and (d) were generated by the difference-based OCTA with a time interval of 110 ms.

3.4.2.2. B-mode OCTA of Dorsal Hand with Increasing Time Interval

To investigate the optimal time interval for visualizing cutaneous blood vessels by FDML OCT system, the difference-based angiographic B-scan images of **Figure 3.8**(c) with different time intervals ($M\Delta t$) were generated (**Figure 3.9**). The B-mode dataset used is the same as in Section 3.4.2.1. The total number of B-scan repeats (N) is 1000. As shown in **Figure 3.9**, with increasing M, the contrast of the angiographic image increases initially and decreases after hitting a plateau. The optimal time interval is around 100 ms ($M = 300$). When $M \leq 30$, the time interval is less than 10 ms which is too quick to record the signal changes caused by the relatively slow blood flow. When $M \geq 600$, the time interval is larger than 200 ms, and the value of $N - M$ is smaller in Equation 3.1. This means that less repeats of $N - M$ are used for averaging the noise and the signal-to-noise ratio (SNR) of the image is decreased.

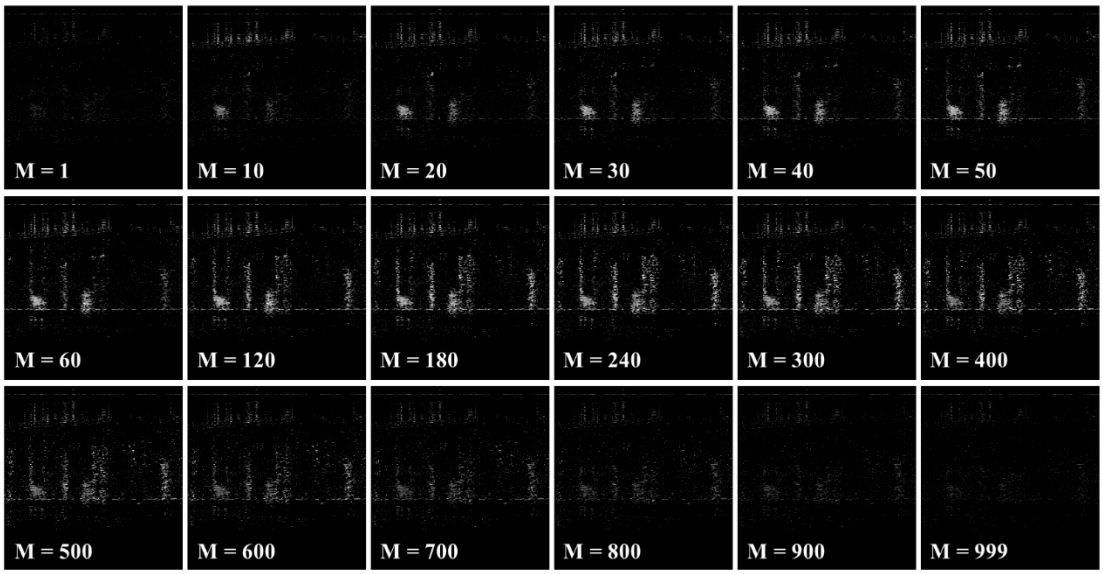

Figure 3.9: The difference-based angiographic B-scan images of **Figure 3.8**(c) with increasing the time intervals ($M\Delta t$), indicating an optimal time interval around 100 ms ($M = 300$) for visualising blood vessels in dorsal hand.

To validate the effect of $N - M$ on the image SNR, **Figure 3.10** presents the difference-based angiographic B-scan images of **Figure 3.8**(c) with different total number of B-scan repeats (N) while remaining $M = 90$. With $N - M$ increasing, the SNR is clearly enhancing. Since the noise is random, large-number averaging can help reduce the noise level. Hence, it is better to acquire a large number N of B-scan repeats and ensure N is much larger than M.

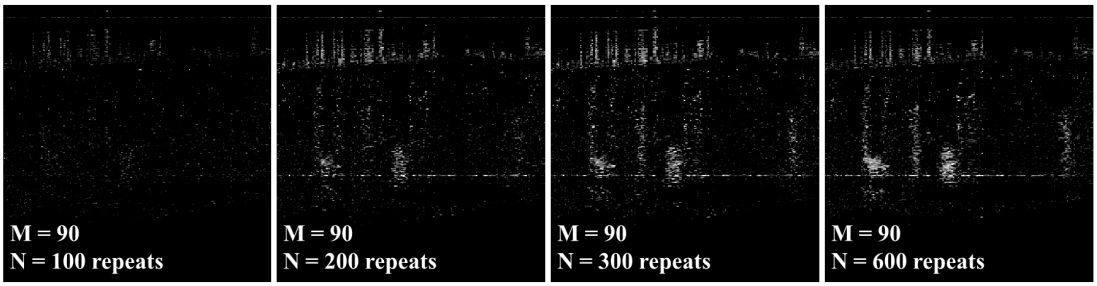

Figure 3.10: The difference-based angiographic B-scan images of **Figure 3.8**(c) with increasing the total number of B-scan repetitions (N) while remaining the time interval as 30 ms ($M = 90$).

3.4.2.3.CM-mode Vasculature Visualization

CM-mode scan was adopted to acquire 10 C-scan repeats of an area of 2.8 mm x 2.8 mm on dorsal hand by FDML OCT system ($N = 10$). **Figure 3.11**(a) shows the enface mean intensity projection of this CM-mode dataset. Difference-based OCTA was then applied to generate the enface angiographic vasculature image with setting the time interval to 110 ms ($M = 1$). **Figure 3.11**(b) demonstrates the enface vasculature image with only background removal and median filtering of 7x3x3 pixels. The skin surface pattern can still be seen as in **Figure 3.11**(a). Therefore, it is useful to apply the surface effect subtraction to enhance the image contrast for visualizing the superficial vasculature, as shown in **Figure 3.11**(c).

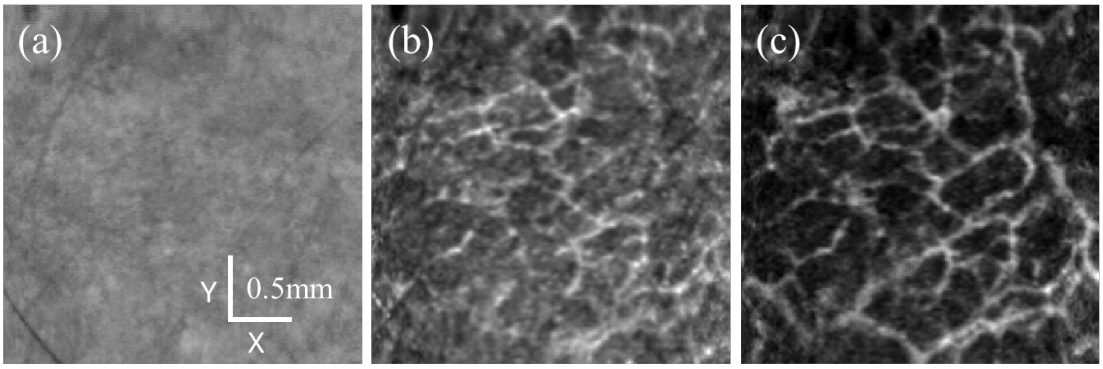

Figure 3.11: (a) 2.8 mm x 2.8 mm enface mean intensity projection of dorsal hand averaged from 10 C-scan repeats taken by the FDML OCT system. (b) Enface superficial vasculature image of (a) processed by the difference-based OCTA with a time interval of 110 ms. The background removal and a three-dimensional median filter of 7x3x3 pixels has been applied to (b). (c) Enface vasculature image of (b) with skin surface effect subtraction, indicating a better image contrast.

3.4.2.4. Comparison of Difference-based and SV OCTA

The above results only show the difference-based OCTA processing. To compare difference-based OCTA with SV OCTA, the same dataset of 10 C-scan repeats (2.8 mm x 2.8 mm) acquired on dorsal hand by FDML OCT is used for calculations. The time interval was set to 220 ms ($M = 2$) for both OCTA processes.

Figure 3.12(a) shows the mean intensity B-scan image of the first frame in the Y axis of this volume. **Figure 3.12**(b) and (c) show the angiographic images processed by difference-based OCTA and SV OCTA respectively, with employing background removal and a two-dimensional median filter of 7x3 pixels. **Figure 3.12**(d) demonstrates the enface intensity mean projection of the C-scan. **Figure 3.12**(e) and (f) visualize the superficial vasculature of this C-scan by difference-based OCTA and SV OCTA respectively. A three-dimensional median filter of 7x3x3 pixels was used. Background removal and surface effect subtraction were also applied.

Both the angiographic B-scan images and enface images processed by difference-based OCTA and SV OCTA are similar. Considering the angiographic B-scan, the SV OCTA wins slightly because of weaker brightness in the tail artefacts. In general, SV OCTA can achieve vascular visualization close to difference-based OCTA.

Additionally, vascular information can be further analysed by both difference-based and SV OCTA. The vascular depth in tissue can be estimated in the surface-flattened OCTA images of **Figure 3.12**(b) and (c). The vascular diameter and density can be measured from the enface vasculature images of **Figure 3.12**(e) and (f).

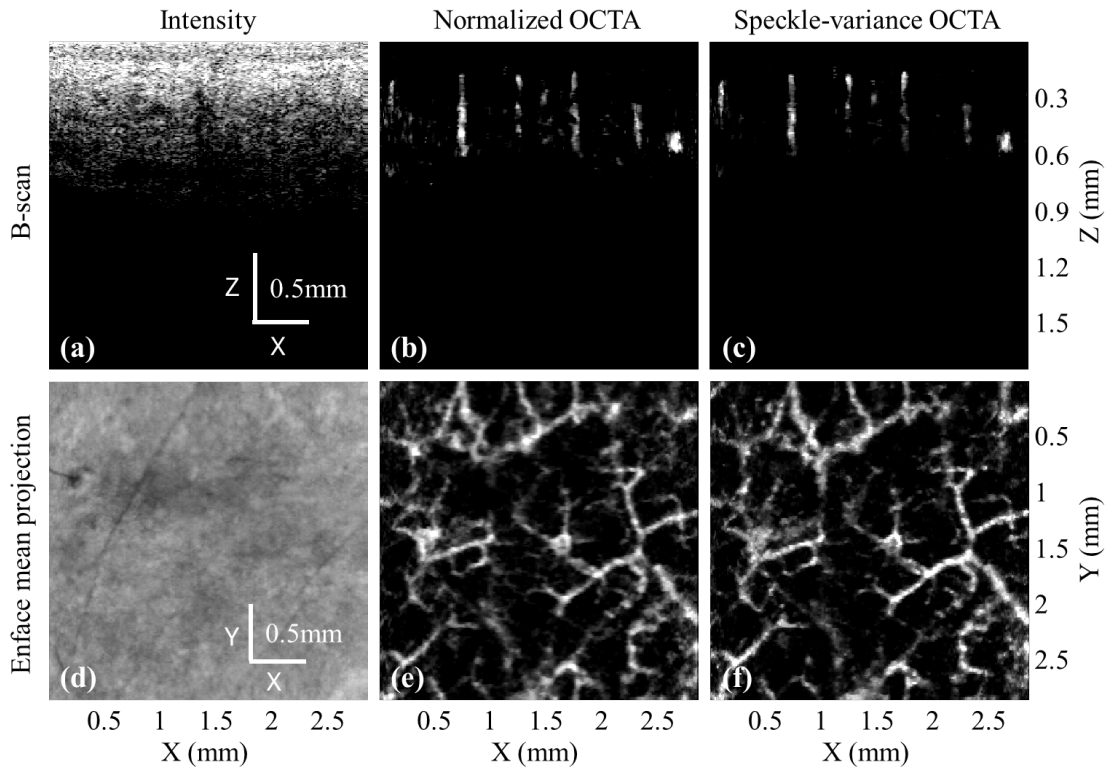

Figure 3.12: Comparison of angiographic imaging using difference-based OCTA and SV OCTA. A dataset of 10 C-scan repeats (2.8 mm x 2.8 mm) was acquired on dorsal hand by FDML OCT. (a) Mean intensity B-scan image of the first frame in the Y axis of this dataset. (b) Angiographic image of (a) processed by difference-based OCTA. (c) Angiographic image of (a) processed by SV OCTA. Background removal and a two-dimensional median filter of 7x3 pixels have been applied to both (b) and (c). (d) Enface intensity mean projection averaged from the 10 C-scan repeats. (e) Superficial vasculature of (d) processed by difference-based OCTA. (f) Superficial vasculature of (d) processed by SV OCTA. A three-dimensional median filter of 7x3x3 pixels, background removal, and surface effect subtraction have been applied to enhance the contrast of (e) and (f). The time interval was set to 220 ms for both OCTA processes.

3.4.2.5. Optimising SV OCTA for Vasculature Visualization

In the previous results sections, to ensure enough data for OCTA calculations, 10 C-scan repetitions were acquired when enabling CM-mode scanning. However, 10 C-scan repetitions take 1.1 seconds. To find the optimal total number of C-scan repetitions (N), **Figure 3.13** shows the SV vasculature images with different N while keeping $M = 1$. We can find that the vasculature image becomes clearer and starts to remain the same when $N > 4$. This indicates that 4 C-scan repeats are enough for OCTA processing to visualize the superficial vasculature, which only takes 0.44 seconds.

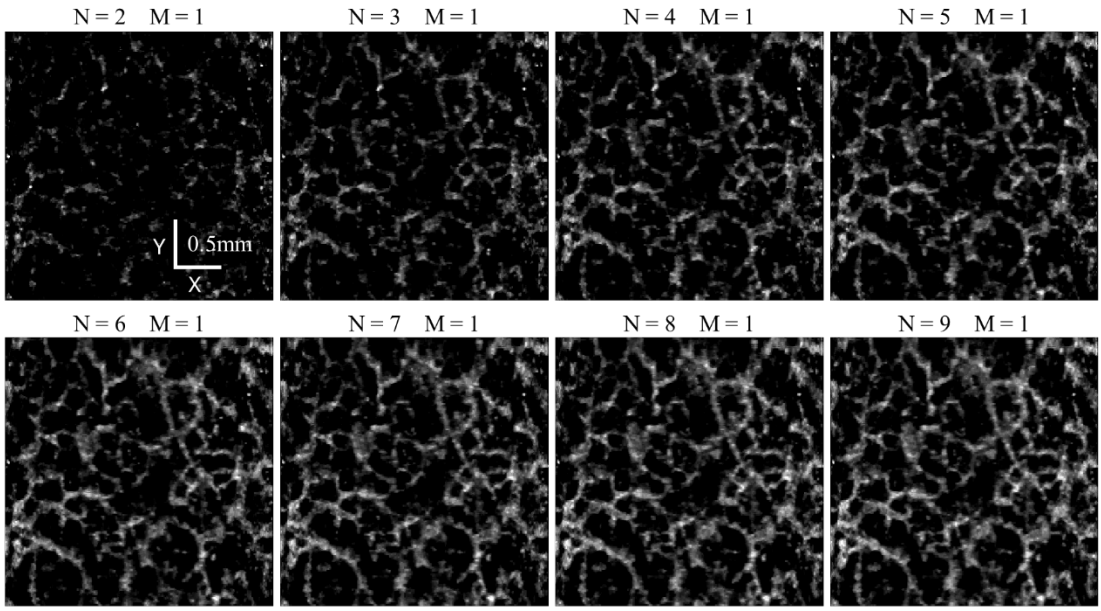

Figure 3.13: Superficial vasculature images of dorsal hand under the FDML OCT system with using different total number of C-scan repetitions (N) for SV OCTA processing while keeping the same time interval of 110 ms ($M = 1$). The optimal N is 4, giving a good image contrast while requiring less acquisition time.

3.5. Conclusion

The in-house high-speed FDML OCT system (illustrated in Chapter 2), with a measured axial resolution of ~13 μm and a lateral resolution of ~25 μm in air, has been applied to detect the epidermal thickness and cutaneous blood vessels on dorsal hand. The FDML OCT runs at a frame rate of 3 kHz, much faster than 40 Hz of Vivosight OCT in our previous work [4], enabling acquisition of one volume scan (2.8 mm x 2.8 mm) in 0.1 seconds that simplify patient compliance.

An automatic algorithm has been developed in MATLAB to segment the skin surface and dermal-epidermal junction (DEJ), involving OCT image filtering, layer detection, and layer smoothing. Additional layer refining process was applied to remove spike artefacts such as hairs to enhance the accuracy of analysing the epidermal thickness. The epidermal thickness of a cross-sectional image on dorsal hand was measured first. A detailed epidermal thickness map overlaid on the enface mean intensity projection was demonstrated, showing the epidermal thickness on dorsal hand ranging from 110 to 150 μm.

Another MATLAB automatic algorithm has been developed based on difference-based and speckle-variance OCTA calculations to achieve angiographic imaging. Several techniques were introduced to enhance the image contrast such as background removal and median filtering. Two scan protocols of B-mode and CM-mode were employed to acquire the FDML OCT data from dorsal hand for the OCTA processing. In B-mode, B-scan repetitions with a fundamental interscan time of 0.33 ms are collected. The superficial blood vessels were revealed in the B-scans. The optimal interval time in B-mode was investigated for achieving the best SNR of the angiographic image. In CM-mode, volume scans or C-scans with a fundamental interscan time of 110 ms are repeated in an area of 2.8 mm x 2.8 mm (XY). The

cutaneous vasculature images were demonstrated. The number of C-scan repetitions was optimised to 4 for visualising the vasculature, which enables the acquisition in only 0.44 seconds. Furthermore, difference-based and speckle-variance OCTA processes were compared, showing similar imaging performance.

Although the OCTA results in this work only showed the visualisation of the blood vessels, the vascular depth, diameter, density can be further estimated. The FDML OCT can provide both the structural and vascular information as useful biomarkers for evaluating AD severity and treatment response more efficiently and patient friendly.

References

[1] R. Yuan, R. Byers, D. Revin, and S. Matcher, "Rapid measurement of epidermal thickness with a 1.6 MHz FDML OCT system," in *Biomedical Spectroscopy, Microscopy, and Imaging III*, 2024, vol. 13006: SPIE, pp. 252-257.

[2] J. Sroka-Tomaszewska and M. Trzeciak, "Molecular mechanisms of atopic dermatitis pathogenesis," *International journal of molecular sciences,* vol. 22, no. 8, p. 4130, 2021.

[3] M. J. Cork *et al.*, "Epidermal barrier dysfunction in atopic dermatitis," *Textbook of Atopic Dermatitis,* pp. 47-70, 2008.

[4] R. A. Byers *et al.*, "Sub-clinical assessment of atopic dermatitis severity using angiographic optical coherence tomography," *Biomedical optics express,* vol. 9, no. 4, pp. 2001-2017, 2018.

[5] R. A. Byers, M. Fisher, N. J. Brown, G. M. Tozer, and S. J. Matcher, "Vascular patterning of subcutaneous mouse fibrosarcomas expressing individual VEGF isoforms can be differentiated using angiographic optical coherence tomography," *Biomedical Optics Express,* vol. 8, no. 10, pp. 4551-4567, 2017.

[6] M. Etemadi, S. Golmohammadi, A. Akbarzadeh, and S. H. Rasta, "Plasmonic photothermal therapy in the near-IR region using gold nanostars," *Applied Optics,* vol. 62, no. 3, pp. 764-773, 2023.

[7] Y. Jia *et al.*, "Split-spectrum amplitude-decorrelation angiography with optical coherence tomography," *Optics express,* vol. 20, no. 4, pp. 4710-4725, 2012.

4. Cutaneous Blood Flow Velocity Mapping using VISTA Processing on a 1.6 MHz FDML OCT System

4.1. Summary

Chapter 3 demonstrated the capability of the in-house FDML OCT system to obtain qualitative cutaneous vascular information. This chapter extends the application of the FDML OCT system to quantify cutaneous blood flow velocity. To achieve this, an optimised VISTA-based auto-fitting algorithm is first proposed to calculate the decorrelation constant for each velocity. The algorithm is first validated using an in-house flow phantom. Subsequently, the scan protocols for VISTA are discussed, and decorrelation constant mapping is performed on B-scan and enface vasculature images of human skin in vivo. Finally, the VISTA-based flow analysis method with the FDML OCT system, along with its limitations and potential applications, is discussed.

Note that parts of the Sections 4.2 and 4.4.1.1 have been published in a conference paper [1].

4.2. Introduction

Atopic dermatitis (AD) is a chronic inflammatory disease of the skin which affects 10-20% of the population in developed countries. The inflammation is caused by the release of histamine from activated mast cells. The histamine would lead to vasodilation which is expected to increase blood flow velocity [2]. Therefore, it is crucial to identify effective methods to quantify blood flow to study this effect for clinical diagnosis.

Laser Doppler flowmetry (LDF) is a widely used, non-invasive technique for measuring microvascular blood flow by detecting Doppler shifts in laser light scattered by moving red blood cells (RBCs). While LDF provides real-time measurements and is effective for superficial tissues, it has limitations in spatial resolution and penetration depth, making it less suitable for deeper vessels [3-5].

In contrast, Optical coherence tomography angiography (OCTA) offers higher resolution and deeper tissue imaging. By detecting the scattering signal from RBCs, OCTA can visualize functional blood flow and provide flow information within vasculature [6-8]. Due to its non-invasive nature, speed, and cost-effectiveness, OCTA has found broad applications in ophthalmology [9, 10], neuroscience [11, 12], gastroenterology [13, 14], and cancer biology [15, 16].

Decorrelation refers to the random change of the complex field caused by transverse motion, rotation, or deformation of the scatterer (such as RBCs) [17]. Based on the type of decorrelation observed, OCTA can be divided into phase-based, intensity-/amplitude-based, and complex signal-based methods [8]. A typical phase-based method is Doppler OCT, which integrates LDF and OCT to measure blood flow velocity based on the phase changes. However, Doppler OCT can only provide the axial velocity of a scatterer due to its angle dependence. Although the total velocity can be calculated by the Doppler angle, it is difficult to determine the Doppler angle in practical applications, especially in vivo [18]. To overcome the angle dependency, multi-beam Doppler OCT was introduced to accurately measure flow velocity [19, 20]. However, the increased system complexity limits the feasibility of using multiple, non-collinear beams in three-dimensional imaging. Another approach is to determine the transverse flow velocity according to its linear relationship with Doppler bandwidth, where the slope depends on the objective's numerical aperture in the sample arm [21,

22]. However, the measurable transverse velocity range is restricted due to Doppler bandwidth saturation above a certain threshold [23], and pre-calibration is required, which significantly limits the method's flexibility and applicability [24]. Additionally, phase-wrapping and phase instability affect the accuracy of these phase-based OCT methods.

To avoid the above-mentioned problems, several intensity-based methods have been proposed, including speckle variance OCT (SVOCT) [25-28], correlation mapping OCT (CMOCT) [29, 30], and split-spectrum amplitude-decorrelation angiography (SSADA) [17, 31]. Most of them have been applied to vasculature imaging while quantitative studies on measuring flow velocity are limited. Although both transverse and axial blood flow can be detected, these methods focus more on segmenting flow areas rather than on quantifying flow velocities. Besides, time-series intensity modulation is affected by random flow [32], Brownian motion [33], multiple-scattering [34], and intravoxel flow velocity gradients [35]. Thus, time-series intensity measurements further increase the difficulty of accurate estimation of blood flow velocity.

Optical microangiography (OMAG) is a complex signal-based method that utilizes both intensity and phase information [6]. The analytical complex signals are built by the Hilbert transform of OCT interference signals. OMAG has great sensitivity of >95dB within the imaging depth of 2.5mm for flow velocity detection [36]. However, it can only measure relative blood flow velocity, and the detectable flow velocity range is greatly limited by the OMAG system parameters such as the angle between beam scanning and flow directions, the angular velocity of the galvanometer, and the offset of incident light [18].

Most recently, Y. Hwang et al. proposed an amplitude-based variable interscan time analysis (VISTA) OCTA using a 600 kHz A-scan rate swept source. This VISTA method enabled the evaluation of different temporal autocorrelation decay constants for different retinal capillary blood flow in vivo [37].

In this chapter, we develop an optimised algorithm by introducing a function of decorrelation curve auto-fitting to the VISTA analysis for automatically estimating the velocity-dependant decorrelation (temporal autocorrelation decay) constant more precisely. To employ this algorithm, three OCTA scan protocols of B-mode, BM-mode, and CM-mode (Section 2.5.2) are specialised for the FDML OCT system (Chapter 2). In B-mode, this VISTA-based auto-fitting algorithm is first validated on a homemade flow phantom with unhomogenized cow milk infused into an 80 μm inner diameter glass capillary tube, showing the decorrelation coefficient mapping of the milk flow on the cross-sectional B-scan image for different predetermined flow velocities (0.3 mm/s - 60 mm/s). The decorrelation coefficient mapping is later achieved on cross-sectional and enface OCTA images of dorsal hand skin in vivo using B-mode and CM-mode, respectively. The B-mode is also used to investigate how the superficial vascular blood flow velocity responds to different levels of irritation caused by Sodium Lauryl Sulphate (SLS) patches on the recruited volunteers' forearms. In BM-mode, the instability of the MEMS scanner is discussed, showing failed angiographic imaging which makes decorrelation coefficient estimation impossible. Furthermore, an optimised CM-mode-guided B-mode is proposed to provide vascular information (vessel diameter) for the cross-sectional vessels with decorrelation coefficients.

4.3. OCTA and VISTA Calculations

In this chapter, all the acquired time-series data is processed using the difference-based OCTA method to evaluate the decorrelation for flow analysis. The normalized decorrelation can be calculated as the normalized mean amplitude difference in Equation 3.1 (Section 3.4.1.1) [37].

To quantify the flow velocity, the normalized decorrelation values over interscan time are then used to generate the temporal autocorrelation decay constant α based on the VISTA temporal autocorrelation fitting model [37]

$$D_{normalized}(M\Delta t) = \beta(1 - e^{-\alpha \cdot M\Delta t}) \tag{4.1}$$

where Δt is the fundamental interscan time, $M\Delta t$ is the time interval between two B-scans, α is a temporal autocorrelation decay constant or decorrelation coefficient, β is a constant modelling the ratio of dynamic versus static contribution to the signal.

For visualising the blood vessels, the speckle-variance OCTA algorithm (Section 3.4.1.1) is employed to process the OCT data of human skin. To eliminate high decorrelation caused by system background noise, a background noise removal process (as illustrated in Section 3.4.1.3) is applied to each raw B-scan.

4.4. Scan Protocols and Results

4.4.1. B-mode Scan Protocol for FDML OCT

First, we use a B-mode scan protocol to collect multiple B-scan repetitions along the same X-axis of the sample by disabling the Y-scanning function of the MEMS scanner. Each frame covers a 2.8 mm scan length on a sample and consists of 280 A-scans, with an A-scan spacing of 10 microns. Using the FDML OCT system, a dataset of 1000 B-scan repeats is acquired in approximately 0.33 seconds.

4.4.1.1. Validating VISTA Flow Velocity Quantification on a Flow Phantom

4.4.1.1.1. Flow Phantom

To quantify flow velocity using the FDML OCT system, a flow phantom setup has been developed to replicate the blood flow in capillaries or vessels beneath the skin surface (**Figure 4.1**(a)). A glass capillary tube (BGCT 0.1, Capillary Tube Supplies Ltd) with an inner diameter of 80 μm and 10 μm wall thickness was mounted on Petri dishes. A syringe filled with undiluted unhomogenized cow milk (supermarket 5% fat milk) was connected to the tube and pumped by a syringe pump.

The fat globule size in the unhomogenized cow milk ranges from 1 to 10 μm which is close to the size of human RBCs (7.5 to 8.7 μm in diameter and 1.7 to 2.2 μm in thickness) [38]. Hence, it can serve as a good alternative to human blood. The pump was programmed to infuse the milk at predetermined flow rates in a range of 0.12 - 368.16 μL/min. The flow velocity (line speed) was calculated by dividing the flow rate by the cross-sectional area of the tube. A dataset of 280 B-scans repetitions was acquired for each flow rate.

Figure 4.1(b) and (c) show typical B-scan images (B-scans) of the glass capillary tube without and with milk. The reflections from the top and bottom glass walls of the tube in **Figure 4.1**(b) were much stronger than the side walls, which makes the side walls invisible. The tube shown in **Figure 4.1**(c) looks stretched in the vertical direction because of the refractive index of milk (1.35) [39].

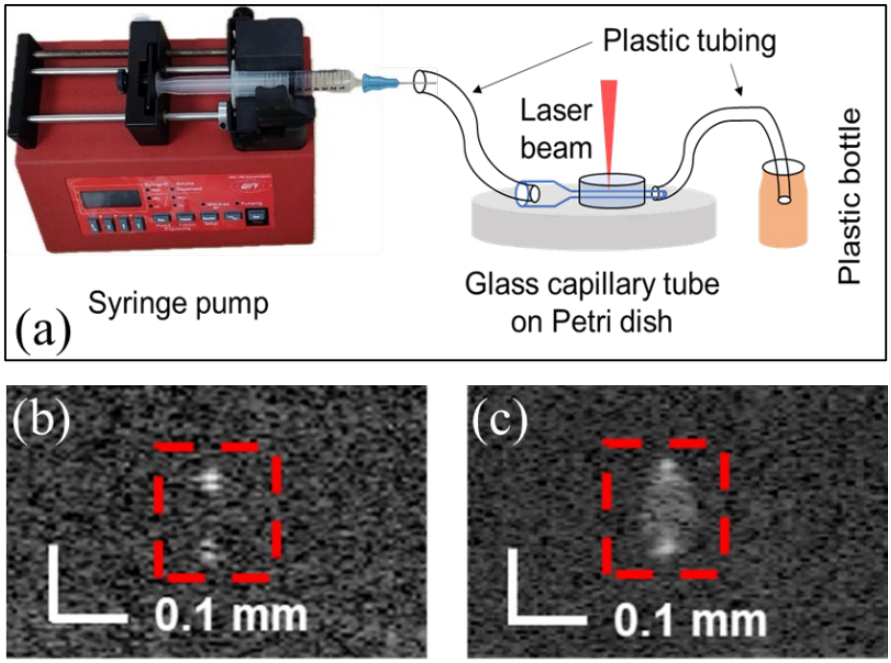

Figure 4.1: (a) Schematic of the homemade flow phantom model. (b) B-scan image of empty glass capillary tube (red dashed box), taken by the FDML OCT system. (c) B-scan image of the tube when infusing milk (red dashed box), taken by the FDML OCT system.

4.4.1.1.2. B-mode VISTA Results on Flow Phantom

Figure 4.2(a) displays a typical B-scan image of the glass capillary tube filled with infused milk, along with six coloured 2x2 pixel regions selected for further analysis. **Figure 4.2**(b) compares the time-series decorrelation trends at these locations for a preset 0.8 mm/s flow velocity after OCTA processing. In the red region at the tube's centre, the normalized OCTA rises from 0.07 and then saturates as the time separation between B-scans used in the calculations increases. The cyan region, located outside the tube, represents the background noise, which corresponds to random scatters (**Figure 4.2**(b), cyan colour) and stays nearly the same for all time separation values. Based on laminar flow, the flow velocity near the tube's periphery approaches zero, which explains why the decorrelation trends at the peripheral locations (magenta, yellow, green, and blue) are similar to those observed in the background (cyan).

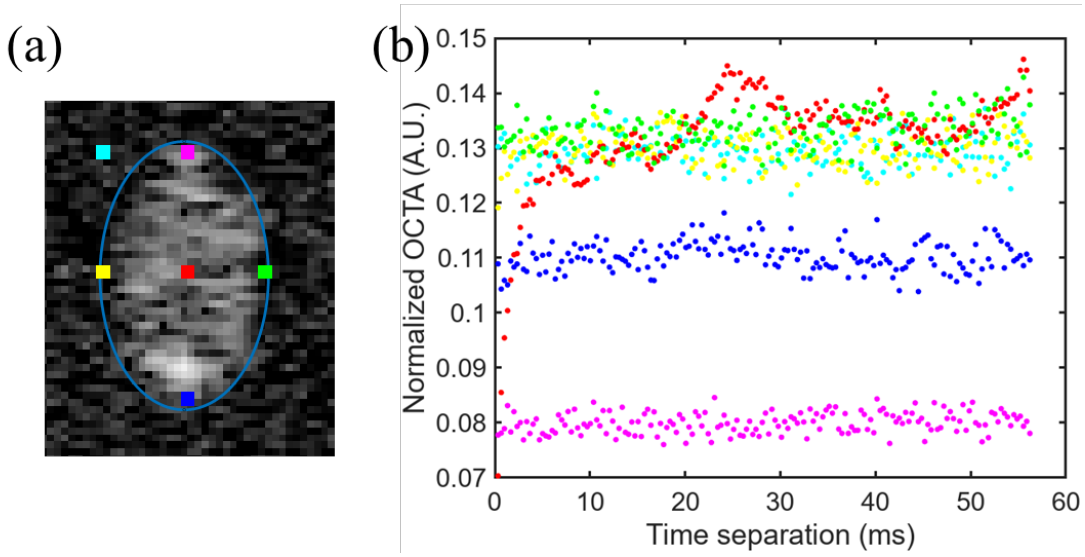

Figure 4.2: (a) A typical glass capillary tube B-scan image with 6 coloured locations of 2x2 pixels (cyan, magenta, yellow, red, green, blue), taken by the FDML OCT system. (b) Decorrelation comparison among the 6 locations of (a) for a preset flow velocity of 0.8 mm/s.

To validate the VISTA temporal autocorrelation fitting model, we estimated the decorrelation coefficient (α) at the tube centre for three different preset milk flow velocities. To account for the axial stretch in the tube flow, a 6x2 (ZX) pixel region is selected to calculate the average decorrelation at the tube centre for each B-scan (**Figure 4.3**(a)). **Figure 4.3**(b) compares the decorrelation trends fitting with Equation 4.1 and their corresponding α values. The decorrelation curves reach a plateau within 8, 3, and 1 ms for flow velocities of 0.4 mm/s, 4 mm/s, and 40 mm/s, respectively. It can be noted that, the smaller the flow velocity, the slower the decorrelation saturates and the smaller the α value.

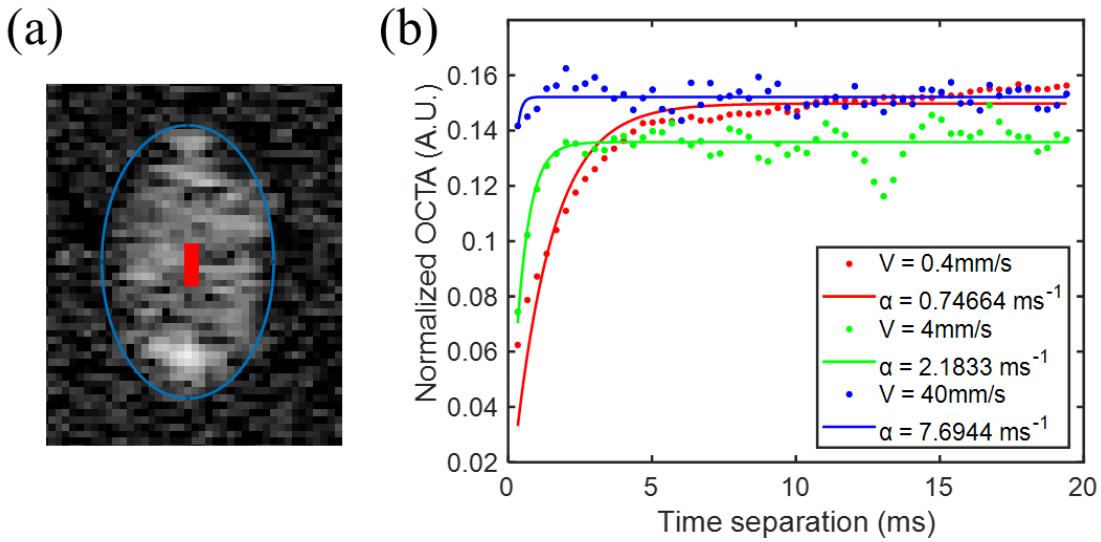

Figure 4.3: (a) A typical glass capillary tube B-scan image with marking a 6x2-pixel area in the centre for decorrelation calculation, taken by the FDML OCT system. (b) Decorrelation coefficient α comparison for the velocities of 0.4 mm/s (red), 4 mm/s (green), and 40 mm/s (blue) in the chosen area of (a).

Additionally, this 6x2-pixel window is applied as a moving average window to estimate the mean decorrelation for each pixel of the tube cross-sectional image in **Figure 4.3**(a). **Figure 4.4**(a) and (b) display the moving-averaged mapping of decorrelation coefficient α and the coefficient of determination (R^2) for the tube under a preset milk flow velocity of 4 mm/s. The mean α value within the tube in **Figure 4.4**(a) is 1.33, considering only those α values with corresponding R^2 values greater than 0.8. This mean α of 1.33 is approximately half of the α value at the tube centre, confirming that the flow velocity at the tube centre is roughly twice the average flow velocity. Furthermore, α values are nearly symmetric about the tube centre, aligning with expectations from fluid mechanics.

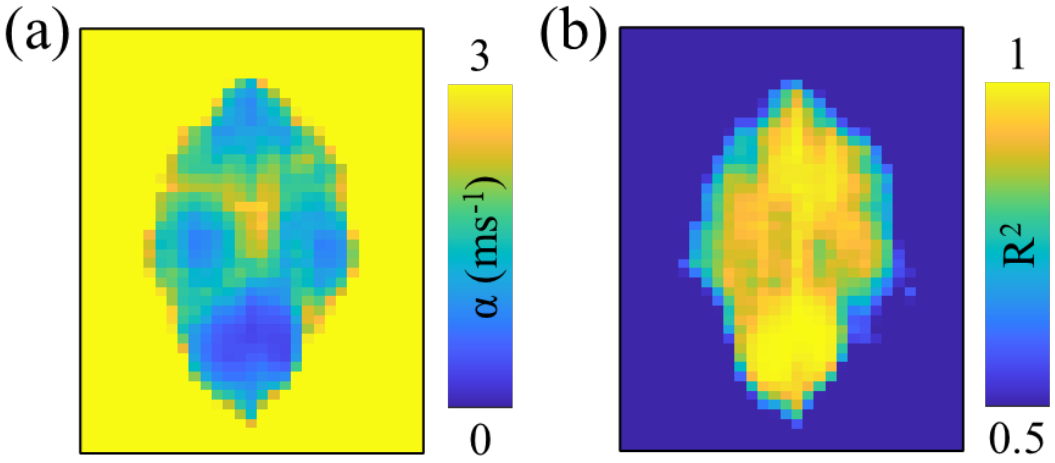

Figure 4.4: (a) Decorrelation coefficient α map of the tube in **Figure 4.3**(a) for a preset flow velocity of 4 mm/s. (b) Coefficient of determination R^2 map of the tube in **Figure 4.3**(a) for a preset flow velocity of 4 mm/s.

The detailed relationship between α and the flow velocity is presented in **Figure 4.5**, where the temporal autocorrelation fitting model was applied at the tube centre. Within the flow velocity range of 0.3 to 20 mm/s, the relationship between α and the flow velocity is close to linear (**Figure 4.5**(a)). This velocity range is within the blood flow velocity range expected for skin blood vessels [37, 40]. Hence, this dependence can be used to predict the flow velocity in blood vessels. However, at high flow velocities (~20 - 60 mm/s), the coefficients of determination (R^2) become much reduced (**Figure 4.5**(b)), indicating poorer fitting due to insufficient data points before saturation at these higher velocities.

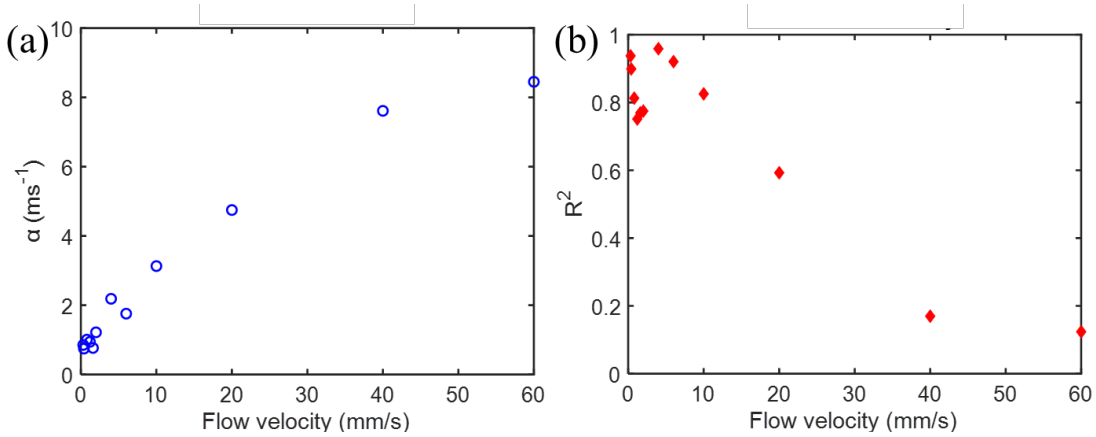

Figure 4.5: (a) Decorrelation coefficient α vs preset flow velocity. (b) Coefficient of determination R^2 vs preset flow velocity.

4.4.1.2. In-vivo VISTA Flow Velocity Quantification on Cutaneous Blood Vessels

4.4.1.2.1. VISTA-based Auto-fitting Algorithm

After validating VISTA on the flow phantom, the fitting model was applied to human skin vessels. **Figure 4.6**(a) presents a typical B-scan image of 1000 B-scan repetitions

(B-mode scanning) on dorsal hand skin, with the green line indicating the detected skin surface. **Figure 4.6**(b) displays the speckle-variance OCTA image from **Figure 4.6**(a) after the skin surface was flattened to the top, revealing the blood vessels and their associated tail artefacts beneath them. The red ellipse (pointed by the red dashed arrow) highlights the vessel area selected for VISTA curve fittings presented in **Figure 4.6**(c)-(f). **Figure 4.6**(c) shows the curve and the fitting across the full-time scale (0 ms to 333 ms), however, the results are poor (very low value of R^2), as the blood flow saturates around 40 ms, and too much irrelevant data was included in the fitting.

To address this, we propose an optimized algorithm based on the VISTA temporal autocorrelation decay fitting model. The key improvement is an automatic selection of the time scale for better curve fitting. In **Figure 4.6**(d), the one-dimensional numerical gradient for the data in **Figure 4.6**(c) is calculated, indicating the locations of the zero crossings. The X-axis of the first zero-crossing should represent the time at which the decorrelation begins to saturate. To minimize errors, the X-axis of the N-th zero-crossing point (the 4th in this study) is chosen as the maximum time separation for a given scale. Here, N is an adjustable parameter determined by the fundamental interscan time. After applying this process, **Figure 4.6**(e) demonstrates improved fitting results for the optimized time scale of 0 ms to 40 ms. However, if the selected time scale is shorter than the saturation time scale, such as 0 ms to 20 ms, the fitting result for the α value becomes inaccurate, even though **Figure 4.6**(f) indicates a high R^2 value.

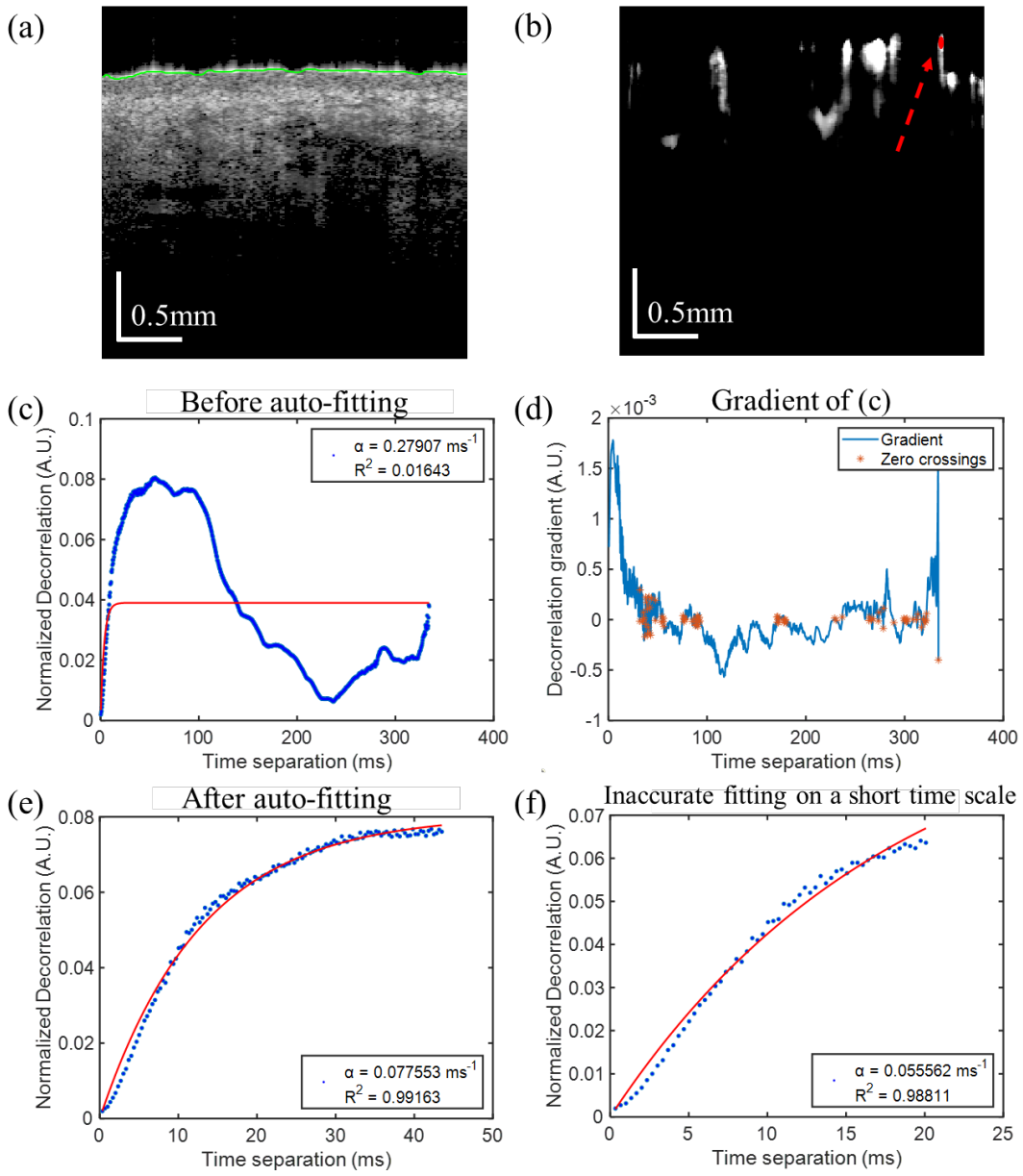

Figure 4.6: (a) A typical B-scan image of dorsal hand skin under FDML OCT (green line: skin surface). (b) The corresponding angiographic image after skin flattening. The red dashed line points to the vessel area (red ellipse) used for VISTA curve fitting in (c)-(f). (c) Decorrelation change over time (0 ms to 333 ms) without auto-fitting process. (d) Gradient of the decorrelation curve in (c), with orange points marking zero crossings. (e) Decorrelation from 0ms to the saturation time (roughly 40 ms) identified by the auto-fitting process. (f) Decorrelation change over a shorter time scale (0 ms to 20 ms) without auto-fitting process.

Figure 4.7 presents a comparison of the α and R^2 mappings from **Figure 4.6**(b), before and after applying the optimized VISTA-based auto-fitting algorithm. **Figure 4.7**(a) and (b) show poor fitting results, with low R^2 values in the vessel region and higher values in the static tissue. After applying the optimized time scale, **Figure 4.7**(c) and (d) display significant improvement, clearly highlighting the flow area as shown in **Figure 4.6**(b). In the flow region (vessels with tail artefacts), all pixels exhibit R^2 values greater than 0.5. A two-dimensional median filter with a 15x3 (ZX) pixel window was applied to **Figure 4.7**(a-d) to reduce the speckle noise.

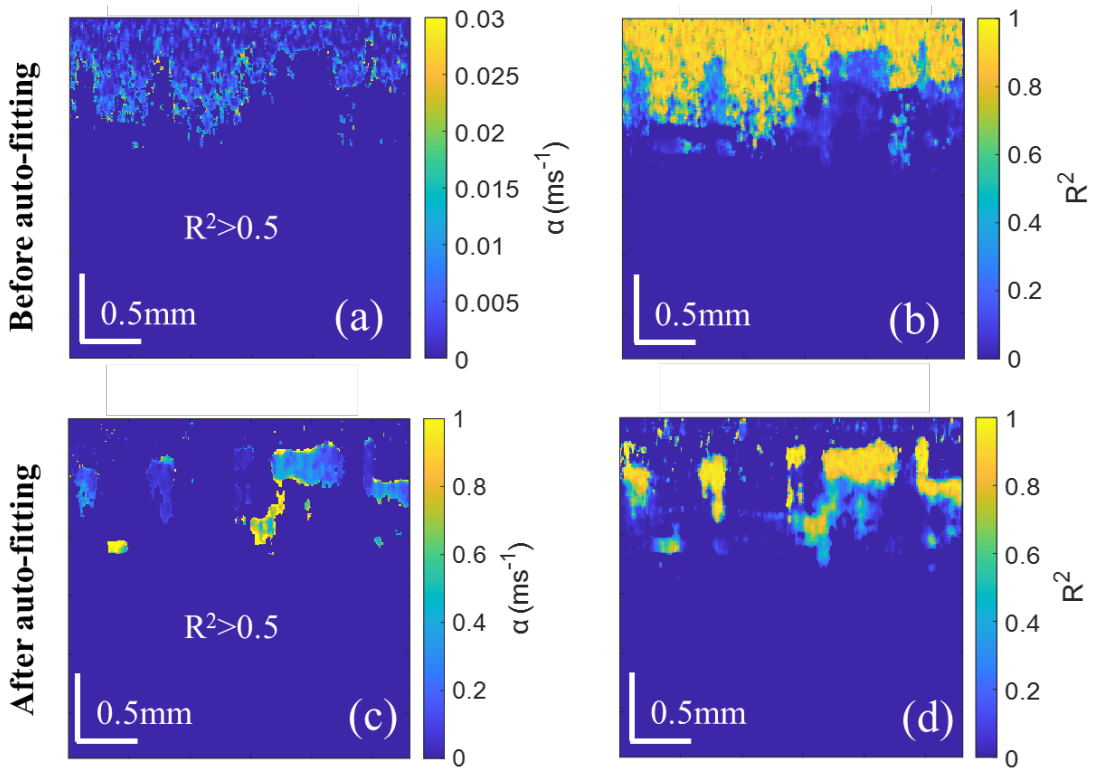

Figure 4.7: VISTA processing for each pixel in **Figure 4.6**(b). (a) α map without the auto-fitting process when $R^2 > 0.5$. (b) R^2 map without the auto-fitting process. (c) α map after applying the auto-fitting process when $R^2 > 0.5$. (d) R^2 map after the auto-fitting process.

4.4.1.2.2. Vessel Masking

Generating an α map enables detailed flow velocity quantification across a B-scan, but performing curve fitting for each pixel can be time-consuming. To reduce computation time, we apply a B-scan mask to limit curve fitting only to pixels containing flow signals. First, the angiographic image of the B-scan is obtained using difference-based OCTA. Then, histogram analysis is applied to this angiographic image, and the upper limit of the first bin is used as a threshold to binarize the image. **Figure 4.8**(a) shows the resulting binarized OCTA mask, where the white pixels are going to be selected for the decorrelation curve fitting. Since the OCTA mask in **Figure 4.8**(a) is coarse and noisy, a second mask generated by speckle-variance OCTA is introduced, which provides a clearer depiction of vessels. **Figure 4.8**(b) shows the binary mask of the speckle-variance angiographic image. After multiplying **Figure 4.8**(a) with **Figure 4.8**(b), the resulting mask in **Figure 4.8**(c) reveals clear vessel locations with reduced noise and artefacts.

Figure 4.8(d) illustrates the α mapping overlaid on the raw intensity B-scan within the white regions of the OCTA mask in **Figure 4.8**(a). **Figure 4.8**(e) demonstrates α mapping in the blood vessels using the refined OCTA mask in **Figure 4.8**(c), along with enhanced visualization of vessel location, depth, and width beneath the skin. To further refine the α mapping, an R^2 threshold can be applied, retaining only α values in pixels with good curve fitting of $R^2 > 0.5$ (**Figure 4.8**(f)).

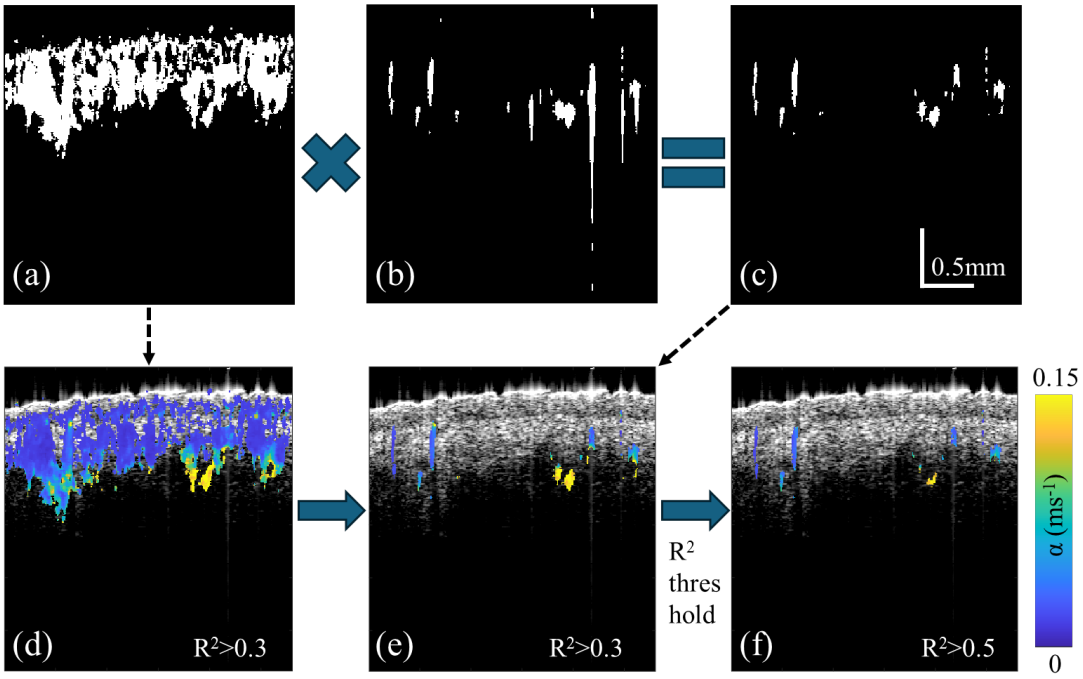

Figure 4.8: Process of generating a vessel mask for flow quantification. (a) Binary image of a typical normalized OCTA B-scan taken by the FDML OCT, thresholded using histogram analysis. (b) Speckle-variance OCTA binary image of the same B-scan. (c) Refined binary vessel mask generated by multiplying (a) and (b). (d) α map (R^2>0.3) obtained after VISTA-based auto-fitting, overlaid on the raw intensity B-scan using (a) as the vessel mask. (e) α map (R^2>0.3) using mask (c). (f) α map (R^2>0.5) using mask (c). Scale bar is the same for (a)-(f).

4.4.1.3.B-mode VISTA Results in Irritated Skin

4.4.1.3.1. Data Collection for Investigating Blood Flow Changes in Irritated Skin

To investigate in vivo changes in flow velocity, volunteers with healthy skin aged from 18 to 50 years were recruited for this study. Since irritation is expected to increase blood

flow in skin vessels and Sodium Lauryl Sulphate (SLS) is known to cause irritation, three SLS patches (water-placebo, 1% SLS, and 2% SLS) with a 2 cm diameter were applied to three different areas on the forearms of the volunteers for 24 hours. SLS is a commonly used ingredient in household products such as shampoo and toothpaste. Individual responses to SLS vary, but most people experience mild irritation or redness at the application site, which is normal and typically subsides within a few days. During this study, informed consent was obtained from each participant before imaging. This study was approved by the University Research Ethics Committee (UREC) of the University of Sheffield, under project reference 059526.

For the data collection, as shown in **Figure 4.9**, B-mode scanning of 1000 B-scan repetitions by the FDML OCT system was performed on four different areas of the forearm: untreated skin, water-placebo patched skin, 1% SLS patched skin, and 2% SLS patched skin. Three random repetitions of B-mode scanning were collected for each area, with each repetition taking approximately 0.33 seconds.

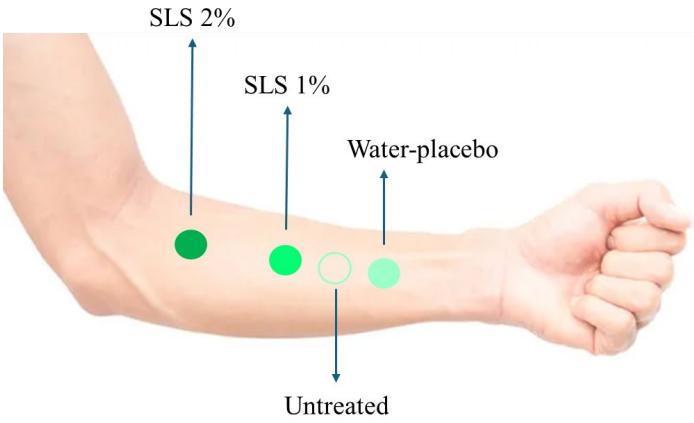

Figure 4.9: Scanning protocol for the SLS study using the FDML OCT system. BM-mode scanning was performed on four areas of the volunteers' forearms: untreated skin, water-placebo treated skin, 1% SLS patched skin, and 2% SLS patched skin. SLS: Sodium Lauryl Sulphate.

4.4.1.3.2. Preliminary VISTA Results of SLS Study

Figure 4.10 presents the VISTA decorrelation coefficient (α) mapping results from one volunteer in the SLS study. Three repetitions of B-mode scanning across four skin areas with varying levels of irritation are compared. All datasets were processed using the optimised VISTA-based auto-fitting algorithm (Section 4.4.1.2). The α mappings are overlaid on intensity B-scans, indicating flow velocities at different positions within the blood vessels. Corresponding angiographic images are also provided for clearer vessel visualization. The skin surfaces of all B-scans were flattened to the top to facilitate vessel depth identification. The Z-axis represents tissue depth, with one A-scan pixel corresponding to approximately 6.18 μm in the tissue under our FDML OCT system [41].

The three repetitions in the untreated area show similar α values for blood vessels as those in the water-placebo treated area, which aligns with expectations. The three repetitions in the 1% and 2% SLS patched areas exhibit faster blood flow, indicated by higher α values compared to the untreated and water-placebo areas. However, not all α mapping results from the SLS 2% patched area (**Figure 4.10**(p)) show a markedly faster blood flow than those from the SLS 1% patched area (**Figure 4.10**(o)). This variation may be attributed to differences in vessel diameter, as wider vessels have faster blood flow [42]. Additionally, the third repetition does not show elevated blood flow in the SLS 1% and 2 % patched areas (Figure 4.10(w) and (x)), which may be due to the scan being conducted outside the actual patched regions, or due to uneven distribution of irritation within the treated area. As only one volunteer has been recruited thus far, the current findings are preliminary. Nevertheless, the results suggest a potential increase in blood flow velocity in response to skin irritation.

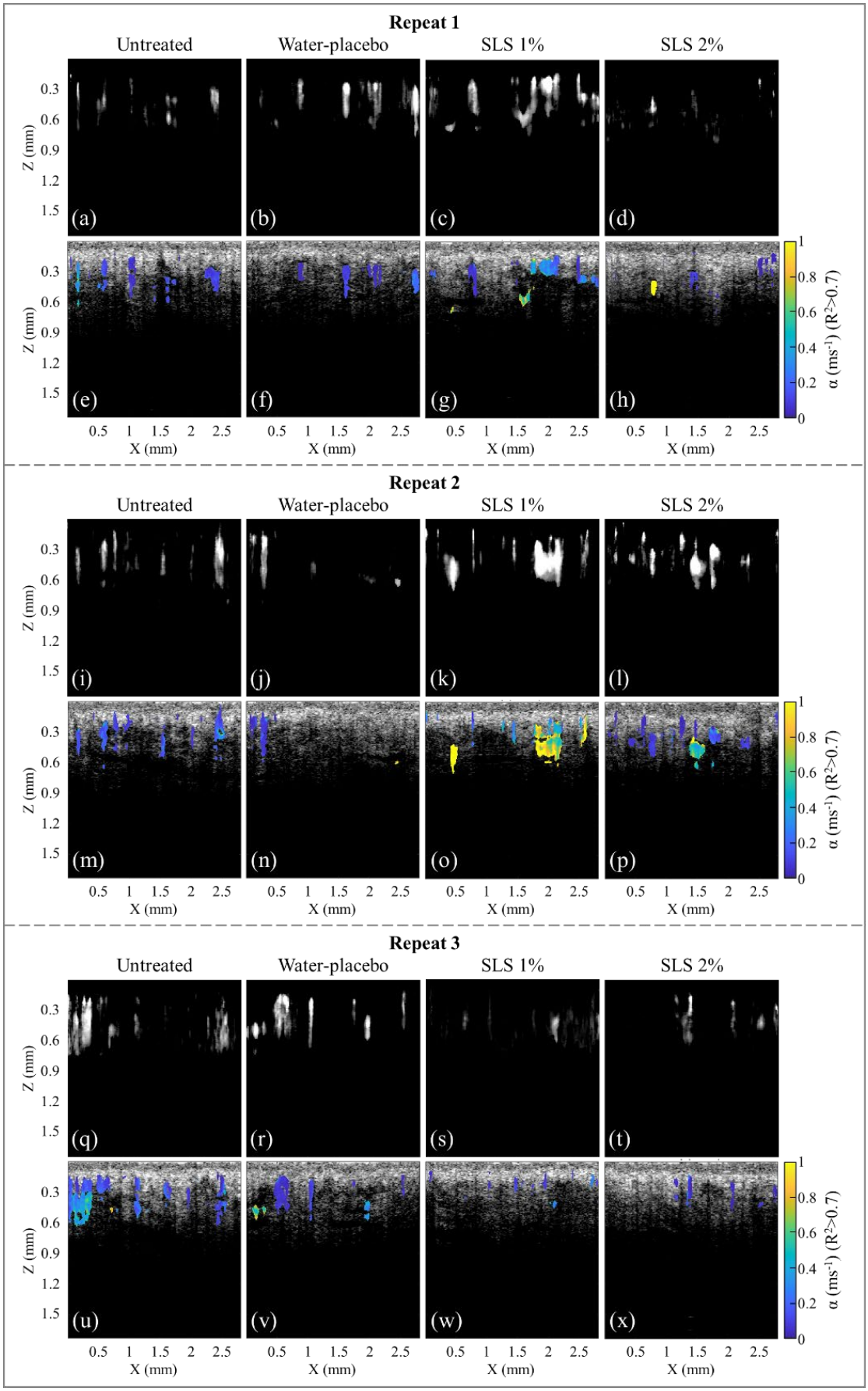
Repeat 1
Untreated
Water-placebo
SLS 1%
SLS 2%
Z (mm)
X (mm)
α (ms⁻¹) (R²>0.7)
(a)
(b)
(c)
(d)
(e)
(f)
(g)
(h)
Repeat 2
(i)
(j)
(k)
(l)
(m)
(n)
(o)
(p)
Repeat 3
(q)
(r)
(s)
(t)
(u)
(v)
(w)
(x)

Figure 4.10: VISTA flow analysis for three repetitions of B-mode scanning across four forearm skin areas: untreated skin, water-placebo patched skin, 1% SLS patched skin, and 2% SLS patched skin. (a-d) Angiographic images of the four areas from the first repetition. (e-h) Corresponding α mappings overlaid on intensity B-scans from (a-d). (i-p) Angiographic images and corresponding α mappings from the second repetition. (q-x) Angiographic images and corresponding α mappings from the third repetition.

4.4.2. BM-mode Scan Protocol for FDML OCT

4.4.2.1.BM-mode Data Collection

B-mode scanning provides only a two-dimensional cross-sectional image of the skin. To enable flow analysis in a three-dimensional region of the skin, the BM-mode scan protocol is applied to the FDML OCT system, collecting multiple B-scan repetitions at each position along the Y-scanning axis [37]. The approach involves performing VISTA-based flow analysis for every Y position, using the time-series B-scan repetitions as in the B-mode scan processing. The decorrelation curves for blood flow in skin vessels (**Figure 4.6**) have a saturation time typically ranging from 20 ms to 200 ms. Given the fundamental interscan time of 0.33 ms, at least 60 B-scan repetitions are necessary for angiographic imaging and VISTA flow analysis. On the other hand, the number of B-scan repetitions is limited by the on-board memory of the digitizer used. Therefore, only 120 B-scan repetitions have been used for each pixel along a 0.5 mm Y-scan, with a B-scan spacing step of 10 microns. A dataset covering a 2.8 mm x 0.5 mm area on dorsal hand skin is obtained in 2 seconds.

4.4.2.2. BM-mode Results on Dorsal Dand

Figure 4.11 was generated from the dataset of BM-mode scanning over a 2.8 mm x 0.5 mm area on dorsal hand skin. **Figure 4.11**(a) shows the en-face mean intensity projection, while **Figure 4.11**(b-f) display the corresponding speckle-variance angiographic vasculatures in the same greyscale. **Figure 4.11**(b-f) were generated using different batches of 30 out of the 120 repeated B-scans for OCTA imaging.

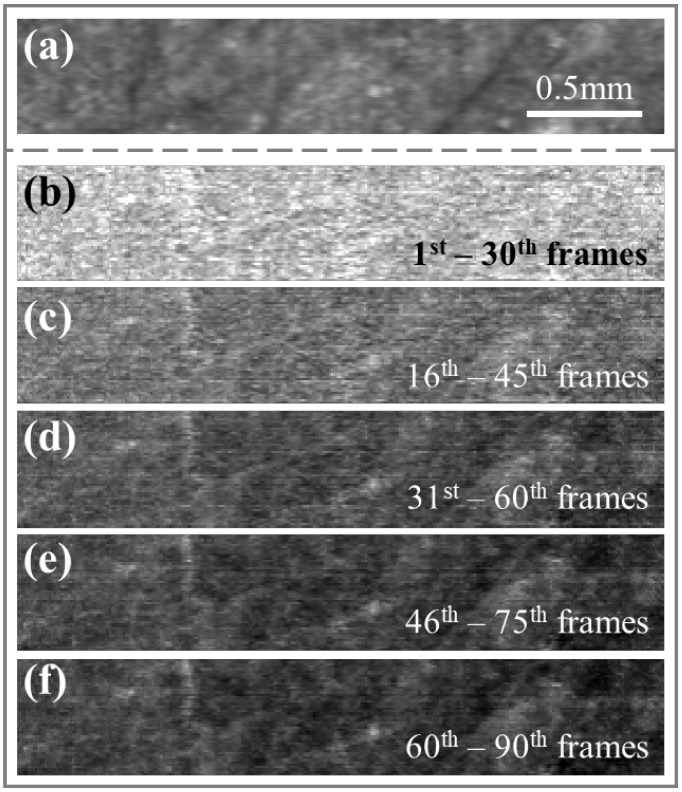

Figure 4.11: BM-mode scanning over a 2.8 mm x 0.5 mm area on dorsal hand skin with 120 B-scan repetitions at each Y position under the FDML OCT system. (a) Enface mean intensity projection of the scanned area. (b) Corresponding speckle-variance angiographic vasculature generated using the 1st–30th frames out of the 120 repeated B-scans. (c) Vasculature from the 16th–45th frames. (d) Vasculature from the 31st–60th frames. (e) Vasculature from the 46th–75th frames. (f) Vasculature from the 60th–90th frames. The greyscale is consistent for (c-f).

Figure 4.11(b), which uses the first 30 repeated frames, shows significant noise, while **Figure 4.11**(c-f) gradually reveal clearer and more stable patterns. This suggests that the MEMS scanner was unstable during the first 30 frames (~10 ms) at each Y position during BM-mode scanning. This instability may be caused by the inertia of the scanning mirror when being rapidly pushed to the next Y position.

To address this issue, instead of acquiring 120 B-scan repeats with a 10-μm spacing, the B-scan step spacing in the Y direction could be reduced to, for example, 0.083 μm (the minimal step possible with the present OCT system), allowing 120 B-scans to be acquired every 10 μm. These 120 B-scans could then be treated as B-scan repeats obtained at the same Y position since the Y-position change is much lower than the lateral resolution of the present OCT system (~25 μm in Section 2.4.3). However, within these 120 B-scan repeats (40 ms) angiographic vasculatures have poor quality (**Figure 4.11**(d-f)) with weak flow signals and strong skin surface noise interference. This occurs because a time separation of 40 ms is insufficient for efficient OCTA imaging. Additionally, the number of B-scan repetitions is limited by the memory capacity of the digitizer (Section 4.4.2.1). Therefore, BM-mode scanning is not suitable for OCTA and VISTA flow analysis with the current FDML OCT system due to the combined issues of MEMS instability and insufficient time separation.

4.4.3. CM-mode Scan Protocol for FDML OCT

4.4.3.1.CM-mode Data Collection

The CM-mode scan protocol is another method for achieving imaging and flow analysis of three-dimensional superficial vasculature by collecting multiple C-scan or volume scan repetitions. Compared to BM-mode scanning, the fundamental interscan time for a B-scan at the same Y position depends on the acquisition time of a single C-scan. **Table 4.1** compares the parameters of four different CM-mode scan protocols with varying Y-axis scan lengths for the FDML OCT system. The maximum field of view (FOV) is 2.9 mm x 2.9 mm (Section 2.4.4), which is limited by the scanning angle of the MEMS scanner used. To achieve a shorter fundamental interscan time, the Y-scan length must be reduced. The datasets from these four CM-mode scans are used for OCTA imaging and VISTA flow analysis.

Table 4.1: Comparison of four different CM-mode scan protocols for the FDML OCT.

FOV	Number of A-scans per B-scan	Number of B-scans per C-scan	Number of Y return steps[a]	C-scan repeats	Fundamental interscan (between B-scans at the same position) time	Total acquisition time
2.8 mm x 2.8 mm	280	280	50	10	110 ms	1.1 s
2.8 mm x 1 mm		100	20	50	40 ms	2 s
2.8 mm x 0.5 mm		50	40	50	30 ms	1.5 s
2.8 mm x 0.2 mm		20	4	200	8 ms	1.6 s

[a]Y return steps refer to the number of backward B-scans along the Y-axis during each C-scan.

These four datasets were acquired from the same area on the dorsal hand skin by the FDML OCT system, with efforts made to keep the hand stationary during the scans. **Figure 4.12** compares the enface mean intensity projection and corresponding speckle-variance angiographic vasculature for the four different FOVs. The time separation for angiographic imaging was set to around 300 ms to optimize SNR. A three-dimensional median filter with a 15x3x3 (ZXY) pixel window was applied to each dataset to reduce noise. The detailed speckle-variance OCTA processing refers to Section 3.4. The red dashed line indicates the centre of the Y direction. By comparing the intensity and angiographic enface images (**Figure 4.12**(a)-(k)), we can observe that the centre of the four scans aligns. This is further confirmed by comparing the central frames along the red dashed line in **Figure 4.12**(c), (f), (i), and (l). The green lines represent the detected skin surface for each B-scan at the centre, and these four central B-scans show nearly identical skin structures and surfaces. Although **Figure 4.12**(k) has a limited FOV and lacks clear vasculature, the matched **Figure 4.12**(b) serves as a good reference.

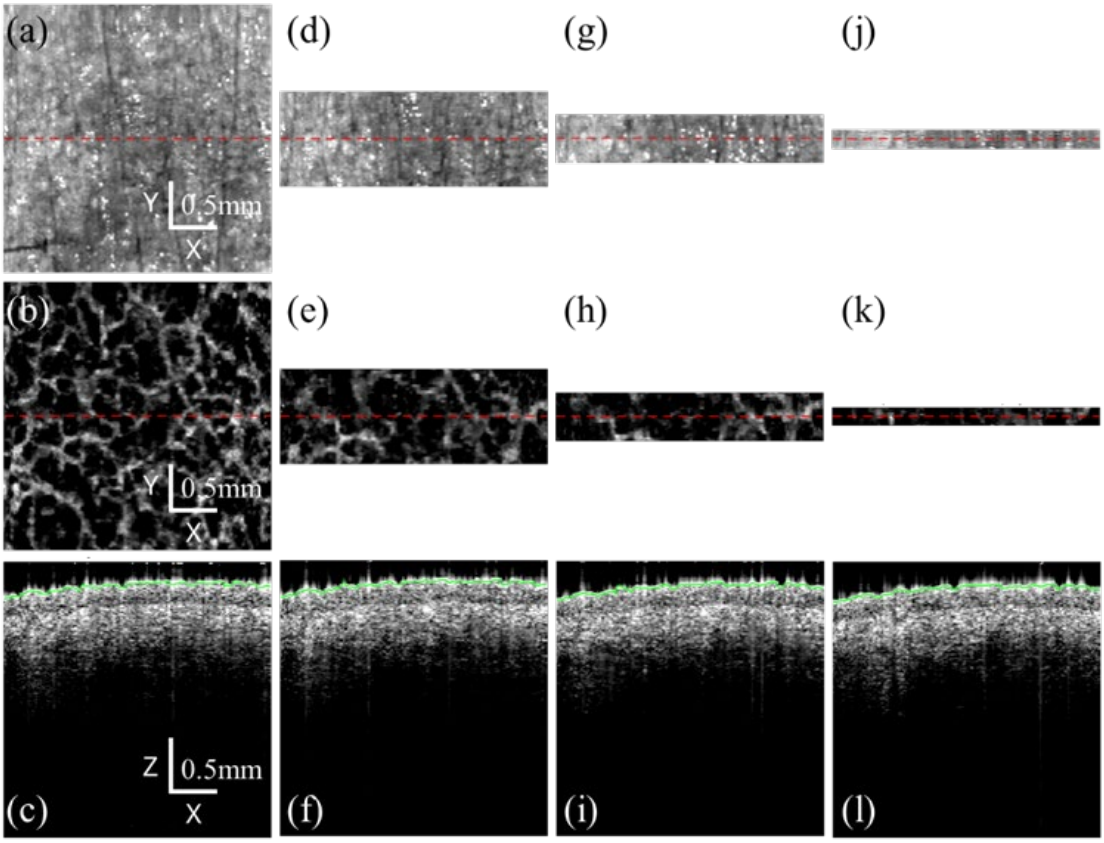

Figure 4.12: Comparison of four different CM-mode scanning using the FDML OCT system. (a) Enface mean intensity projection for a 2.8 mm x 2.8 mm scanning area on dorsal hand skin. (b) Corresponding enface angiographic image of (a) from 0 to 2 mm depth range. (c) Intensity B-scan of the centre frame along the Y-axis (indicated by the red dashed line in (a)), with the green line marking the skin surface. (d)-(f) Corresponding images for a 2.8 mm x 1 mm scanning area. (g)-(i) Corresponding images for a 2.8 mm x 0.5 mm scanning area. (j)-(l) Corresponding images for a 2.8 mm x 0.2 mm scanning area. Scale bar is the same for all enface images.

4.4.3.2.CM-mode VISTA Results on Dorsal Hand

From Section 4.4.3.1, we acquired CM-mode datasets for four different FOVs on dorsal hand skin using the FDML OCT system. Only the dataset covering the FOV of 2.8 mm x 0.2 mm (**Figure 4.12**(j)) could be analysed using the VISTA-based auto-fitting algorithm to generate the α mapping since the other three scan protocols had an intervolume time separation greater than 30 ms, which was insufficient to provide the necessary sample points for VISTA curve fitting. **Figure 4.13** presents the VISTA-analysed results over the 2.8 mm x 0.2 mm area. **Figure 4.13**(a) shows the binary angiographic image corresponding to **Figure 4.12**(k). **Figure 4.13**(b) and (c) display the enface α and R^2 mappings respectively, using maximum projection over the vasculature. All mappings in **Figure 4.13**(a-c) were filtered with an R^2 threshold of 0.7. **Figure 4.13**(d) features a fly-through video of the α mappings overlaid on 20 intensity B-scans along the Y-axis.

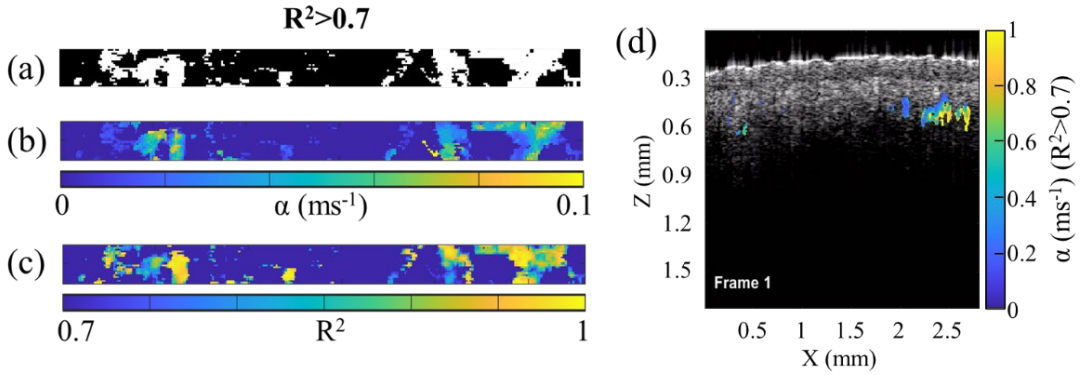

Figure 4.13: CM-mode scanning over a 2.8 mm x 0.2 mm area on dorsal hand skin by the FDML OCT system (**Figure 4.12**(j)). (a) Binary angiographic vasculature image with $R^2 > 0.7$. (b) En-face α mapping using maximum projection over the vasculature with $R^2 > 0.7$. (c) En-face R^2 mapping using maximum projection over the vasculature with $R^2 > 0.7$. (d) Fly-through video of the α mappings overlaid on 20 intensity B-scans along the Y-axis.

4.4.4. CM-mode-guided B-mode Scan Protocol for FDML OCT

4.4.4.1. CM-mode-guided B-mode Data Collection

Based on the centre-aligned scanning mode of the MEMS scanner (verified in Section 4.4.3.1), we propose a CM-mode-guided B-mode scan protocol that combines CM-mode and B-mode scanning. While keeping the hand stationary, we first collect a CM-mode scan with 6 C-scan repetitions, followed by a B-mode scan with 1000 B-scan repetitions, using the FDML OCT system. The B-scans from the B-mode are expected to align with the central B-scan along the Y-axis of the CM-mode. This approach allows the B-mode scan to perform VISTA flow analysis with a fundamental interscan time of 0.33 ms, enabling the quantification of fast flows. Meanwhile, the vasculature enface image generated from the CM-mode dataset can guide vessel-related information in the centre, such as vascular diameter.

Figure 4.14(a) and (b) show the enface mean intensity and angiographic projections over a 2.8 mm x 2.8 mm area of skin. **Figure 4.14**(c) and (d) display the intensity and angiographic B-scan images at the centre (red dashed line) of the CM-mode dataset. **Figure 4.14**(e) and (f) present the intensity and angiographic B-scan images from the B-mode dataset.

Comparing **Figure 4.14**(c) and (e), the detected skin surfaces (green) and tissue structures in the two B-scans are almost identical, despite exhibiting different vertical artefacts across the depth direction. These vertical artefacts may result from the instability of the MEMS scanner or hand drift during scanning. Ignoring these uncontrollable artefacts, the B-mode B-scan can be considered aligned with the Y-axis central B-scan (red dashed line) of the CM-mode scan.

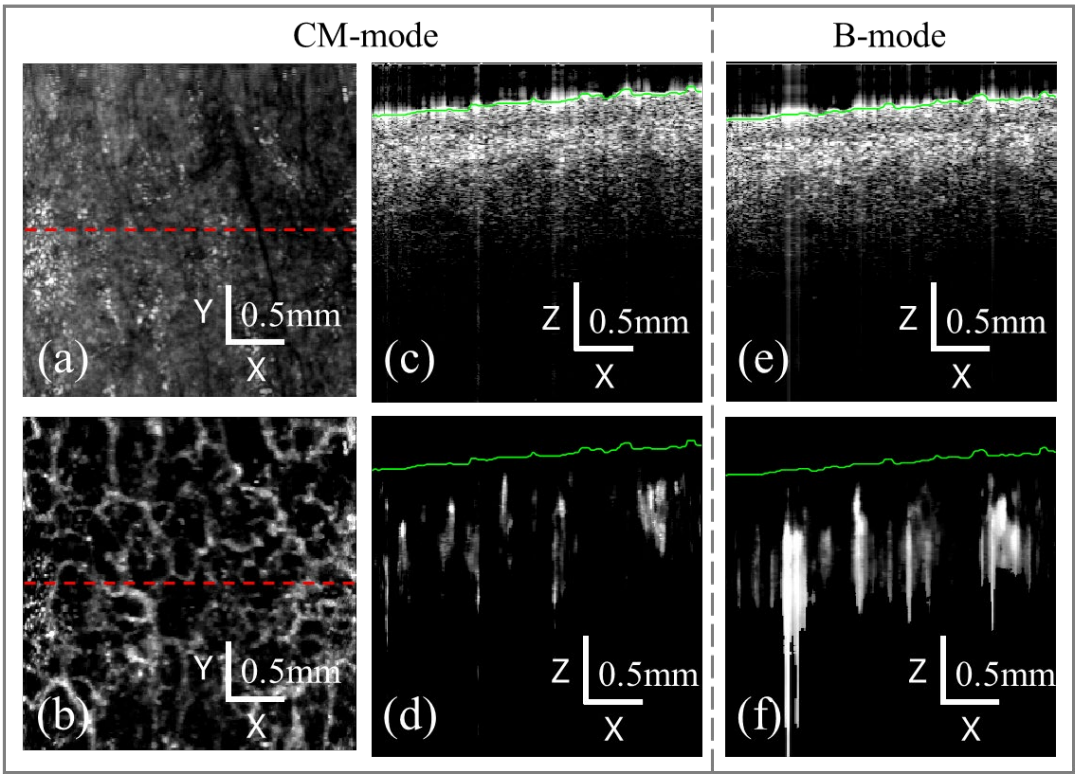

Figure 4.14: Comparison between CM-mode and B-mode scanning using the FDML OCT system. (a) Enface mean intensity projection over a 2.8 mm x 2.8 mm scanning area on dorsal hand skin. (b) Corresponding enface angiographic image from (a). (c) Intensity B-scan of the central frame along the Y-axis (red dashed line) from the 2.8 mm x 2.8 mm CM-mode scan. (d) Speckle-variance image of (c). (e) Intensity B-scan from a B-mode scan (without Y-axis scanning) of the same area on the hand. The hand was kept stationary during both CM-mode and B-mode scanning. (f) Speckle-variance image corresponding to (e). Green: detected skin surface by the automatic layer segmentation algorithm in Chapter 3.

However, the corresponding angiographic B-scans in **Figure 4.14**(d) and (f) differ significantly. **Figure 4.14**(f) displays more artefacts in addition to the vessels and tail artefacts, because the B-mode, with a much shorter fundamental interscan time of 0.33

ms, captures more detailed signal fluctuations. The magnitude of the calculated variance of the flow signal (vessels and tail artefacts) is comparable to or smaller than that of the vertical artefacts. In contrast, the CM-mode, with a much longer fundamental interscan time of 110 ms, produces a calculated variance of the blood flow signal that is significantly stronger than that of vertical artefacts. As a result, **Figure 4.14**(d) presents a much cleaner and clearer vessel distribution with a better signal-to-noise ratio (SNR).

Therefore, while the B-mode dataset is used for VISTA analysis, the CM-mode central frame (**Figure 4.14**(d)) can be used as the vessel mask instead of **Figure 4.14**(f), providing more accurate ZX positions of the vessels. Additionally, the CM-mode vasculature (**Figure 4.14**(b)) demonstrates the directions and diameters of the vessels along the Y-axis central line.

4.4.4.2. CM-mode-guided B-mode VISTA Results on Dorsal Hand

Figure 4.15 presents the VISTA-analysed results of the CM-mode-guided B-mode datasets (described in Section 4.4.4.1) on dorsal hand skin. As discussed in the previous section, the CM-mode central angiographic B-scan (**Figure 4.14**(d)) was binarized, surface-flattened, and used as the vessel mask (**Figure 4.15**(a)) to refine the flow area for decorrelation mapping by analysing the B-mode dataset (1000 B-scan repetitions) using the VISTA-based auto-fitting algorithm. The CM-mode vessel guide was cropped along the Y-axis from the enface vasculature image in **Figure 4.14**(b), instructing the vascular information (vessel direction and diameter). All the arrows point to the vessels across the Y central line (red dashed line) of the vasculature, which are aligned with the vessels in B-scans.

After VISTA-based flow analysis of the B-mode dataset, **Figure 4.15**(b) shows the α mapping in the CM-mode central masked flow areas, overlaid on the surface-flattened intensity B-scan of **Figure 4.14**(e). Only α values with positive R^2 values are kept. To further improve the reliability of the flow analysis, an R^2 threshold of 0.7 was applied to **Figure 4.15**(b). **Figure 4.15**(c) shows the corresponding binary OCTA image of the α map ($R^2 > 0.7$) in **Figure 4.15**(d) to better reveal the vessel locations (pointed by the green arrows). With this CM-mode-guided B-mode scan protocol, not only the vessel depth can be provided but also the vessel diameter and direction can be demonstrated.

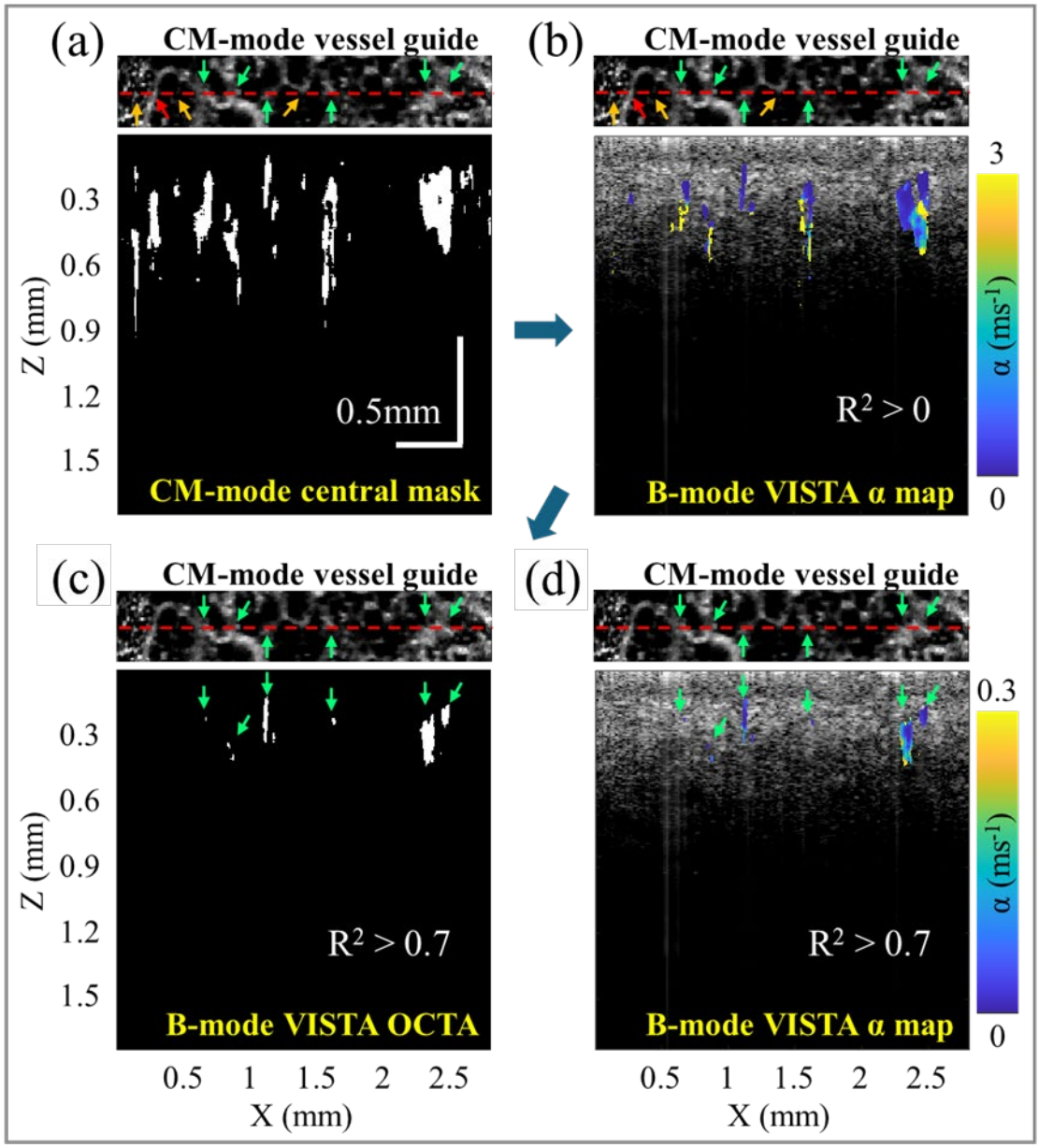

Figure 4.15: VISTA-analysed results of the CM-mode-guided B-mode datasets (described in Section 4.4.4.1) on dorsal hand skin acquired by the FDML OCT system. The CM-mode vessel guide is the same in (a-d) and was cropped along the Y-axis from the enface vasculature image in **Figure 4.14**(b). All the arrows point to the detected vessels. (a) Binary surface-flattened angiographic mask generated from the CM-mode central angiographic B-scan (**Figure 4.14**(d)). (b) α mapping in flow areas masked by (a) when $R^2 > 0$, overlaid on the surface-flattened intensity B-scan of **Figure 4.14**(e). (c) Binary OCTA image of the α map when $R^2 > 0.7$. (d) α mapping in flow areas masked by (a) when $R^2 > 0.7$. (b-d) were generated by using the B-mode dataset of 1000 repeated B-scans. Scale bar is the same for the CM-mode vessel guide and (a-d).

From **Figure 4.15**, we can notice that the VISTA-based algorithm fails to generate α values for the vessels indicated by the orange and red arrows. The orange arrows point to vessels with weak or noisy OCTA signals in the CM-mode vessel guide. To investigate this, VISTA curve fitting was manually applied to three chosen regions (orange, cyan, green) in **Figure 4.16**(a). **Figure 4.16**(b) shows the α and R^2 values for the time-series curve in the static tissue area (cyan) where the decorrelation should be dominated by background noise variance, which is aligned with the expected horizontal line. The orange area (vessel 1 in **Figure 4.16**(c)) corresponds to one of the weak vessels indicated by the orange arrows, and the green area (vessel 2 in **Figure 4.16**(d)) represents one of the vessels with successful α mapping in **Figure 4.15**.

The curve in **Figure 4.16**(c) is similar to that in **Figure 4.16**(d), with a close α value of less than 0.01, indicating a very slow blood flow velocity. Although the R^2 values are both larger than 0.7, the curve fittings are not ideal because the curves do not appear to saturate within 300 ms. This means that the B-mode dataset of 1000 B-scan repetitions (spanning 0-300 ms) is insufficient to estimate the full decorrelation curve, leading to bad curve fitting and incomplete or inaccurate α mapping. Therefore, the number of B-scan repetitions in B-mode needs to be significantly increased beyond 1000 to enable accurate VISTA α mapping for all detected cutaneous vessels on dorsal hand.

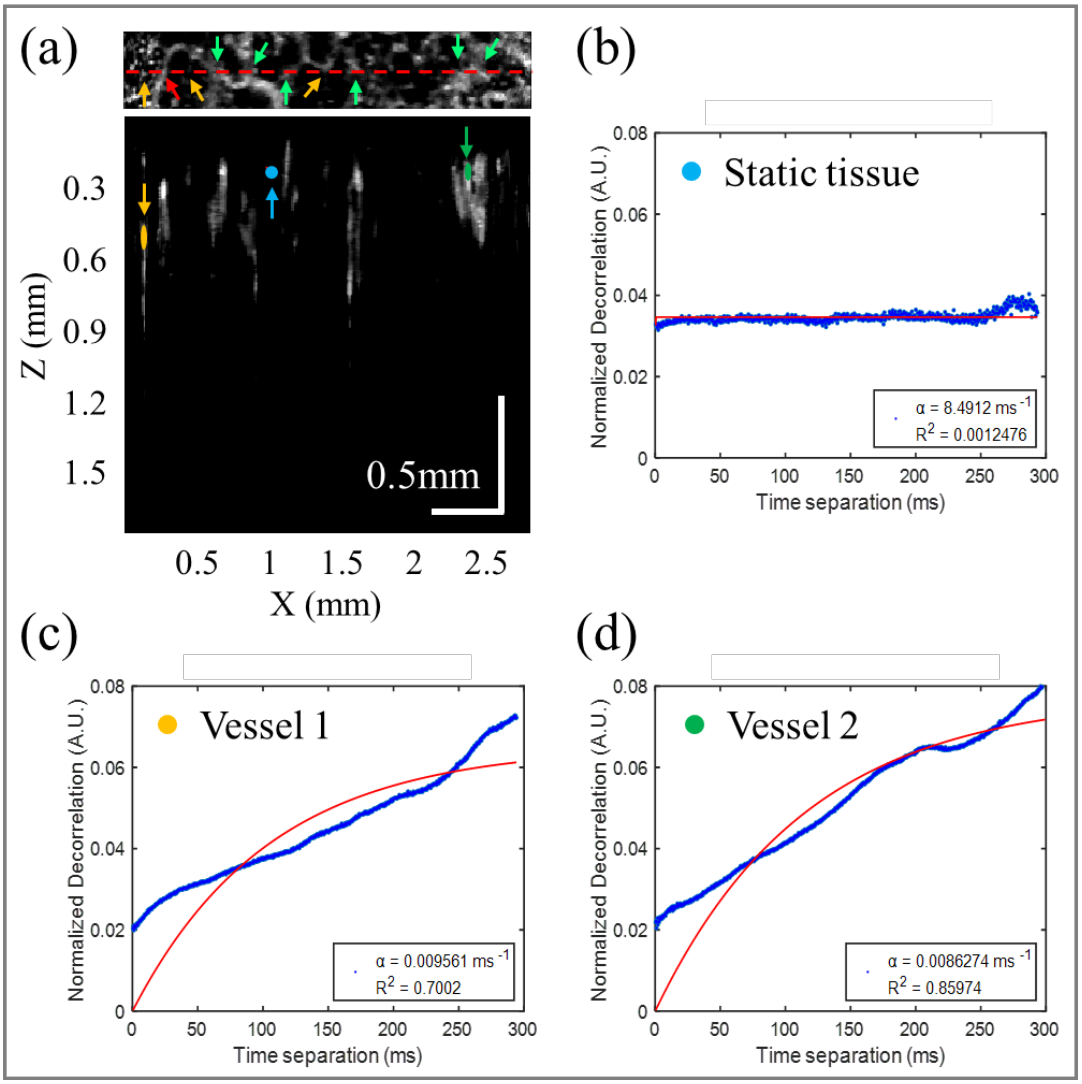

Figure 4.16: (a) Surface-flattened CM-mode central angiographic B-scan of **Figure 4.14**(d), marking three regions (orange, cyan, green) chosen for VISTA curve fitting. (b) VISTA curve fitting for static tissue in the cyan area. (b) VISTA curve fitting for vessel 1 in the orange area. (d) VISTA curve fitting for vessel 2 in the green area.

4.5. Discussion

4.5.1. Blood Flow Velocity Quantification for Skin Vessels

There have been few studies quantifying blood flow velocity in skin vessels. Using VISTA flow analysis with an FDML OCT system, we demonstrate the capability to achieve this. However, due to the limited lateral resolution and imaging penetration depth of the current OCT setup, we can only quantify blood flow in vessels within a 2 mm tissue depth and with a diameter larger than the measured lateral resolution of ~25 μm (Section 2.4.3).

Compared to the quantification of blood flow velocity in retinal capillaries and micro-vessels [37, 42], our study acquires more sample points for VISTA curve fitting. This is because the general saturation time of detected skin vessels is much longer, but the fundamental interframe time is much shorter in our FDML OCT system. The longer saturation time can be attributed to the fact that RBCs in skin vessels require more time to transverse the larger transverse point spread function (PSF) of our system, and/or that the superficial dermal blood flow velocity is lower. .

As discussed in Section 4.4.4.2, the superficial vessels beneath the dorsal hand skin yield very slow blood flow velocities. By adopting the CM-mode-guided B-mode scan protocol, we can increase the number of B-scan repetitions in B-mode scanning to obtain sufficient sample points covering the long saturation time, allowing for an accurate estimation of the decorrelation constant (α), while vessel depth, direction, and diameter can be guided by the CM-mode vasculature. The current α mapping also includes tail artefacts of vessels, which can be mitigated by techniques such as Optimally Oriented Flux (OOF) [43].

Additionally, the current VISTA process provides an indirect measurement of blood flow velocity. In Section 4.4.1.1, we showed a nearly linear relationship between α and flow velocity for milk (**Figure 4.5**). Although skin vessel diameters vary, and the glass capillary tube used in our experiments has a fixed diameter of 80 μm, we measure the line velocity of the milk flow, not the flow rate, allowing us to predict the line velocity of blood flow in skin vessels without considering vessel diameter. For an α value of 1 ms^{-1}, the predicted line velocity is 2 mm/s. Most α values in our study are less than 1 ms^{-1}, indicating a predicted blood flow velocity of less than 2 mm/s in vessels beneath the dorsal hand and forearm skin. Although the linear relationship found in the phantom data is undersampled, especially in the lower flow velocity range, and the phantom scatterers are not RBCs, it nonetheless demonstrates the potential to measure actual blood flow velocity using VISTA with the FDML OCT system. A better flow model, considering the complex dynamics of blood flow (e.g., pulsatility, non-Newtonian behavior, and vessel wall interactions), will be needed to reveal the accurate decorrelation relationship for real blood flow velocity prediction. Furthermore, to ensure consistency in flow quantification, all α values should be measured under the same OCT setup with the same system parameters such as transverse PSF and scan rate.

4.5.2. Limitations and Applications of FDML OCT System

The limitations of the current FDML OCT system primarily stem from the MEMS scanner and the scan lens in the sample arm. Firstly, the beam size is constrained by the 2 mm diameter mirror of the MEMS scanner (Section 2.2.3), which is not optimal for the LSM03 scan lens and results in a larger transverse PSF. Secondly, the maximum FOV is limited to 2.9 mm x 2.9 mm (Section 2.4.4) due to the need to reduce the scanning angle of the MEMS scanner to achieve faster scanning frequencies. Thirdly, the instability of the MEMS scanner restricts the use of the BM-mode scan protocol

(Section 4.4.2). Therefore, depending on the specific requirements for flow imaging, scan parameters such as transverse PSF and FOV can be improved by upgrading the scanner.

The current FDML OCT system features a high A-scan rate. While this speed may exceed the requirements for quantifying blood flow velocity in skin vessels, it presents a distinct advantage in applications involving faster fluid dynamics. By adopting different scan protocols, the system can cover a wide range of detectable flow velocities. Additionally, the system enables high-speed angiographic imaging and rapid blood flow quantification in vivo, with the short acquisition time making the diagnostic process more convenient for patients.

4.6. Conclusion

We have applied the in-house FDML OCT system with a short inter-frame time of 0.33 milliseconds for quantifying blood flow velocity. A flow phantom, incorporating an 80-μm glass capillary tube, was utilized to validate the system's performance. Unhomogenized milk was infused at flow velocities ranging from 0.3 mm/s to 60 mm/s using a syringe pump, and datasets of 280 sequential B-scans at the same Y position were acquired for each velocity. Using the VISTA fitting model, the temporal autocorrelation decay or decorrelation constants (α) for all predetermined flow velocities were evaluated, revealing a strong linear correlation between the calculated decorrelation coefficients and the set flow velocities.

Subsequently, an optimized VISTA algorithm, introducing a function of automatically finding the proper time scale for decorrelation curve fitting, was applied for superficial blood flow velocity mapping in vivo under the forearm and dorsal hand skin. We employed three scan protocols of B-mode, BM-mode, and CM-mode to collect the data for OCTA and VISTA analysis. In B-mode, VISTA results (α mapping on B-scan) were obtained from the SLS study, indicating a potential impact of irritation on blood flow velocity. In BM-mode, the instability of the MEMS scanner was observed, stopping the OCTA and VISTA analysis. In CM-mode, different fundamental inter-volume scan times were discussed, and α mapping was achieved on a 2.8 mm x 0.2 mm enface vasculature of the dorsal hand with a fundamental interscan time of 8 ms. Furthermore, the datasets acquired by the MEMS scanner with B-mode or CM-mode were found centre-aligned. Based on this, a CM-mode-guided B-mode scan protocol is proposed, demonstrating the flexibility of quantifying blood flow using the B-mode dataset while utilizing CM-mode vasculature to guide vessel direction and diameter.

We later discussed the detectable skin blood vessels and the potential to estimate actual blood flow velocity using VISTA. The limitations and potential applications of the FDML OCT system were also explored, emphasizing its capability for high-speed angiographic imaging and rapid in vivo flow quantification. This chapter highlights the potential of using blood flow velocity as a biomarker for diagnosing skin conditions such as atopic dermatitis.

References

[1] R. Yuan, D. Revin, R. Byers, and S. Matcher, "Towards cutaneous blood flow velocity estimation using VISTA processing on a 1.6 MHz FDML OCT system," in *Biomedical Spectroscopy, Microscopy, and Imaging III*, 2024, vol. 13006: SPIE, pp. 77-83.

[2] J. Faught, C. Bierl, B. Barton, and A. Kemp, "Stress in mothers of young children with eczema," *Archives of disease in childhood,* vol. 92, no. 8, pp. 683-686, 2007.

[3] P. Hoskins, "A review of the measurement of blood velocity and related quantities using Doppler ultrasound," *Proceedings of the Institution of Mechanical Engineers, Part H: Journal of Engineering in Medicine,* vol. 213, no. 5, pp. 391-400, 1999.

[4] J. Naqvi, K. H. Yap, G. Ahmad, and J. Ghosh, "Transcranial Doppler ultrasound: a review of the physical principles and major applications in critical care," *International journal of vascular medicine,* vol. 2013, no. 1, p. 629378, 2013.

[5] S. Wei and J. U. Kang, "Optical flow optical coherence tomography for determining accurate velocity fields," *Optics Express,* vol. 28, no. 17, pp. 25502-25527, 2020.

[6] R. K. Wang, S. L. Jacques, Z. Ma, S. Hurst, S. R. Hanson, and A. Gruber, "Three dimensional optical angiography," *Optics express,* vol. 15, no. 7, pp. 4083-4097, 2007.

[7] R. K. Wang, Q. Zhang, Y. Li, and S. Song, "Optical coherence tomography angiography-based capillary velocimetry," *Journal of biomedical optics,* vol. 22, no. 6, pp. 066008-066008, 2017.

[8] J. Zhu, C. W. Merkle, M. T. Bernucci, S. P. Chong, and V. J. Srinivasan, "Can OCT angiography be made a quantitative blood measurement tool?," *Applied sciences,* vol. 7, no. 7, p. 687, 2017.

[9] W. Choi *et al.*, "Choriocapillaris and choroidal microvasculature imaging with ultrahigh speed OCT angiography," *PloS one,* vol. 8, no. 12, p. e81499, 2013.

[10] A. C. Werner and L. Q. Shen, "A review of OCT angiography in glaucoma," in *Seminars in ophthalmology*, 2019, vol. 34, no. 4: Taylor & Francis, pp. 279-286.

[11] V. J. Srinivasan *et al.*, "Optical coherence tomography for the quantitative study of cerebrovascular physiology," *Journal of Cerebral Blood Flow & Metabolism,* vol. 31, no. 6, pp. 1339-1345, 2011.

[12] P. Shin, W. Choi, J. Joo, and W.-Y. Oh, "Quantitative hemodynamic analysis of cerebral blood flow and neurovascular coupling using optical coherence tomography angiography," *Journal of Cerebral Blood Flow & Metabolism,* vol. 39, no. 10, pp. 1983-1994, 2019.

[13] T.-H. Tsai *et al.*, "Endoscopic optical coherence angiography enables 3-dimensional visualization of subsurface microvasculature," *Gastroenterology,* vol. 147, no. 6, pp. 1219-1221, 2014.

[14] H.-C. Lee *et al.*, "Circumferential optical coherence tomography angiography imaging of the swine esophagus using a micromotor balloon catheter," *Biomedical optics express,* vol. 7, no. 8, pp. 2927-2942, 2016.

[15] Y. Jung, Z. Zhi, and R. K. Wang, "Three-dimensional optical imaging of microvascular networks within intact lymph node in vivo," *Journal of biomedical optics,* vol. 15, no. 5, pp. 050501-050501-3, 2010.

[16] B. J. Vakoc *et al.*, "Three-dimensional microscopy of the tumor microenvironment in vivo using optical frequency domain imaging," *Nature medicine,* vol. 15, no. 10, pp. 1219-1223, 2009.
[17] J. Tokayer, Y. Jia, A.-H. Dhalla, and D. Huang, "Blood flow velocity quantification using split-spectrum amplitude-decorrelation angiography with optical coherence tomography," *Biomedical optics express,* vol. 4, no. 10, pp. 1909-1924, 2013.
[18] P. Chen *et al.*, "Velocity range estimation for liquid flow based on optical micro-angiography," *Results in Physics,* vol. 14, p. 102402, 2019.
[19] W. Trasischker *et al.*, "In vitro and in vivo three-dimensional velocity vector measurement by three-beam spectral-domain Doppler optical coherence tomography," *Journal of biomedical optics,* vol. 18, no. 11, pp. 116010-116010, 2013.
[20] R. Haindl, W. Trasischker, A. Wartak, B. Baumann, M. Pircher, and C. K. Hitzenberger, "Total retinal blood flow measurement by three beam Doppler optical coherence tomography," *Biomedical optics express,* vol. 7, no. 2, pp. 287-301, 2016.
[21] H. Ren, K. M. Brecke, Z. Ding, Y. Zhao, J. S. Nelson, and Z. Chen, "Imaging and quantifying transverse flow velocity with the Doppler bandwidth in a phase-resolved functional optical coherence tomography," *Optics letters,* vol. 27, no. 6, pp. 409-411, 2002.
[22] S. G. Proskurin, Y. He, and R. K. Wang, "Determination of flow velocity vector based on Doppler shift and spectrum broadening with optical coherence tomography," *Optics letters,* vol. 28, no. 14, pp. 1227-1229, 2003.
[23] G. Liu, A. J. Lin, B. J. Tromberg, and Z. Chen, "A comparison of Doppler optical coherence tomography methods," *Biomedical optics express,* vol. 3, no. 10, pp. 2669-2680, 2012.
[24] V. X. Yang *et al.*, "High speed, wide velocity dynamic range Doppler optical coherence tomography (Part I): System design, signal processing, and performance," *Optics Express,* vol. 11, no. 7, pp. 794-809, 2003.
[25] A. Mariampillai *et al.*, "Speckle variance detection of microvasculature using swept-source optical coherence tomography," *Optics letters,* vol. 33, no. 13, pp. 1530-1532, 2008.
[26] A. Mariampillai *et al.*, "Optimized speckle variance OCT imaging of microvasculature," *Optics letters,* vol. 35, no. 8, pp. 1257-1259, 2010.
[27] S. Guo, S. Wei, S. Lee, M. Sheu, S. Kang, and J. U. Kang, "Intraoperative speckle variance optical coherence tomography for tissue temperature monitoring during cutaneous laser therapy," *IEEE journal of translational engineering in health and medicine,* vol. 7, pp. 1-8, 2019.
[28] S. Lee *et al.*, "Selective retina therapy monitoring by speckle variance optical coherence tomography for dosimetry control," *Journal of biomedical optics,* vol. 25, no. 2, pp. 026001-026001, 2020.
[29] J. Enfield, E. Jonathan, and M. Leahy, "In vivo imaging of the microcirculation of the volar forearm using correlation mapping optical coherence tomography (cmOCT)," *Biomedical optics express,* vol. 2, no. 5, pp. 1184-1193, 2011.
[30] E. Jonathan, J. Enfield, and M. J. Leahy, "Correlation mapping method for generating microcirculation morphology from optical coherence tomography (OCT) intensity images," *Journal of biophotonics,* vol. 4, no. 9, pp. 583-587, 2011.

[31] Y. Jia *et al.*, "Split-spectrum amplitude-decorrelation angiography with optical coherence tomography," *Optics express,* vol. 20, no. 4, pp. 4710-4725, 2012.
[32] A. S. Nam, I. Chico-Calero, and B. J. Vakoc, "Complex differential variance algorithm for optical coherence tomography angiography," *Biomedical optics express,* vol. 5, no. 11, pp. 3822-3832, 2014.
[33] N. Weiss, T. G. van Leeuwen, and J. Kalkman, "Simultaneous and localized measurement of diffusion and flow using optical coherence tomography," *Optics express,* vol. 23, no. 3, pp. 3448-3459, 2015.
[34] J. Kalkman, R. Sprik, and T. van Leeuwen, "Path-Length-Resolved Diffusive Particle Dynamics in Spectral-Domain<? format?> Optical Coherence Tomography," *Physical review letters,* vol. 105, no. 19, p. 198302, 2010.
[35] N. Uribe-Patarroyo and B. E. Bouma, "Velocity gradients in spatially resolved laser Doppler flowmetry and dynamic light scattering with confocal and coherence gating," *Physical Review E,* vol. 94, no. 2, p. 022604, 2016.
[36] R. K. Wang and S. Hurst, "Mapping of cerebro-vascular blood perfusion in mice with skin and skull intact by Optical Micro-AngioGraphy at 1.3 μm wavelength," *Optics express,* vol. 15, no. 18, pp. 11402-11412, 2007.
[37] Y. Hwang *et al.*, "Retinal blood flow speed quantification at the capillary level using temporal autocorrelation fitting OCTA," *Biomedical Optics Express,* vol. 14, no. 6, pp. 2658-2677, 2023.
[38] M. Diez-Silva, M. Dao, J. Han, C.-T. Lim, and S. Suresh, "Shape and biomechanical characteristics of human red blood cells in health and disease," *MRS bulletin,* vol. 35, no. 5, pp. 382-388, 2010.
[39] A. Jääskeläinen, K.-E. Peiponen, and J. Räty, "On reflectometric measurement of a refractive index of milk," *Journal of dairy science,* vol. 84, no. 1, pp. 38-43, 2001.
[40] Y. Zhou, J. Liang, and L. V. Wang, "Cuffing-based photoacoustic flowmetry in humans in the optical diffusive regime," *Journal of biophotonics,* vol. 9, no. 3, pp. 208-212, 2016.
[41] R. Yuan, R. Byers, D. Revin, and S. Matcher, "Rapid measurement of epidermal thickness with a 1.6 MHz FDML OCT system," in *Biomedical Spectroscopy, Microscopy, and Imaging III*, 2024, vol. 13006: SPIE, pp. 252-257.
[42] F. Tanaka *et al.*, "Developing quantitative analysis program of blood flow velocity according to vessel diameter for neovascular age-related macular degeneration using OCTA-VISTA," *Scientific Reports,* vol. 14, no. 1, p. 16352, 2024.
[43] M. W. Law and A. C. Chung, "Three dimensional curvilinear structure detection using optimally oriented flux," in *Computer Vision–ECCV 2008: 10th European Conference on Computer Vision, Marseille, France, October 12-18, 2008, Proceedings, Part IV 10*, 2008: Springer, pp. 368-382.

5. Further Development of FDML OCT

5.1. Summary

Although the previous chapters show the ability to detect skin structural and vascular information using the in-house FDML OCT system, this OCT system can do more than that. This chapter introduces two other applications of the FDML OCT. First, this OCT system is used to acquire volume scans to generate enface images for repeatability measurements and skin topographical matching. Second, the system is applied to align and test an in-house colposcopic scanning probe.

5.2. Skin Topographical Matching

OCT normally has an mm^2 size scanning area on the skin. The skin features in this area can be extracted for biometric recognition. One typical application is fingerprint matching using OCT to extract 3D biometric features [1-6]. The fingerprint pattern is considered unique. However, there is no skin matching study on accurately tracking skin lesions or treatment on such an mm^2 size area [7]. In practice, it is difficult for doctors or patients to remember the precise treated or scanned position on the skin. Although methods such as using a marker pen can be useful for marking the skin site, the ink is too easy to remove. Water-soluble inks can be washed off immediately, while "permanent" inks can degrade when exposed to solvents (e.g., paraffin), which are often major components of the skin creams being evaluated.

Similar to fingerprint recognition, OCT as a non-invasive imaging technique can record the skin pattern on a specific area. By comparing the skin patterns on different

volume scans and calculating their similarity, the original scanned position can be found. Additionally, a volume scan of 2.8 mm x 2.8 mm only takes approximately 0.1 seconds using our FDML OCT system. This can enable real-time rapid matching for the ease of patients especially for children.

This section first introduces the data preparation for skin topographical matching and discusses the repeatability of the measurements. After obtaining the volume datasets, intensity-based projection is applied to generate enface images. Two algorithms of fingerprint matching and MATLAB computer vision toolbox are separately used to extract features for matching from the enface images. The corresponding results are shown and discussed although this section only demonstrates the initial validation of our hypothesis.

5.2.1. Skin Data Preparation

5.2.1.1.Scan Protocol

Figure 5.1(a) shows a photo marking three scanned locations on the dorsal hand for scanning using the FDML OCT system. **Figure 5.1**(b-d) shows the enlarged photos from these three locations indicating the rough scanned areas in red boxes. Each area corresponds to a 2.8 mm x 2.8 mm volume scan with a 10-micron step size in both the X and Y axes. The X-axis scanning frequency of 3 kHz enables the acquisition time of 0.1 seconds for each volume scan.

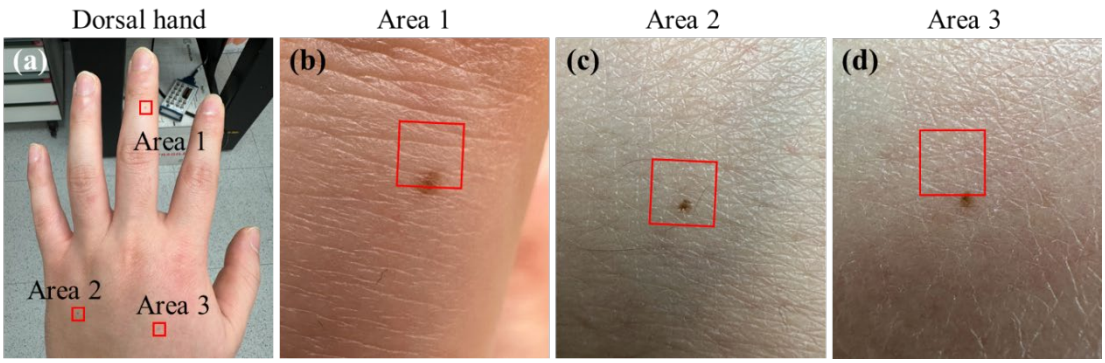

Figure 5.1: (a) Photo marking three scanned locations, corresponding to three volume scans of 2.8 mm x 2.8 mm on the dorsal hand acquired by the FDML OCT system. (b-d) Enlarged photos from these three locations, indicating the rough scanned areas in red boxes.

5.2.1.2. Data Processing for Generating OCT Enface Images

After obtaining the volume scan on the three areas (**Figure 5.2**(a-c)), the three-dimensional dataset is processed to generate two-dimensional enface images of the skin (**Figure 5.2**(d-f)). This can be achieved by averaging the intensity values of each A-scan along the Z direction to get the enface mean intensity projection. From **Figure 5.2**(d-f), we can identify the skin furrows as shown in **Figure 5.2**(a-c). **Figure 5.2**(g-i) show the B-scans in the locations marked in red dashed line in **Figure 5.2**(d-f). The green lines show the detected skin surfaces while the yellow arrows indicate the skin furrows. In the skin furrow positions, the corresponding A-scans have fewer pixels with high brightness hence it is darker in the enface image when averaging.

Additionally, the enface image can be immediately presented by our FDML control software as illustrated in Chapter 2. The current processing time to show an enface image is 2 to 3 seconds which is limited by the current old PC configuration. This

processing time can be speeded up when upgrading the PC configuration for real-time enface imaging or even enface matching.

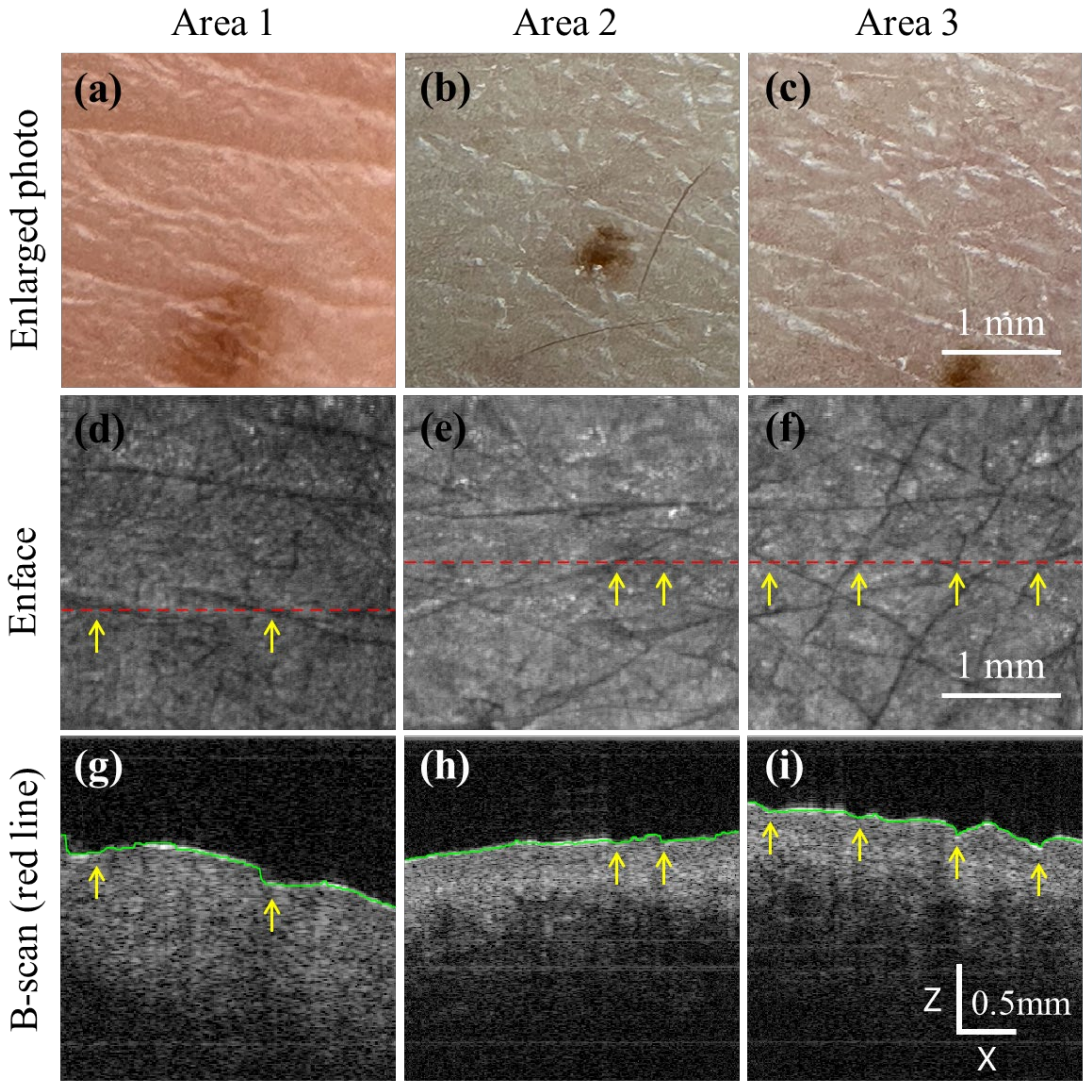

Figure 5.2: (a-c) 2.8 mm x 2.8 mm rough scanned areas in the three enlarged photos of **Figure 5.1**(b-d). (d-f) Enface mean intensity projections of the skin achieved by averaging the intensity values of each A-scan along the Z direction under the FDML OCT system. (g-i) B-scan images in the locations marked in red dashed line in (d-f) under the FDML OCT system. Yellow arrows indicate the skin furrows.

5.2.1.3. Raw Data Collection – Repeatability Measurements

To assess the repeatability of OCT measurements for skin matching, **Figure 5.3** shows the enface images taken on the rough same areas as the three areas in **Figure 5.2** for 128 days. The imaging location was guided by skin surface landmarks i.e. moles in **Figure 5.2**(a-c), and then finetuned using OCT visible enface landmarks i.e. skin furrows. The skin areas were matched as closely as possible, and the OCT engine settings remained the same over the 128 days. As shown in **Figure 5.3**, for each imaging area, the enface skin pattern in each day remains recognisable and matches quite well although the intensity of those images varies in different days. For each measurement, the hand was placed in the sample arm of the FDML OCT system and adjusted by the operator. The height and orientation of the hand cannot be maintained. Hence, the enface images in the same area might have different geometric transformations. Also, this can cause different amplitudes of the back-scattered optical signal from the same area. The intensity difference might be also caused by the optical re-alignment of the FDML OCT system or the fluctuation of the FDML laser.

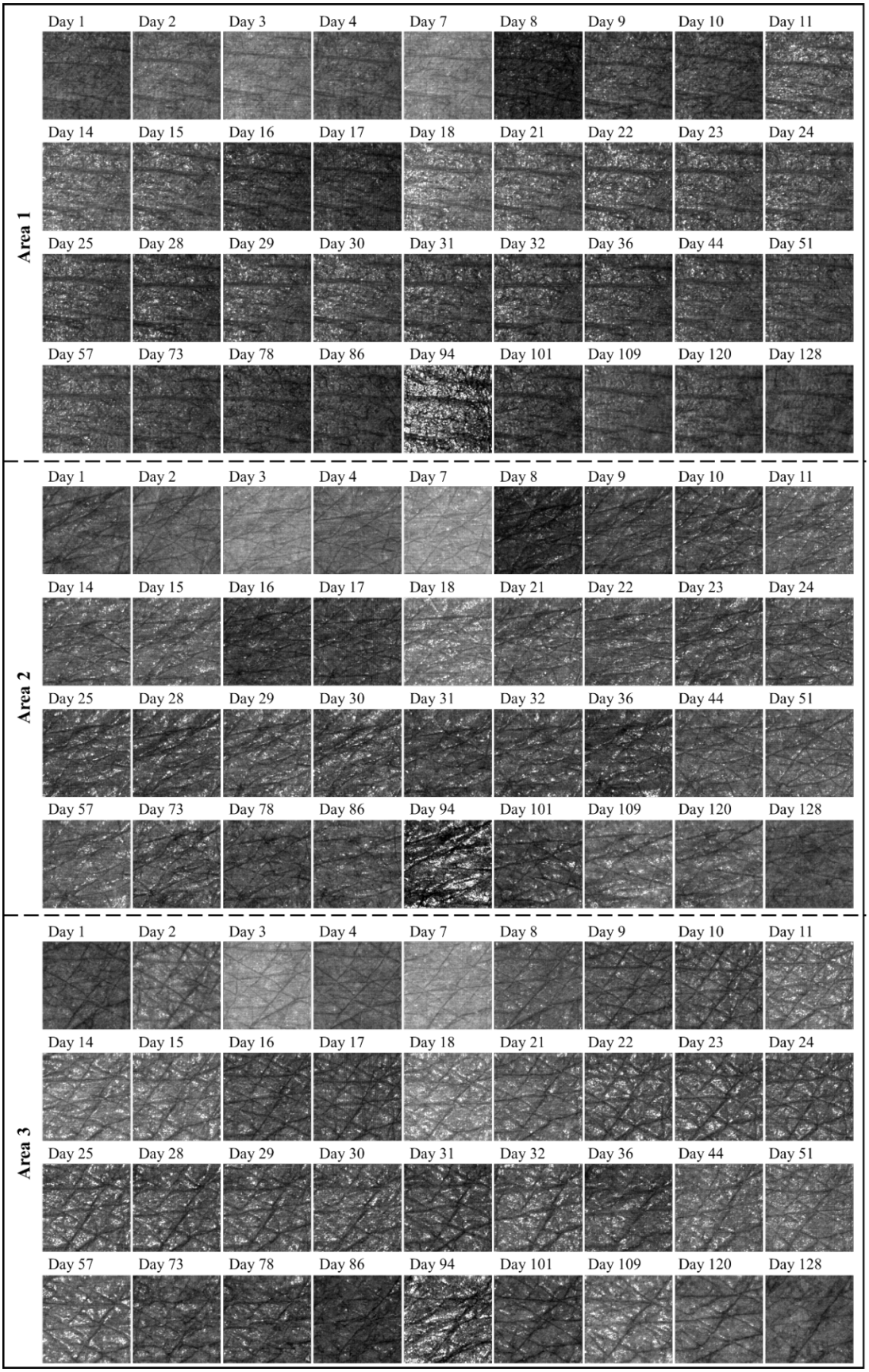

Figure 5.3: Repeated enface mean intensity projections in three areas of 2.8 mm x 2.8 mm on dorsal hand (**Figure 5.2**) for 128 days under FDML OCT. Same greyscale.

5.2.1.4.Enface Image Processing for Matching

After collecting the raw volume scans for 128 days, four imaging processing ways for preparing the enface images for matching are shown in **Figure 5.4**. **Figure 5.4**(a) and (b) show the typical raw enface images by averaging the intensity across different depth ranges from 0 to 4.9 mm and from 0 to 2 mm. **Figure 5.4**(c) and (d) are the enface images after applying image binarization and a 5-by-5 two-dimensional median filter to **Figure 5.4**(a) and (b). These four types of enfaces will be used as input for skin matching.

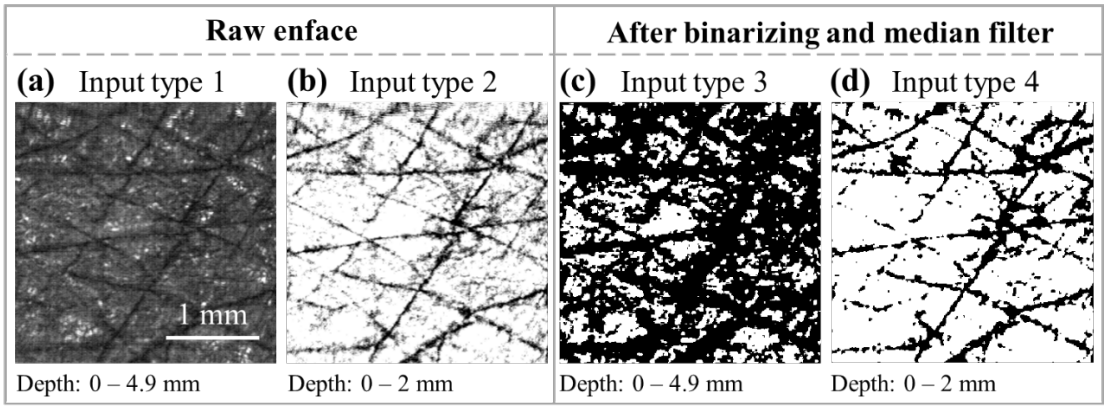

Figure 5.4: Enface image processing for topographical matching. (a) Typical raw enface mean intensity projection by averaging the intensity across the depth range from 0 to 4.9 mm. (b) Raw enface mean intensity projection averaged from 0 to 2 mm. (c-d) Corresponding enface images after applying image binarization and a 5-by-5 two-dimensional median filter to (a-b).

5.2.2. Skin Matching using Fingerprint Match Tool

Fingerprint matching as a technique of pattern recognition has been widely researched and used in many areas such as mobile payment, access control, and personal

identification [5, 6]. Similar to the fingerprint, the enface images generated from our OCT datasets also show clear skin patterns (furrows). Hence, in this section, we directly apply the fingerprint-matching algorithms for OCT skin matching.

5.2.2.1.Method

Most fingerprint-matching algorithms are developed based on minutiae matching [3, 8]. Here, a simple MATLAB fingerprint-matching tool from GitHub is used for finding the minutiae of the enface skin pattern [9]. **Figure 5.5** shows the technical route for fingerprint matching using this MATLAB tool. The first step is to preprocess the source and target fingerprint images including image enhancement, binarization, and thinning. Then the processed images are used for feature extraction i.e. finding minutiae. Finally, the minutiae images are registered for further calculating the similarity score. Some arguments in this MATLAB fingerprint matching algorithm have been slightly modified for our OCT enface skin pattern matching.

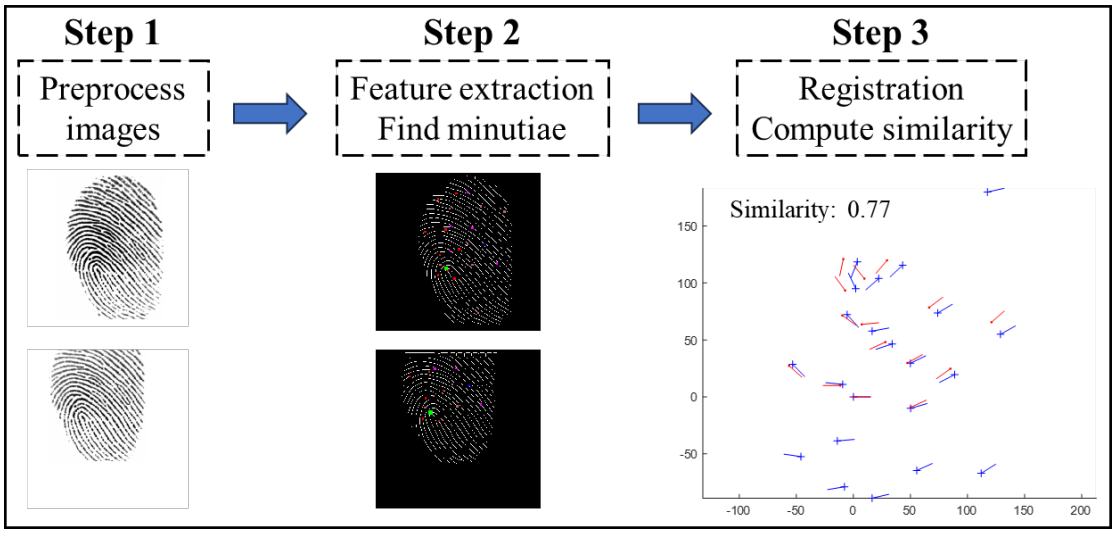

Figure 5.5: Technical route of a MATLAB fingerprint-matching tool from GitHub for finding the minutiae of the enface skin pattern [9].

5.2.2.2. Results

To validate the fingerprint matching tool for OCT skin matching, it was applied to the OCT enface images acquired in Section 5.2.1. **Figure 5.6** shows the skin matching results for three types of input enface images. All the source and target enface images in the three types were processed from the same two repetitions of volume scans in area 3 on day 16 in **Figure 5.3**. The measured similarity scores are 0.70, 0.53, and 0.40 for input types 1, 2, and 4, respectively. Input type 1 achieved the highest matching score for the repeats taken in area 3 on the same day.

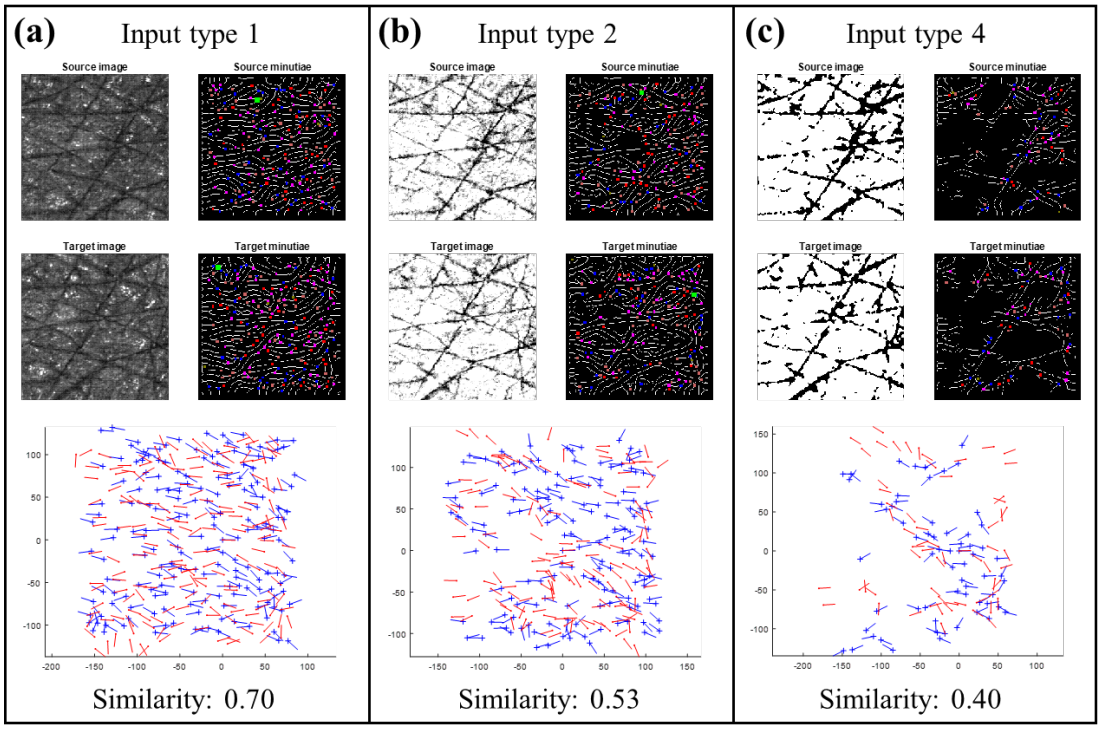

Figure 5.6: (a) Skin matching results by the fingerprint matching tool for input type 1 source and target images generated from the same two repetitions of volume scans in area 3 on day 16 in **Figure 5.3**, showing a measured similarity score of 0.70. (b) Corresponding skin matching results for input type 2, showing a measured similarity score of 0.53. (c) Corresponding skin matching results for input type 4, showing a measured similarity score of 0.40.

While **Figure 5.6** shows the matching results between skin enface images taken on the same day, **Figure 5.7** shows the matching results for images taken on different days but from the same area. **Figure 5.7**(a) shows the source image taken on day 1 and the target image taken on day 15, both from area 1 in **Figure 5.3**. **Figure 5.7**(b) shows the calculated similarity of 0.66, which is comparable to the score in **Figure 5.6**(a). Despite the images in **Figure 5.7**(a) having different brightness levels, the similarity score between the skin patterns taken on different days remains reasonably high.

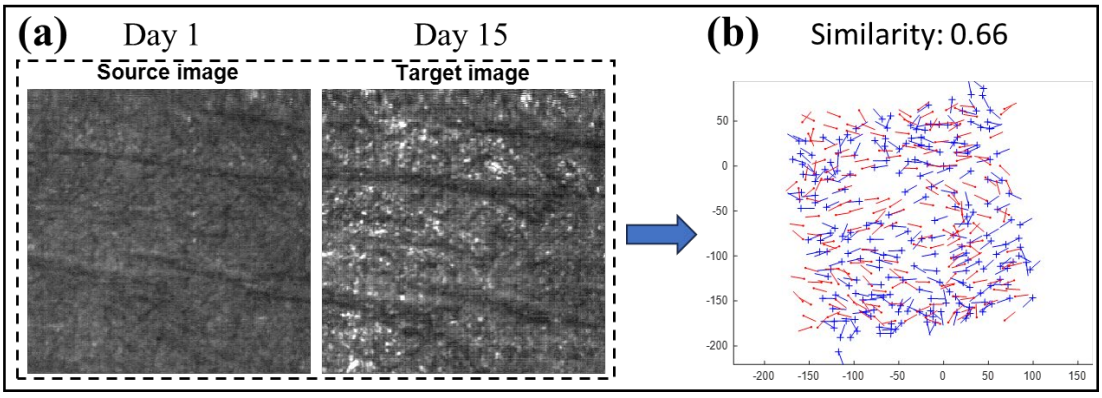

Figure 5.7: (a) Input type 1 source image (day 1) and target image (day 15) from area 1 in **Figure 5.3**. (b) Calculated similarity of 0.66.

Lastly, we tried the matching between the enface images taken in different areas. **Figure 5.8**(a) shows the skin patterns from area 3 and area 2. **Figure 5.8**(b) gives a similarity of 0.6, which is very close to the similarity in **Figure 5.7**. This result may indicate a false matching between different skin patterns.

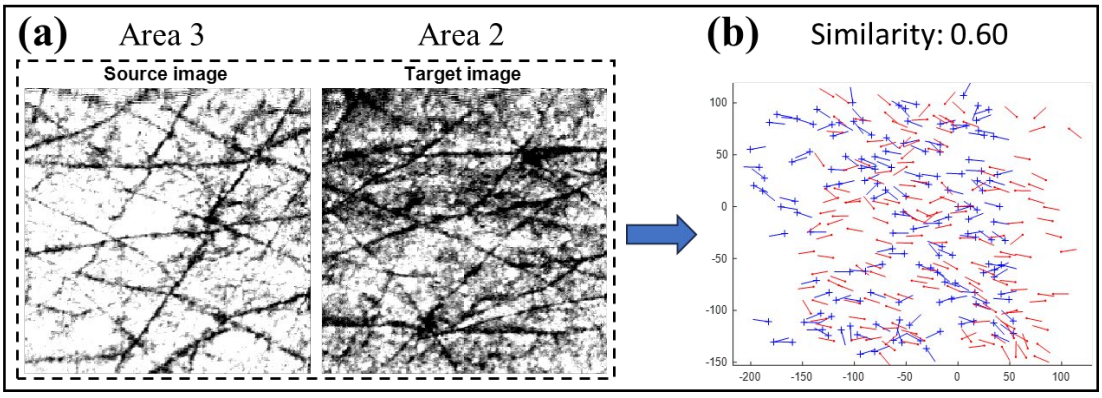

Figure 5.8: (a) Input type 2 source image (area 3) and target image (area 2) on Day 16 from **Figure 5.3**. (b) Calculated similarity of 0.6.

5.2.2.3. Discussion

Although the above similarity calculations indicate it is not very reliable for matching the enface skin patterns using the fingerprint matching tool, it still shows the potential to detect the minutiae and measure the similarities for OCT skin enface images. This algorithm needs to be adjusted to properly extract the features on OCT skin enface images and some parameter settings need to be finely set in future processing.

Additionally, the skin enface images do not have a good contrast and clear pattern as the fingerprint. A better image preprocessing method may be developed to remove the noisy and unnecessary information from the skin enface images and only leave the skin patterns.

Another issue with using this fingerprint-matching tool is the calculation speed. The current skin enfaces have too many minutiae, which takes 3 s for feature extracting, 3-25 s for similarity calculations using a desktop computer with GPU acceleration, and ~120 s for similarity calculations using only the computer. It is more time-consuming

than fingerprint matching. The feature extraction step needs to be optimised to detect fewer but key minutiae for more efficient matching.

5.2.3. Skin Matching using Feature Detection and Extraction Functions

Apart from a quick trial for skin matching using the above fingerprint matching tool, another solution using feature detection and extraction functions in MATLAB computer vision toolbox is tried and discussed in this section.

5.2.3.1.Method

This MATLAB Computer Vision Toolbox from MathWorks provides the functions of feature detection, extraction, and matching [10]. Since the OCT enface skin images mainly involve geometric transformation acquired in the same skin area, this toolbox can be used to transform the distorted image back to the source image i.e. match the two input images to the same position if the two images are from the same area.

Figure 5.9 shows the technical route of processing the OCT enface images for skin matching. The first step shows two typical enface images taken in the same area 3 and same day 16 as the inputs. Then the features on these two inputs will be detected and matched for estimating the transformation between these two enface images. Lastly, the toolbox will solve for the scale and rotation angle of the target image from this transformation and recover the target image to the status of the source image. The scale of 0.98 means that the recovered target image is obtained by reducing the target image by 0.98 times. The rotation angle of 1.28 means rotating the target image 1.28 degrees to the left (positive values).

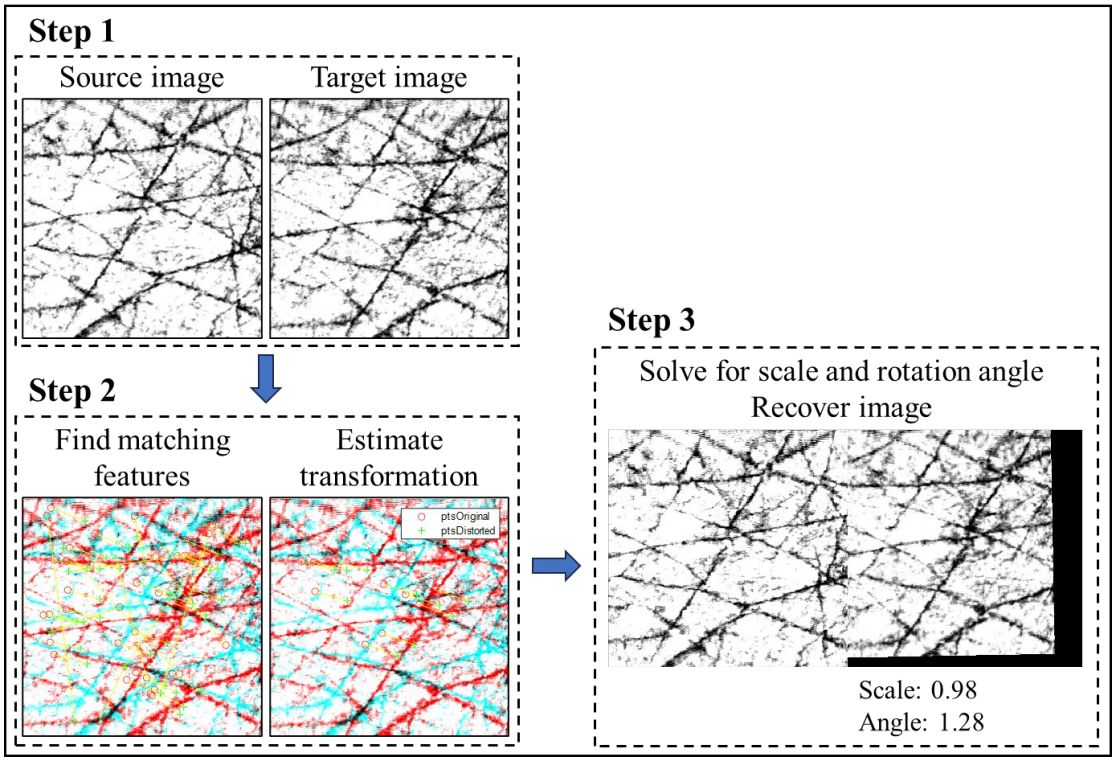

Figure 5.9: Technical route of an algorithm based on MATLAB Computer Vision Toolbox from MathWorks including the functions of feature detection, extraction, and matching [10], for processing the OCT enface images for skin matching.

5.2.3.2.Results

First, this feature detection and extraction algorithm is applied for skin matching between the enface images taken in the same area and same day.

1) Skin matching for images taken on the same day

Figure 5.10(a) and (b) show the matching results between two raw enface images from area 3 and day 16 using type 1 inputs while **Figure 5.10**(c) and (d) show the results for type 3 inputs i.e. the median-filtered binary images of **Figure 5.10**(a). **Figure 5.10**(b) shows an estimated scale of 0.94 and rotation angle of -77.31 degrees for the type 1 inputs while **Figure 5.10**(d) shows a scale of 0.99 and rotation angle of 2.28 degrees

for the type 3 inputs. We can find that the toolbox gives a better match for the median-filtered binary skin enface images.

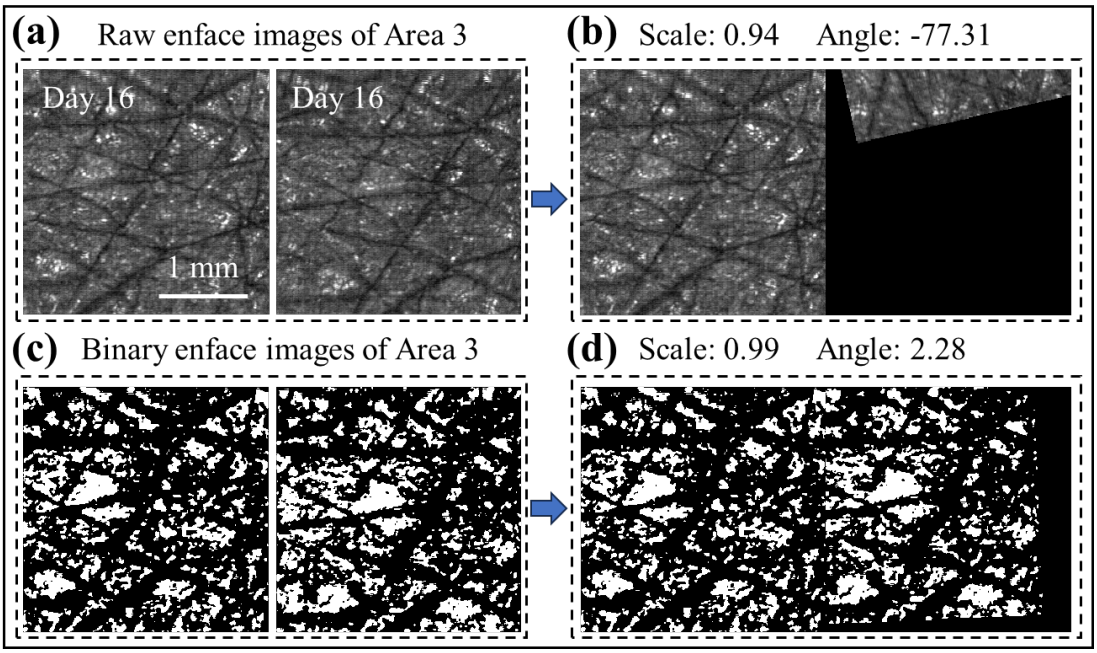

Figure 5.10: (a) Type 1 inputs of two raw enface images from area 3 and day 16 in **Figure 5.3**. (b) Matching results (scale and rotation angle) between two input images in (a) by the feature detection and extraction algorithm. (c) Type 3 inputs of the median-filtered binary images of (a). (d) Corresponding matching results of (c).

Additionally, the matching results are shown for enface images from area 1 and area 2 on the same day in **Figure 5.11**. Type 3 input enface images are used in **Figure 5.11**(a), giving a scale of 1.02 and rotation of 1.37 degrees for the transformation in **Figure 5.11**(b). The contrast of images in **Figure 5.11**(c) was enhanced by histogram equalization, showing a scale of 1.09 and a rotation angle of -11.35 degrees. Both of these two matching results demonstrate a good image recovery.

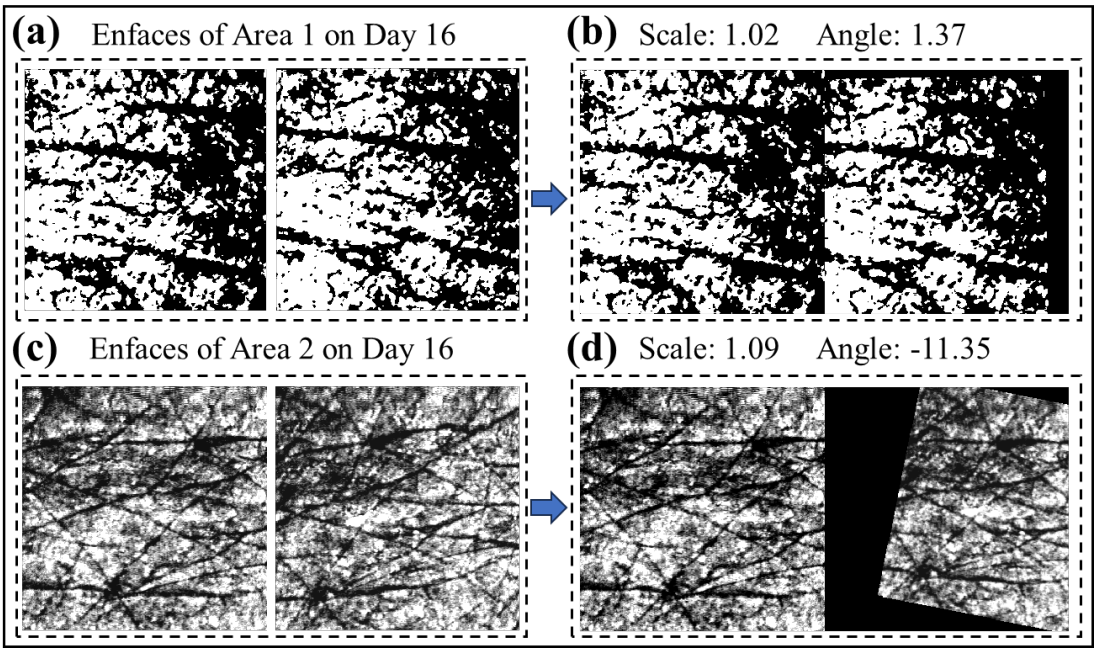

Figure 5.11: (a) Type 3 inputs of two median-filtered binary images from area 1 and day 16 in **Figure 5.3**. (b) Matching results (scale and rotation angle) between two input images in (a) by the feature detection and extraction algorithm. (c) Type 2 inputs of two raw enface images from area 2 and day 16 after histogram equalization. (d) Corresponding matching results of (c).

2) Skin matching for images taken on different days

Figure 5.12 shows the skin matching results for the enface images taken on different days using this toolbox. **Figure 5.12**(a) shows the type 1 raw enface images from area 3 taken on day 1 and day 16. **Figure 5.12**(b) matches the brightness between the two images of **Figure 5.12**(a) by matching their histograms. However, there are no transformation results found for both inputs in **Figure 5.12**(a) and (b). **Figure 5.12**(c) shows the matching results for median-filtered binary images of **Figure 5.12**(b) with a scale of 1.52 and rotation angle of -33.18 degrees. Although the transformation is found, the large rotation angle indicates a bad matching.

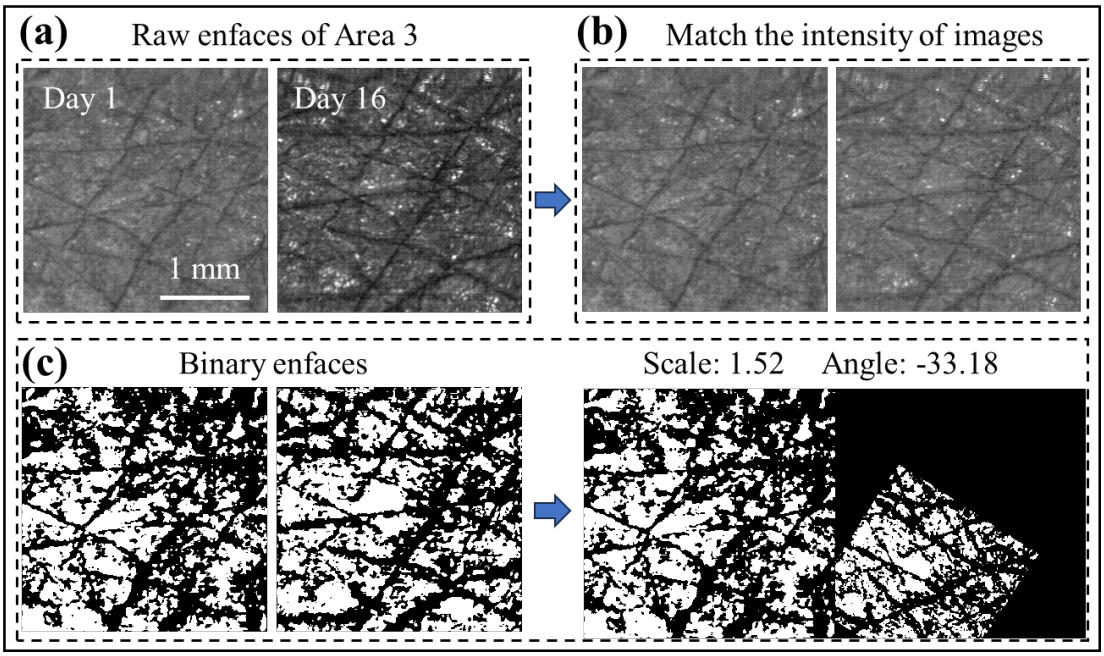

Figure 5.12: (a) Type 1 inputs of two raw enface images (Day 1 and 16) from area 3 in **Figure 5.3**. (b) Two images of (a) after brightness matching. (c) Type 3 inputs of two median-filtered binary images of (b). (d) Matching results (scale and rotation angle) between two input images in (c) by the feature detection and extraction algorithm.

3) Skin matching for images taken in different areas

Lastly, to validate the ability to identify different patterns using this toolbox, **Figure 5.13**(a) provides two enface images from area 2 and area 3 for skin matching. **Figure 5.13**(b) shows a scale of 5.53 and a rotation angle of 170.99 degrees. The ridiculously large scale and rotation angle indicate the mismatch between the images from different areas, meaning that the unmatched skin patterns can be identified by setting a threshold of scale or rotation angle.

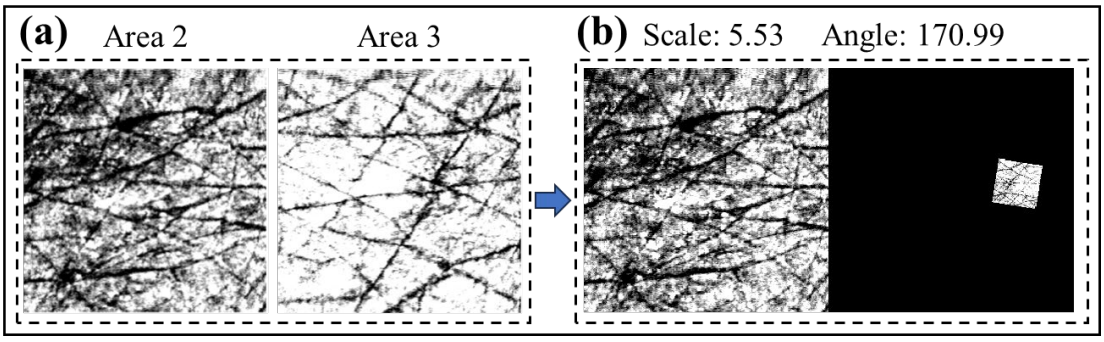

Figure 5.13: (a) Type 2 inputs of two raw enface images (Area 2 and 3). (b) Matching results (scale and rotation angle) between two input images in (a) by the feature detection and extraction algorithm.

5.2.3.3. Discussion

Compared with the fingerprint matching algorithm, the MATLAB feature detection and extraction algorithm shows a better and more reliable analysis of skin matching. However, the matching between images taken on different days is still challenging. The raw enface images need to be further processed to extract the key pattern or contour information. Additionally, after finding the transformation, the overlapping area between the images can be estimated according to the scale and rotation angle. Hence, the similarity can be calculated in the next step as the ratio between the overlapping area and the original image size.

5.2.4. Optimising Enface Image Processing for More Efficient Skin Topographical Matching

The previous sections presented the initial data processing and results of a skin topographical matching study. Using simple image processing techniques (Section 5.2.1.4), the raw or median-filtered binary images of enface intensity mean projections from OCT volume scan datasets were used as input for skin matching with a MATLAB fingerprint matching tool and a feature detection and extraction algorithm based on the MATLAB Computer Vision Toolbox. However, these simply processed input images exhibited very noisy skin surfaces and unclear skin patterns, leading to unreliable matching with the fingerprint matching tool. Although the computer-vision-based algorithm achieved better matching, it remains challenging to match skin patterns between images taken on different days. To address this issue and enable more efficient skin matching, we have developed an optimised image processing algorithm for generating input images with refined clean skin surfaces.

5.2.4.1. Optimised Image Processing Algorithm for Skin Matching

Figure 5.14 shows the schematic of the optimised input enface image processing algorithm for skin topographical matching developed in MATLAB. Clearer skin topographical features with improved SNR on the skin surface can be extracted by the following steps:

1) Raw enface generation: The first step is to obtain the enface mean intensity projection from a volume scan dataset on skin by the FDML OCT system (refer to Section 5.2.1.2).
2) Skin surface detection: An automatic skin layer segmentation algorithm (Section 3.3.1) is used to detect the skin surface (green) for each B-scan in this

volume. Then this skin surface is median filtered using a large Kernel size (e.g. 50 pixels).

3) Enface surface projections: After surface detection for all B-scans in the volume scan, an enface image of surface projection can be obtained for both raw and median-filtered skin surfaces. A one-dimensional median filter of 50 pixels needs to be applied to the Y axis of the median-filtered enface surface projection. The Gray value in each XY pixel corresponds to the depth value of this pixel on the detected surface.
4) Surface subtraction: By subtracting the enface surface projection from the median-filtered enface surface projection or inversely, the enface images showing skin ridges or furrows can be obtained. As shown in Step 2, skin ridges are defined as the parts in the raw surface (green) higher than the median-filtered surface (yellow) i.e. negative values of the depth difference. Skin furrows are defined as the parts in the raw surface (green) lower than the median-filtered surface (yellow) i.e. positive values of the depth difference.
5) Image sharpening: An image sharpening function in MATLAB is used to improve the contrast of the enface skin ridge or furrow image.
6) Image rescaling and binarization: The sharpened enface skin ridge or furrow image is rescaled to 0 – 1, followed by an image binarization function in MATLAB.
7) Median filtering: Lastly, a two-dimensional median filter is applied to the binary enface skin ridge or furrow image to remove the speckle noise.

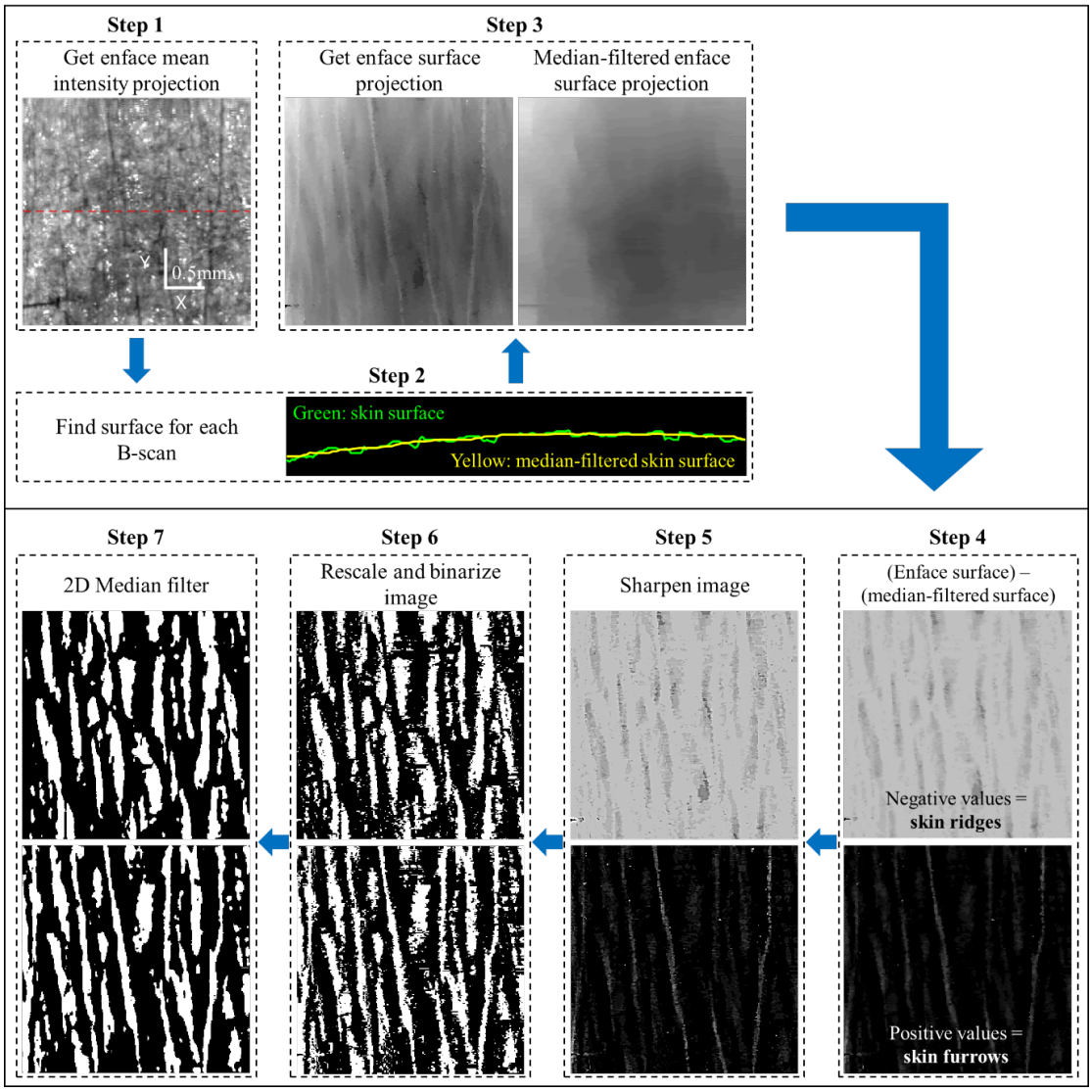

Figure 5.14: Schematic of the optimised enface image processing algorithm developed in MATLAB for generating the input for skin topographical matching.

To validate this optimized image processing algorithm, **Figure 5.15** compares the surface pattern (furrows and ridges) along the Y-axis central line of the enface image with the detected surface in the corresponding Y-axis central B-scan image. **Figure 5.15**(a) presents the enface mean intensity projection of a 2.8 mm × 2.8 mm volume scan of dorsal hand skin acquired with the FDML OCT system. **Figure 5.15**(b) and (c) display the sharpened enface skin furrow and ridge images derived from **Figure 5.15**(a),

with cyan and magenta arrows indicating furrows and ridges along the red line, respectively. **Figure 5.15**(d) shows the raw intensity B-scan image along the Y-axis central line (red dashed line) of **Figure 5.15**(a), highlighting the detected skin surface (green). **Figure 5.15**(e) and (f) present the same detected skin surface with cyan and magenta arrows marking the furrows and ridges, respectively, on the green surface.

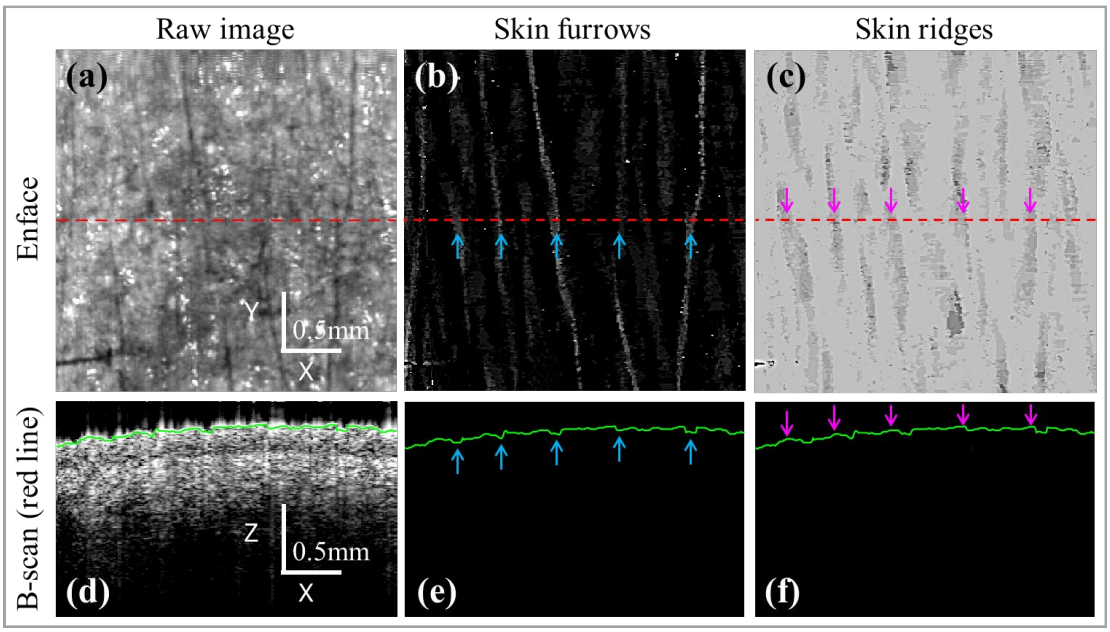

Figure 5.15: Comparison between the surface pattern (furrows and ridges) along the Y-axis central line of the enface image and the detected surface in the corresponding Y-axis central B-scan image. (a) Enface mean intensity projection of a 2.8 mm × 2.8 mm volume scan of dorsal hand skin acquired using the FDML OCT system. (b-c) Sharpened enface skin furrow and ridge images derived from (a) by the optimised enface image processing, with cyan and magenta arrows indicating furrows and ridges along the red line. (d) Raw intensity B-scan image along the Y-axis central line (red dashed line) of (a), with the detected skin surface (green). (e-f) Same detected skin surface as in (d) with cyan and magenta arrows marking the furrows and ridges on the green surface.

It can be observed that the X positions of all arrows in the B-scan surface (green) align precisely with the X positions of the arrows in the enface images. This alignment confirms that the optimized enface image processing algorithm accurately generates enface images, clearly depicting skin furrows and ridges.

5.2.4.2. Application of the Optimised Process to Enface Images

To check if the input images produced by the optimised image processing algorithm can contribute to better matching, **Figure 5.16** compares the enface images generated from four volume scans with different FOVs acquired by the FDML OCT system. **Figure 5.16**(a) shows the enface mean intensity projections of dorsal hand skin on scanning areas of 2.8 mm x 2.8 mm, 2.8 mm x 1 mm, 2.8 mm x 0.5 mm, and 2.8 mm x 0.2 mm, respectively (from **Figure 4.12**). The hand was trying to be kept stationary during the four different scans. We can find that the Y-axis centres (red dashed line) of those four enface images are almost aligned. **Figure 5.16**(b-d) display the corresponding enface surface projections, enface skin furrow images, and binary enface skin furrow images of **Figure 5.16**(a) processed by the optimised image processing algorithm. Compared with the noisy surfaces in **Figure 5.16**(a), **Figure 5.16**(b-d) with cleaner surface patterns show more obvious topographical matching among those surfaces in the Y centre, especially **Figure 5.16**(d) with much higher image contrast than **Figure 5.16**(b) and (c).

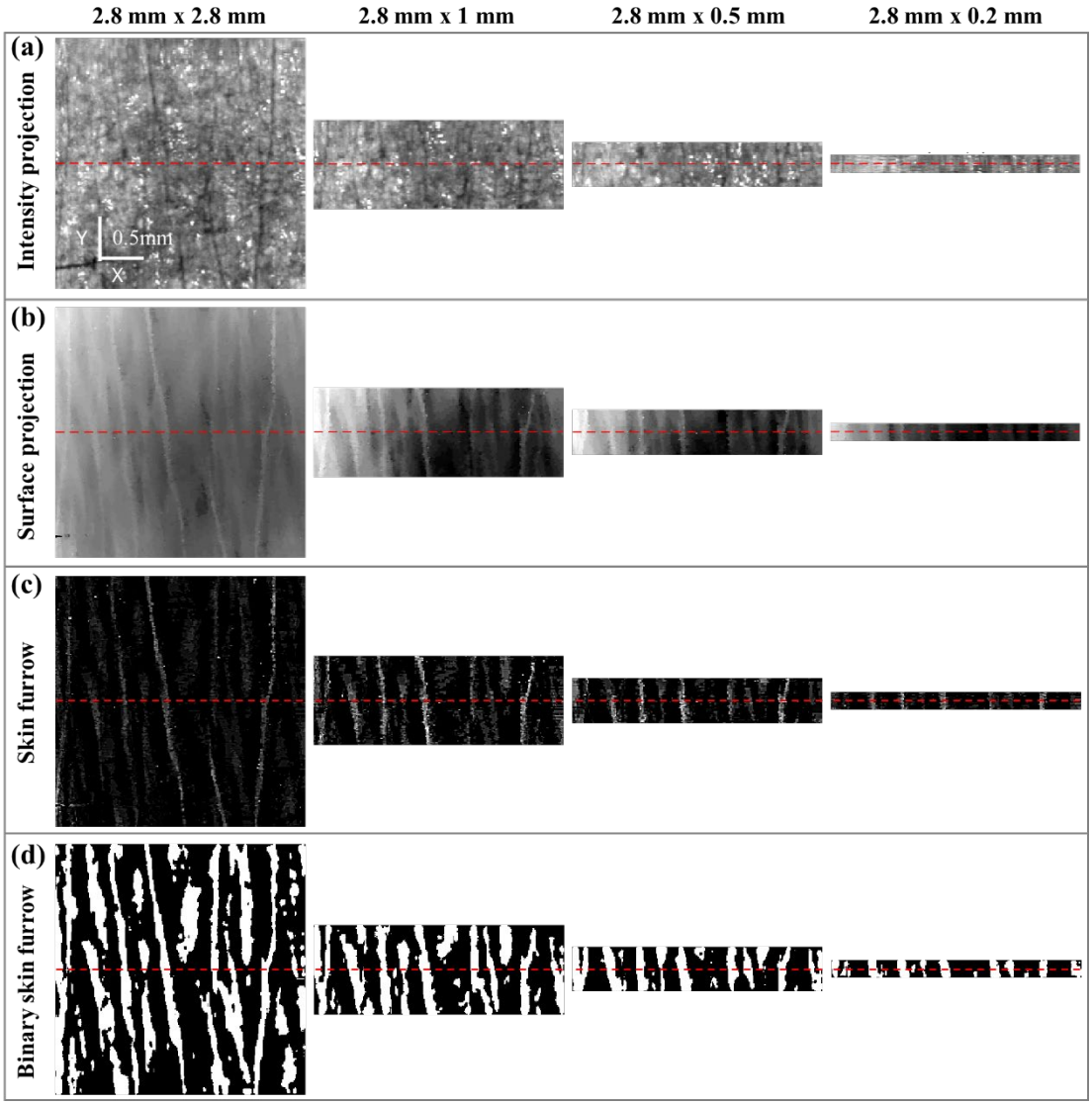

Figure 5.16: Comparison of the enface images generated from four volume scans with different FOVs at the same site acquired by the FDML OCT system. (a) Enface mean intensity projections of dorsal hand skin on scanning areas of 2.8 mm x 2.8 mm, 2.8 mm x 1 mm, 2.8 mm x 0.5 mm, and 2.8 mm x 0.2 mm, respectively (from **Figure 4.12**). The hand was trying to be kept stationary during the four different scans. (b-d) Corresponding enface surface projections, enface skin furrow images, and binary enface skin furrow images of (a) processed by the optimised image processing algorithm.

While **Figure 5.16** demonstrates the potential of achieving more efficient matching between skin enface images in different FOVs, **Figure 5.17** compares the 2.8 mm x 2.8 mm enface images of dorsal hand skin generated from two volume scans at the same site acquired by the FDML OCT system. **Figure 5.17**(a-c) show the enface mean intensity projection, enface skin furrow image, and binary enface skin furrow image of the first volume scan repeat processed by the optimised enface image processing algorithm. **Figure 5.17**(d-f) display the corresponding enface images of the second volume scan repeat. Comparing **Figure 5.17**(a-c) with **Figure 5.17**(d-f), we can obtain the same conclusion that the binary enface skin furrow image can serve as an input for better topographical matching due to the cleaner and higher contrast skin features.

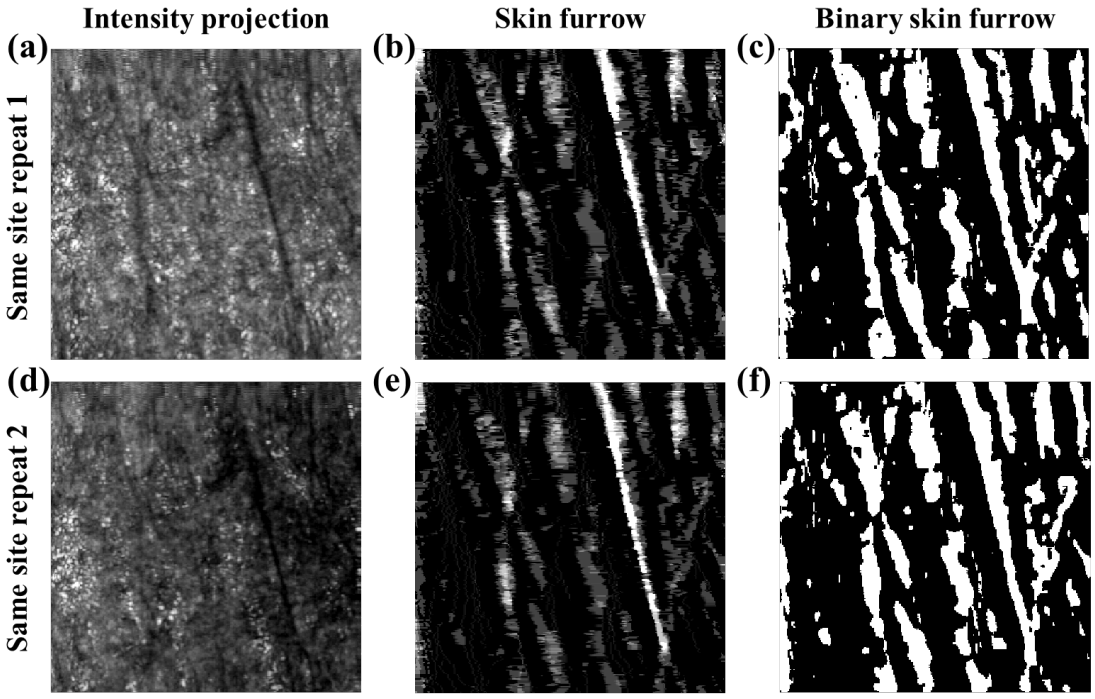

Figure 5.17: Comparison of enface images generated from two volume scans at the same 2.8 mm x 2.8 mm site on dorsal hand skin acquired by the FDML OCT system. (a-c) Enface mean intensity projection, enface skin furrow image, and binary enface skin furrow image of the first volume scan processed by the optimised enface image processing algorithm. (d-f) Corresponding enface images of the second volume scan.

To further demonstrate the suitability of binary skin furrow images for topographical matching, the feature detection and extraction algorithm was applied to the enface image pairs shown in **Figure 5.17**. The estimated rotation angles and scale values for each image type are presented in **Figure 5.18**. Among the three image formats, the binary skin furrow image pairs produced the most accurate and consistent transformation results, confirming their advantage for reliable matching due to their enhanced contrast and reduced background interference.

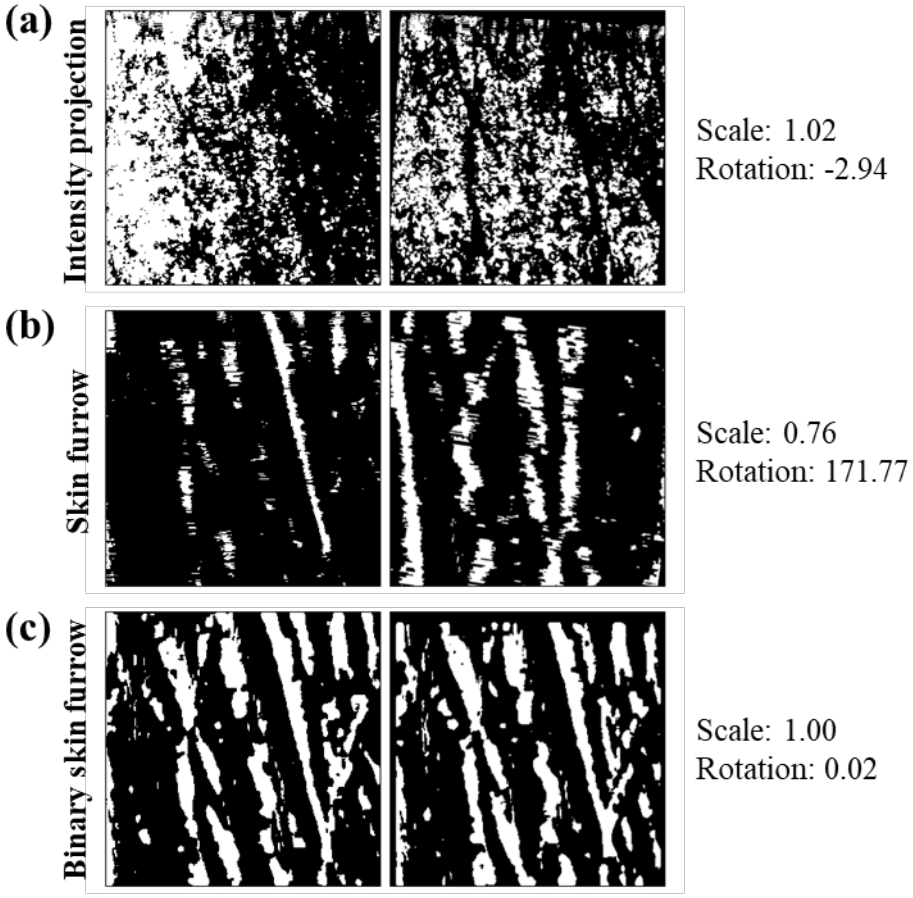

Figure 5.18: Matching results of enface image pairs from **Figure 5.17** using feature detection and extraction algorithm. Each row shows results for a different image type: (a) mean intensity projections, (b) skin furrow images, and (c) binary skin furrow images. Binary images yield the most consistent transformation results.

5.2.5. Discussion

Due to the time limit of my PhD, Section 5.2 only presents the initial algorithm development for skin topographical matching. With basic data processing for generating the enface mean intensity projections as input images from FDML OCT volume scans, both the fingerprint matching tool and the feature detection and extraction algorithm show potential for calculating similarities in skin matching. However, the current data processing produces images that are too noisy and display unclear skin patterns, leading to imperfect matching.

To address this issue, an optimised enface image processing algorithm is proposed to reduce speckle noise on the skin surface and refine the skin patterns (ridges and furrows). This algorithm has been applied to refine the enface mean intensity projections, resulting in cleaner enface ridge or furrow images, demonstrating the potential for more efficient skin topographical matching. The new inputs generated from this optimised enface image processing algorithm will be used for matching, and skin matching algorithms will be optimised in future work.

Additionally, the skin matching is not limited to our FDML OCT system and can be applied to different OCT systems and applications. Although our FDML OCT system provides a limited field of view for skin matching, its rapid scanning speed can enable fast volume acquisition and quick matching.

5.3. Colposcopic Scanning Probe Imaging using FDML OCT

In addition to skin matching, the FDML engine was used to assess the alignment and key performance metrics of an in-house designed colposcopic probe. The probe was designed to provide handheld and portable OCT scanning of cervical tissue structure assessment in vivo. This probe is developed by my colleague and its design and simulation has been published in [11].

In this section, we only show the brief characteristics and imaging performance of the probe with assistance of our FDML OCT system. More details of the probe and relevant work will be published in my colleague's publications and PhD thesis.

5.3.1. Testing Colposcopic Scanning Probe by FDML OCT

To test the probe, it was connected to our FDML OCT system first with replacing the sample arm optics. The signal output port of the 50:50 fibre coupler in the interferometer emits the light into the probe (refer to the FDML OCT schematic in Chapter 2). A specifically designed reference arm optics also replaces the FDML reference arm for better dispersion compensation. The FDML laser, rest of the interferometer, data acquisition unit, and the software remains the same.

This probe employs a low-speed MEMS scanner (A8L2.2, Mirrorcle Technologies Inc.) with a resonate frequency at 364 Hz. Compared to the MEMS scanner used in our FDML OCT, this low-speed MEMS runs at a slower scanning frequency but provides a larger scanning range and mirror size. Before running this low-speed MEMS scanner for OCT imaging, its scanning behaviour and frequency response were verified using the same method for the verification of the high-speed MEMS described in Chapter 2.

First, **Figure 5.19** shows the measured and simulated frequency response of the embedded 6th order Bessel low-pass filters in the MEMS driver board with setting the cut-off frequency to 12 Hz, 120 Hz, and 1.2 kHz, respectively. With increasing the cut-off frequency, the attenuation for the driven differential voltage decreases. In our case, the scanning frequency of the MEMS is optimized to 500 Hz. Hence, the cut-off frequency is set to 1.2 kHz to have a magnitude of nearly 1 without attenuating the differential voltage for driving the MEMS.

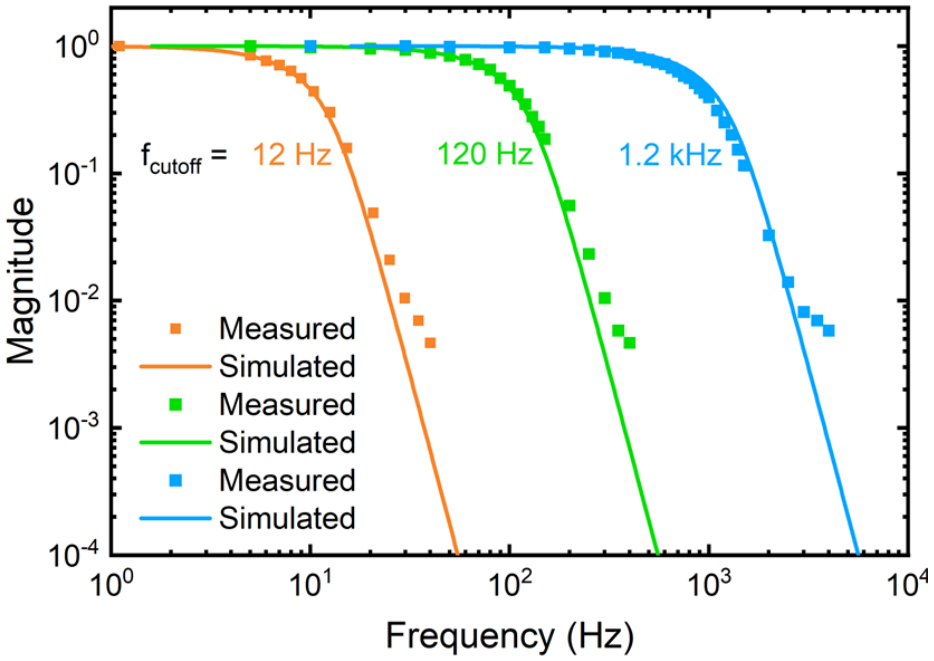

Figure 5.19: Frequency response of the embedded 6th order Bessel low-pass filters in the MEMS driver board with a cut-off frequency of 12 Hz (orange), 120 Hz (green), and 1.2 kHz (blue). Dots represent measured normalised magnitudes. The solid curves indicate the simulated response from MATLAB.

Figure 5.20(a) verified the relationship between the mechanical tilt angle and the differential voltage for each MEMS mirror axis. The MEMS was driven by a 102 Hz

waveform with varying voltage amplitudes. **Figure 5.20**(b) verified the relationship between the magnitude of the mechanical tilt angle of the MEMS mirror and the scanning frequency applied to the X axis, under an input waveform with its Pk-Pk voltage fixed to 0.4 volts. Both results show a close match between our verification and the curves provided in the manufacturer's test report.

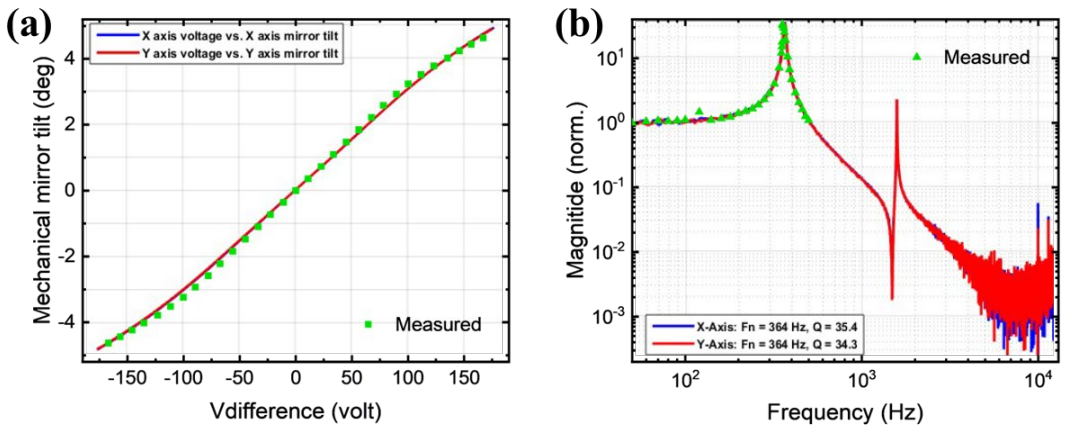

Figure 5.20: (a) Relationship between the mechanical tilt angle of the MEMS mirror and the differential voltage applied to the X axis. (b) Relationship between the magnitude of the mechanical tilt angle of the MEMS mirror and the scanning frequency applied to the X axis. Green dots indicate the measured results. The blue and red curves are from the manufacturer's test report.

After validating the MEMS scanner, it is enabled to scan for imaging using the FDML OCT system and the FDML control software. **Figure 5.21** shows the enface mean intensity projections of a US Air Force (USAF) 1951 resolution test target taken by the colposcopic scanning probe combined with the FDML OCT system. Due to the larger mechanical tilt angle range, this low-speed MEMS can enable a larger field of view of 5 mm x 5 mm. While the design of the probe enables a sphere focal plane, either

the edge or the middle of the sample can be placed in focus as the blurred centre of the images is shown in **Figure 5.21**. To estimate the optimal lateral resolution, the target centre was moved to the edge in focus (**Figure 5.21**(b)). **Figure 5.21**(c) presents the enlarged image of the red box in **Figure 5.21**(b), indicating a measured lateral resolution of 44 μm in air corresponding to the smallest resolvable line pairs in element 4 of group 4. While this probe is still in development, the lateral resolution can be improved with better alignment and the blurring problem may be mitigated by applying adaptive optics or post-processing algorithms to correct the spherical field curvature in the future. Additionally, the axial resolution and imaging depth of an OCT system depend on the central wavelength and FWHM of the spectrum of the light source and number of the spectral sampling channels. Hence, by using the same FDML laser, this combined setup should have the same axial resolution of 13 μm and the same imaging depth of 4.8 mm in the air as demonstrated in Chapter 2.

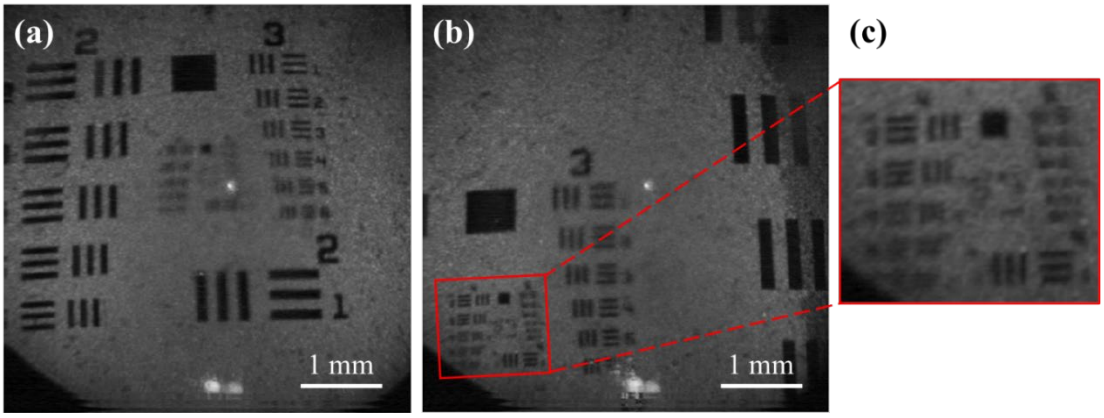

Figure 5.21: Enface mean intensity projections of a US Air Force (USAF) 1951 resolution test target taken by the colposcopic scanning probe combined with the FDML OCT system. (a-b) Typical 5 mm x 5 mm enface images of the USAF, showing a blurred centre because the sphere focal plane of the probe was placed on the edge of the USAF. (c) Enlarged image of the red box in (b), indicating a measured lateral resolution of 44 μm in air corresponding to the smallest resolvable line pairs in element 4 of group 4.

5.3.2. Imaging Results

Figure 5.22 shows the typical B-scans and enface mean intensity projections of a ribbon cable and dorsal hand skin imaged by the colposcopic scanning probe under the FDML OCT system. The combined system has a frame rate of 500 Hz and 4 repeated A-scans are acquired in each lateral step position. Those four A-scan repetitions are averaged to reduce the background noise during image processing. The B-scans (5mm in X) in **Figure 5.22**(a) and (b) are taken from the middle lines of the Y direction of the enface images (5 mm x 5 mm in XY) in **Figure 5.22**(c) and (d).

From **Figure 5.22**(a) and (b), we can clearly identify the structure of the sample such as the cable surface, skin surface, and dermal-epidermal junction. This enables structural analysis such as epidermal thickness estimation. Although the surfaces are bent due to the changing distance between the sample surface and the probe when scanning, this can be calibrated according to the sphere curve by software in the future. **Figure 5.22**(c) and (d) show the enface images within a circular scanning area, indicating that the scanning beam hits the probe edge and achieves the maximum scanning angle limited by the probe optical design. Although the centres are blurred, the surface patterns can still be recognised. This shows the potential of fast and clear imaging and analysis of hard-to-access samples by this colposcopic scanning probe.

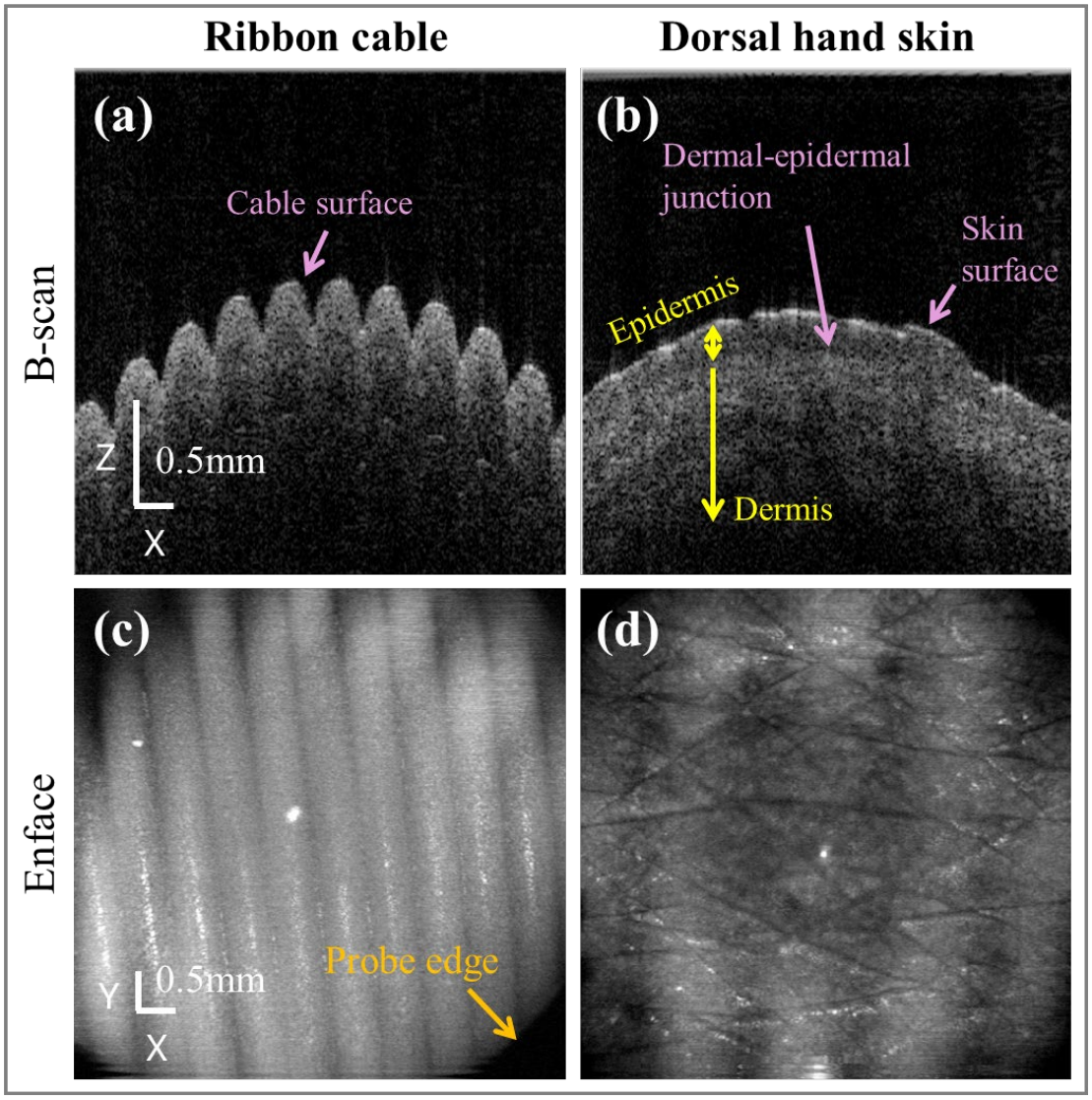

Figure 5.22: Typical B-scans (5mm in X) and enface mean intensity projections (5 mm x 5 mm in XY) of a ribbon cable and dorsal hand skin imaged by the colposcopic scanning probe under the FDML OCT system. (a) B-scan of the ribbon cable. (b) B-scan of the dorsal hand skin showing the epidermis and dermis. (c) Enface image of the ribbon cable. (d) Enface image of the dorsal hand skin.

Additionally, the imaging of the colposcopic scanning probe with FDML OCT is compared to the imaging of our original FDML OCT setup. **Figure 5.23**(a) and (b) shows the enface mean intensity projections on a scanning area of 2.8 mm x 2.8 mm

and 5 mm x 5mm on dorsal hand skin with our original FDML OCT setup and the combined FDML probe setup respectively. **Figure 5.23**(a) shows approximately the same area as the red box in **Figure 5.23**(b). The image distortion is caused by the optical distortion and the changed orientation of the hand surface. With a larger FOV, the enface images taken by the combined FDML probe setup can enable more efficient skin matching. Additionally, the match of the skin patterns between **Figure 5.23**(a) and (b) also indicates that skin matching can be used to find the same location across the enface images taken from different OCT setups.

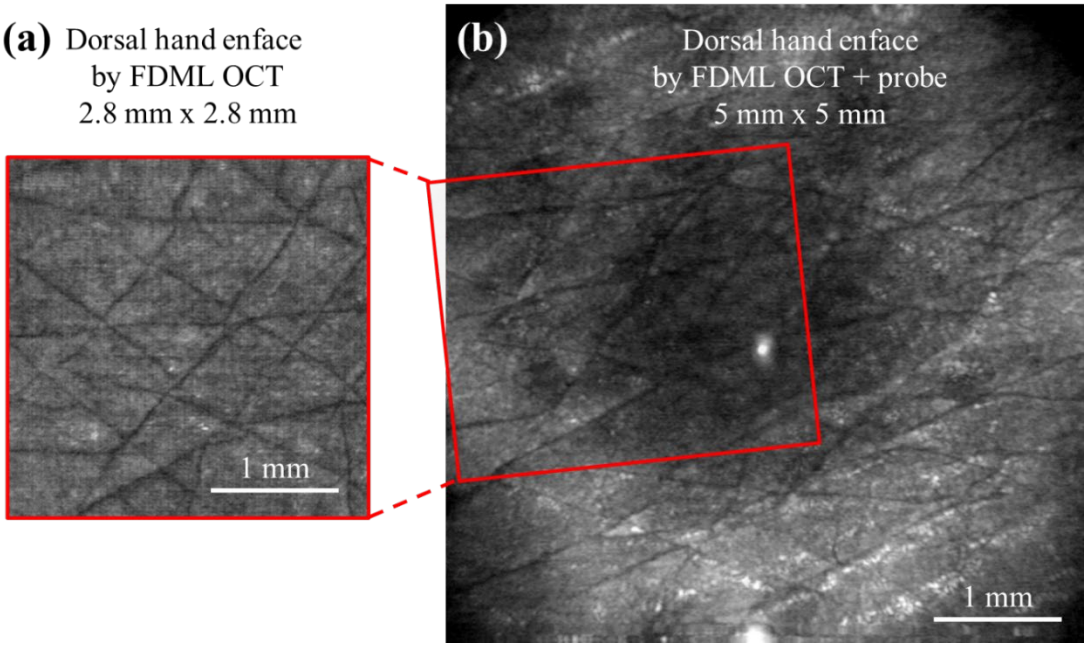

Figure 5.23: (a) Typical enface mean intensity projection on a scanning area of 2.8 mm x 2.8 mm on dorsal hand skin taken by the original FDML OCT setup. (b) Enface mean intensity projection on a scanning area of 5 mm x 5 mm on the close skin site as (a) taken by the combined FDML OCT and colposcopic scanning probe, with a red box marking the roughly same skin patterns.

In general, the colposcopic scanning probe not only shows a good imaging with the assistance of the FDML OCT engine, but also shows the ability for skin analysis such as epidermal thickness estimation and skin matching.

5.4. Conclusion

This chapter demonstrated the extended applications of our FDML OCT system. It is applied first for skin topographical matching. The enface images acquired by FDML OCT in different days show recognisable and repeatable patterns on the dorsal hand skin. Referring to fingerprint recognition, a simple minutiae-based fingerprint matching tool was directly adopted for dorsal hand skin pattern matching. Another algorithm based on the MATLAB computer vision toolbox was also tried. It gave a more reliable skin matching than the fingerprint matching tool although the matching between images in different days is still not satisfying. The feature detection and extraction in both skin matching methods still need improvement. Hence, an optimised enface image processing algorithm was developed in MATLAB to extract the skin ridges or furrows from the enface mean intensity projections of the skin surface. The new input images of skin ridges or furrows show much cleaner surface features, which may contribute to more efficient skin topographical matching.

Secondly, our FDML OCT engine was connected to an in-house colposcopic scanning probe for aligning, characterizing and imaging testing. This probe is developed for cervical imaging in vivo. The frequency response of the low-speed MEMS scanner integrated into this probe was validated first. After enabling the MEMS scanner, the combined FDML probe setup was characterized, showing a measured lateral resolution of 44 μm, an axialresolution of 13 μm, and an imaging depth of 4.8

mm in air. With MEMS running at an X-axis scanning frequency of 500 Hz, this probe was used to image a ribbon cable and dorsal hand skin in a scanning area of 5 mm x 5 mm. Although a blurring problem exists, the B-scans and enface images clearly indicate the structural information of the samples. The results show the ability to analyse skin epidermal thickness and skin patterns for matching by this combined setup.

In summary, this section shows the flexible performance range of applications of our FDML OCT system, which can be upgraded depending on the clinical needs.

References

[1] L. N. Darlow and J. Connan, "Efficient internal and surface fingerprint extraction and blending using optical coherence tomography," *Applied optics,* vol. 54, no. 31, pp. 9258-9268, 2015.

[2] H. S. G. da Costa, L. Silva, O. R. Bellon, A. K. Bowden, and R. K. Czovny, "3D Matching techniques using OCT fingerprint point clouds," in *Imaging, Manipulation, and Analysis of Biomolecules, Cells, and Tissues XV*, 2017, vol. 10068: SPIE, pp. 33-39.

[3] R. K. Czovny, O. R. Bellon, L. Silva, and H. S. Costa, "Minutia matching using 3D pore clouds," in *2018 24th International Conference on Pattern Recognition (ICPR)*, 2018: IEEE, pp. 3138-3143.

[4] F. Liu, G. Liu, Q. Zhao, and L. Shen, "Robust and high-security fingerprint recognition system using optical coherence tomography," *Neurocomputing,* vol. 402, pp. 14-28, 2020.

[5] B. Ding *et al.*, "Surface and internal fingerprint reconstruction from optical coherence tomography through convolutional neural network," *IEEE Transactions on Information forensics and security,* vol. 16, pp. 685-700, 2020.

[6] B. Ding, H. Wang, R. Liang, Y. Zhang, and P. Chen, "End-to-end surface and internal fingerprint reconstruction from optical coherence tomography based on contour regression," *IEEE Transactions on Information Forensics and Security,* vol. 18, pp. 162-176, 2022.

[7] K. Korotkov *et al.*, "An improved skin lesion matching scheme in total body photography," *IEEE journal of biomedical and health informatics,* vol. 23, no. 2, pp. 586-598, 2018.

[8] J. Abraham, P. Kwan, and J. Gao, "Fingerprint matching using a hybrid shape and orientation descriptor," *State of the art in Biometrics,* pp. 25-56, 2011.

[9] V. K. Alilou. "FingerPrint Matching: A simple approach." GitHub. https://github.com/alilou63/fingerprint (accessed Jan 09, 2025).

[10] MathWorks. "Automatically Find Image Rotation and Scale." MathWorks. https://uk.mathworks.com/help/vision/ug/find-image-rotation-and-scale-using-automated-feature-matching.html (accessed Jan 09, 2025).

[11] F. S. Hooper, R. Yuan, D. G. Revin, D. O. Anumba, and S. J. Matcher, "Optical design and simulation of a cervical scanning probe for polarization-sensitive optical coherence tomography using Ansys Zemax OpticStudio," in *European Conference on Biomedical Optics*, 2023: Optica Publishing Group, p. 126321U.

6. Conclusion and Future work

6.1. Summary

This chapter first concludes the thesis of the previous five chapters. Then four promising directions extended from this work are discussed in the future work.

6.2. Conclusions

Optical coherence tomography (OCT) has been widely used for the clinical research and diagnosis of many dermatological applications, such as non-melanoma skin cancers (NMSC), inflammatory skin, treatment monitoring, wound healing, and tattoo removal. However, the current commercially available OCT setups for skin imaging have very slow scan rates and acquisition speeds. To solve this problem, an in-house near-infrared high-speed Fourier-domain mode-locking (FDML) OCT system was introduced in this work.

Chapter 2 first described the construction, optimisation, and characterisation of this FDML OCT system. To achieve rapid imaging, this system employed a 1310 nm FDML laser providing a high A-scan rate of 1.67 MHz, an ultrafast MEMS scanner enabling a scanning frequency of 3 kHz, and a data acquisition unit (photodetector and digitizer) allowing a high spectral sampling rate of 1.9 GHz. The optics in the Michelson interferometer of the FDML OCT have been optimised for obtaining the interference spectrum efficiently and safely from the human skin in vivo. After hardware alignment, the FDML OCT system has been characterised by a measured axial and lateral resolution of ~13 μm and ~25 μm in air, a lateral FOV of 2.9 x 2.9 mm^2, a measured sensitivity of ~100 dB, and an imaging depth of ~4.8 mm in air. These capabilities enable good imaging performance in the human hand. Imaging results have

been demonstrated on the thumbnail, index fingertip skin, palmar skin, dorsal hand skin, and forearm skin. Additionally, software has been developed to control the FDML OCT system for real-time cross-sectional imaging and data collection using different OCT scan protocols.

In Chapter 3, this FDML OCT system has been applied to detect the structural and vascular information of the dorsal hand in vivo. An automatic algorithm has been developed in MATLAB to segment the skin surface and dermal-epidermal junction (DEJ) from the cross-sectional OCT intensity B-scan image for estimating the epidermal thickness. A detailed map of epidermal thickness ranging from 110 to 150 μm was overlaid on a 2.8 mm x 2.8 mm enface mean intensity projection of dorsal hand skin, showing the epidermal thickness in each position. Another MATLAB algorithm has been developed to identify the blood flow caused by the red blood cells (RBCs) based on the difference-based and speckle-variance OCT angiographic calculations for visualising the skin's superficial vascular plexus. Two OCTA scan protocols of B-mode and CM-mode have been employed to achieve the cross-sectional (2.8 mm in X) and enface (2.8 mm x 2.8 mm in XY) imaging of the blood vessels beneath dorsal hand skin, with a fundamental interscan time of 0.33 ms and 110 ms, respectively. The optimal time interval in B-mode has been found at around 100 ms to have the best image contrast, and the total number of volume repetitions in CM-mode has been optimised to 4, reducing the acquisition time to 0.44 seconds while maintaining clear vasculature imaging. Although only visualisation of the blood vessels has been demonstrated, the vascular information such as vascular depth, diameter, and density can be further analysed.

However, only qualitative vascular information can be analysed by this OCTA algorithm. By investigating the decorrelation relationship between the normalised

amplitude difference of the flow signal from two B-scan repeats at the same position and their time interval, Chapter 4 shows the capability of using FDML OCT to quantify the cutaneous blood flow velocity. A MATLAB algorithm has been developed based on the variable interscan time analysis (VISTA) processing with introducing an auto-curvefitting improvement to determine the decorrelation coefficient for each flow velocity. This VISTA-based auto-fitting algorithm has been validated first by quantifying the flow velocity of milk infused into an 80-μm glass capillary tube, showing a high correlation between the calculated decorrelation coefficients and the preset flow velocities in a range of 0.3 mm/s to 60 mm/s. By utilising the B-mode and CM-mode scan protocols, with a fundamental interscan time of 0.33 ms and 8 ms respectively, the decorrelation coefficient mapping of the cutaneous blood flow has been achieved on the cross-sectional and enface superficial vasculature. An optimised scan protocol of CM-mode-guided B-mode has been proposed to align the same vessels visualised in B-mode and CM-mode, showing the decorrelation coefficient while instructing the vascular diameter for each vessel.

The capability of quantifying the blood perfusion using the FDML OCT system accelerates the translation of OCT to clinics for assessing more dermatological diseases. In clinics, it is important to monitor the biomarker changes or treatment of the affected skin for the diagnosis and pathological understanding by the dermatologists. One current challenge of OCT imaging is that the mm^2-level field of view is too small to be remembered by dermatologists or patients for precise monitoring. Although tools like marker pens can be used to mark the skin position, the inks usually can be easily removed. Chapter 5 provides a non-invasive solution of using skin surface patterns shown in the OCT enface images as the reference to record the information at the same site. A 128-day repeated measurement of imaging three skin sites using the FDML OCT

system proves the idea of using the unique skin pattern as a stable marker. Based on this, the following preliminary study demonstrates the potential of matching the skin pattern automatically with a computer vision toolbox to accurately locate the scanned skin site for monitoring.

Furthermore, in Chapter 5, the FDML OCT system has also been applied to assess the alignment and imaging performance of an in-house colposcopic probe developed by my colleague for imaging the cervical structure in vivo.

In summary, this thesis has presented a high-speed in-house FDML OCT engine for non-invasively assessing skin biomarkers such as epidermal thickness, vascular morphology, and cutaneous blood flow velocity. This FDML OCT engine not only shows the various functional uses for clinics but also provides rapid scanning, enabling real-time imaging and more efficient data collection for the convenience of the patients.

6.3. Future work

This thesis has successfully achieved the project aim of developing a high-speed near-infrared FDML OCT system for dermatological applications. While the in-house system has demonstrated its ability to capture both structural and vascular information from human skin, several practical barriers remain that hinder its widespread clinical adoption.

One of the primary challenges is the high cost of the FDML OCT system, largely due to the use of a Fourier-Domain Mode-Locked (FDML) laser, which alone exceeds $70,000. This considerable expense limits its accessibility for many clinical settings. Additionally, although the system offers fast volumetric imaging, it still requires

technically skilled operators to perform alignment, calibration, and data processing, which complicates its use in routine clinical practice. The current version of the system also lacks user-friendly features, automated interpretation tools, and integration with clinical workflows, all of which are necessary for broader deployment. Moreover, the time required for data acquisition, image processing, and analysis may still be considered inefficient in high-throughput environments.

Despite these challenges, there are still four promising directions for future development: 1) the OCTA algorithm can be improved, and more functions can be added to measure the vascular depth, diameter, and density. 2) the VISTA-based auto-fitting algorithm and FDML OCT setup can be improved for blood flow analysis. 3) the skin topographical matching can be achieved by using the input images generated from the optimised image processing algorithm. 4) the functionality of the FDML OCT system can be expanded.

6.3.1. Improving the OCTA Algorithm and Measuring Additional Vascular Biomarkers Using FDML OCT

In Chapter 3, we presented an OCTA algorithm that can automatically visualise the skin superficial vascular plexus. However, only the angiographic morphology has been demonstrated, and no quantitative vascular information can be obtained by this OCTA algorithm. In 2018, our previous study reported the potential of using quantitative vascular metrics for the sub-clinical assessment of atopic dermatitis. By measuring the vascular metrics (vessel depth, diameter, length, density, and fractal dimension), Rob et al have found a correlation between these metrics and the severity of atopic dermatitis. Therefore, measuring these vascular metrics quantitatively is important for determining the severity of the skin conditions [1].

6.3.1.1. Measuring Vascular Depth

To measure vascular depth, in Section 3.4, we have introduced an image processing technique of skin flattening to flatten the skin surface to the top horizontal line of the OCT B-scan image. The tissue below the skin surface will be also displaced to the top line correspondingly. As shown in **Figure 3.12**(a-c), the Z-axis scale shows the physical distance in tissue, and the vascular depth can be easily measured by counting the number of vertical pixels from the top line to each vessel position (top edge of each bright tail).

6.3.1.2. Measuring Vascular Diameter, Length, and Density

Figure 3.12(e-f) shows the enface vasculature images with the scale in millimetres, allowing a rough estimation of the vascular metrics such as vessel diameter, length, and density. To quantitatively determine these metrics, referring to our previous work [1], the core processing steps are: 1) apply a multi-scale Hessian filter [2] to the enface vasculature image (e.g. **Figure 3.12**(e)) to get a vesselness mask. 2) binarize the Hessian-filtered enface image by an automatically determined threshold based on Otsu's method [3]. 3) generate a vessel skeleton using the binarized enface image.

Utilising the binarized data and vessel skeleton, the vascular diameter can be defined as double the mean distance (radius) from the pixel in the skeleton (vessel centre) to the closest 0-value pixel in the binarized image (vessel edge). The vascular length can be defined as the mean length of each segment between branching points in the skeleton [4]. The vascular density can be defined as the result of dividing the total number of vessel segments by the scanning area size in the enface image.

6.3.1.3. Mitigating the Vessel Tail Artefacts

The vessel tail artefacts occur due to the shadowing effect caused when the vertically incident laser beam first illuminates the vessels. As shown in **Figure 3.12**(b) and (c), with the current OCTA algorithm (Section 3.4), the vessel tail artefacts below the vessels have not yet been removed, which makes it difficult to visualise the exact shape of the vessels. Therefore, it is useful to remove or mitigate the vessel tail artefacts.

There are two solutions to mitigate the tail artefacts in the angiographic B-scan image:

1) Adapting vessel diameter: If an enface vasculature image can be generated and the vessels in the B-scan image can be aligned with the same vessels in the enface image, assuming the shape of blood vessels as a cylinder, the vertical diameter of a vessel in the B-scan should be equal to the lateral diameter measured in the enface image. By applying the vascular diameter to each vessel in the angiographic B-scan, only the vessel area within this vascular diameter will remain. Hence, the tail artefacts can be removed.
2) Optimally Oriented Flux (OOF): OOF is first proposed by Law and Chung [5]. OOF computes the image gradient flux after determining the optimal axis for projecting the image gradient. By localizing the computation to the boundaries of spherical regions, OOF avoids accounting for closely located adjacent structures. Consequently, when applying OOF to compute the angiographic B-scan image, vessel tail artefacts are ignored, and only the planar structure of the vessels is detected. Hwang et al have applied OOF to the difference-based angiographic image of retinal capillaries with suppressing the vessel tail artefacts [6].

After removing or reducing the vessel tail artefacts, the three-dimensional vasculature can be further obtained by clearly demonstrating the vessel depth, direction, and shape.

6.3.2. Improving VISTA-Based Flow Velocity Quantification with FDML OCT

In Chapter 4, we presented an optimised VISTA-based curve auto-fitting algorithm for quantifying the vascular blood flow velocity and achieved the decorrelation coefficient mapping on the cross-sectional and enface vasculature beneath human skin in vivo. The decorrelation coefficient calculation for each position is based on a time-series measurement of the backscattered optical signal fluctuations in this position.

6.3.2.1. Calibrating Flow Velocity by Angle of Blood Vessel

During this measurement, the laser beam and the skin stay motionless, and only the horizontal flow perpendicular to the cross-sectional B-scan plane is detected. However, the direction of each vessel beneath the skin is different, and not always perpendicular to the B-scan plane. This means that the current algorithm only measures the transverse vector of the blood flow velocity for each vessel. Since the three-dimensional angiographic vasculature can be achieved by CM-mode scan protocol using the FDML OCT system, the angle θ between each vessel and the B-scan plane can be further calculated. The real blood flow velocity can be calibrated by dividing the current quantified horizontal flow velocity by the $\sin\theta$.

6.3.2.2. Blood Flow Velocity vs Vascular Diameter

The vessels normally have different diameters with different blood perfusion rates. In 2024, Tanaka et al quantitatively analysed the relationship between the blood flow velocity and the vessel diameter for retinal vessels using OCTA-VISTA, showing higher blood flow parameters in vessels with larger diameters [7]. Therefore, we can also investigate the relationship between the blood flow velocity and the vessel diameter for the skin's superficial vascular plexus. Monitoring or comparing the blood flow in vessels with similar diameters can contribute to a more accurate diagnosis and understanding of the pathology. For instance, in the FDML SLS study (Section 4.4.1.3), it is more rigorous to evaluate the relationship between the blood flow velocity and the skin irritation level by comparing the blood flow velocity in different-site vessels with different irritation levels but similar diameters.

6.3.2.3. Improving Flow Detection by Split-spectrum Process

As discussed in Section 6.3.2.1, the FDML OCT system mainly detects the lateral cutaneous blood flow using VISTA-based flow analysis. However, the FDML OCT system has a lower lateral resolution of ~25 μm than the axial resolution of ~13 μm, resulting in a lower sensitivity of detecting the flow signal fluctuations caused by the lateral RBCs' motion.

To improve the SNR of lateral flow detection, a split-spectrum method was proposed to reduce the motion noise in only the axial direction by decreasing the axial resolution without losing any lateral flow signal [8]. The core procedures of this method are to 1) equally split the interference spectrum recorded by the FDML OCT system into different wavenumber bands by Gaussian bandpass filtering, 2) calculate the

normalised difference or decorrelation of the flow signal for each band, 3) average the normalised difference or decorrelation values from all bands.

Figure 6.1 compares the difference-based OCTA processing without and with the split-spectrum method. **Figure 6.1**(a) shows a typical intensity B-scan image of dorsal hand skin taken by the FDML OCT system, and **Figure 6.1**(b) shows its normalised amplitude difference angiographic image processed by the difference-based OCTA (Section 3.4.1). After applying the split-spectrum process to **Figure 6.1**(a) and (b), **Figure 6.1**(c) shows the intensity B-scan image with worse axial resolution, and **Figure 6.1**(d) shows the split-spectrum normalised OCTA image, with significantly improved SNR than **Figure 6.1**(b). This proves that the split-spectrum can further improve the transverse flow detection for VISTA flow velocity quantification. Therefore, the split-spectrum method can be introduced into the decorrelation estimation progress of the current VISTA-based auto-fitting algorithm.

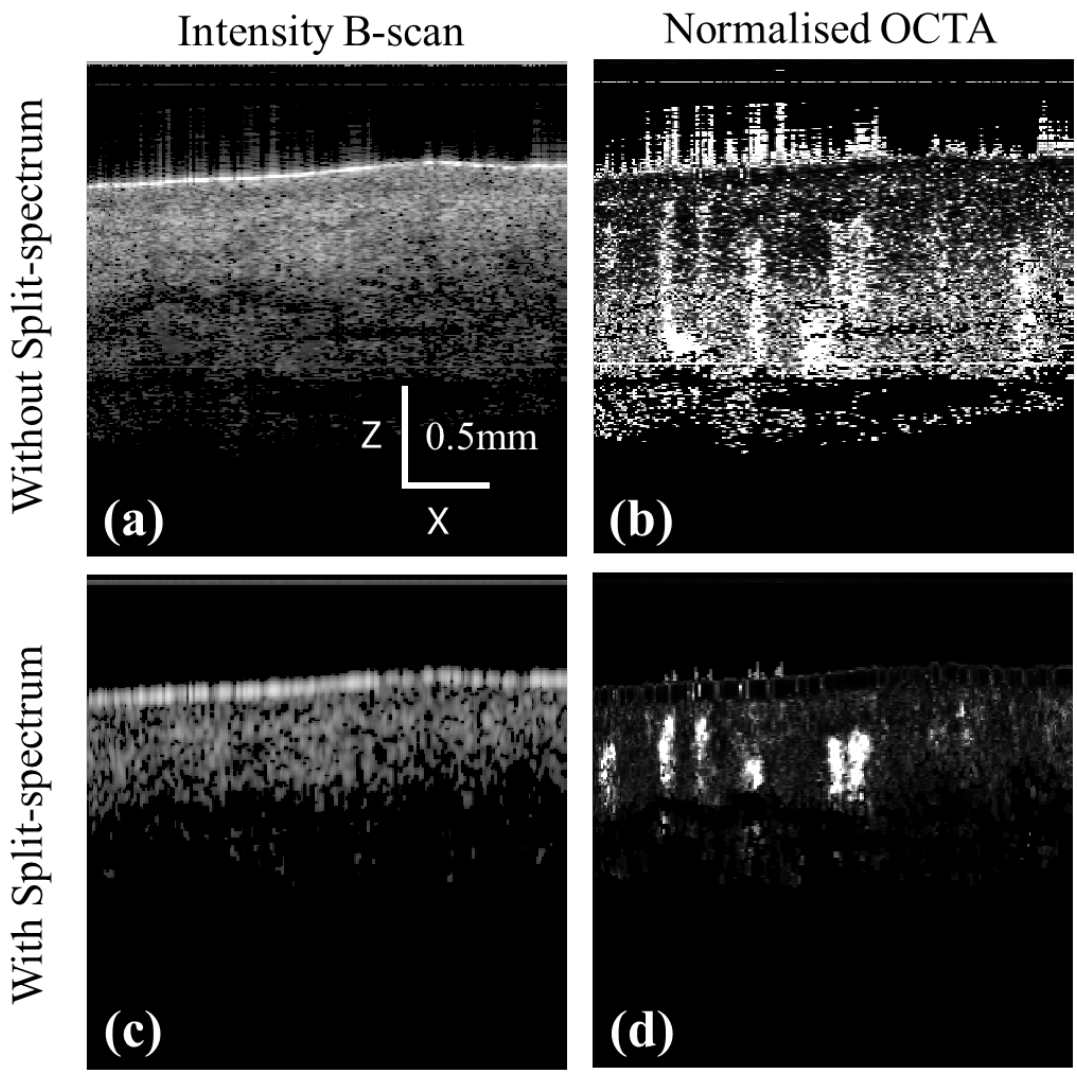

Figure 6.1: Comparison of the difference-based OCTA processing without and with split-spectrum method. The interference spectrum recorded by the FDML OCT system was equally split into four wavenumber bands. (a) Typical intensity B-scan image of dorsal hand skin taken by the FDML OCT system. (b) Normalised amplitude difference angiographic image of (a) processed by the difference-based OCTA (Section 3.4.1). (c)-(d) Corresponding images of (a)-(b) with applying the split-spectrum processing before the difference-based OCTA.

6.3.2.4. Upgrading the FDML OCT Setup for VISTA Flow Analysis

The current FDML OCT system has a fundamental interscan time of 0.33 ms, which is too short for VISTA flow analysis of superficial blood flow in the skin. In other words, the MEMS scanner operates too quickly, while the cutaneous blood flow is relatively slow, resulting in a long decorrelation saturation time of more than 300 ms and an excessive number of time-series measurements at the same position during this period (Section 4.5). To optimise the lengthy data collection and reduce the number of sample points required, two solutions can be considered: (1) decreasing the frame rate to increase the fundamental interscan time, or (2) reducing the decorrelation saturation time of blood flow.

To decrease the frame rate, the MEMS scanner can be operated at a lower scanning frequency. To reduce the saturation time, a shorter lateral point spread function (PSF) is required for RBCs to displace along (Section 4.5.1). This can be achieved by using an objective with a higher numerical aperture to replace the current LSM03 objective in the sample arm of the FDML OCT system, resulting in a smaller spot size (i.e., lateral PSF or resolution). However, as discussed in Section 2.4.3, the LSM03 objective has not been fully utilized to achieve a smaller spot size with an incident beam size of 4 mm because the current beam diameter is limited by the MEMS mirror diameter of 2 mm. Therefore, a scanner with a larger diameter mirror could be employed to address this limitation.

Additionally, Section 4.4.2 demonstrated the instability of the MEMS scanner, which leads to failed OCTA imaging and VISTA flow analysis when using the BM-mode scan protocol. A more stable scanner, such as a galvo resonant scanner, could be employed to replace the current MEMS scanner. Once the number of time-series

repeated measurements is reduced using one of the two solutions mentioned above, the BM-mode can be utilized to acquire datasets for VISTA analysis at more Y positions, with fewer B-scan repetitions at each Y position, without exceeding the digitizer's on-board memory. By implementing this approach, decorrelation coefficient mapping can be generated and overlaid on a larger FOV enface vasculature image compared to the current CM-mode decorrelation mapping shown in **Figure 4.13** (2.8 mm × 0.2 mm FOV).

Lastly, the current computer configuration used in the FDML OCT system is quite outdated and can be improved by upgrading to a more powerful CPU and GPU to enhance computation, image processing and software running speeds, as well as replacing the SSD to improve data writing and reading speeds. These upgrades may enable real-time volume and OCTA vasculature imaging. Since the VISTA-based auto-fitting algorithm requires a relatively long time to quantify the blood flow velocity, a potential solution is to select a specific vessel visualised in the real-time vasculature and focus on quantifying the blood flow velocity in this vessel in real-time.

6.3.3. Achieving More Efficient Skin Topographical Matching

In Section 5.2, we first tried the skin topographical matching for the enface surface images of dorsal hand skin taken by the FDML OCT system, using two algorithms based on a fingerprint-matching tool and a MATLAB Computer Vision Toolbox with feature detection and extraction functions. Although the two algorithms show the potential of topographical matching, the matching results are not ideal. To improve the matching results, we proposed an optimised enface image processing algorithm to extract the skin ridges or furrows from the raw skin surface enface projections. The

refined enface image demonstrates much clearer and cleaner patterns of the ridges or furrows than the noisy raw enface. Therefore, the new refined enface images can be used as inputs into the two skin-matching algorithms and a more efficient topographical matching is assumed to be achieved.

Once accurate and efficient matching can be achieved, the matching score or similarity can be determined. Considering the clinical uses, real-time skin matching and similarity computing will be the next step, which is very useful for doctors to quickly identify or monitor the treated skin sites of patients.

Additionally, the current skin topographical matching algorithms only match the skin surface patterns. From the enface angiographic vasculature images of **Figure 4.12**(b), (e), (h), and (k), it is obvious that the vasculatures in the Y middle part of those images are matched. Hence, it is also possible to match the superficial vascular plexus beneath the skin in the future.

6.3.4. Expanding the Functionality of the FDML OCT Setup

The current FDML OCT system can only generate structural and angiographic images. By introducing a polarisation delay unit (**Figure 6.2**), the system can be enhanced to enable polarisation-sensitive imaging. This unit splits the laser beam into two polarised beams with horizontal and vertical polarisation states using a polarisation beam splitter (PBS) and two quarter-wave plates (QWPs). An optical path length difference of Δz is introduced in this unit to create a delay between the two polarised beams. A polarisation-maintaining coupler is then used to split the interference signal into two PBSs while preserving the polarisation states of the beams. These PBSs separate the horizontal and vertical interference signals, which are sent to two dual-balanced

photoreceivers for suppressing the direct current (DC) signal and amplifying both polarised signals.

As a result, this FDML polarisation-sensitive (PS) OCT system can estimate the local birefringence of a sample by measuring the phase retardance caused by birefringent materials. For instance, in clinical applications, it could be used to detect collagen beneath human skin [9, 10]. Thus, the FDML PS-OCT system offers expanded functionality, making it more versatile for clinical diagnosis.

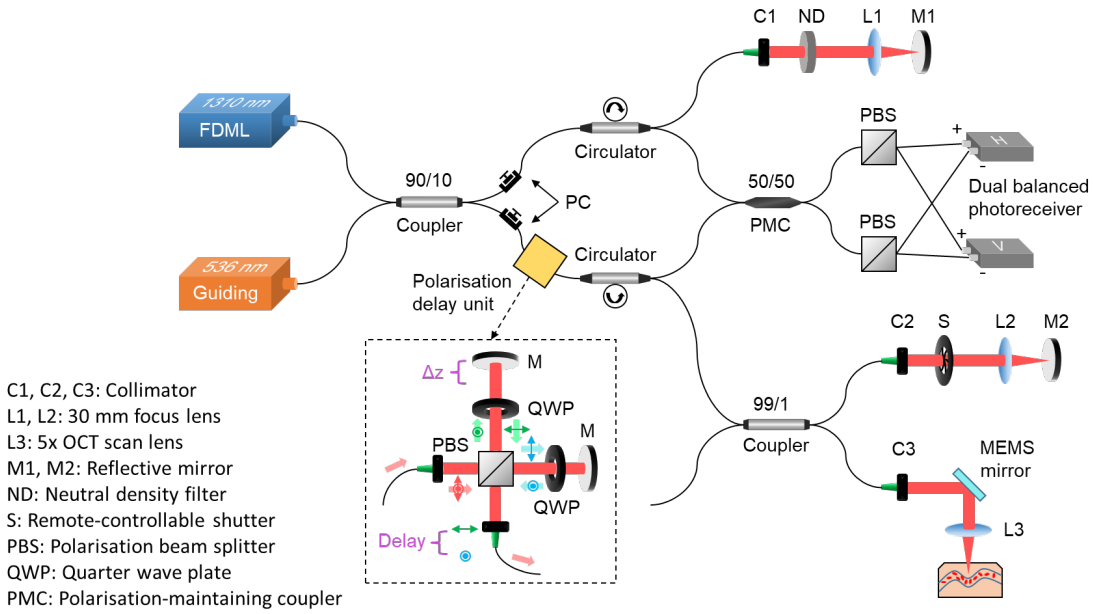

Figure 6.2: The schematic of a high-speed FDML polarisation-sensitive (PS) OCT system.

References

[1] R. A. Byers *et al.*, "Sub-clinical assessment of atopic dermatitis severity using angiographic optical coherence tomography," *Biomedical optics express,* vol. 9, no. 4, pp. 2001-2017, 2018.

[2] A. F. Frangi, W. J. Niessen, K. L. Vincken, and M. A. Viergever, "Multiscale vessel enhancement filtering," in *Medical Image Computing and Computer-Assisted Intervention—MICCAI'98: First International Conference Cambridge, MA, USA, October 11–13, 1998 Proceedings 1*, 1998: Springer, pp. 130-137.

[3] N. Otsu, "A threshold selection method from gray-level histograms," *Automatica,* vol. 11, no. 285-296, pp. 23-27, 1975.

[4] P. Soille and P. Soille, "Geodesic transformations," *Morphological Image Analysis: Principles and Applications,* pp. 183-218, 2004.

[5] M. W. Law and A. C. Chung, "Three dimensional curvilinear structure detection using optimally oriented flux," in *Computer Vision–ECCV 2008: 10th European Conference on Computer Vision, Marseille, France, October 12-18, 2008, Proceedings, Part IV 10*, 2008: Springer, pp. 368-382.

[6] Y. Hwang *et al.*, "Retinal blood flow speed quantification at the capillary level using temporal autocorrelation fitting OCTA," *Biomedical Optics Express,* vol. 14, no. 6, pp. 2658-2677, 2023.

[7] F. Tanaka *et al.*, "Developing quantitative analysis program of blood flow velocity according to vessel diameter for neovascular age-related macular degeneration using OCTA-VISTA," *Scientific Reports,* vol. 14, no. 1, p. 16352, 2024.

[8] Y. Jia *et al.*, "Split-spectrum amplitude-decorrelation angiography with optical coherence tomography," *Optics express,* vol. 20, no. 4, pp. 4710-4725, 2012.

[9] M. C. Pierce, R. L. Sheridan, B. H. Park, B. Cense, and J. F. De Boer, "Collagen denaturation can be quantified in burned human skin using polarization-sensitive optical coherence tomography," *Burns,* vol. 30, no. 6, pp. 511-517, 2004.

[10] P. Tang *et al.*, "Polarization sensitive optical coherence tomography with single input for imaging depth-resolved collagen organizations," *Light: Science & Applications,* vol. 10, no. 1, p. 237, 2021.

7. Appendices

7.1. Photograph of the Setup for Measuring the Mechanical Tilt Angle of the MEMS Mirror

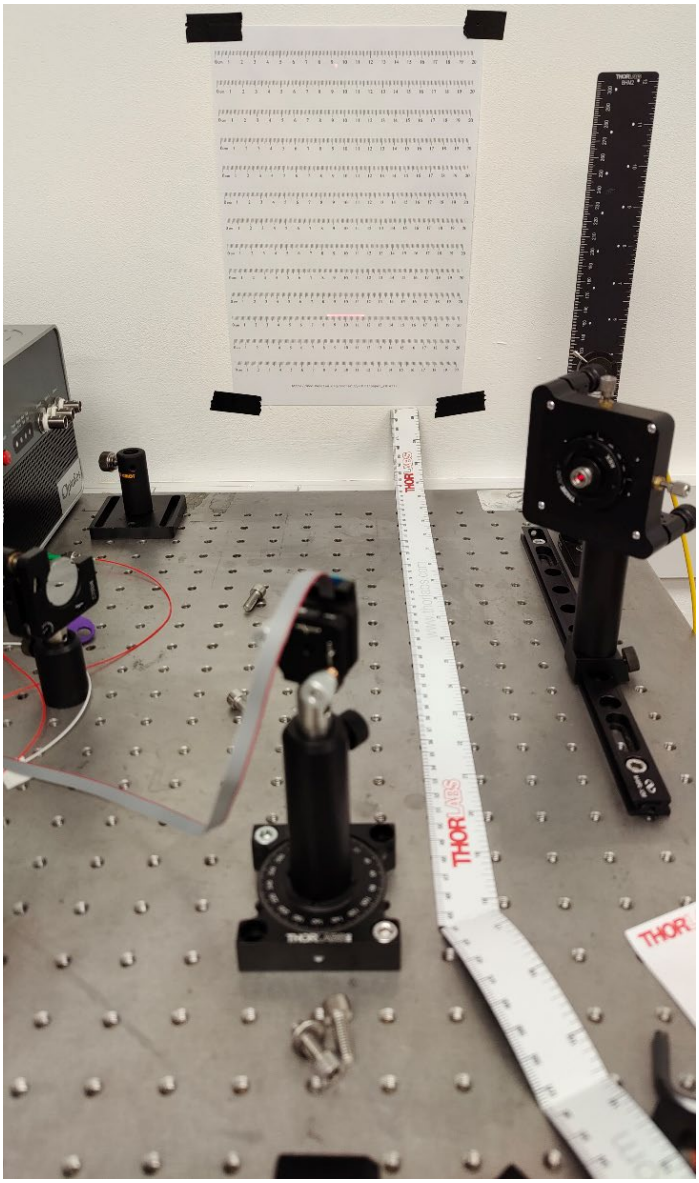

Figure 7.1: Photograph of the setup used to measure the mechanical tilt angles of the MEMS mirror driven by different differential voltages. A red laser beam was collimated to the MEMS mirror and reflected to the wall. The mechanical tilt angle was estimated based on the scan length on the wall and the distance between the scanner and the wall.

7.2. Photograph of the Sample Arm of the In-house FDML OCT System

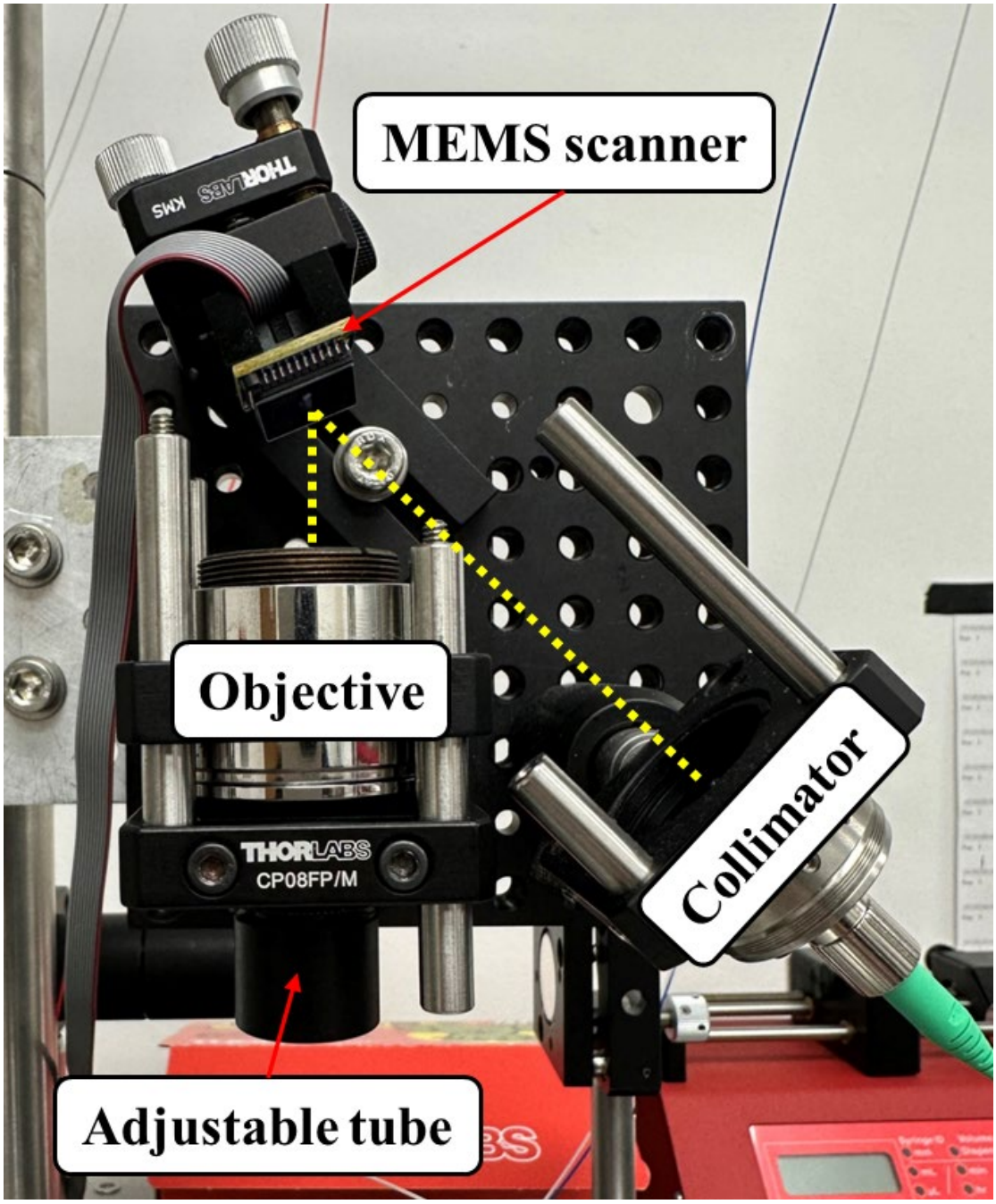

Figure 7.2: Photograph of the sample arm of the in-house FDML OCT system, showing the collimator, MEMS scanner, objective, and adjustable lens tube for stabilising the hand.

7.3. Photograph of the In-house Designed Flow Phantom

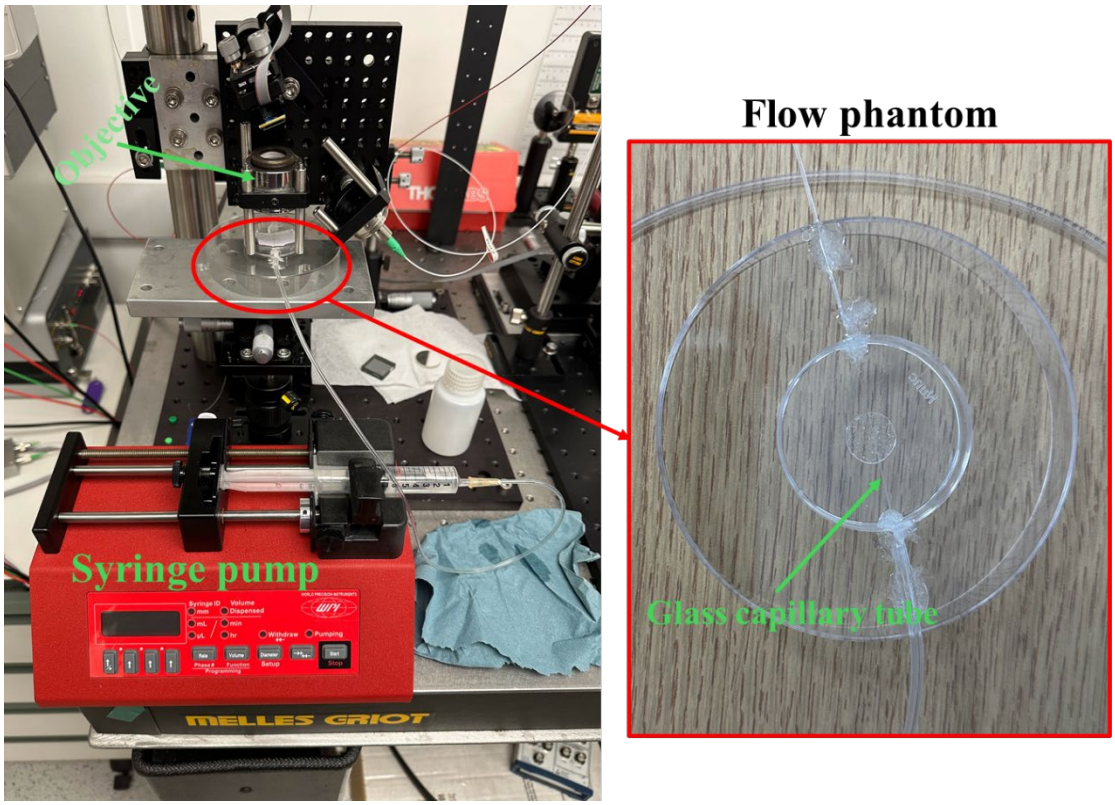

Figure 7.3: Left: Photograph of the setup used to collect OCT datasets of milk flow in the flow phantom, with preset flow velocities controlled by a syringe pump for VISTA flow velocity quantification. Right: Photograph of the in-house-designed flow phantom featuring an 80-µm inner diameter glass capillary tube glued at the centre on top of a Petri dish.